The Super Fine-Grained Detector for the Near Detector Upgrade of the T2K Experiment: From Construction and Commissioning to the First Physics Analysis

A Dissertation Presented

by

Jiayu Ji

to

The Graduate School

in Partial Fulfillment of the Requirements

for the Degree of

Doctor of Philosophy

in

Physics

Stony Brook University

August 2026

Stony Brook University

The Graduate School

Jiayu Ji

We, the dissertation committee for the above candidate for the Doctor of Philosophy degree, hereby recommend acceptance of this dissertation.

Clark McGrew – Dissertation Advisor
Associate Professor, Department of Physics and Astronomy

Ciro Riccio – Chairperson of Defense
Assistant Professor, Department of Physics and Astronomy

Rouven Essig
Professor, C.N. Yang Institute for Theoretical Physics

Guang Yang
Scientist, Brookhaven National Laboratory

This dissertation is accepted by the Graduate School.

Celia Marshik
Dean of the Graduate School

Abstract of the Dissertation

The Super Fine-Grained Detector for the Near Detector Upgrade of the T2K Experiment: From Construction and Commissioning to the First Physics Analysis

by

Jiayu Ji

Doctor of Philosophy

in

Physics

Stony Brook University

2026

The T2K (Tokai to Kamioka) experiment is a long-baseline accelerator neutrino oscillation experiment designed to measure neutrino oscillation parameters θ_{13}, θ_{23}, Δm^2_{32}, and to constrain the Dirac phase δ_{CP}. The neutrino beam is produced at the Japan Proton Accelerator Research Complex (J-PARC) in Tokai. The beam is first measured by the T2K near detector complex, located 280 meters downstream of the beam source, and then detected at Super-Kamiokande, a water Cherenkov far detector 295 km away.

The near detector measures the beam before oscillation and constrains flux and cross-section systematic uncertainties for the far detector prediction. To further reduce the uncertainties in the predicted event rates at Super-Kamiokande, ND280 was upgraded with the Super Fine-Grained Detector (SuperFGD), two High-Angle Time Projection Chambers, and six Time-of-Flight planes. The SuperFGD is a highly granular plastic scintillator detector made of optically isolated 1 cm^3 cubes read out by wavelength-shifting fibers in three orthogonal directions.

It serves as both an active neutrino interaction target and a charged-particle tracker, providing three-dimensional track reconstruction.

This dissertation presents work on the SuperFGD from construction and commissioning to its first physics analysis, including detector assembly, charge calibration, electronics response studies, Michel electron tagging, and the selection of inclusive ν_μ charged-current (CC) interactions. After construction and commissioning, the upgraded near detector began taking neutrino beam data in June 2024. The first physics analysis in this thesis selects inclusive ν_μ CC interactions with vertices within the SuperFGD fiducial volume using Run 13c data taken from June 6 to June 28, 2024, corresponding to 1.57×10^{20} protons on target. This analysis demonstrates the performance of the upgraded near detector and establishes the foundation for future neutrino cross-section and oscillation analyses.

To my parents, for their endless love and support.

Contents

List of Figures **ix**

List of Tables **xv**

Acknowledgements **xvi**

Outline **xvii**

1 Introduction **1**
1.1 A brief history of the neutrino discovery 1
1.2 Neutrinos in the Standard Model 3
1.3 Neutrino oscillation 4
1.3.1 Three-flavor neutrino oscillation framework 5
1.3.2 Experimental measurements and open questions 11
1.4 Neutrino-nucleus interactions 13
1.4.1 Neutrino-nucleon interactions 13
1.4.2 Nuclear effects 14

2 The T2K Experiment **16**
2.1 Neutrino beamline 17
2.2 Near detector complex 20
2.2.1 INGRID on-axis detector 21
2.2.2 ND280 off-axis detector 21
2.3 Super-Kamiokande 24
2.4 T2K oscillation analysis strategy 25

3 Near Detector Upgrade **27**
3.1 Motivation for the ND280 upgrade 27
3.2 Upgraded near detector configuration 28
3.2.1 High-angle time projection chambers 28
3.2.2 Time-of-flight detector 29

3.3 Installation . . . 32
3.4 Data and Monte Carlo production . . . 32
3.5 Reconstruction . . . 33

4 The Super Fine-Grained Detector 34
4.1 Overview of the SuperFGD . . . 34
4.2 Detector System . . . 35
4.2.1 Cube . . . 35
4.2.2 Wavelength-shifting fibers . . . 37
4.2.3 Multi-pixel photon counter . . . 37
4.2.4 LED calibration system . . . 38
4.2.5 Mechanical box . . . 39
4.2.6 Electronics architecture . . . 40
4.2.7 Front-end boards . . . 41
4.3 Assembly . . . 42
4.4 Charge calibration . . . 46
4.4.1 High-gain and pedestal calibration . . . 46
4.4.2 Low-gain calibration . . . 48
4.4.3 Time over threshold (ToT) calibration . . . 49
4.5 SuperFGD reconstruction . . . 52

5 Michel Electron Tagging in the SuperFGD 54
5.1 Stopping muon control sample . . . 54
5.2 Michel electron tagging . . . 57
5.3 Summary . . . 60

6 ν_μ Charged-Current Inclusive Interactions with Upgraded ND280 62
6.1 Inputs and corrections . . . 62
6.2 Event and signal topology definition . . . 63
6.3 Event selection . . . 64
6.3.1 Common selection steps . . . 66
6.3.2 Muon selection cuts . . . 67
6.3.3 Veto cuts . . . 69
6.4 Selection results . . . 72
6.4.1 Binning . . . 72
6.4.2 Selected MC samples . . . 75
6.4.3 Efficiency and purity . . . 79
6.4.4 Data and MC comparisons . . . 84
6.5 Systematic uncertainties . . . 85
6.5.1 Flux systematic uncertainties . . . 88
6.5.2 Detector systematic uncertainties . . . 90

6.5.3 Summary of the systematic uncertainties 93
6.6 Summary 97

7 Conclusion **98**

Bibliography **100**

A Impact of Individual Systematic Uncertainties **107**
A.1 Variation-type systematics 108
A.2 Weight-like systematics 116

B Markov Chain Monte Carlo in GUNDAM **136**
B.1 Bayesian inference and MCMC 136
B.2 The MCMC algorithm in GUNDAM 137
B.3 Validate the MCMC algorithm using the OA2022 near detector inputs 139
B.3.1 Burn-in steps 139
B.3.2 MCMC posterior samples 142
B.3.3 Comparisons of MINUIT and MCMC data fit results 144
B.4 Summary 148

C Potential Scale Reduction **149**

List of Figures

1.1 Beta-decay electron energy spectrum for carbon-14 [1]. The red line is the expected electron energy if only an electron were produced. The blue curve is the measured electron energies. 1
1.2 The Standard Model of particle physics [2]. 3
1.3 Examples of neutrino interaction Feynman diagrams. 4
1.4 Feynman diagrams for coherent forward scattering processes relevant for the neutrino matter effect. 8
1.5 Charged-current muon-neutrino and muon-antineutrino cross section divided by the neutrino energy, shown as a function of neutrino energy. The points are the world data, and the curves show the model prediction separated into the quasi-elastic, resonant, and deep inelastic channels [3]. 13
1.6 Example Feynman diagrams of charged-current ν_μ interactions on a neutron. 14
1.7 Schematic of the final-state interactions of a pion produced in a neutrino interaction inside a nucleus [4]. 15

2.1 A schematic of the T2K experiment [5]. 16
2.2 Overview of the T2K neutrino beamline [6]. 17
2.3 Neutrino energy from two-body pion decay as a function of the pion energy for different values of the angle between the pion and the outgoing neutrino in the laboratory frame. 18
2.4 Neutrino flux and oscillation probability at different off-axis angles [5]. . . . 18
2.5 Neutrino mode flux prediction [5]. 19
2.6 The near detector complex. The ND280 off-axis detector enclosed inside the magnet is located on the upper floor. The horizontal INGRID modules occupy the floor below, and the vertical INGRID modules extend across the bottom two floors [5]. 20
2.7 Schematics of the INGRID detector [7]. 21
2.8 The ND280 off-axis detectors. [8] 22
2.9 A simplified cut-away drawing of the TPC [8] 23
2.10 The Super-Kamiokande detector. [9] 24
2.11 Super-Kamiokande event displays [5]. 25

3.1 The upgraded ND280 off-axis detectors [5]. 28
3.2 A schematic of the High-Angle TPC [10]. 29
3.3 Schematics of a normal bulk Micromegas and a resistive Micromegas [10]. . . 30
3.4 A schematic of ToF planes [10]. 30
3.5 A picture of the SuperFGD and two HA-TPCs installed in the ND280 pit [5]. 31
3.6 An event display example of a ν_μ CC0π interaction candidate in the upgraded ND280. The event is from the 2024 neutrino beam run [5]. 31
3.7 Data and MC production flow 32

4.1 A schematic of the SuperFGD [10]. 34
4.2 A sketch of a charged particle generating scintillation light in the SuperFGD cubes. The red dashed arrow represents a charged particle. The yellow line is the scintillation light. 35
4.3 Comparison of the scintillator structure of the FGD and the SuperFGD. [11]. 36
4.4 SuperFGD scintillator cubes. 36
4.5 Photosensor and MPPC-PCB used in the SuperFGD [12]. 37
4.6 LED calibration system [12]. 38
4.7 SuperFGD mechanical box [5]. 39
4.8 Overview of the SuperFGD electronics architecture [12]. 40
4.9 Picture of the FEB board [12]. 41
4.10 Schematic of the CITIROC circuit [12]. 42
4.11 Assembly of the SuperFGD scintillator cube layers into the mechanical box [5]. 43
4.12 Installation of WLS fibers and MPPC-PCBs on the SuperFGD mechanical box [5]. 44
4.13 Assembled SuperFGD with readout cables [5]. 45
4.14 High gain calibration [12]. 46
4.15 Pedestal calibration [12]. 47
4.16 Example of low-gain ADC versus high-gain ADC for one MPPC channel [12]. 48
4.17 Gain calibrated hit charge versus hit ToT for one MPPC channel using June 2024 beam data. The ToT is in the unit of TDC count which is 1.25 ns per count. The red curve shows the fitted ToT calibration curve. The discontinuity in the calibration curve is due to the piecewise calibration function defined in Equation 4.3. 49
4.18 Gain calibrated hit charge versus hit ToT for all MPPC channels using June 2024 beam data. The red line shows the exponential fit $\exp\left[C \cdot (\mathrm{ToT} - 34) + D\right]$ in the range $34 \leq \mathrm{ToT} \leq 58$ TDC counts. 50
4.19 Comparison of the hit charges obtained from the gain calibration and from the ToT calibration. 51
4.20 Compare quadratic calibration parameters A and B for two ToT tables. One table is extracted on June 7, 2024 and the other one is on June 20, 2024. There is a two-week gap between them. 52

5.1 Schematic of an event in the stopping-muon control sample. 55
5.2 Reconstructed $\cos\theta_\mu$ and momentum of the muons selected in the stopping-muon control sample. 56
5.3 Delayed time distribution between the stopping muon candidate and the tagged Michel electron candidate. The distributions are normalized to unit area and fitted in the range 500 ns $< \Delta t <$ 10000 ns using equation 5.1. . . . 58
5.4 Distance distribution between the stopping muon candidate and the tagged Michel electron candidate. 59
5.5 Reconstructed SuperFGD hit and node number of the tagged Michel electron candidates. 60

6.1 Schematic of the three subsamples used in the inclusive ν_μ charged-current analysis. 64
6.2 ν_μ CC-inclusive selection flow 65
6.3 Number of selected UsECal veto track candidates before applying any veto cuts. The distributions are stacked by true topology [13]. 70
6.4 Distance between the selected UsECal veto-track and the muon track candidate before applying any veto cuts. The arrow indicates which events are kept in the cut for the HA-TPC muon sample, while for the TPC and SuperFGD-contained muon samples, all events in this histogram are rejected [13]. 70
6.5 Number of selected upstream-ToF veto track candidates before applying any veto cuts. The distributions are stacked by true topology [13]. 71
6.6 Distance between the selected upstream-ToF veto-track and the muon track candidate before applying any veto cuts. The arrow indicates which events are kept in the cut for the HA-TPC muon sample, while for the TPC and SuperFGD-contained muon samples, all events in this histogram are rejected [13]. 71
6.7 Scalar product of the directions of the two SuperFGD segments selected as candidates for the additional sand-muon veto, after the UsECal veto and Upstream-ToF veto cuts. The arrows indicate the events that are kept in this cut [13]. 72
6.8 Reconstructed momentum and $\cos\theta_\mu$ of the muon candidate for the selected MC events in the three samples (TPC, HA-TPC and SuperFGD-contained muon) [13]. The stacking shows the true particle type of the muon candidate. 76
6.9 Reconstructed momentum and $\cos\theta_\mu$ of the muon candidate for the selected MC events in the three samples (TPC, HA-TPC and SuperFGD-contained muon) [13]. The stacking shows the true topology of the selected vertex. . . 77
6.10 Reconstructed momentum and $\cos\theta_\mu$ of the muon candidate for the selected MC events in the three samples (TPC, HA-TPC and SuperFGD-contained muon) [13]. The stacking shows the true reaction type of the selected vertex. 78

6.11 Selection purity as a function of reconstructed muon momentum (left) and $\cos\theta_\mu$ (right) for the TPC, HA-TPC and SuperFGD-contained muon samples [13]. Each sample is shown over its own momentum range, up to about 5000, 2000, and 600 MeV/c for the TPC, HA-TPC, and SuperFGD-contained samples, respectively. 80
6.12 Selection efficiency ϵ_{det} as a function of true muon momentum (left) and $\cos\theta_\mu$ (right) for the TPC, HA-TPC and SuperFGD-contained muon samples [13]. Each sample is shown over its own momentum range, up to about 5000, 2000, and 600 MeV/c for the TPC, HA-TPC, and SuperFGD-contained samples, respectively. 81
6.13 Overall ν_μCC selection efficiency ϵ as a function of the true muon momentum (left) and $\cos\theta_\mu$ (right), split into the TPC, HA-TPC and SuperFGD-contained muon samples. The total efficiency is given in the legend [13]. Each sample is shown over its own momentum range, up to about 5000, 2000, and 600 MeV/c for the TPC, HA-TPC, and SuperFGD-contained samples, respectively. 82
6.14 Two dimensional histogram of the overall ν_μCC-inclusive selection efficiency ϵ in bins of the true muon momentum p_μ and $\cos\theta_\mu$. The efficiency value is shown by the color scale [13]. 83
6.15 Reconstructed muon-candidate momentum (left column) and $\cos\theta_\mu$ (right column) for the ν_μCC inclusive TPC, HA-TPC and SuperFGD-contained muon samples (top to bottom). The error bands show the MC statistical uncertainty (pink), the MC statistical and detector systematic uncertainties (green), and the MC statistical, detector and flux systematic uncertainties (yellow) [13]. . 86
6.16 Reconstructed muon-candidate momentum (left) and $\cos\theta_\mu$ (right) for the ν_μCC inclusive TPC, HA-TPC and SuperFGD-contained muon samples (top to bottom), with the corresponding ratio shown beneath each panel. The data are compared with the nominal MC prediction and with the same model reweighted to the best-fit flux and neutrino-interaction parameters from the pre-upgrade FGD-based ν_μCC analysis (ND OA2024) [13]. 87
6.17 Correlation matrix for flux parameters. 88
6.18 Relative systematic uncertainty on the reconstructed muon momentum (left) and $\cos\theta_\mu$ (right) for the TPC, HA-TPC and SuperFGD-contained samples. The red line is the detector-only systematics, and the blue line is the detector and flux systematics [13]. 95
6.19 Five largest relative systematic uncertainties on the reconstructed muon momentum (left) and $\cos\theta_\mu$ (right) for the TPC, HA-TPC and SuperFGD-contained samples. The legend in each panel ranks the systematics [13]. . . . 96

A.1 Relative systematic uncertainty from the SuperFGD momentum bias [13]. . . 108
A.2 Relative systematic uncertainty from the momentum scale [13]. 109

A.3 Relative systematic uncertainty from the momentum resolution [13]. 110
A.4 Relative systematic uncertainty from the TPC PID [13]. 111
A.5 Relative systematic uncertainty from the HA-TPC PID [13]. 112
A.6 Relative systematic uncertainty from the magnetic-field distortion [13]. . . . 113
A.7 Relative systematic uncertainty from the ToF resolution [13]. 114
A.8 Relative systematic uncertainty from the SuperFGD momentum resolution [13].115
A.9 Relative systematic uncertainty from the flux [13]. 116
A.10 Relative systematic uncertainty from the sand-muon background [13]. 117
A.11 Relative systematic uncertainty from the Michel-electron tagging efficiency [13].118
A.12 Relative systematic uncertainty from the SuperFGD PID [13]. 119
A.13 Relative systematic uncertainty from the pile-up [13]. 120
A.14 Relative systematic uncertainty from the pion secondary interactions [13]. . . 121
A.15 Relative systematic uncertainty from the proton secondary interactions [13]. 122
A.16 Relative systematic uncertainty from the charge identification [13]. 123
A.17 Relative systematic uncertainty from the SuperFGD mass [13]. 124
A.18 Relative systematic uncertainty from the TPC tracking efficiency [13]. 125
A.19 Relative systematic uncertainty from the HA-TPC tracking efficiency [13]. . 126
A.20 Relative systematic uncertainty from the ToF tracking efficiency [13]. 127
A.21 Relative systematic uncertainty from the SuperFGD tracking efficiency [13]. 128
A.22 Relative systematic uncertainty from the TPC cluster efficiency [13]. 129
A.23 Relative systematic uncertainty from the HA-TPC cluster efficiency [13]. . . 130
A.24 Relative systematic uncertainty: HA-TPC–TPC matching efficiency 131
A.25 Relative systematic uncertainty: TPC–SuperFGD matching efficiency 132
A.26 Relative systematic uncertainty: HA-TPC–SuperFGD matching efficiency . . 133
A.27 Relative systematic uncertainty: SuperFGD–HA-TPC–ToF matching efficiency134
A.28 Relative systematic uncertainty from the out-of-fiducial-volume background [13].135

B.1 $\hat{R}$ of the three MCMC chains as a function of chain length. Each plot is the distribution of $\hat{R}$ over all MCMC parameters, evaluated from the first n steps of the window ($n = 10\,000,\ 20\,000,\ \ldots,\ 0.5$ million). In (a), evaluated over the first 0.5 million steps, two parameters remain above 1.1. In (b), evaluated over the 5.0–5.5 million step window, all parameters are below 1.1. 140
B.2 Traces of the two slowest-converging parameters, `Pauli Blocking O nubar` (left) and `2p2h shape C np` (right), in one of the three chains. Top row: the first 0.5 million (warm-up) steps, before covariance optimization, where neither parameter has converged. Bottom row: the 5.0–5.5 million step window, after optimization, where both traces are stationary and weakly autocorrelated.141
B.3 Examples of posterior distributions. The histograms are scaled to the parameters' effective sample size, and the error bars account for a finite effective sample size. 142
B.4 Auto-correlation as a function of lag for all parameters. 143

B.5 Comparison between GUNDAM MINUIT and GUNDAM MCMC in terms of the flux parameters obtained from the data fit. The red points and pink error bands represent pre-fit central values and pre-fit errors. The black points and error bars indicate the post-fit values and errors of MINUIT. The blue points and error bands correspond to the posterior central values and errors of MCMC. 144
B.6 Comparison between GUNDAM MINUIT and GUNDAM MCMC in terms of the detector parameters obtained from the data fit. The red points and pink error bands represent pre-fit central values and pre-fit errors. The black points and error bars indicate the post-fit values and errors of MINUIT. The blue points and error bands correspond to the posterior central values and errors of MCMC. 145
B.7 Comparison between GUNDAM MINUIT and GUNDAM MCMC in terms of the cross-section parameters obtained from the data fit (part 1 of 2). The red points and pink error bands represent pre-fit central values and pre-fit errors. The black points and error bars indicate the post-fit values and errors of MINUIT. The blue points and error bands correspond to the posterior central values and errors of MCMC. 146
B.8 Comparison between GUNDAM MINUIT and GUNDAM MCMC in terms of the cross-section parameters obtained from the data fit (part 2 of 2). The red points and pink error bands represent pre-fit central values and pre-fit errors. The black points and error bars indicate the post-fit values and errors of MINUIT. The blue points and error bands correspond to the posterior central values and errors of MCMC. 147

List of Tables

1.1 Summary of the neutrino oscillation parameters from the NuFIT 6.0 global analysis, including Super-Kamiokande atmospheric data. The quoted uncertainties are the 1σ intervals, and the ranges show the 3σ allowed intervals [14]. 12

5.1 True particle type of the selected stopping muon track in the beam and sand MC sample, with the MC POT normalized to the data POT. 57
5.2 Summary of the Michel electron tagging efficiency for data and MC. 58
5.3 True particle type of the tagged Michel-electron candidate with the MC POT normalized to the data POT. 59

6.1 T2K Run 13c data sample and the corresponding POT used in this analysis for the data and MC samples. 63
6.2 Reconstructed momentum bin edges (MeV/c) for the TPC muon, HA-TPC muon and SFGD-contained muon samples [13]. 73
6.3 Reconstructed $\cos\theta_\mu$ bin edges for the TPC muon, HA-TPC muon and SFGD-contained muon samples [13]. 74
6.4 Number of selected events in each sample for the data and for the MC prediction. The MC is normalized to the data exposure of 1.574×10^{20} POT. . 84
6.5 χ^2 and p-value of the nominal MC/data comparison for each sample, evaluated in bins of reconstructed muon momentum and $\cos\theta_\mu$. 85
6.6 Flux systematic parameters for the inclusive ν_μ CC analysis 89
6.7 Integrated relative systematic uncertainties (in %) from each detector and flux error source, evaluated for each ν_μCC sample [13]. 94

Acknowledgements

First, I would like to deeply thank my advisor, Prof. Clark McGrew, for his guidance throughout my Ph.D. study. My journey in neutrino physics began with the CAPTAIN experiment as an undergraduate under his supervision, and I am grateful for the opportunity to have continued working with him on the T2K experiment during my Ph.D. His office door was always open to me for any questions, and he could always point me in the right direction.

I would like to thank my thesis committee, Prof. Ciro Riccio, Prof. Rouven Essig, and Dr. Guang Yang, for taking the time to read this thesis.

I would like to thank all members of the Neutrino and Nucleon Decay Group for their support throughout my Ph.D. studies, and especially Prof. Chang Kee Jung for the many barbecue parties he hosted at his home. His leadership of the group and of the department has been an inspiration to me.

I would also like to thank the T2K collaboration, in particular the SuperFGD working group and the Near Detector Upgrade First Analysis Task Force. This dissertation would not have been possible without their work.

I am also grateful to my friends at Stony Brook for the many good memories we made together.

Finally, I would like to thank my family, my parents and my brother, for their love and support throughout my life.

Outline

This dissertation first introduces the neutrino, neutrino oscillations, and the T2K experiment, which provide the background and motivation for the author's contributions. It then focuses on the author's work on the SuperFGD detector, from its construction and commissioning to the first physics analysis performed with the upgraded T2K near detector.

Chapter 1 reviews the discovery of the neutrino and its description in the Standard Model. It then introduces neutrino oscillation, covering the discovery history, the three-flavor oscillation framework, the experimental measurements of the oscillation parameters, and the open questions. It finally introduces neutrino–nucleus interactions, which are the dominant source of systematic uncertainty in neutrino oscillation measurements.

Chapter 2 describes the T2K experiment, including the neutrino beamline, the near detector complex located 280 m downstream, the Super-Kamiokande far detector 295 km away, and the T2K oscillation analysis strategy.

Chapter 3 presents the ND280 Upgrade. It explains the motivation for the upgrade and introduces two of the three new subdetectors, the High-Angle TPCs and the Time-of-Flight detector. The SuperFGD is described separately in Chapter 4. It also describes the data and Monte Carlo production used in the analysis and the reconstruction of the upgraded detector.

Chapter 4 focuses on the SuperFGD detector. It first introduces the detector concept and detector system, and then describes the assembly of the detector, the charge calibration, and the reconstruction. This work was carried out by the SuperFGD working group and led to a publication [12]. The author contributed to the SuperFGD assembly, commissioning, electronics response studies, and the development of the Time-over-Threshold (ToT) calibration.

Chapter 5 develops Michel electron tagging in the SuperFGD. It introduces the stopping-muon control sample and describes the Michel-electron tagging method and its efficiency. The author developed the Michel-tagging procedure using the existing stopping-muon control sample and compared the tagging efficiency between data and Monte Carlo.

Chapter 6 presents the first physics analysis with the upgraded near detector: the selection of inclusive ν_μ charged-current (CC) interactions in the SuperFGD, using Run 13c data taken in June 2024 and corresponding to 1.57×10^{20} protons on target. This is the core analysis of the dissertation. The selected sample is divided into the TPC, HA-TPC, and

SuperFGD-contained muon samples, based on where the muon candidate is reconstructed. This work was performed by the Near Detector Upgrade First Analysis Task Force. The author contributed the SuperFGD-contained muon sample, exploring several cut strategies and developing a Michel-electron tagging cut to identify the muon candidates.

Chapter 7 summarizes the results of the dissertation and discusses their implications for future cross-section and oscillation analyses.

Appendix B introduces the Markov Chain Monte Carlo (MCMC) algorithm in the fitting framework GUNDAM, a new framework for the oscillation and cross-section analyses of the upgraded T2K experiment. This fitting framework is also used by the DUNE experiment. The author contributed to the development and validation of the MCMC algorithm in GUNDAM. Because this dissertation focuses on the SuperFGD detector and its analysis, this work is presented in an appendix rather than in the main chapters.

Chapter 1

Introduction

1.1 A brief history of the neutrino discovery

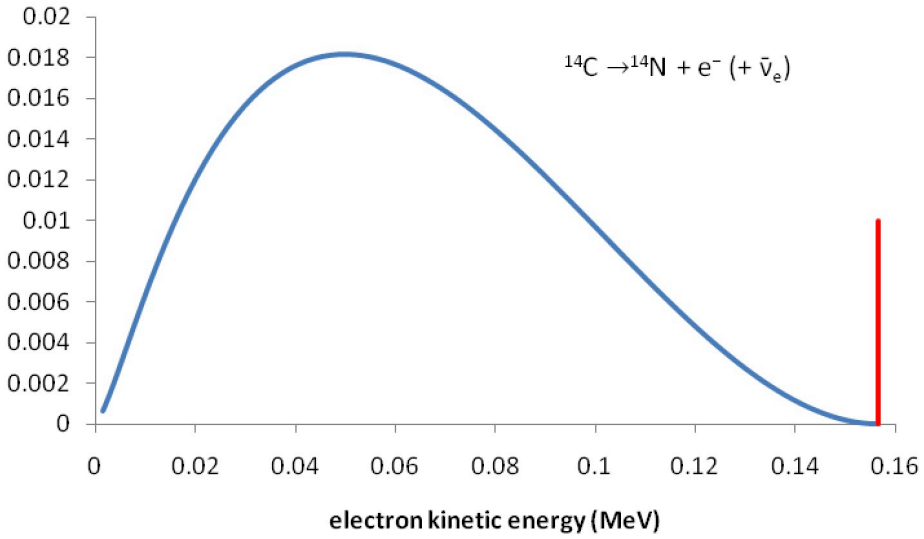


Figure 1.1: Beta-decay electron energy spectrum for carbon-14 [1]. The red line is the expected electron energy if only an electron were produced. The blue curve is the measured electron energies.

The history of the neutrino began with the puzzle of nuclear beta decay, in which a nucleus transforms into a daughter nucleus while emitting an electron. If beta decay were a two-body decay, the emitted electron would have a fixed energy determined by energy conservation. However, in 1914, Chadwick found that beta-decay electrons have a continuous energy spectrum rather than a single discrete energy [15]. From 1920 to 1927, Ellis, along with Chadwick and colleagues, further confirmed that the beta decay spectrum is continuous.

Figure 1.1 shows the electron spectrum for carbon-14 beta decay. The red line indicates the electron energy expected for a two-body decay, while the blue curve shows the observed continuous distribution. This observation suggests that the beta decay process seems to violate energy conservation.

To solve the beta decay energy puzzle, in 1930, Wolfgang Pauli postulated the existence of an undetected neutral particle that carries the missing energy in beta decay [16]. Pauli originally called this particle the "neutron". After Chadwick discovered the particle now known as the neutron in 1932, Enrico Fermi named the undetected neutral particle "neutrino," meaning "little neutral one". Fermi incorporated the neutrino into his theory of beta decay. In modern physics, neutron beta decay can be written as

$$n \to p + e^- + \bar{\nu}_e,$$

where $\bar{\nu}_e$ is the electron antineutrino, which carries away part of the decay energy. Fermi's theory laid the foundation for the weak interaction description of beta decay.

Due to their extremely weak interaction with matter, neutrinos were not directly detected until more than two decades after Pauli's proposal. In 1953, Reines and Cowan carried out an experiment at the Hanford reactor to search for reactor antineutrinos, but the significance was too low to claim a discovery [17]. In 1956, Clyde Cowan and Frederick Reines detected electron antineutrinos from a nuclear reactor through the inverse beta-decay reaction [18],

$$\bar{\nu}_e + p \to e^+ + n.$$

The positron was observed by detecting 511 keV photons from positron-electron annihilation, and the neutron was detected by neutron capture on cadmium, which emits a photon with a few microseconds delay. This was the first direct evidence of the neutrinos.

Following the direct detection of electron antineutrinos, the next important discovery was that neutrinos have more than one type. In 1962, Leon Lederman, Melvin Schwartz, Jack Steinberger discovered the muon neutrino at Brookhaven National Laboratory (BNL) [19]. They used the Alternating Gradient Synchrotron (AGS) to fire a high energy proton beam onto a beryllium target, producing secondary pions. These pions decayed into muons and neutrinos, producing a neutrino beam. When the neutrinos interacted in the detector, the charged-current events produced muons rather than electrons, which demonstrated that the neutrino associated with the muon is different from the electron neutrino. This newly discovered neutrino was the muon neutrino, ν_μ.

The discovery of the tau lepton in 1975 suggested the existence of the tau neutrino, ν_τ [20]. The tau neutrino was finally directly detected by the DONUT experiment at Fermilab in 2000 [21]. Precision measurements of the decay of the Z^0 boson produced in e^+e^- collisions at LEP limited the neutrino generation to three [22]. These discoveries established the three neutrino flavors: the electron neutrino ν_e, muon neutrino ν_μ, and tau neutrino ν_τ. In the Standard Model, these neutrinos are neutral leptons associated with the three charged

leptons, as described in the next section.

1.2 Neutrinos in the Standard Model

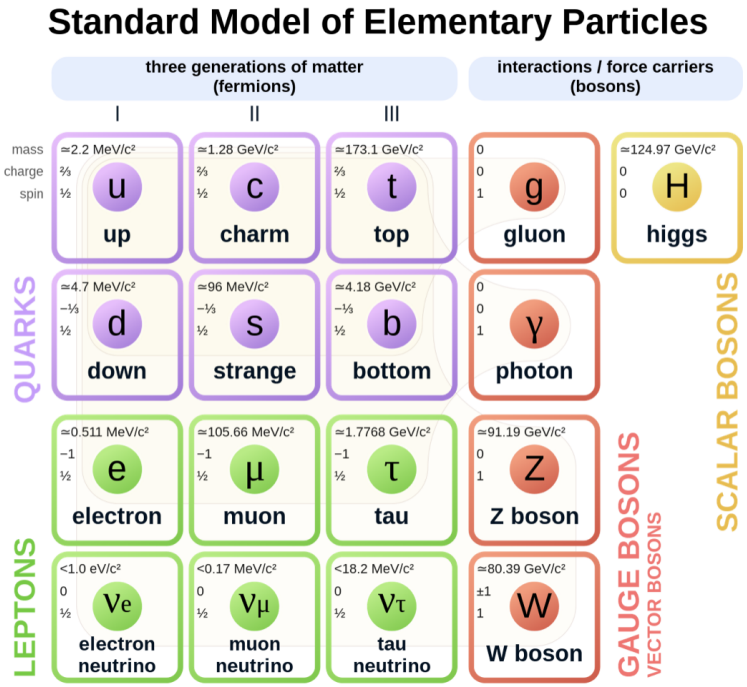
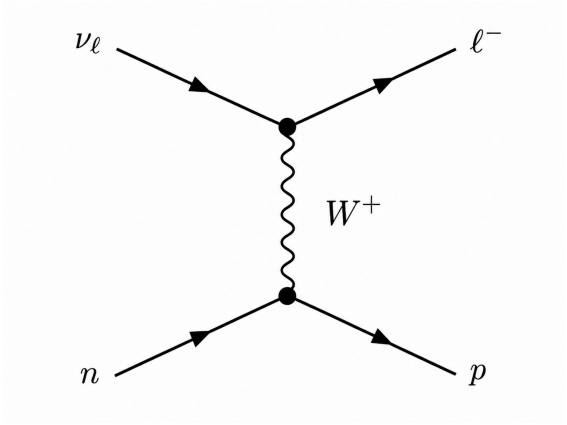


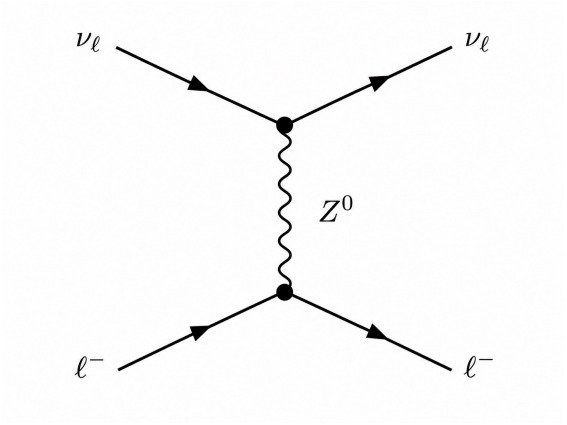
Figure 1.2: The Standard Model of particle physics [2].

The Standard Model of particle physics describes the known elementary particles and their interactions through the electromagnetic, strong, and weak forces, but it does not include gravity. As shown in Figure 1.2, the elementary particles are divided into fermions and bosons. The fermions make up the matter and are further divided into quarks and leptons, and each of them has three generations. The bosons mediate interactions: the photon mediates the electromagnetic interaction, gluons mediate the strong interaction, and the W and Z bosons mediate the weak interaction. The Higgs field generates the masses of charged fermions and the W and Z bosons through the Higgs mechanism. The framework of the Standard Model was established in the mid-1970s and has been tested by many experiments over several decades. The final missing particle predicted by the Standard Model, the Higgs boson, was discovered in 2012 [23][24].

In the Standard Model, neutrinos are massless left-handed fermions and have three flavors: electron neutrino ν_e, muon neutrino ν_μ, and tau neutrino ν_τ. Neutrinos have no electric charge or color charge, so they do not participate in electromagnetic or strong interactions. They interact with matter only through the weak interactions. Figure 1.3 shows examples



(a) Charged-current neutrino interaction with a neutron.



(b) Neutral-current neutrino interaction with a charged lepton.

Figure 1.3: Examples of neutrino interaction Feynman diagrams.

of neutrino interactions, which have two types: charged-current interaction and neutral-current interaction. The charged-current interaction is mediated by a W boson, while the neutral-current interaction is mediated by a Z boson.

1.3 Neutrino oscillation

In the mid-1960s, Raymond Davis Jr. started the Homestake experiment in the Homestake Mine in South Dakota to measure electron neutrinos from the Sun. The measured solar neutrino flux was only about one third of the value predicted by the standard solar model [25][26]. This discrepancy was known as the "solar neutrino problem". The deficit was later confirmed by the Kamiokande experiment in the late 1980s [27], and by the GALLEX/GNO [28] and SAGE experiments in the 1990s [29].

A possible solution to the solar neutrino problem was neutrino oscillation in which a neutrino produced with one flavor can be detected as a different flavor after traveling a distance. The idea of neutrino oscillation was first proposed by Bruno Pontecorvo in 1957 by analogy with neutral kaon oscillations [30]. After the solar neutrino deficit was observed, Gribov and Pontecorvo suggested that electron neutrinos could transform into other flavors when they travel from the Sun to the Earth [31].

The first compelling evidence for atmospheric neutrino disappearance came from the Super-Kamiokande experiment in 1998. Atmospheric neutrinos are produced when cosmic rays interact with nuclei in the atmosphere. Super-Kamiokande showed that the number of atmospheric muon neutrino events depended on the zenith angle [32]. The upward-going muon neutrino events were fewer than the downward-going ones. If there were no neutrino oscillations, the two would be expected to be approximately the same. Upward-going neutrinos

travel about 10^4 km through the Earth before reaching the detector, while downward-going neutrinos travel only about 20 km from the atmosphere to the detector. This dependence of the muon neutrino deficit on the propagation distance was strong evidence for flavor conversion, but the zenith-angle measurement alone did not distinguish neutrino oscillation from alternative explanations such as neutrino decay or decoherence. A later dedicated Super-Kamiokande analysis observed a dip in the L/E distribution, as expected from the oscillatory survival probability, which disfavored the neutrino-decay and decoherence hypotheses [33].

The Sudbury Neutrino Observatory (SNO) resolved the solar neutrino problem. SNO used a heavy-water (D_2O) detector to measure both the electron neutrino flux and the total neutrino flux from the Sun. In 2001, the experiment found that the electron neutrino flux was smaller than the standard solar model prediction [34], and in 2002, the experiment showed that the total neutrino flux was consistent with solar model prediction [35]. This showed that the missing solar electron neutrinos had converted to other neutrino flavors, resolving the solar neutrino problem. This flavor conversion is consistent with neutrino oscillation, which was later confirmed by the KamLAND reactor experiment [36].

Neutrino oscillation implies that neutrinos cannot have all zero masses. This phenomenon is beyond the Standard Model and is of great theoretical and experimental interest.

1.3.1 Three-flavor neutrino oscillation framework

Oscillations in vacuum.

Neutrinos interact with matter in flavor eigenstates and propagate in mass eigenstates. The flavor eigenstates, denoted by $|\nu_\alpha\rangle$ with $\alpha = e, \mu, \tau$, are superpositions of mass eigenstates, denoted by $|\nu_k\rangle$ with $k = 1, 2, 3$:

$$|\nu_\alpha\rangle = \sum_{k=1}^{3} U^*_{\alpha k} |\nu_k\rangle, \qquad (\alpha = e, \mu, \tau) \tag{1.1}$$

where U is the unitary Pontecorvo-Maki-Nakagawa-Sakata (PMNS) matrix [30][37]. The PMNS matrix can be parameterized by three mixing angles θ_{12}, θ_{13}, and θ_{23}, one Dirac

phase $\delta_{\rm CP}$, and two Majorana phases η_1 and η_2:

$$\begin{aligned} U &= \begin{pmatrix} U_{e1} & U_{e2} & U_{e3} \\ U_{\mu 1} & U_{\mu 2} & U_{\mu 3} \\ U_{\tau 1} & U_{\tau 2} & U_{\tau 3} \end{pmatrix} \\ &= \begin{pmatrix} 1 & 0 & 0 \\ 0 & c_{23} & s_{23} \\ 0 & -s_{23} & c_{23} \end{pmatrix} \begin{pmatrix} c_{13} & 0 & s_{13}e^{-i\delta_{\rm CP}} \\ 0 & 1 & 0 \\ -s_{13}e^{i\delta_{\rm CP}} & 0 & c_{13} \end{pmatrix} \begin{pmatrix} c_{12} & s_{12} & 0 \\ -s_{12} & c_{12} & 0 \\ 0 & 0 & 1 \end{pmatrix} \begin{pmatrix} e^{i\eta_1} & 0 & 0 \\ 0 & e^{i\eta_2} & 0 \\ 0 & 0 & 1 \end{pmatrix} \\ &= \begin{pmatrix} c_{12}c_{13} & s_{12}c_{13} & s_{13}e^{-i\delta_{\rm CP}} \\ -s_{12}c_{23} - c_{12}s_{13}s_{23}e^{i\delta_{\rm CP}} & c_{12}c_{23} - s_{12}s_{13}s_{23}e^{i\delta_{\rm CP}} & c_{13}s_{23} \\ s_{12}s_{23} - c_{12}s_{13}c_{23}e^{i\delta_{\rm CP}} & -c_{12}s_{23} - s_{12}s_{13}c_{23}e^{i\delta_{\rm CP}} & c_{13}c_{23} \end{pmatrix} \begin{pmatrix} e^{i\eta_1} & 0 & 0 \\ 0 & e^{i\eta_2} & 0 \\ 0 & 0 & 1 \end{pmatrix}, \end{aligned} \tag{1.2}$$

where $c_{ij} \equiv \cos\theta_{ij}$ and $s_{ij} \equiv \sin\theta_{ij}$. The angles θ_{ij} can be taken to lie in the first quadrant, $\theta_{ij} \in [0, \pi/2]$, and the phases $\delta_{\rm CP}, \eta_i \in [0, 2\pi]$. If neutrinos are Dirac fermions, the phases η_1 and η_2 are unphysical and can be removed by rephasing the neutrino fields.

For a relativistic neutrino traveling a distance L in vacuum, the mass eigenstate $|\nu_i\rangle$ evolves as a plane wave, and the evolution can be written as

$$|\nu_i(t, \boldsymbol{x})\rangle = \exp\left[-i\left(E_i t - \boldsymbol{p}_i \cdot \boldsymbol{x}\right)\right] |\nu_i(0)\rangle, \tag{1.3}$$

where E_i and $\boldsymbol{p}_i$ are the energy and momentum of the mass eigenstate. The propagation direction is along the neutrino momentum, so that $\boldsymbol{p}_i \cdot \boldsymbol{x} = p_i L$. In natural units, $\hbar = c = 1$, the neutrino travels approximately at the speed of light, so $t \simeq L$. Therefore, the phase becomes

$$E_i t - \boldsymbol{p}_i \cdot \boldsymbol{x} \simeq (E_i - p_i) L \tag{1.4}$$

Since the neutrino mass is very small compared with its energy, $m_i \ll E_i$, we obtain

$$E_i = \sqrt{p_i^2 + m_i^2} \simeq p_i + \frac{m_i^2}{2E} \tag{1.5}$$

Substituting this into the propagation phase gives

$$|\nu_i(t)\rangle = \exp\left(-i\frac{m_i^2 L}{2E}\right) |\nu_i(0)\rangle. \tag{1.6}$$

Therefore, an initial flavor eigenstate $|\nu_\alpha\rangle$ evolves as

$$|\nu_\alpha(t)\rangle = \sum_i U_{\alpha i}^* \exp\left(-i\frac{m_i^2 L}{2E}\right) |\nu_i\rangle. \tag{1.7}$$

The amplitude for observing this state as a flavor eigenstate $|\nu_\beta\rangle$ is

$$\begin{aligned} A_{\alpha\to\beta} &= \langle\nu_\beta|\nu_\alpha(t)\rangle \\ &= \sum_i U^*_{\alpha i} U_{\beta i} \exp\left(-i\frac{m_i^2 L}{2E}\right). \end{aligned} \tag{1.8}$$

The oscillation probability of $\nu_\alpha \to \nu_\beta$ is then

$$\begin{aligned} P(\nu_\alpha \to \nu_\beta) &= |A_{\alpha\to\beta}|^2 \\ &= \sum_{i,j} U^*_{\alpha i} U_{\beta i} U_{\alpha j} U^*_{\beta j} \exp\left(-i\frac{\Delta m_{ij}^2 L}{2E}\right), \end{aligned} \tag{1.9}$$

where $\Delta m^2_{ij} \equiv m_i^2 - m_j^2$ with $i, j = 1, 2, 3$. Using the unitarity of the PMNS matrix, this expression can be written as

$$\begin{aligned} P(\nu_\alpha \to \nu_\beta) = \delta_{\alpha\beta} &- 4\sum_{i>j} \mathrm{Re}\left(U^*_{\alpha i} U_{\beta i} U_{\alpha j} U^*_{\beta j}\right) \sin^2\left(\frac{\Delta m_{ij}^2 L}{4E}\right) \\ &+ 2\sum_{i>j} \mathrm{Im}\left(U^*_{\alpha i} U_{\beta i} U_{\alpha j} U^*_{\beta j}\right) \sin\left(\frac{\Delta m_{ij}^2 L}{2E}\right). \end{aligned} \tag{1.10}$$

The case $\alpha \neq \beta$ is called an appearance probability, while the case $\alpha = \beta$ is called a disappearance probability. Equation 1.10 shows that the Majorana phases cancel out in the oscillation probability. Neutrino oscillations require at least one nonzero mass-squared difference, $\Delta m^2_{ij} \neq 0$, and non-trivial mixing, $U \neq I$.

The oscillation probability therefore depends on the three mixing angles θ_{12}, θ_{13}, and θ_{23}, the Dirac phase δ_{CP}, and the mass-squared differences Δm^2_{21} and Δm^2_{31}.

For antineutrinos, the flavor eigenstates and mass eigenstates are related by

$$|\bar{\nu}_\alpha\rangle = \sum_i U_{\alpha i} |\bar{\nu}_i\rangle. \tag{1.11}$$

To obtain the oscillation probability of $\bar{\nu}_\alpha \to \bar{\nu}_\beta$, U must be replaced by U^* in Equation 1.10. Consequently, the real term in Equation 1.10 is unchanged, while the imaginary term changes sign:

$$\begin{aligned} P(\bar{\nu}_\alpha \to \bar{\nu}_\beta) = \delta_{\alpha\beta} &- 4\sum_{i>j} \mathrm{Re}\left(U^*_{\alpha i} U_{\beta i} U_{\alpha j} U^*_{\beta j}\right) \sin^2\left(\frac{\Delta m_{ij}^2 L}{4E}\right) \\ &- 2\sum_{i>j} \mathrm{Im}\left(U^*_{\alpha i} U_{\beta i} U_{\alpha j} U^*_{\beta j}\right) \sin\left(\frac{\Delta m_{ij}^2 L}{2E}\right). \end{aligned} \tag{1.12}$$

CP violation in neutrino oscillations is measured by comparing an oscillation process with its CP-conjugate process, $P(\nu_\alpha \to \nu_\beta)$ and $P(\bar{\nu}_\alpha \to \bar{\nu}_\beta)$. For disappearance channels, $\alpha = \beta$, the oscillation probability in vacuum becomes

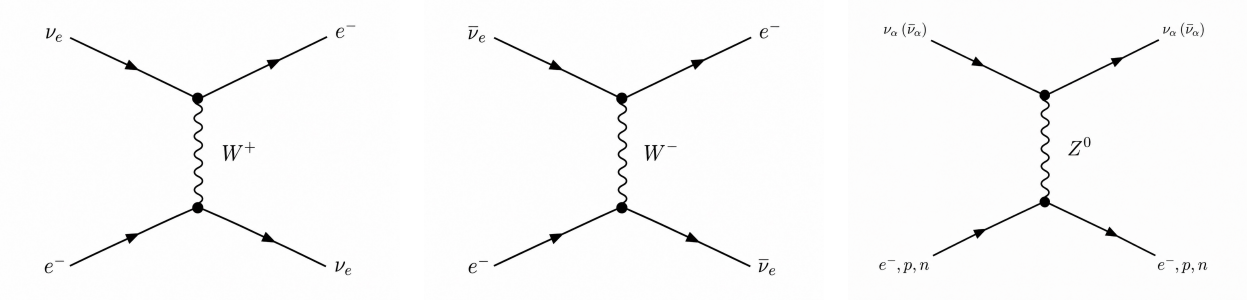
$$P(\nu_\alpha \to \nu_\alpha) = 1 - 4\sum_{i>j} |U_{\alpha i}|^2 |U_{\alpha j}|^2 \sin^2\left(\frac{\Delta m^2_{ij} L}{4E}\right) = P(\bar{\nu}_\alpha \to \bar{\nu}_\alpha). \tag{1.13}$$

Therefore, CP violation in neutrino oscillations can be measured only through appearance channels with $\alpha \neq \beta$. The CP violation can be characterized by the quantity $\Delta P_{\alpha\beta} = P(\nu_\alpha \to \nu_\beta) - P(\bar{\nu}_\alpha \to \bar{\nu}_\beta)$. One can show that

$$\Delta P_{\alpha\beta} = \pm 16 J \sin\left(\frac{\Delta m^2_{21} L}{4E}\right) \sin\left(\frac{\Delta m^2_{31} L}{4E}\right) \sin\left(\frac{\Delta m^2_{32} L}{4E}\right), \tag{1.14}$$

where $J = c_{12}s_{12}c_{23}s_{23}c^2_{13}s_{13}\sin\delta_{\rm CP}$ is the Jarlskog invariant [38]. The sign of $\Delta P_{\alpha\beta}$ is positive if (α, β, γ) is an even permutation of (e, μ, τ) and negative if it is an odd permutation. Therefore, CP violation in neutrino oscillations requires that all three mixing angles are nonzero, $\theta_{ij} \neq 0$, the Dirac phase is not 0 or π, $\delta_{\rm CP} \neq 0, \pi$, and the three neutrino masses are not degenerate, $\Delta m^2_{ij} \neq 0$.

Matter effects.



(a) ν_e CC scattering (b) $\bar{\nu}_e$ CC scattering (c) NC scattering

Figure 1.4: Feynman diagrams for coherent forward scattering processes relevant for the neutrino matter effect.

When neutrinos propagate through matter, their evolution is modified by coherent forward scattering with the particles in the medium. The relevant Feynman diagrams for coherent forward scattering are shown in Figure 1.4. Ordinary matter contains electrons, protons, and neutrons, but no muons or taus. Therefore, electron (anti-)neutrinos have an additional charged-current elastic forward scattering on electrons, while all (anti-)neutrino flavors have neutral-current forward scattering.

For a medium with electron number density N_e, the charged-current forward scattering

contributes an effective potential $V_{\rm CC}$ to the Hamiltonian:

$$V_{\rm CC} = \sqrt{2} G_F N_e, \tag{1.15}$$

where $G_F = 1.17 \times 10^{-5}$ GeV^{-2} is the Fermi constant. For antineutrinos, the sign of $V_{\rm CC}$ is negative. The neutral-current forward scattering is common to all flavors, so its effective potential does not affect neutrino oscillation probabilities and can be neglected from the Hamiltonian.

The effective Hamiltonian in matter can be written as

$$H = H_{\rm vac} + H_{\rm mat}, \tag{1.16}$$

where $H_{\rm vac}$ is the vacuum Hamiltonian and $H_{\rm mat}$ is the matter potential term.

In the flavor state space, the effective Hamiltonian for neutrinos can be written as

$$H = \frac{1}{2E} \left[U \begin{pmatrix} 0 & 0 & 0 \\ 0 & \Delta m^2_{21} & 0 \\ 0 & 0 & \Delta m^2_{31} \end{pmatrix} U^\dagger + \begin{pmatrix} A_{\rm CC} & 0 & 0 \\ 0 & 0 & 0 \\ 0 & 0 & 0 \end{pmatrix} \right], \tag{1.17}$$

where

$$A_{\rm CC} \equiv 2EV_{\rm CC} = 2\sqrt{2} G_F N_e E. \tag{1.18}$$

For antineutrinos, the potential $V_{\rm CC}$ changes sign and the mixing matrix is complex conjugated, $U \to U^*$.

To show how matter affects the neutrino oscillation probability, we consider the two-flavor case for simplicity. For two-flavor mixing, the flavor and mass eigenstates are related by

$$\begin{pmatrix} \nu_e \\ \nu_\mu \end{pmatrix} = \begin{pmatrix} \cos\theta & \sin\theta \\ -\sin\theta & \cos\theta \end{pmatrix} \begin{pmatrix} \nu_1 \\ \nu_2 \end{pmatrix}. \tag{1.19}$$

In vacuum, the oscillation probability is

$$P(\nu_e \to \nu_\mu) = \sin^2 2\theta \sin^2 \left(\frac{\Delta m^2 L}{4E} \right). \tag{1.20}$$

In matter, after removing terms proportional to the identity matrix, the two-flavor Hamiltonian in flavor state space can be written as

$$H = \frac{\Delta m^2}{4E} \begin{pmatrix} -\cos 2\theta + A & \sin 2\theta \\ \sin 2\theta & \cos 2\theta - A \end{pmatrix}, \tag{1.21}$$

where

$$A \equiv \frac{2EV_{\rm CC}}{\Delta m^2} = \frac{2\sqrt{2} G_F N_e E}{\Delta m^2}. \tag{1.22}$$

For antineutrinos, A becomes $-A$.

This Hamiltonian can be written in the same form as the vacuum Hamiltonian, but with an effective mixing angle θ_M and an effective mass-squared difference Δm^2_M:

$$H = \frac{\Delta m^2_M}{4E} \begin{pmatrix} -\cos 2\theta_M & \sin 2\theta_M \\ \sin 2\theta_M & \cos 2\theta_M \end{pmatrix}, \tag{1.23}$$

where

$$\sin 2\theta_M = \frac{\sin 2\theta}{\sqrt{(\cos 2\theta - A)^2 + \sin^2 2\theta}}, \tag{1.24}$$

and

$$\Delta m^2_M = \Delta m^2 \sqrt{(\cos 2\theta - A)^2 + \sin^2 2\theta}. \tag{1.25}$$

Therefore, assuming the constant electron density, the oscillation probability in matter becomes

$$P_M(\nu_e \to \nu_\mu) = \sin^2 2\theta_M \sin^2 \left(\frac{\Delta m^2_M L}{4E} \right). \tag{1.26}$$

Equation 1.24 shows that the effective mixing angle θ_M can become maximal even when the vacuum mixing angle is small. For neutrinos, this resonance occurs when $\Delta m^2 \cos 2\theta > 0$ and $A = \cos 2\theta$ or equivalently

$$N_e = \frac{\Delta m^2 \cos 2\theta}{2\sqrt{2} G_F E}. \tag{1.27}$$

For antineutrinos, $A \to -A$, so the resonance condition becomes $\Delta m^2 \cos 2\theta < 0$ and $N_e = -\frac{\Delta m^2 \cos 2\theta}{2\sqrt{2} G_F E}$. This resonance is known as the Mikheyev-Smirnov-Wolfenstein (MSW) effect [39][40].

Matter effects provide a window to determine the neutrino mass ordering. High-energy solar ν_e are produced in the dense solar core, where the matter potential given by Equation 1.22 is large. The electron flavor state approximately coincides with the second matter eigenstate, $|\nu_e\rangle \approx |\nu_2^m\rangle$. Because the evolution is adiabatic, this state exits the Sun as ν_2, leading to the survival probability

$$P_{ee} \simeq |\langle \nu_e | \nu_2 \rangle|^2 = \sin^2 \theta_{12}. \tag{1.28}$$

This matches well with the high-energy part of the ^{8}B solar-neutrino spectrum and determines $\Delta m^2_{21} \cos 2\theta_{12} > 0$ [38]. The standard convention chooses $\Delta m^2_{21} > 0$.

Matter effects can also produce $P(\nu_\mu \to \nu_e) \neq P(\bar{\nu}_\mu \to \bar{\nu}_e)$ even in the absence of CP violation, so it is important to disentangle the matter effect from CP violation in CP-violation measurements.

$\overset{(-)}{\nu}_\mu \to \overset{(-)}{\nu}_e$ appearance with matter effects

Accelerator-based long-baseline experiments measure neutrino CP-violation by measuring

the (anti-)electron neutrino appearance channel, $\overset{(-)}{\nu}_\mu \to \overset{(-)}{\nu}_e$. For constant matter density, the leading-order probability can be written as [38]

$$\begin{aligned} P(\nu_\mu \to \nu_e) \simeq\ & \sin^2\theta_{23}\sin^2 2\theta_{13}\frac{\sin^2\left[(A-1)\Delta_{31}\right]}{(A-1)^2} \\ & + \alpha^2\cos^2\theta_{23}\sin^2 2\theta_{12}\frac{\sin^2\left(A\Delta_{31}\right)}{A^2} \\ & - \alpha\sin 2\theta_{12}\sin 2\theta_{13}\sin 2\theta_{23}\cos\theta_{13}\sin\delta_{\mathrm{CP}}\frac{\sin\Delta_{31}\sin\left(A\Delta_{31}\right)\sin\left[(1-A)\Delta_{31}\right]}{A(1-A)} \\ & + \alpha\sin 2\theta_{12}\sin 2\theta_{13}\sin 2\theta_{23}\cos\theta_{13}\cos\delta_{\mathrm{CP}}\frac{\cos\Delta_{31}\sin\left(A\Delta_{31}\right)\sin\left[(1-A)\Delta_{31}\right]}{A(1-A)}. \end{aligned} \tag{1.29}$$

where

$$\alpha \equiv \frac{\Delta m^2_{21}}{\Delta m^2_{31}}, \qquad \Delta_{ji} \equiv \frac{\Delta m^2_{ji} L}{4E}, \qquad A \equiv \frac{2\sqrt{2}G_F n_e E}{\Delta m^2_{31}}. \tag{1.30}$$

The antineutrino probability is obtained by replacing

$$A \to -A, \qquad \delta_{\mathrm{CP}} \to -\delta_{\mathrm{CP}}. \tag{1.31}$$

This equation shows that matter effects produce a difference between $P(\nu_\mu \to \nu_e)$ and $P(\bar{\nu}_\mu \to \bar{\nu}_e)$ through the sign of the term A even in the absence of CP violation. This asymmetry also depends on the sign of Δm^2_{31}, which provides sensitivity to the neutrino mass ordering. Because both matter effects and δ_{CP} contribute to the neutrino-antineutrino appearance asymmetry, matter effects must be included in oscillation analyses to avoid a biased measurement of δ_{CP}.

1.3.2 Experimental measurements and open questions

The neutrino oscillation probability depends on the neutrino flavor and the ratio of the travel distance to the neutrino energy, L/E_ν, so the six oscillation parameters are measured by experiments with a dedicated neutrino source, energy, and baseline. Table 1.1 summarizes the oscillation parameters from the NuFIT 6.0 global analysis [14]. The mixing angles θ_{12} and θ_{13}, the mass-squared difference Δm^2_{21}, and $|\Delta m^2_{31}|$ are precisely measured, while the octant of θ_{23}, the sign of Δm^2_{31} (the mass ordering), and the value of δ_{CP} remain only partially constrained.

Table 1.1: Summary of the neutrino oscillation parameters from the NuFIT 6.0 global analysis, including Super-Kamiokande atmospheric data. The quoted uncertainties are the 1σ intervals, and the ranges show the 3σ allowed intervals [14].

Parameter	Ordering	Best fit $\pm 1\sigma$	3σ range
$\sin^2\theta_{12}$	NO	$0.308^{+0.012}_{-0.011}$	$0.275 \to 0.345$
	IO	$0.308^{+0.012}_{-0.011}$	$0.275 \to 0.345$
$\sin^2\theta_{23}$	NO	$0.470^{+0.017}_{-0.013}$	$0.435 \to 0.585$
	IO	$0.550^{+0.012}_{-0.015}$	$0.440 \to 0.584$
$\sin^2\theta_{13}$	NO	$0.02215^{+0.00056}_{-0.00058}$	$0.02030 \to 0.02388$
	IO	$0.02231^{+0.00056}_{-0.00056}$	$0.02060 \to 0.02409$
$\delta_{\rm CP}$ [°]	NO	212^{+26}_{-41}	$124 \to 364$
	IO	274^{+22}_{-25}	$201 \to 335$
Δm^2_{21} [$10^{-5}\,\mathrm{eV}^2$]	NO	$7.49^{+0.19}_{-0.19}$	$6.92 \to 8.05$
	IO	$7.49^{+0.19}_{-0.19}$	$6.92 \to 8.05$
Δm^2_{31} [$10^{-3}\,\mathrm{eV}^2$]	NO	$+2.513^{+0.021}_{-0.019}$	$+2.451 \to +2.578$
Δm^2_{32} [$10^{-3}\,\mathrm{eV}^2$]	IO	$-2.484^{+0.020}_{-0.020}$	$-2.547 \to -2.421$

NO and IO denote normal ordering and inverted ordering, respectively. For the atmospheric mass-squared splitting, the normal-ordering value is reported as Δm^2_{31}, while the inverted-ordering value is reported as Δm^2_{32}, following the NuFIT 6.0 convention.

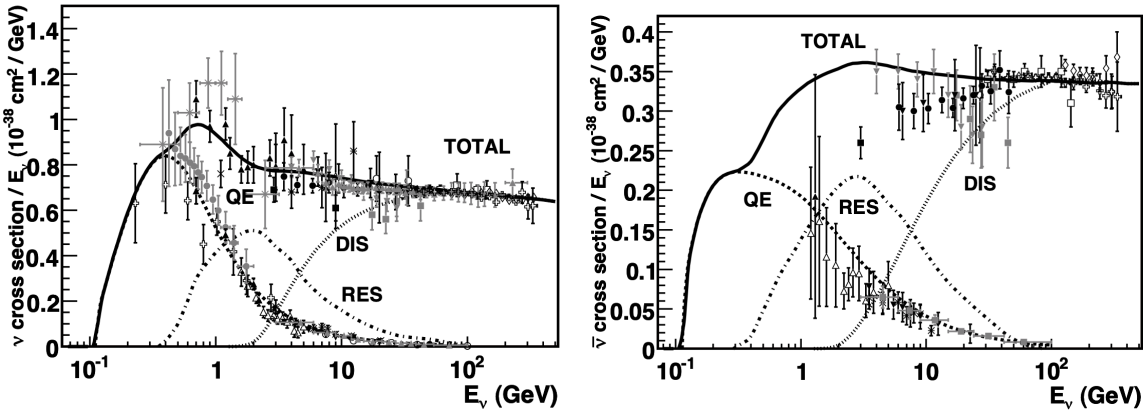
The mixing angle θ_{12} and the mass-squared difference Δm^2_{21} are measured by solar and reactor neutrino experiments, through $\nu_e \to \nu_e$ and $\bar{\nu}_e \to \bar{\nu}_e$ disappearance. The mixing angle θ_{13} is primarily measured by reactor neutrino experiments, through $\bar{\nu}_e \to \bar{\nu}_e$ disappearance. θ_{23} and $|\Delta m^2_{32}|$ are measured by atmospheric and accelerator experiments, through ${}^{(-)}\nu_\mu \to {}^{(-)}\nu_\mu$ disappearance. $\delta_{\rm CP}$ is measured by accelerator experiments, through ${}^{(-)}\nu_\mu \to {}^{(-)}\nu_e$ appearance.

The sign of Δm^2_{32} (the neutrino mass ordering), the octant of θ_{23}, and the value of $\delta_{\rm CP}$ are not yet determined. The value of $\delta_{\rm CP}$ and the octant of θ_{23} are currently constrained mainly by the long-baseline accelerator experiments T2K and NOvA [41][42], and will be measured more precisely by the DUNE and Hyper-Kamiokande experiments [43][44]. The mass ordering is expected to be determined by the JUNO and DUNE experiments [45][43].

1.4 Neutrino-nucleus interactions

Neutrino oscillation is studied by measuring neutrino-nucleus interactions in the detector, so a better understanding of neutrino interactions is important. The modeling of these interactions is one of the leading systematic uncertainties in oscillation measurements [4]. For the T2K experiment, the neutrino flux energy peaks around 0.6 GeV, which is the focus energy range of this section [8]. In practice, neutrinos interact with nucleons bound in a nucleus, so the neutrino-nucleon interaction is introduced first, followed by the nuclear effects.

1.4.1 Neutrino-nucleon interactions



(a) Neutrino (b) Antineutrino

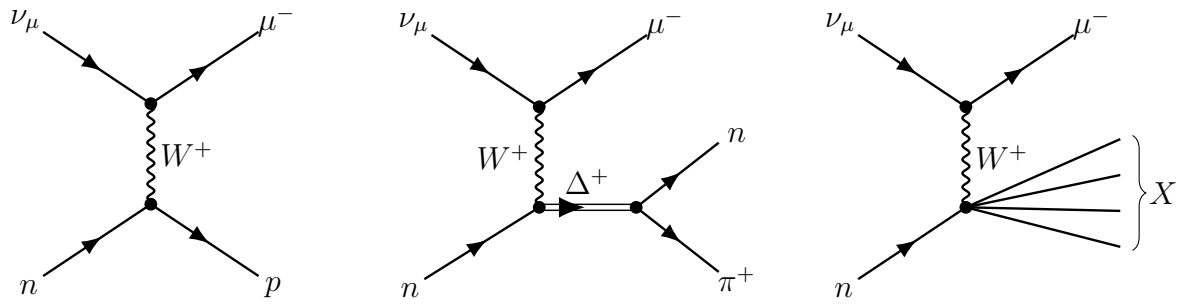
Figure 1.5: Charged-current muon-neutrino and muon-antineutrino cross section divided by the neutrino energy, shown as a function of neutrino energy. The points are the world data, and the curves show the model prediction separated into the quasi-elastic, resonant, and deep inelastic channels [3].

Figure 1.5 shows the ν_μ and $\bar{\nu}_\mu$-nucleon cross section divided by the neutrino energy [3]. It shows that in different energy regimes the interaction is dominated by different channels. As the neutrino energy increases, the channel changes from quasi-elastic to resonance production and then deep inelastic interaction.

Quasi-elastic scattering

The quasi-elastic interaction dominates in the sub-GeV energy range, where the neutrino scatters off an entire nucleon. Figure 1.6a shows an example of a muon-neutrino charged-current quasi-elastic (CCQE) interaction, which converts a neutron into a proton and produces a muon,

$$\nu_\mu + n \rightarrow \mu^- + p.$$



(a) Quasi-elastic scattering (b) Resonant production (c) Deep inelastic scattering

Figure 1.6: Example Feynman diagrams of charged-current ν_μ interactions on a neutron.

Resonant single-pion production

At larger momentum transfer, the neutrino can excite the nucleon to a baryon resonance, which decays to a nucleon and a pion. As shown in Figure 1.6b, a muon neutrino excites a neutron to a Δ^+ resonance that decays into a neutron and a charged pion,

$$\nu_\mu + n \to \mu^- + n + \pi^+.$$

This process dominates at neutrino energies of about 1 to a few GeV.

Deep inelastic scattering

In deep inelastic scattering, the neutrino interacts with an individual quark inside the nucleon, which produces a shower of hadrons. As shown in Figure 1.6c, a muon neutrino scatters off a quark in a neutron and produces a muon and a hadronic shower,

$$\nu_\mu + n \to \mu^- + X.$$

This process dominates above about 10 GeV.

1.4.2 Nuclear effects

When a neutrino interacts with a nucleus, it interacts with a nucleon bound inside the nucleus, and the surrounding nucleons affect the interaction. Some example nuclear effects are the Fermi motion of the bound nucleons, interactions on correlated nucleon pairs, and the final-state interactions of the produced hadrons. These nuclear effects change the observed final state, so the neutrino interaction channel (quasi-elastic, resonant production, or deep inelastic scattering) cannot be reconstructed directly from the final particles. The neutrino events are instead classified by their final-state topology, such as the number of pions. The modeling of these effects is a leading source of systematic uncertainty in the oscillation measurement.

The bound nucleons are not static. The motion of the bound nucleons can be described by the Fermi gas model [46]. This Fermi motion smears the reconstructed energy of the incoming neutrino [4].

The neutrino can also interact with a correlated pair of nucleons rather than a single nucleon. For example, two-particle two-hole (2p2h) interactions eject two nucleons without producing a pion [47, 48]. This interaction can mimic a quasi-elastic final state if only one of the produced nucleons is reconstructed.

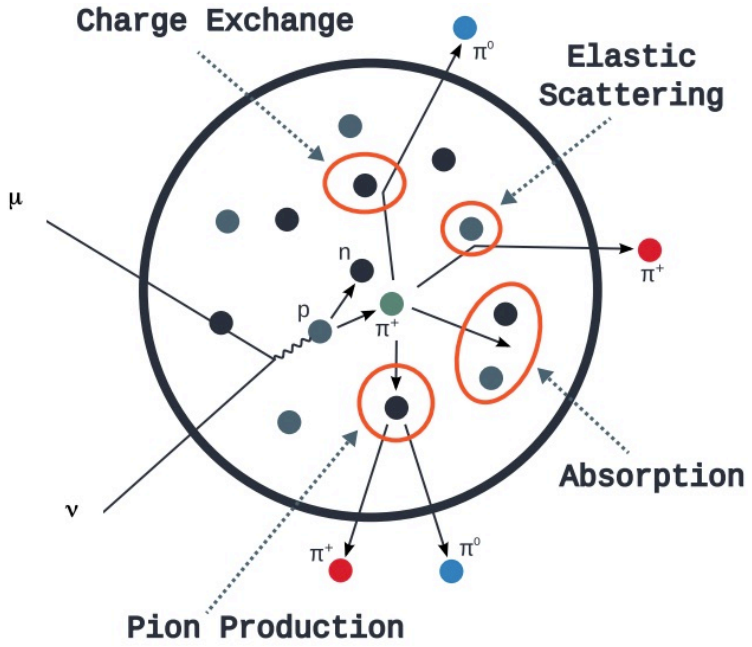


Figure 1.7: Schematic of the final-state interactions of a pion produced in a neutrino interaction inside a nucleus [4].

The hadrons produced from the neutrino interaction interact with the surrounding nucleons. Figure 1.7 shows an example of the final-state interactions (FSI) of the produced π^+. Before escaping the nucleus, the pion can scatter elastically, exchange charge, be absorbed, or induce further pion production, so the detected hadrons differ from those produced in the neutrino interaction.

Chapter 2

The T2K Experiment

The T2K (Tokai-to-Kamioka) experiment [8] is a long-baseline neutrino experiment built with the purpose of measuring the mixing angle θ_{13} and constraining the CP phase δ_{CP} through the (anti-)electron neutrino appearance measurements $\nu_\mu(\bar{\nu}_\mu) \to \nu_e(\bar{\nu}_e)$, along with precision measurements of θ_{23} and Δm^2_{32} through the (anti-)muon neutrino disappearance measurements $\nu_\mu(\bar{\nu}_\mu) \to \nu_\mu(\bar{\nu}_\mu)$. T2K also pursues various neutrino-nucleus cross section measurements and searches for sterile neutrinos.

Figure 2.1 illustrates the overall layout of the T2K experiment. A neutrino beam is generated by the Japan Proton Accelerator Research Complex (J-PARC) located in Tokai, Ibaraki. The near detector sitting at 280 meters from the target station measures the neutrino flux before it oscillates. The Super-Kamiokande [9], serving as the far detector of T2K, measures the neutrino flux 295 km from the near detectors.

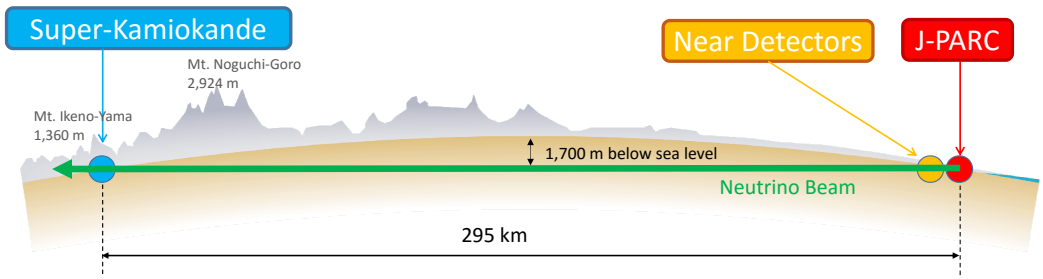


Figure 2.1: A schematic of the T2K experiment [5].

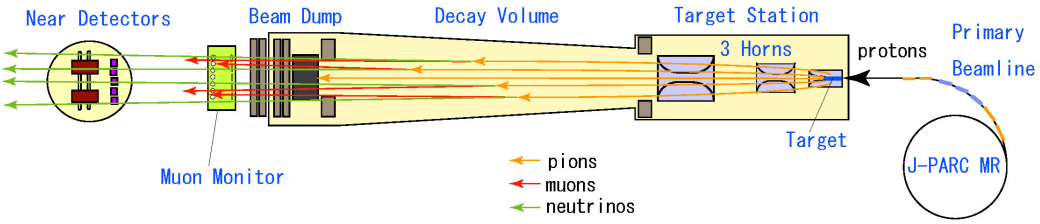


Figure 2.2: Overview of the T2K neutrino beamline [6].

2.1 Neutrino beamline

Three accelerators make up J-PARC: a linear accelerator (LINAC), a rapid-cycling synchrotron (RCS), and the main ring (MR) synchrotron. The LINAC accelerates an H^- beam up to 400 MeV, and charge-stripping foils convert it to an H^+ beam at the RCS injection. The beam is further accelerated by the RCS up to 3 GeV, and about 5% of the beam is supplied to the MR. The MR then accelerates the proton beam to 30 GeV. Each proton beam spill has a width of 5 μs and consists of 8 bunches. The proton beam is then extracted from the MR to the T2K neutrino beamline, where it is used to produce the neutrino beam. [8].

Figure 2.2 shows an overview of the T2K neutrino beamline, which consists of two sequential sections: the primary and the secondary beamline. The primary beamline directs the extracted proton beam toward Kamioka. In the secondary beamline the beam hits a graphite target 91.4 cm long and 2.6 cm in diameter with a density of 1.8 g/cm^3, which produces mostly $\pi^\pm$ and $K^\pm$ secondary particles. Three magnetic horns excited by a 250 kA current pulse focus the positively or negatively charged secondary particles. The horn current was 250 kA in T2K phase I and was raised to 320 kA in phase II, which includes the Run 13c data used in this analysis. When the magnetic horns operate in the forward horn current (FHC) mode, π^+ and K^+ are focused, which produces a ν_μ beam, whereas the reverse horn current (RHC) mode focuses π^- and K^-, producing a $\bar{\nu}_\mu$ beam.

After passing through the magnetic horns, the charged secondary particles are sent through a 96 m long decay volume, where they decay and produce ν_μ ($\bar{\nu}_\mu$) mainly by the following channels [49]:

$$\begin{aligned} \pi^+ &\to \mu^+ + \nu_\mu, & K^+ &\to \mu^+ + \nu_\mu \text{ (FHC)} \\ \pi^- &\to \mu^- + \bar{\nu}_\mu, & K^- &\to \mu^- + \bar{\nu}_\mu \text{ (RHC)} \end{aligned} \tag{2.1}$$

The produced ν_μ ($\bar{\nu}_\mu$) beam can have contamination (anti-)neutrinos due to wrong-sign mesons and other decay channels. The beam dump sitting at the end of the decay volume stops hadrons and muons below 5 GeV. Muons above 5 GeV can go through the beam dump and reach the downstream muon monitor, which monitors the neutrino beam direction by measuring the distribution profile of muons.

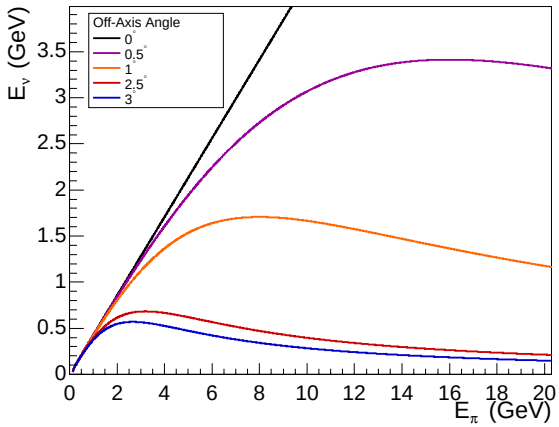


Figure 2.3: Neutrino energy from two-body pion decay as a function of the pion energy for different values of the angle between the pion and the outgoing neutrino in the laboratory frame.

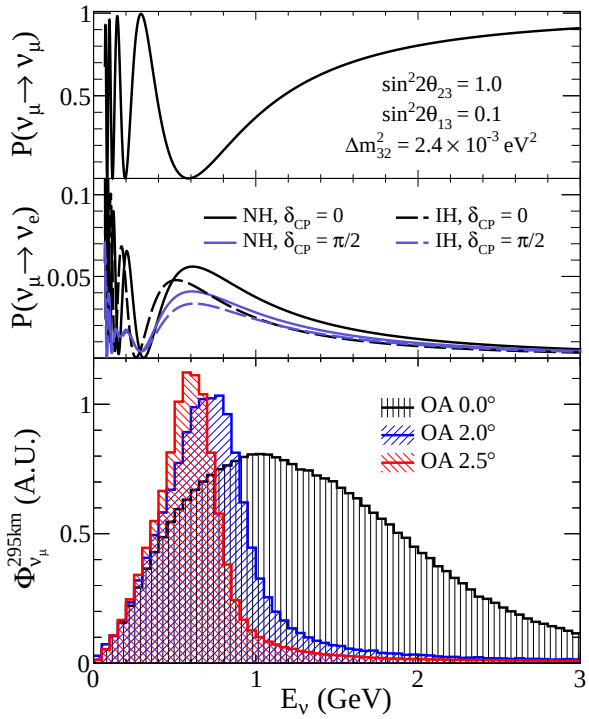
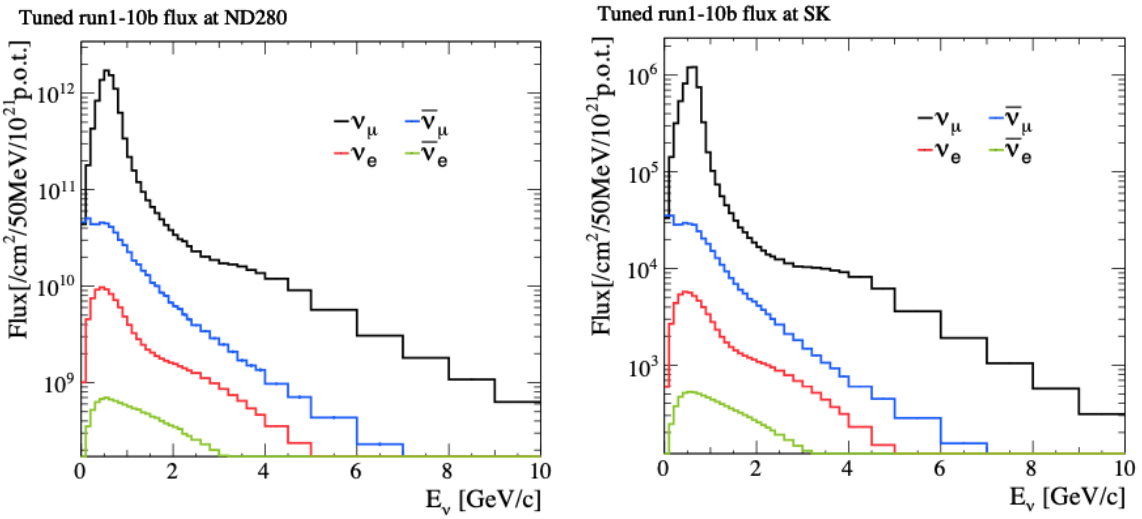


Figure 2.4: Neutrino flux and oscillation probability at different off-axis angles [5].

Since the neutrino beam is mainly produced from two-body pion decays, the neutrino energy can be given by Equation 2.2.

$$E_\nu = \frac{m_\pi^2 - m_\mu^2}{2\left(E_\pi - p_\pi \cos\theta\right)} \tag{2.2}$$

where E_ν is the neutrino energy, m_π is the pion mass, m_μ is the muon mass, E_π is the pion energy, p_π is the pion momentum, and θ is the angle between the pion and the produced neutrino. Figure 2.3 shows the neutrino energy versus the pion energy with different angles between the pion and neutrino in the laboratory frame. The off-axis angle can reduce the E_ν dependence on E_π and produce a narrow-band neutrino beam. Figure 2.4 shows the un-oscillated ν_μ flux at SK and oscillation probability $\nu_\mu \to \nu_e$ and $\nu_\mu \to \nu_\mu$ at different off-axis angles. T2K applies the off-axis method by designing the neutrino beam direction 2.5° off-axis from the baseline connecting the proton target and the Super-Kamiokande. As shown in Figure 2.4, when the off-axis angle is 2.5°, the neutrino energy peaks at 600 MeV, where the neutrino oscillation probability is maximum. The dominant neutrino-nucleus interaction is quasi-elastic scattering, which is relatively well understood and allows for better neutrino energy reconstruction.



(a) The predicted neutrino mode flux at ND280.

(b) The predicted neutrino mode flux at SK.

Figure 2.5: Neutrino mode flux prediction [5].

Neutrino flux prediction is essential for the prediction of neutrino interaction rates at the T2K detectors and is also important for neutrino oscillation and cross section measurements [49]. The FLUKA 2008 [50][51] package is used to simulate the interactions between the proton beam and the graphite target. GEANT3 [52] is used to simulate the horn focusing,

out-of-target interactions, and decay into neutrinos. Data from NA61/SHINE [53][54] at the CERN SPS, which measures the hadron production from a 30 GeV proton beam impinging on a replica of the T2K target, is used to tune the hadron interaction models. Figure 2.5 shows the prediction of the neutrino mode beam flux at ND280 and SK [55].

2.2 Near detector complex

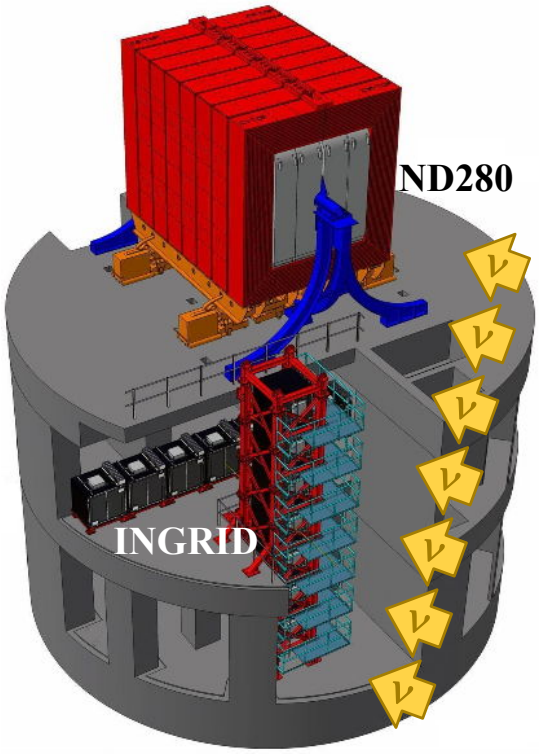
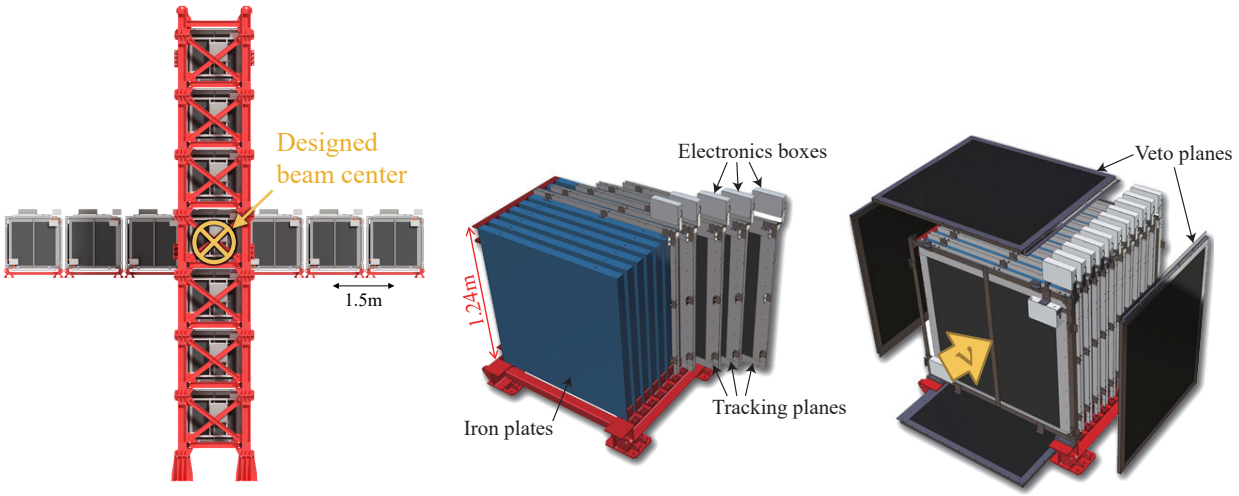


Figure 2.6: The near detector complex. The ND280 off-axis detector enclosed inside the magnet is located on the upper floor. The horizontal INGRID modules occupy the floor below, and the vertical INGRID modules extend across the bottom two floors [5].

The near detector complex, located 280 m downstream of the production target, measures the energy spectrum, flavor content, and interaction rates of the unoscillated neutrino flux, which are used to predict neutrino interactions at SK [8]. Figure 2.6 shows a schematic of the near detector complex. INGRID (Interactive Neutrino GRID) is an on-axis near detector. It monitors the center and intensity of the neutrino beam profile. The off-axis detector (ND280), enclosed in the recycled UA1 magnet, is the primary detector at the 280 m site. ND280 aims at measuring the unoscillated (anti)neutrino flux.

2.2.1 INGRID on-axis detector



(a) INGRID front view. (b) An individual INGRID module.

Figure 2.7: Schematics of the INGRID detector [7].

INGRID uses identical modules laid out as a cross along the horizontal and vertical axes, as shown in Figure 2.7a. The configuration of INGRID has been updated over time. The center of the INGRID cross corresponds to the neutrino beam center, where an extra module, called the Proton Module, is placed, which detects muons and protons produced by the neutrino beam in INGRID. Figure 2.7b shows an individual INGRID module, which consists of a sandwich structure of iron plates and tracking scintillator planes. Veto scintillator planes around the module reject interactions from outside it. The INGRID measures the neutrino beam direction with a precision better than 0.4 mrad by neutrino interactions in iron [7], and its data is not used directly in this thesis analysis.

2.2.2 ND280 off-axis detector

The ND280 off-axis detector, placed 2.5° off-axis from the neutrino beam, serves to measure the unoscillated $\nu_\mu(\bar{\nu}_\mu)$ flux, $\nu_e(\bar{\nu}_e)$ contamination, along with measuring exclusive neutrino interaction rates. As shown in Figure 2.8, ND280 consists of several subdetectors, including a pi-zero detector (PØD), three Time Projection Chambers (TPCs), and two Fine-Grained Detectors (FGDs). All of them are placed inside a metal frame container, called the "basket". The basket is surrounded by Electromagnetic Calorimeter (ECal) modules. The recycled UA1 magnet, instrumented with scintillator modules, encloses the ND280 and also serves as part of a side muon range detector (SMRD).

Pi-zero detector (PØD)

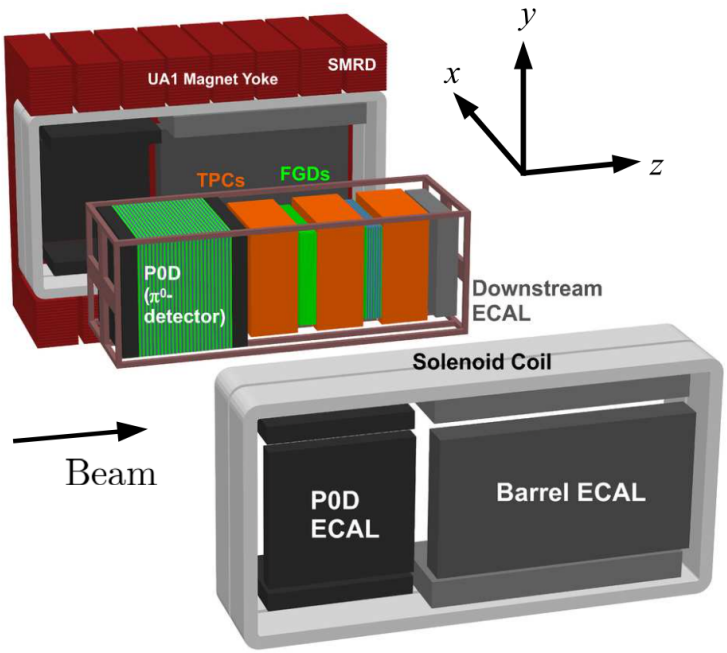


Figure 2.8: The ND280 off-axis detectors. [8]

PØD, placed at the upstream end of the ND280 basket, consists of tracking planes of X-Y scintillator bars alternating with fillable water bags and lead or brass sheets. The primary goal of PØD is to measure the neutral current process $\nu_\mu + N \rightarrow \nu_\mu + N + \pi^0 + X$ on a water target [8][56]. In October 2022, the PØD water targets and central ECal module were removed from the basket and replaced by a new set of subdetectors for the upgraded ND280, which is described in Chapter 3.

Fine-grained detector (FGD)

Downstream of the PØD sit two FGD detectors. They act as the target mass for neutrino interactions and track the charged particles produced in neutrino interactions [8][57]. The upstream FGD arranges its scintillator bars into 30 layers that alternate between the X and Y directions perpendicular to the neutrino beam. The downstream FGD consists of seven XY plastic scintillator modules alternating with six 2.5 cm thick layers of water, which also provide water targets, the same as the SK, for neutrino interactions.

Time projection chamber (TPC) TPCs provide charged particle tracking, momentum measurement, and particle identification. Figure 2.9 shows a TPC drawing [8]. In each TPC the argon-based drift gas is held in an inner box and the surrounding outer box holds CO_2 as an insulating gas. The gap between the inner box and the outer box is 6.8 cm on the top and sides and 11.8 cm on the bottom [58]. The inner box is divided by a central cathode

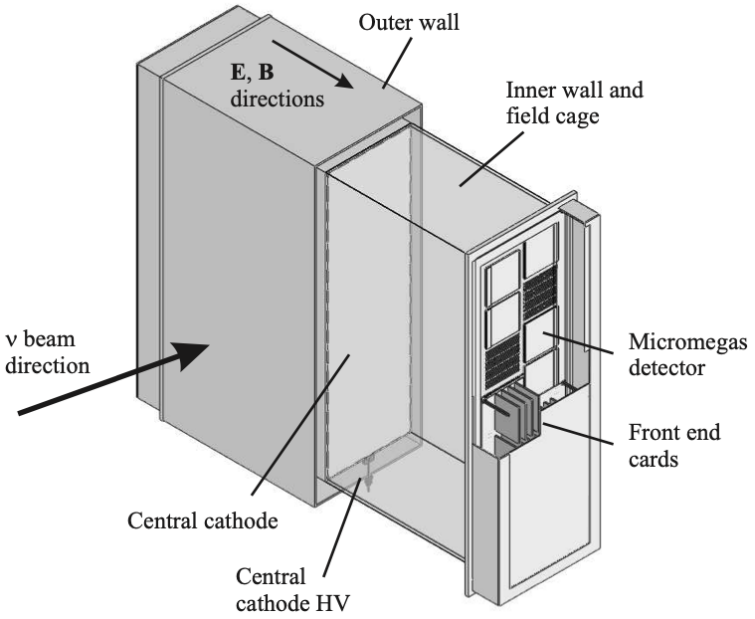


Figure 2.9: A simplified cut-away drawing of the TPC [8]

into two drift regions, with Micromegas readout planes located on both sides. When charged particles travel through the TPCs, they produce ionization electrons along their trajectories. These electrons drift under the applied electric field toward the readout planes, where they are multiplied and sampled. The signal pattern in the readout planes, combined with the signal arrival time, gives 3D images of the charged-particle tracks. Since the TPCs operate inside the ND280 magnetic field, the curvature of reconstructed tracks is used to determine the particle charge and momentum. The energy loss of charged particles in the drift gas provides information for particle identification [8][58].

Electromagnetic calorimeter (ECal)

The ECals surround the inner subdetectors (PØD, TPCs, and FGDs), and have multiple independent modules, including PØD-ECal modules surrounding the PØD, Barrel-ECal modules surrounding the tracker, and a downstream ECal module behind the tracker. Each module is composed of alternating layers of plastic scintillator bars and lead absorber sheets. The ECals complement the inner detectors and enable full event reconstruction. The design of the ECals promotes electromagnetic shower measurements. A key role of ECals is the reconstruction of π^0 produced from neutrino interactions [8][59].

Side muon range detector (SMRD)

The SMRD is built from 440 scintillator modules that fill the gaps between the steel plates of the UA1 magnet yoke. The primary role of the SMRD is to provide a trigger

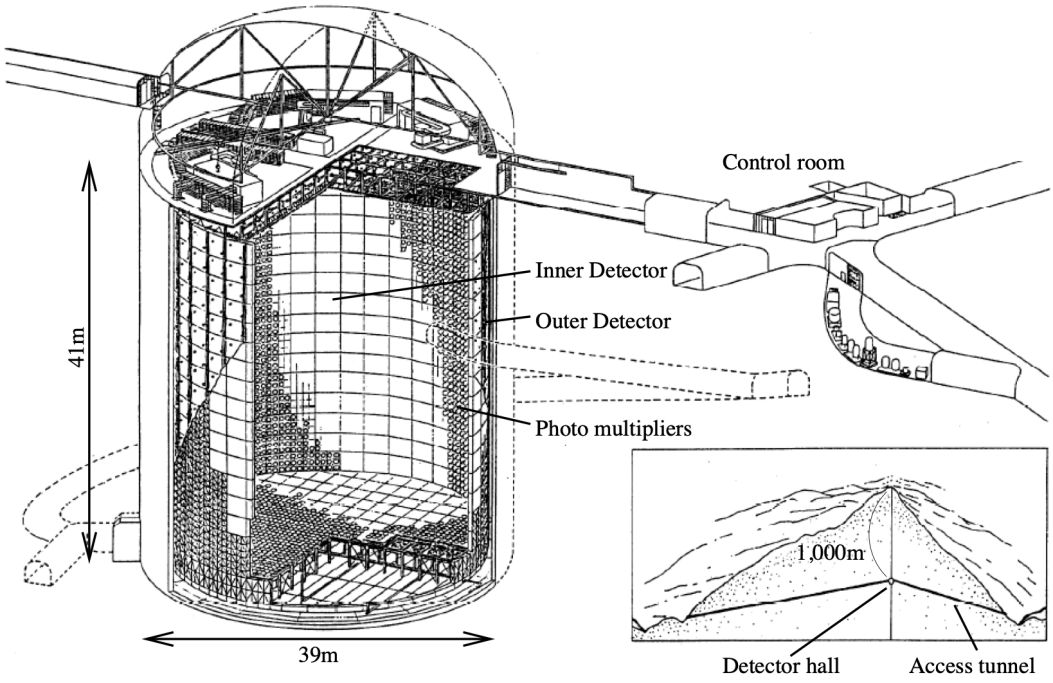


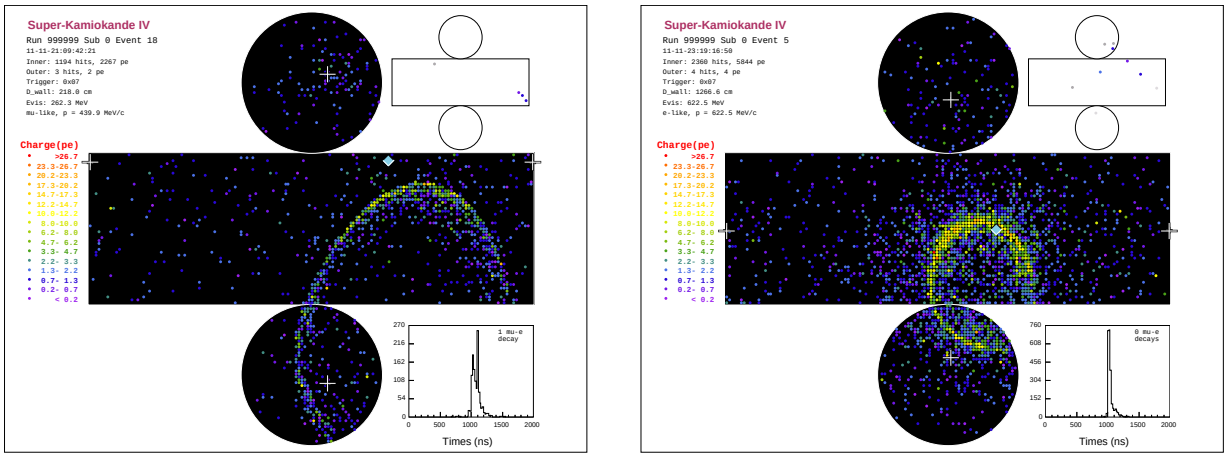
Figure 2.10: The Super-Kamiokande detector. [9]

for cosmic-ray muons crossing the ND280 detector and to detect muons that exit the inner detectors at large angles with respect to the beam direction [8][60].

2.3 Super-Kamiokande

T2K uses Super-Kamiokande (SK) as its far detector. The detector is located 295 km west of the beam source and measures the neutrino flux after oscillations. The detector sits 1 km deep inside Mt. Ikenoyama to shield it from cosmic rays. SK is a cylindrical tank with a height of 41.4 m and a diameter of 39.3 m, which is filled with 50 kton ultrapure water and is instrumented with around 13,000 photomultiplier tubes (PMTs) [9]. Figure 2.10 shows a schematic of SK. It has an outer detector (OD) and an inner detector (ID), optically separated by a cylindrical stainless steel structure that is about 50 cm thick radially. The ID is a cylinder 33.8 m across and 36.2 m tall, and its inner walls carry 11,129 inward-facing 50 cm diameter PMTs. The effective PMT surface coverage of the ID is 40%, which provides sufficient spatial resolution for SK to infer physical quantities from the imaged neutrino interactions. [8] The OD is a 2 m radially thick cylindrical space, instrumented with 1,885 outward-facing 20 cm diameter PMTs. It serves as an active veto against incoming cosmic rays and other backgrounds.

The flavor composition of the neutrino flux at SK is determined by measuring the leptons



(a) ν_μ event candidate.

(b) ν_e event candidate.

Figure 2.11: Super-Kamiokande event displays [5].

produced from neutrino-water interactions. When leptons travel through water above a threshold energy, they will produce Cherenkov light, which is detected by the PMTs on the detector walls. The ring-shaped hit pattern of the Cherenkov light is used to identify the type of charged particle and to reconstruct the neutrino interaction. Figure 2.11 shows an example of a ν_μ candidate event display and a ν_e candidate event display. Muons, measured for the ν_μ disappearance study, are resilient to scattering when traveling through water due to their relatively large mass. As a result, the Cherenkov light from the muons forms well-defined cones, producing clear, sharp rings of PMT hits. In contrast, the electrons, measured for the ν_e appearance study, scatter easily and produce electromagnetic showers due to their smaller mass and their energies in SK. The Cherenkov rings from these electrons are "fuzzy" in the PMTs. This difference in the Cherenkov ring pattern in SK is used to extract the neutrino interaction type.

Gadolinium sulfate octahydrate ($Gd_2(SO_4)_3{\cdot}8H_2O$) was loaded into the SK tank in the summers of 2020 and 2022 to reach about 40 tons in total and a Gd concentration of 0.03% [61][62]. Gd captures neutrons with a large cross section, and each capture produces a γ-ray cascade of about 8 MeV. This enhances SK's ability to identify inverse beta decay (IBD) events: $\bar{\nu}_e + p \rightarrow e^+ + n$, and improves SK's sensitivity to supernova neutrinos and other rare events.

2.4 T2K oscillation analysis strategy

T2K extracts the neutrino oscillation parameters by comparing the neutrino flux measured at the near detector, before oscillation, with the oscillated flux measured at the far detector. The observed event rate, as a function of the neutrino energy E_ν, depends on the

neutrino flux, the neutrino interaction cross section, and the detector efficiency. For the near detector the event rate is given by

$$N^{\mathrm{ND}}(E_\nu) = \Phi^{\mathrm{ND}}(E_\nu)\,\sigma(E_\nu)\,\epsilon^{\mathrm{ND}}(E_\nu), \tag{2.3}$$

where $\Phi^{\mathrm{ND}}(E_\nu)$ is the neutrino flux at the near detector, $\sigma(E_\nu)$ is the neutrino interaction cross section, and $\epsilon^{\mathrm{ND}}(E_\nu)$ is the near detector efficiency. The far detector event rate has a similar form, with an additional neutrino oscillation probability term,

$$N^{\mathrm{FD}}(E_\nu) = \Phi^{\mathrm{FD}}(E_\nu)\,\sigma(E_\nu)\,\epsilon^{\mathrm{FD}}(E_\nu)\,P(E_\nu), \tag{2.4}$$

where $\Phi^{\mathrm{FD}}(E_\nu)$ and $\epsilon^{\mathrm{FD}}(E_\nu)$ are the far detector flux and efficiency, and $P(E_\nu)$ is the neutrino oscillation probability. The Monte Carlo (MC) predicts the event rate using a set of parameters that model the flux, the cross section, and the detector response. The agreement between the data and the prediction is described by a binned likelihood $\mathcal{L}(D \mid \boldsymbol{\theta})$, where D is the observed data and $\boldsymbol{\theta}$ is the vector of model parameters. This likelihood can be formed as a product of a statistical term and a penalty term. The statistical term compares the observed and predicted number of events, and the penalty term constrains each parameter to its prior value.

Fitting the MC to the data for near detector samples constrains the parameters of flux, interaction model, and detector response. Since the near and far detectors share the same flux and cross-section model, the post-fit values and covariance of the flux and cross-section parameters can be used as inputs to the far detector oscillation analysis, while the near detector detector-response parameters are not used, because the two detectors are based on different technologies and the far detector evaluates its own detector systematics. Constraining the flux and interaction model with the near detector data greatly reduces the systematic uncertainties in the far detector oscillation analysis. The oscillation parameters are extracted from the far detector fit using a binned likelihood, and the flux, cross-section, and far detector systematic parameters are treated as nuisance parameters.

Both the near detector and far detector fits can be carried out in two statistical frameworks, the frequentist and the Bayesian. The frequentist framework finds the best-fit values that maximize the likelihood $\mathcal{L}(D \mid \boldsymbol{\theta})$, while the Bayesian framework samples the posterior distribution $P(\boldsymbol{\theta} \mid D)$ of the parameters through Markov chain Monte Carlo (MCMC) chains. To meet the statistical challenges of the upgraded T2K experiment and of next-generation long-baseline experiments such as DUNE, which involve larger data samples and more complex parameter spaces, a new fitting framework, GUNDAM (Generalized and Unified Neutrino Data Analysis Methods) [63], was developed. The author contributed to the implementation and validation of an adaptive MCMC algorithm in this framework. This work is presented in Appendix B.

Chapter 3

Near Detector Upgrade

3.1 Motivation for the ND280 upgrade

The ND280 detector plays a key role in the neutrino oscillation analysis by constraining uncertainties related to neutrino-nucleus interactions and neutrino fluxes, which are used to predict the event rates at Super-Kamiokande. One of the major backgrounds to the $\nu_\mu \to \nu_e$ appearance measurement is neutral-current (NC) π^0 production ($\nu_\mu + N \to \nu_\mu + N + \pi^0 + X$). This background was studied with the PØD [56]. The next step is to further constrain the neutrino-interaction-model systematic uncertainty so that the uncertainty in the predicted event rate at Super-Kamiokande can be reduced from 6% to about 4% in the T2K–II phase [10]. This motivates the ND280 upgrade.

One of the major limitations of the previous ND280 was its non-uniform angular acceptance. The previous ND280 had a higher reconstruction efficiency for forward-going charged particles entering the downstream TPCs. Charged particles emitted at large angles or backward with respect to the beam direction have a lower reconstruction efficiency. As a result, the original ND280 constrained the interaction model most in the forward phase space. Super-Kamiokande instead has a more uniform angular acceptance.

The other main limitation is that the previous ND280 had limited sensitivity to low-momentum hadrons. Protons and pions that did not reach a TPC were reconstructed in two dimensions in the FGDs. The threshold for proton detection is about 450 MeV/c. Since low-momentum hadrons carry important information about nuclear effects, this limitation weakened the ability of ND280 to constrain the neutrino interaction models. SuperFGD, the key component of the upgraded ND280, will lower the proton threshold to about 300 MeV/c [10].

The ND280 upgrade was designed to address these limitations. The PØD water target and the central ECal modules were removed in October 2022 and replaced by a SuperFGD, two High-Angle TPCs, and six Time-of-Flight planes, which will be described in the next section in detail. The other subdetectors of the ND280, including the PØD upstream ECal, are

kept in the original configuration. The upgraded ND280 provides a highly granular neutrino interaction target, improved high-angle tracking, and precise timing information. These improvements constrain neutrino-interaction uncertainties relevant to the T2K oscillation analysis.

3.2 Upgraded near detector configuration

Figure 3.1 shows the configuration of the upgraded ND280. The upgraded components include a Super Fine-Grained Detector (SuperFGD), two High-Angle TPCs (HA-TPCs), and six Time-of-Flight (ToF) planes. The SuperFGD is located between the two HA-TPCs. The SuperFGD and two HA-TPCs are enclosed by six ToF planes. This section describes the HA-TPCs and ToF planes in detail. The SuperFGD will be described in Chapter 4.

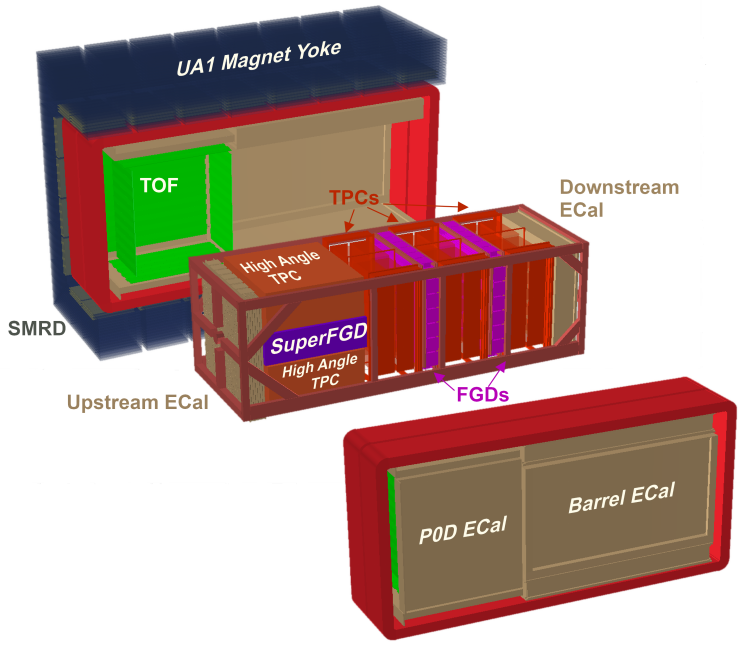


Figure 3.1: The upgraded ND280 off-axis detectors [5].

3.2.1 High-angle time projection chambers

Two HA-TPCs are placed on the top and bottom of the SuperFGD detector to measure high-angle charged particles exiting from the SuperFGD, which improves the ND280 angular acceptance. Figure 3.2 shows the design of HA-TPCs, which is similar to the downstream

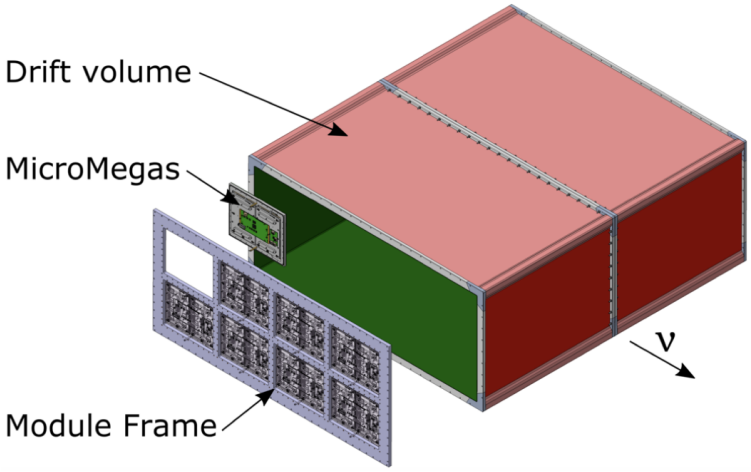


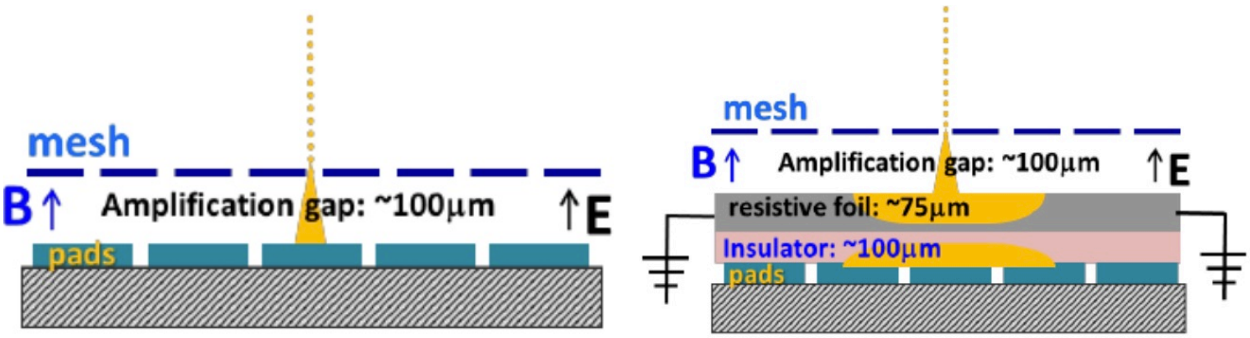
Figure 3.2: A schematic of the High-Angle TPC [10].

vertical TPCs. The dimensions of each HA-TPC are 2.0 m × 0.8 m × 1.8 m. It consists of a rectangular gas tight box serving as the TPC field cage that holds drift gas, which is a mixture of Ar-CF_4-iC_4H_{10} as 95:3:2. A central cathode divides the box into two drift regions. The electrical potential of the cathode is operated at -27 kV, and the drift electric field is kept at 275 V/cm uniform field, which is the same as the vertical TPC's drift field. The field cage is built from an insulating layer bonded to a composite support panel, which keeps the inactive material low and leaves as much of the active volume as possible for tracking [10].

Two anode read-out planes are located on the sides opposite to the central cathode. The module frame of each anode plane holds eight Encapsulated Resistive Anode Micromegas (ERAM) [64]. Figure 3.3b shows a schematic of the ERAM. A layer of insulator covers the pads of the resistive Micromegas and a layer of resistive foil covers the insulator. When electrons are drifted to the mesh, an avalanche will be generated in the amplification gap. The avalanche charge is then collected and spread by the resistive foil. The resistive foil, coupled with the insulator, forms a resistor-capacitor circuit generating an induced signal on multiple adjacent pads. The normal bulk Micromegas, as shown in Figure 3.3a, was applied in vertical TPCs. In this Micromegas, however, the avalanche charge is usually measured by a single pad. Therefore, compared with normal Micromegas, resistive Micromegas improve HA-TPC's spatial resolution.

3.2.2 Time-of-flight detector

Six Time-of-Flight (ToF) planes enclose the SuperFGD and the two HA-TPCs, as shown in Figure 3.4. These planes measure the crossing time of charged particles with sub-nanosecond resolution [10]. Together with the SuperFGD timing, the ToF timing determines the direction of a charged particle. This separates particles produced in (anti-)neutrino in-



(a) Normal bulk Micromegas (b) Resistive Micromegas

Figure 3.3: Schematics of a normal bulk Micromegas and a resistive Micromegas [10].

teractions inside the SuperFGD from background particles that enter from the surrounding material. The ToF also provides cosmic triggers for the SuperFGD and the HA-TPCs. Each plane holds 20 plastic scintillator bars that are 1 cm thick and 12 cm wide. The bottom plane is an exception, holding only 18 bars to accommodate the cabling [65]. Arrays of silicon photomultipliers (SiPMs) read out both ends of each bar.

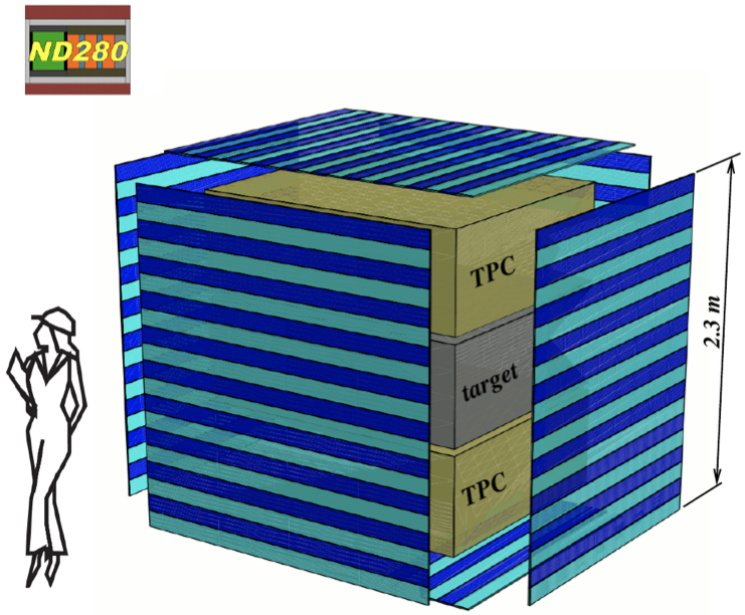


Figure 3.4: A schematic of ToF planes [10].

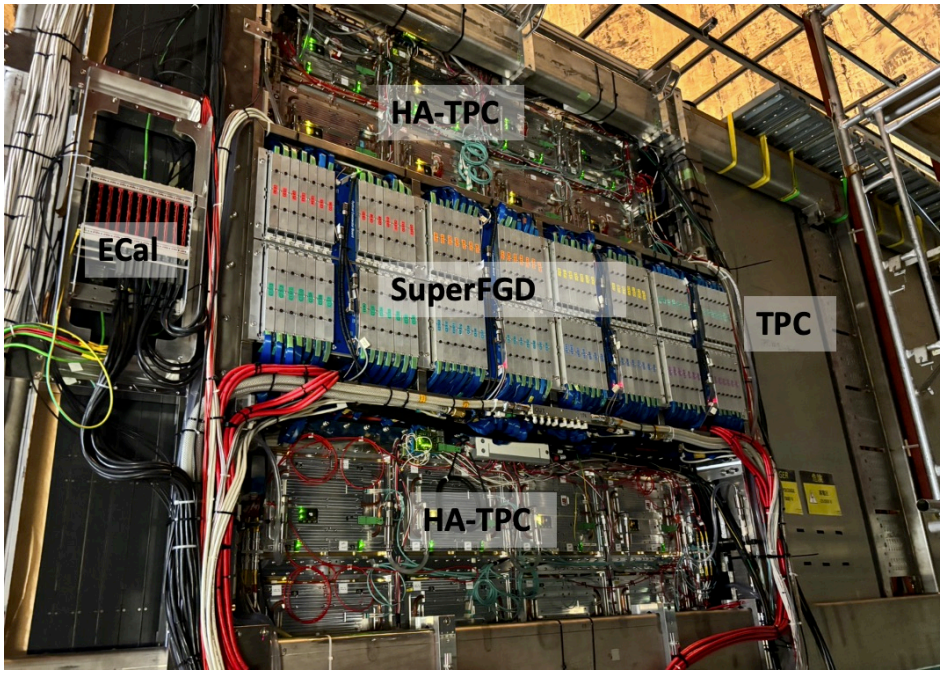


Figure 3.5: A picture of the SuperFGD and two HA-TPCs installed in the ND280 pit [5].

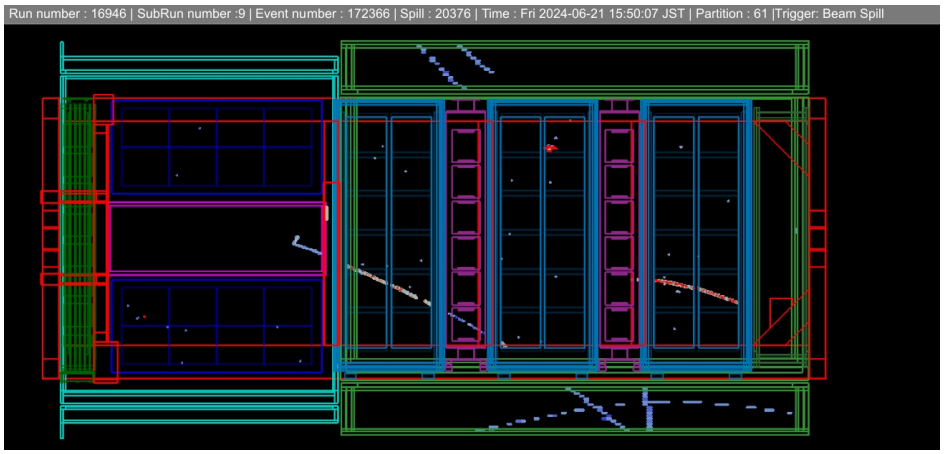


Figure 3.6: An event display example of a ν_μ CC0π interaction candidate in the upgraded ND280. The event is from the 2024 neutrino beam run [5].

3.3 Installation

After successfully assembling and testing, all upgraded subdetectors were installed into the ND280 pit. The bottom HA-TPC was installed in the summer of 2023 before the SuperFGD, and the top HA-TPC was installed in early 2024. The ToF detector was installed in the ND280 between July 2023 and May 2024 in three separate phases [65]. Figure 3.5 shows the SuperFGD and two HA-TPCs in the ND280 pit. After careful testing and commissioning, the upgraded ND280 began taking neutrino beam data in June 2024 in full configuration. Figure 3.6 shows an event display of a ν_μ CC0π candidate in this beam run.

3.4 Data and Monte Carlo production

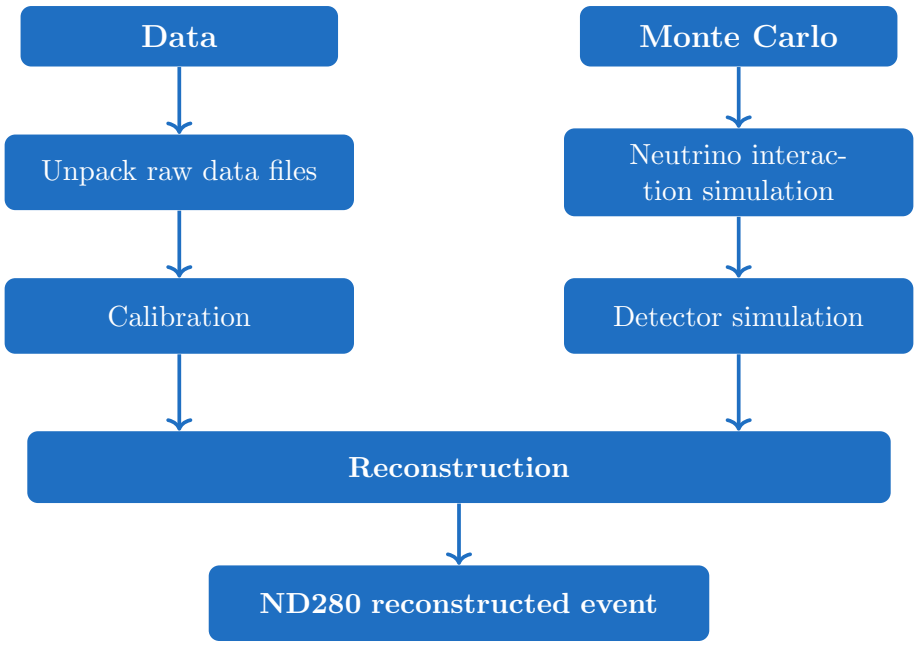


Figure 3.7: Data and Monte Carlo production flow for the upgraded ND280.

The process to produce data and Monte Carlo (MC) simulation neutrino events in the upgraded ND280 for the physics analysis is shown in Figure 3.7. For the MC production, the neutrino interactions in ND280 are simulated by the NEUT event generator [66]. The energy deposition and secondary interactions of the final-state particles are then simulated by Geant4 [67], and the resulting detector signals are produced by the detector response simulation. These signals are then passed to the event reconstruction, which is the same as the one used for the data.

For the data production, the raw data from all ND280 sub-detectors are recorded by the MIDAS framework in a binary format [8]. The unpacking step decodes the raw data into

digital readouts. These readouts are then converted into calibrated hits with charge and time, using the calibration constants of each sub-detector stored in a MySQL database [8]. The calibrated hits are finally passed to the reconstruction.

3.5 Reconstruction

The calibrated hits in an event are reconstructed into tracks and clusters in two stages: the local reconstruction and the global reconstruction. In the local reconstruction, each sub-detector reconstructs its own track segments from its hits, so a particle that crosses several sub-detectors has one reconstructed segment in each of them. The global reconstruction then matches the segments belonging to the same particle and combines them into a single global track. The momentum and particle identification of the global track are reconstructed from the combined information of all the sub-detectors that the track crosses. The local reconstruction of the HA-TPCs and the ToF detectors is described below. The SuperFGD reconstruction is introduced in Section 4.5.

HA-TPC reconstruction

In the HA-TPCs, a charged particle ionizes the gas, and the ionized electrons drift to the ERAM readout planes [68]. The readout planes spread the collected charge across several neighbouring pads, and each pad records its charge and time as a digitized waveform. The reconstruction first builds a hit by locating the peak of the waveform, where the peak height gives the charge and its time gives the electron arrival time. The pad hits are then collected and reconstructed into tracks by a pattern recognition algorithm. The momentum of the track is reconstructed from the curvature of the track in the magnetic field. The particle identification hypothesis (e, μ, π, p) is estimated from the energy loss per unit length, dE/dx.

ToF reconstruction

The ToF reconstruction combines the signals from the two ends of each scintillator bar into clusters. Each cluster provides the time and position of a track's crossing of a ToF plane [65].

Chapter 4

The Super Fine-Grained Detector

4.1 Overview of the SuperFGD

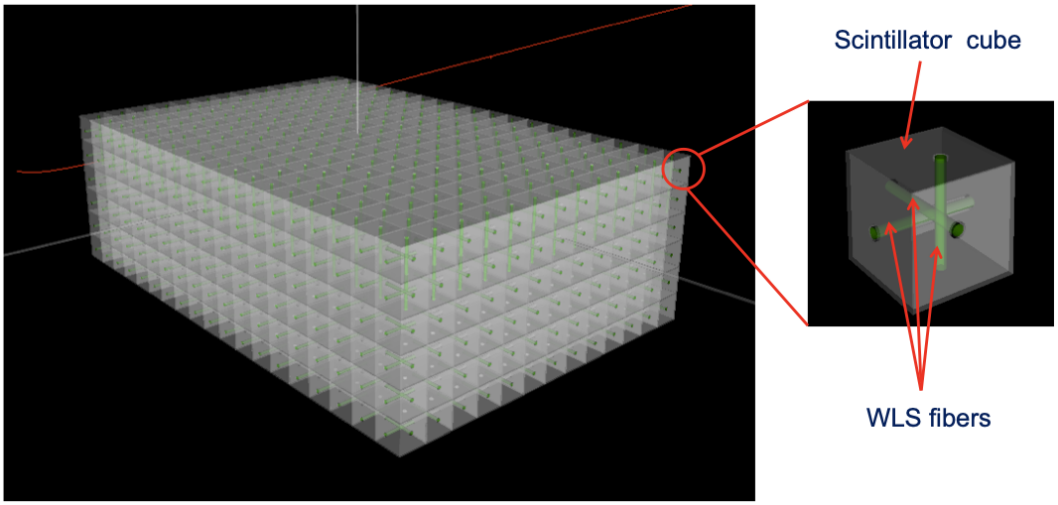


Figure 4.1: A schematic of the SuperFGD [10].

The Super Fine-Grained Detector (SuperFGD) serves as an active (anti-)neutrino interaction target and charged particle tracker in the upgraded ND280 [10][12]. Figure 4.1 shows the design of the SuperFGD. It consists of $182 \times 192 \times 56$ plastic scintillator cubes, weighing approximately 2 tons. Each cube is 1 cm^3 and is covered with a reflecting layer, so they are optically isolated from each other. Each cube is threaded by three orthogonal wavelength-shifting fibers (WLS), which guide scintillation light from the cubes to the photosensors.

Figure 4.2 shows how the SuperFGD measures a charged particle. When charged particles pass through the SuperFGD cubes, they deposit energy and generate scintillation light inside

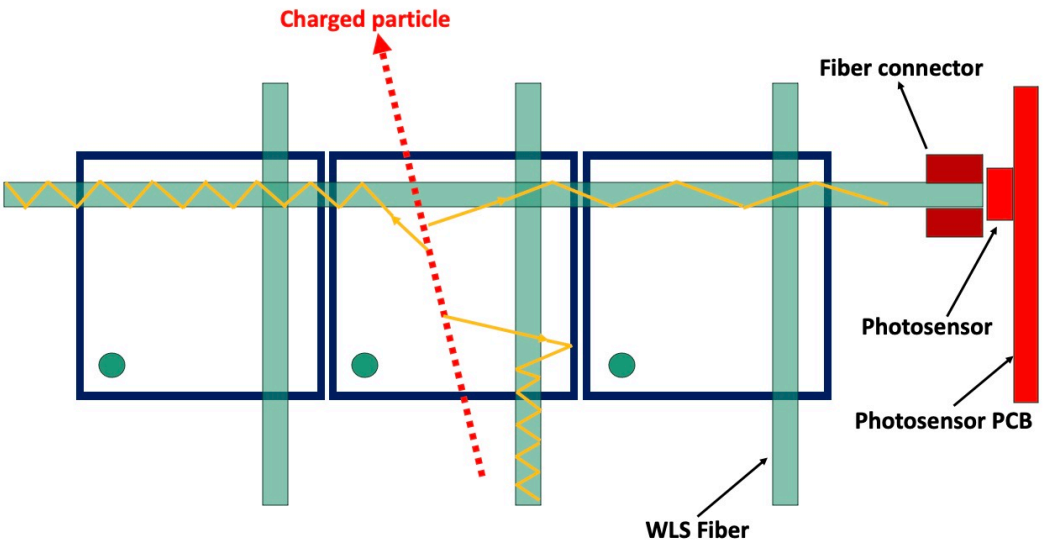


Figure 4.2: A sketch of a charged particle generating scintillation light in the SuperFGD cubes. The red dashed arrow represents a charged particle. The yellow line is the scintillation light.

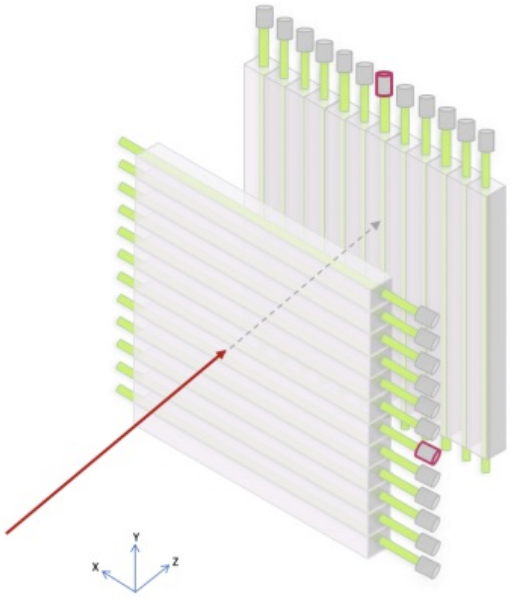
the plastic scintillator cubes. Since the cubes are optically isolated from each other, the detector can determine the position of the charged particle track at the cube level. The WLS collects scintillation light, converts it to a longer wavelength, and guides it to the photosensors. By combining the signals from three WLS directions, the track of the charged particle can be reconstructed in three dimensions.

Figure 4.3 shows the advantage of the SuperFGD over the existing FGDs. The FGDs consist of plastic scintillator bars arranged in either the X or Y direction, perpendicular to the beam direction, so charged particle tracks are reconstructed from two-dimensional projections. This limits the detection efficiency of short tracks and tracks with high angles. The scintillator cubes of the SuperFGD can be read in three orthogonal directions, providing three-dimensional views of charged-particle tracks and isotropic particle tracking. As a result, the SuperFGD improves the reconstruction of short tracks and high-angle tracks, which are essential for constraining the systematics related to neutrino-nucleus interactions [10][12].

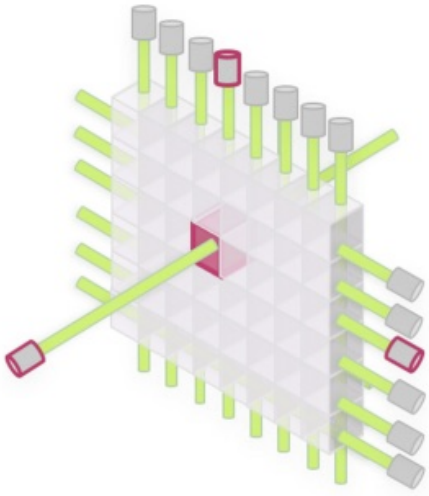
4.2 Detector System

4.2.1 Cube

The size of a SuperFGD cube is 1 cm $\times$ 1 cm $\times$ 1 cm, which provides fine granularity for the SuperFGD. Each cube has three mutually orthogonal 1.5 mm diameter cylindrical holes, through which 1 mm diameter WLS fibers pass. Figure 4.4a shows a prototype in which

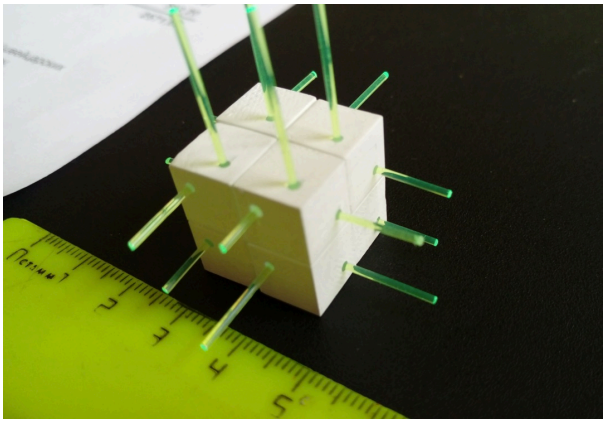


(a) FGD XY scintillator bars.

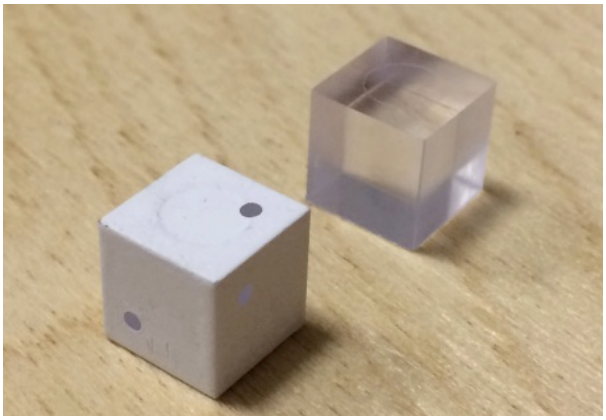


(b) SuperFGD scintillator cubes.

Figure 4.3: Comparison of the scintillator structure of the FGD and the SuperFGD. [11].



(a) Eight scintillator cubes threaded with WLS fibers [69].



(b) Scintillator cubes before and after chemical etching [12] .

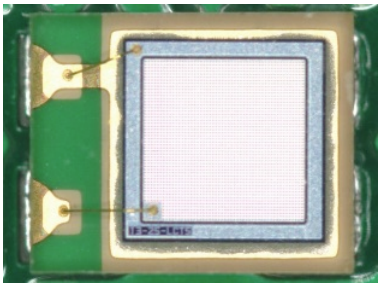
Figure 4.4: SuperFGD scintillator cubes.

eight cubes are assembled using WLS fibers. Each cube is an optical-quality polystyrene scintillator doped with paraterphenyl (PTP) at 1.5% and POPOP at 0.01% [12]. After fabrication, the cube surface is covered by a chemically etched white diffusing reflector, which optically isolates neighboring cubes, as shown in Figure 4.4b. Since the SuperFGD contains nearly two million cubes, the cube dimensions and hole positions must be controlled precisely to allow smooth fiber insertion. The variation of the cube size is attributed to the thickness of the reflector, which is 60–70 μm [12]. The variation of the cube hole position is determined to be about 0.1 mm, which is well within the required tolerance [12].

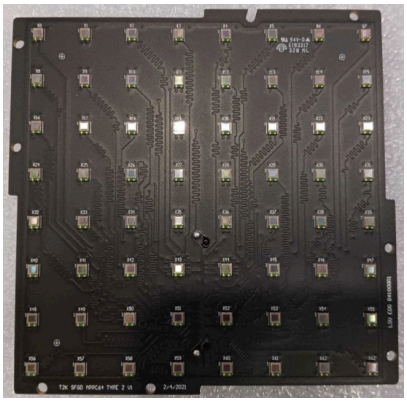
4.2.2 Wavelength-shifting fibers

The wavelength-shifting fibers (WLS) send the scintillation light from the cubes to the photosensors. The SuperFGD uses 1.0 mm diameter Kuraray Y-11(200) fibers with a round, multi-cladding structure [12]. The fiber's absorption spectrum peaks at 430 nm, which matches the peak of the scintillation light emitted by the cubes. Attenuation makes the emission spectrum depend on the fiber length. For a 1 meter fiber it peaks at about 505 nm [12]. A plastic ferrule is glued to one end of the fiber and fixed in the SuperFGD mechanical box where it provides an optical interface with the corresponding photosensor.

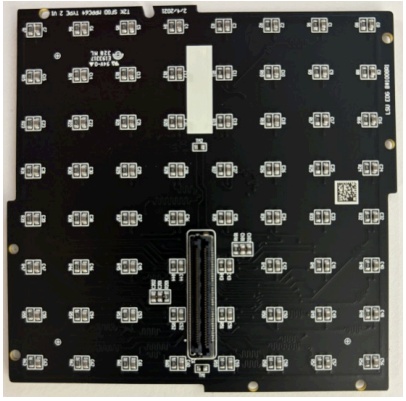
4.2.3 Multi-pixel photon counter



(a) Hamamatsu S13360-1325PE MPPC.



(b) MPPC-PCB photosensor side showing the 8×8 array of MPPCs.



(c) MPPC-PCB connector side.

Figure 4.5: Photosensor and MPPC-PCB used in the SuperFGD [12].

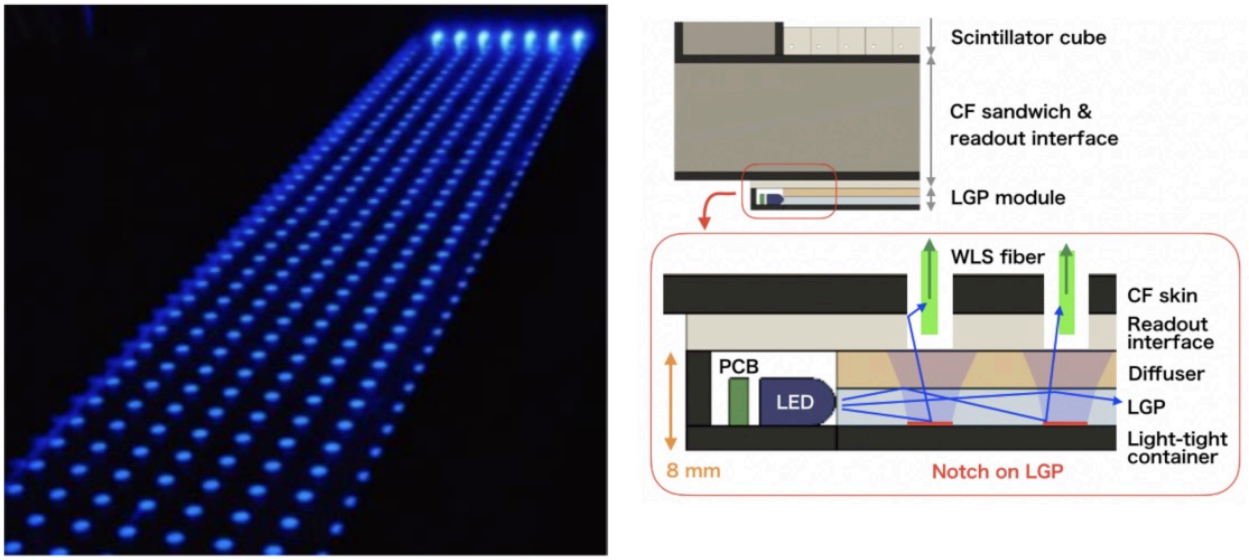
The scintillation from the WLS fibers is detected by Multi-Pixel Photon Counters (MPPCs), the photosensors used in the SuperFGD, which convert photons into electrical signals. MPPCs are silicon photomultipliers composed of many independent Geiger-mode avalanche

photodiode pixels. MPPCs are suitable for SuperFGD due to their compactness and insensitivity to magnetic fields.

The SuperFGD uses the Hamamatsu S13360-1325PE MPPC [70]. Figure 4.5a shows an MPPC. Its photosensitive area, 1.3 mm × 1.3 mm, is slightly larger than the 1 mm diameter of the WLS fibers, which ensures that the photons from the fibers are collected [12]. The pixel pitch is 25 μm, corresponding to 2668 pixels per MPPC, providing a larger dynamic range than other MPPCs used in ND280 subdetectors. In addition, compared with the S10362-13-050C MPPCs used in the original ND280, the S13360-1325PE has about one order of magnitude lower dark count rate, optical cross-talk probability, and afterpulse probability [12].

The MPPCs are mounted on printed circuit boards (PCBs), as shown in Figure 4.5b. Each MPPC-PCB holds 64 MPPCs in an 8×8 grid with 10.3 mm spacing between neighboring MPPCs [12]. The PCB measures 83.8 mm × 83.8 mm, and its outer edges are designed for close tiling within the SuperFGD mechanical box. The PCB distributes two separate bias voltages to two groups of 32 MPPCs. The front-end readout board can modulate the bias voltage of each individual MPPC within a group by ±1.25 V [12]. The MPPC signals are routed through an 80-pin SAMTEC connector mounted on the PCB, as shown in Figure 4.5c, and then propagated via a ribbon cable to the front-end boards. Two versions of the PCBs are designed with different connector locations to optimize cable routing [12].

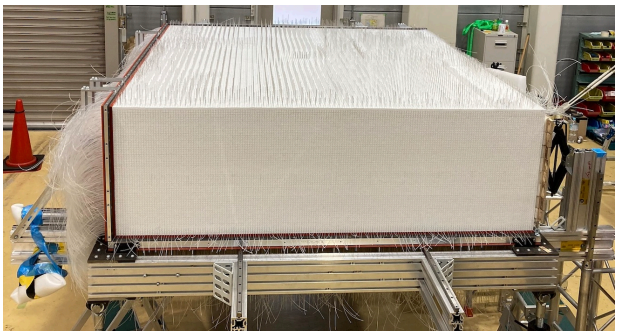
4.2.4 LED calibration system



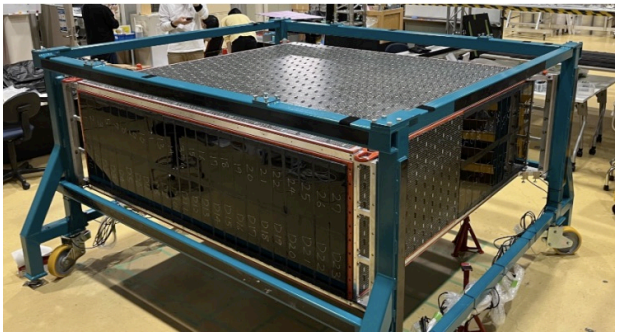
(a) Light Guide Plate.

(b) A schematic of the LED calibration system.

Figure 4.6: LED calibration system [12].



(a) Assembled mechanical box containing the scintillator cubes.



(b) Mechanical box after integration of the MPPC-PCBs and LED modules.

Figure 4.7: SuperFGD mechanical box [5].

The SuperFGD carries an LED calibration system used for regular electronic gain calibration, long-term stability monitoring, and detector commissioning. The system is required to provide sufficient uniform photoelectrons to many MPPC channels and be compact due to limited space. The optical distributor is a Light Guide Plate (LGP), shown in Figure 4.6a. Figure 4.6b shows a conceptual schematic of the LED calibration system, which consists of a notched LGP, a diffuse plate, an LED-array PCB with a collimator, and a black light-tight container [12]. The LGP receives pulsed blue LED light. The 3 mm diameter notches aligned with the WLS fiber ends scatter this light into the fibers and the fibers then transport it to the MPPCs. The diffuse plate is included to spread the LED light more uniformly. LGP modules are mounted on the downstream, bottom, and side walls of the SuperFGD mechanical box to cover all MPPC channels. The LEDs are controlled by custom LED drivers, which generate pulses with adjustable height and width for each LED channel.

4.2.5 Mechanical box

The SuperFGD mechanical box provides mechanical support for the detector and ensures alignment of the scintillator cubes, WLS fibers, MPPC-PCBs, and LED calibration systems. It holds $1,956,864$ scintillator cubes and allows $55,888$ WLS fibers to exit the box's inner volume. The box also provides the mechanical interface to the MPPC-PCBs and to the LED calibration system. The box itself and the front-end electronics bring the total supported weight to about 2.5 tonnes [12].

The box must preserve the alignment between the cubes, the WLS fibers, and the cube holes on the box panels. Misalignment could cause stress on the WLS fibers and potentially damage them. The box must compress the cubes enough to reduce air gaps between them and prevent cube movement. The compression must not be so great that it damages the crossing WLS fibers.

The box has six panels that each cover one side of the detector. Each panel of the

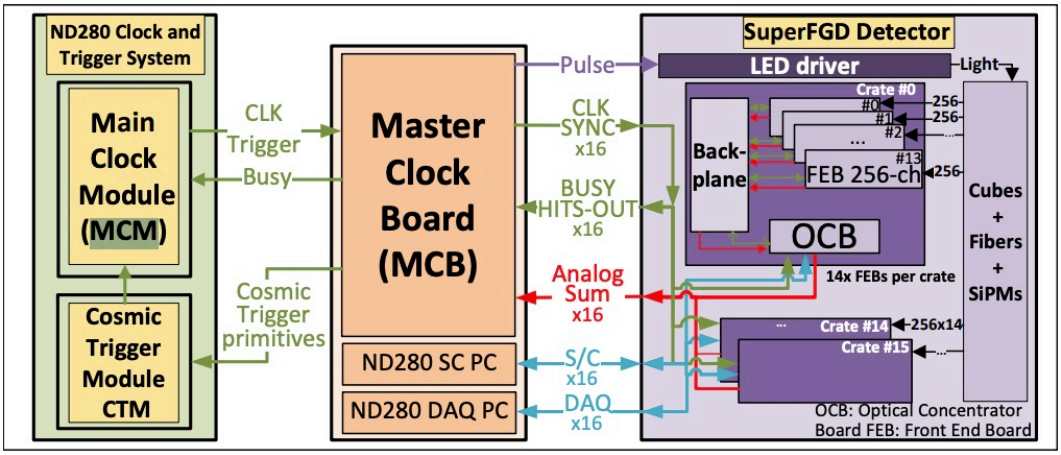


Figure 4.8: Overview of the SuperFGD electronics architecture [12].

box is made from several layers glued together with epoxy. The outer surfaces of the box have fiberglass mounting plates to hold the MPPC-PCBs and the LED modules. The box also includes holes through which the WLS fibers exit the detector. These holes have a conical shape, with a 5 mm inner diameter and a 3 mm outer diameter, allowing for small misalignments between the cube holes and the box holes [12].

Figure 4.7 shows the SuperFGD mechanical box during and after integration. The left photo shows the assembled box containing the scintillator layers. The right photo shows the box after the MPPC-PCBs and LED modules were installed, and the detector was fixed to the support frame.

4.2.6 Electronics architecture

The SuperFGD electronics system digitizes the analog signals from the MPPCs and transfers the digitized data to the ND280 data acquisition system (DAQ). Figure 4.8 shows the architecture of the electronics. The system consists of 16 electronic crates, with eight crates installed on each side of the detector. Each crate contains 14 Front-End Boards (FEBs) and one Optical Concentrator Board (OCB) [12].

Four MPPC-PCBs are connected to a single FEB through SAMTEC cables and an MPPC Interface Board (MIB), so each FEB reads out 256 MPPC channels. Inside each crate, the FEBs and the OCB are connected to a backplane. The backplane distributes the low voltage power, the MPPC bias voltage, and the digital communication links between the FEBs and the OCB. The OCB serves as a DAQ data concentrator and a slow control command dispatcher for the FEBs in a crate, such as the configuration of the CITIROC and the FPGA [12]. The FEB receives triggers, synchronization signals, slow control, and the MPPC bias voltage from the OCB and sends DAQ and slow control data back to the OCB, which sends them to the DAQ via Ethernet. The Master Clock Board (MCB) provides links between the

ND280 master clock module (MCM) and the SuperFGD electronics system. It distributes triggers and synchronization signals to the OCBs, which then pass them to the FEBs via the backplanes [12].

4.2.7 Front-end boards

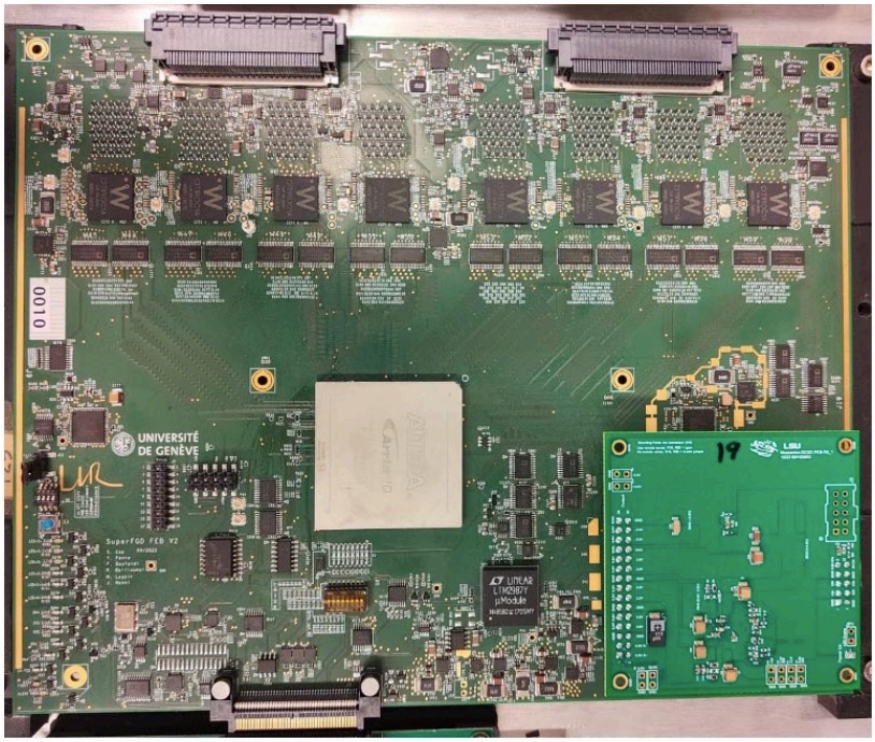


Figure 4.9: Picture of the FEB board [12].

The Front-End Boards (FEBs) process and digitize the MPPC signals. Figure 4.9 shows the FEB used in the SuperFGD. The MPPC connectors and CITIROC chips are located in the analog region at the top of the board, while the field-programmable gate array (FPGA) and digital readout components are located in the center and bottom of the board. One FEB is structured around eight CITIROCs, which were used in the BabyMIND detector for the WAGASCI Experiment [71].

A CITIROC is an application-specific integrated circuit (ASIC) with 32 channels [72]. Figure 4.10 shows the internal structure of the CITIROC [12]. Each CITIROC channel has two independent programmable preamplification and shaping circuits to read the analog signals from the MPPC. The two circuits have different input capacitances: 1.5 pF in the low-gain (LG) path and 15 pF in the high-gain (HG) path. The gains can be tuned through the feedback capacitance. There are two signal sampling modes: fixed-delay Track & Hold circuit

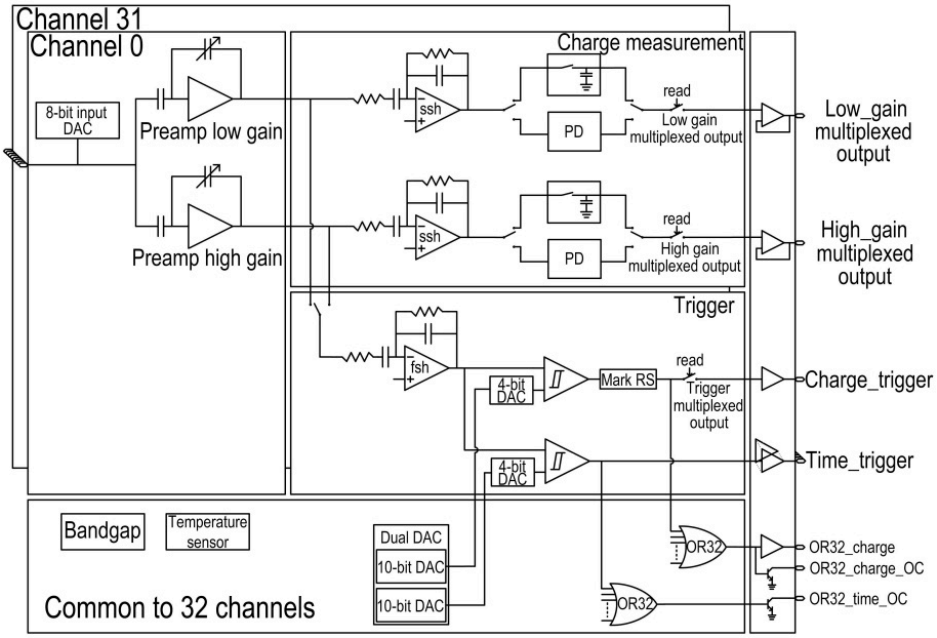
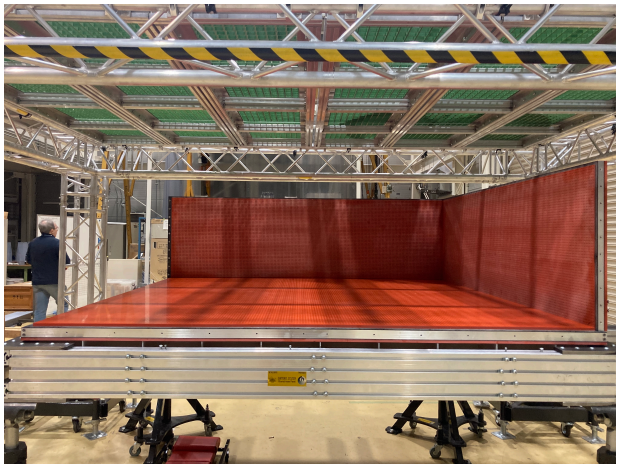


Figure 4.10: Schematic of the CITIROC circuit [12].

mode and Peak Detector mode. The Peak Detector mode is the default for the SuperFGD, which records the maximum amplitude of the shaped pulse. The high-gain and low-gain analog outputs are then digitized by analog-to-digital converter (ADC) chips outside of the CITIROC. The analog charge readout is controlled by the gate signal sent from the MCB. The gate length depends on the run modes, including the beam, cosmic, and LED calibration modes. When the gate is open, the first MPPC signal triggers the CITIROC peak detector for the corresponding channel, and the FEB programmable hold delay allows signals to be sampled. At the end of the gate, ADC conversion begins, resulting in approximately 10 μs of analog dead time for the charge readout. In parallel with the charge measurement path, the timing readout uses a fast shaper with a fixed shaping time of 15 ns. The input to this fast shaper is either the high-gain or low-gain preamplifier output, as selected by the user. A discriminator with a programmable threshold controlled by a digital-to-analog converter (DAC) generates triggers at the signal's rising and falling edges. These triggers are sampled by the FPGA at a frequency of 400 MHz, which records the rising and falling edge time stamps with respect to the global time stamp (GTS) provided by the MCB.

4.3 Assembly

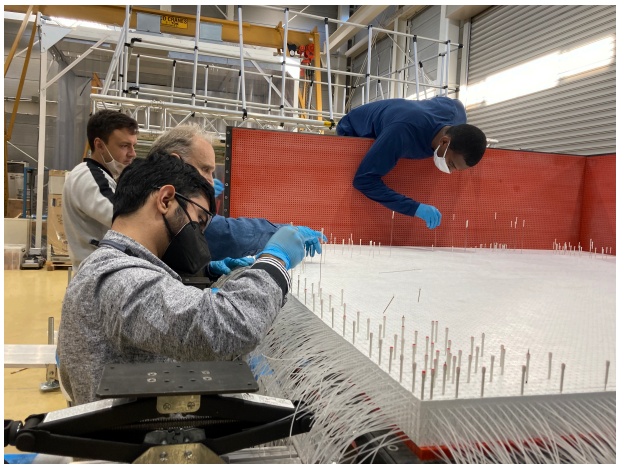
The SuperFGD assembly was performed in several stages. The cubes were preassembled into 56 layers with a dimension of 192 $\times$ 182 using fishing lines. These fishing lines passed



(a) The SuperFGD mechanical box is half-assembled before cube layer installation



(b) A cube layer is installed, and fishing lines are inserted through the corresponding holes in the mechanical box



(c) After each new cube layer is installed, the cube layers are vertically aligned using knitting needles.

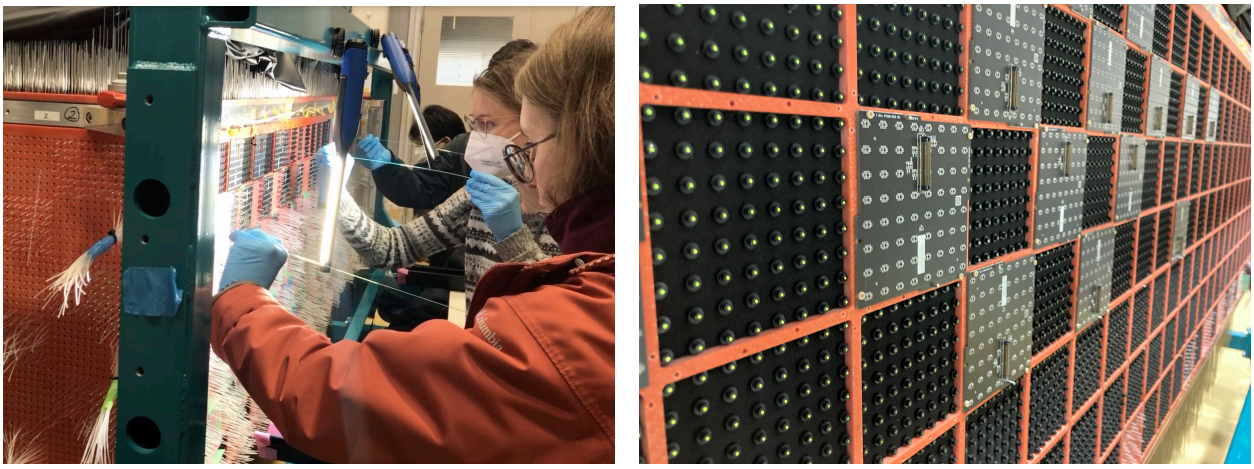


(d) After all cube layers are assembled, the remaining mechanical box panels are installed, and welding rods are inserted to maintain the vertical alignment of the cubes.

Figure 4.11: Assembly of the SuperFGD scintillator cube layers into the mechanical box [5].

through the cube holes, keeping the cubes aligned. The scintillator cube layers were then shipped to J-PARC for installation into the SuperFGD mechanical box. The scintillator cube layers were first assembled to the half-assembled mechanical box, and then the box was closed. After this, the WLS fibers, MPPC-PCBs, LED calibration system, light barrier, and readout cables were installed on the mechanical box. This whole process took place from October 2022 to April 2023.

Figure 4.11 shows the installation of the scintillator cube layers into the mechanical box. The mechanical box was first half-assembled. The cube layers were then installed into the box one by one. Each new cube layer was placed on top of the existing layers, and the fishing lines of the layer were inserted through the corresponding holes in the mechanical box. The vertical alignment between the cube layers was improved using knitting needles. Once all layers had been installed, the remaining side and top panels of the mechanical box were then installed, closing the box. After the box was closed, the assembled detector was moved to a stainless-steel support frame. Longer welding rods were then inserted vertically through the cube holes to maintain the vertical alignment of the full cube stack.



(a) WLS fibers are inserted.

(b) MPPC-PCBs are mounted on the mechanical box.

Figure 4.12: Installation of WLS fibers and MPPC-PCBs on the SuperFGD mechanical box [5].

After the mechanical box was closed and moved to the support frame, the fishing lines were replaced by WLS fibers. To preserve the cube alignment during this process, the fishing lines were not removed all at once. Instead, the replacement was performed channel unit by channel unit, where each unit corresponded to one MPPC-PCB. The light yield of the installed fibers was checked using LED light, and fibers with poor response would be replaced. The MPPC-PCBs were then mounted on the mechanical box, and coupled to the fiber ends, as shown in Figure 4.12.

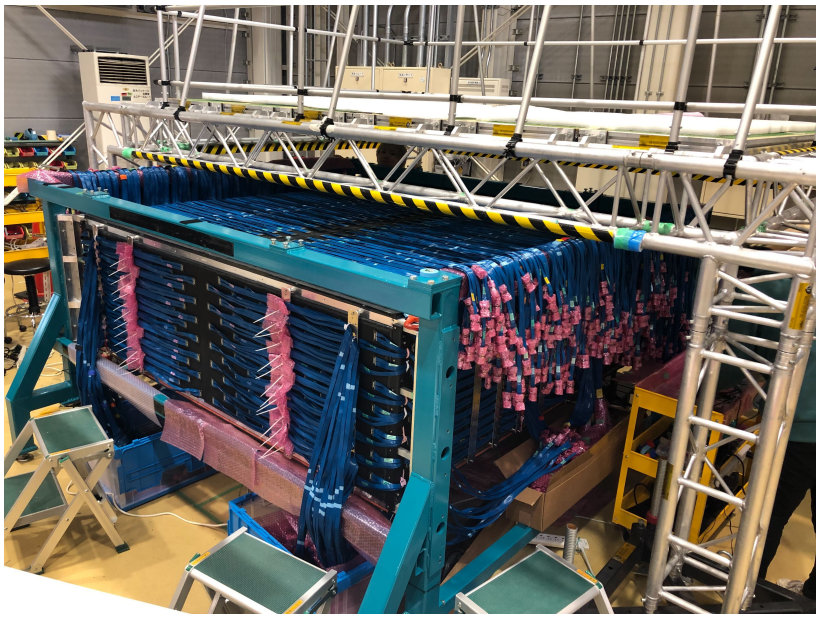


Figure 4.13: Assembled SuperFGD with readout cables [5].

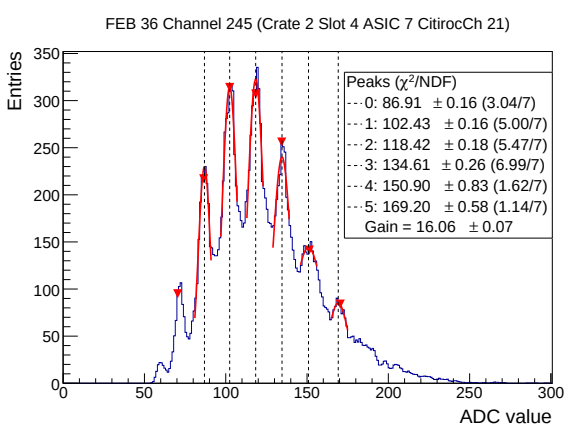
After the WLS fibers and MPPC-PCBs were installed, the LGP modules were mounted on the mechanical box. The light shielding sheets were then installed to reduce external light, and the readout cables were connected to the MPPC-PCBs. Figure 4.13 shows the assembled SuperFGD after the installation of the light shielding sheets and readout cables.

Before being installed into the ND280 pit, the assembled detector was tested on the surface. LED-light injection was used to check the LGP modules and MPPC-PCBs. Cosmic-ray data were also taken to test FEBs and detector response. After these surface tests, the SuperFGD was installed in the ND280 pit, as shown in Figure 3.5.

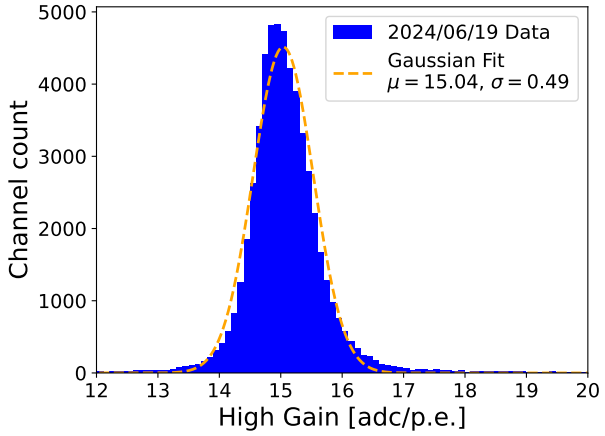
4.4 Charge calibration

The light yield of a hit is used to estimate the energy deposition of a charged particle in the SuperFGD. As described in Section 4.2.7, during an event gate, the FEB charge readout records the maximum pulse amplitude in each channel as high-gain (HG) and low-gain (LG) ADC values. In parallel, the timing readout records the rising-edge and falling-edge timestamps of the discriminator signal. The difference between the falling-edge and rising-edge timestamps is defined as the Time-over-Threshold (ToT) of the hit. The purpose of the charge calibration is to estimate the hit light yield in photoelectron units from the hit amplitude or ToT.

4.4.1 High-gain and pedestal calibration



(a) Example of the ADC distribution for one MPPC channel in a LED calibration run.



(b) Distribution of the high gain values for all calibrated MPPC channels.

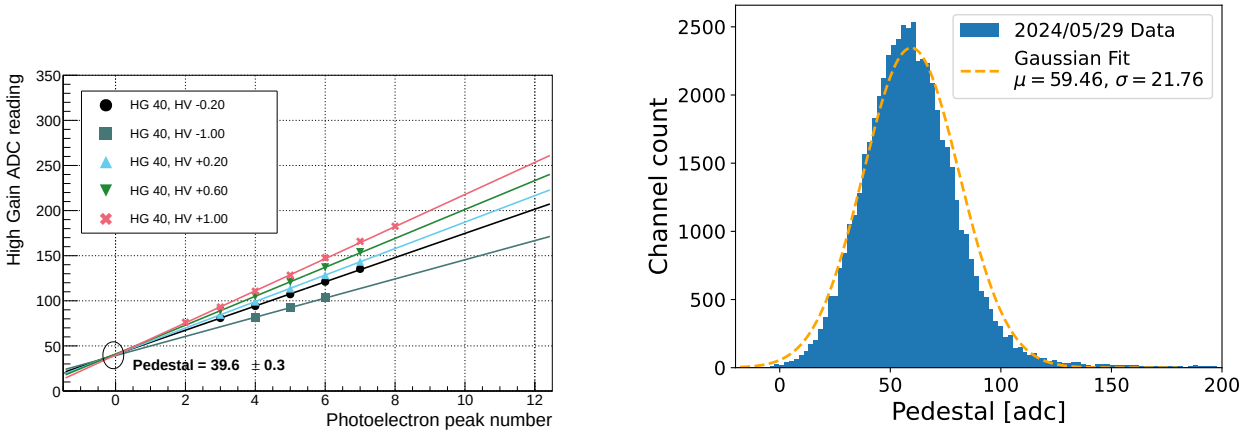
Figure 4.14: High gain calibration [12].

The HG ADC value recorded for a hit can be described by a linear relation between the light yield and the pedestal:

$$A_{\mathrm{HG}} = G_{\mathrm{HG}} \times N_{\mathrm{p.e.u.}} + P \tag{4.1}$$

where A_{HG} is the HG ADC value, G_{HG} is the high gain calibration constant in units of (ADC/p.e.u), $N_{\mathrm{p.e.u.}}$ is the light yield in photoelectron units (p.e.u), and P is the pedestal, corresponding to the ADC value for the zero photoelectron.

The HG calibration is performed using LED data. Light pulses from the LED calibration system are injected into the MPPC channels. The HG ADC distribution shows an evenly spaced multi-peak structure, as shown in Figure 4.14a. Each peak in the spectrum corresponds to a specific number of photoelectrons. The distance between the two neighboring



(a) Example of extrapolated pedestal value.

(b) Distribution of the electronic pedestal values for calibrated MPPC channels.

Figure 4.15: Pedestal calibration [12].

peaks gives the high-gain constant, which is approximately constant across the HG dynamic range. To extract this constant accurately, the fitted peak positions are plotted as a function of the peak index and fitted with a linear function [11]. The slope of this fit gives the high-gain constant. Figure 4.14b shows the distribution of the high-gain constant for all calibrated MPPC channels during June 2024. The distribution is fitted with a Gaussian function, which gives a mean of 15.04 ADC/p.e.u and a standard deviation of 0.49 ADC/p.e.u.

The pedestal is the HG ADC value corresponding to the zero-photoelectron peak. Since the electronics baseline is set below the discriminator threshold, the pedestal cannot be measured directly. Instead, the pedestal is calibrated using LED ADC spectra taken at several MPPC bias high voltages. By varying the MPPC high voltages, the high-gain constant changes, while the pedestal is assumed to remain constant. For each MPPC high voltage setting, the fitted HG ADC peak positions are plotted against the photoelectron peak number and fitted with a straight line. The extrapolation of these lines to the zero-photoelectron point gives the pedestal, as shown in Figure 4.15a. Figure 4.15b shows the distribution of pedestal values for all calibrated MPPC channels from the May 2024 calibration data, giving a mean of 59.46 ADC and a standard deviation of 21.76 ADC.

After the high-gain constant and the pedestal have been determined, the hit charge in photoelectron units $N_{\text{p.e.u.}}$ can be calculated using its HG ADC value as

$$N_{\text{p.e.u.}} = (A_{\text{HG}} - P)/G_{\text{HG}} \tag{4.2}$$

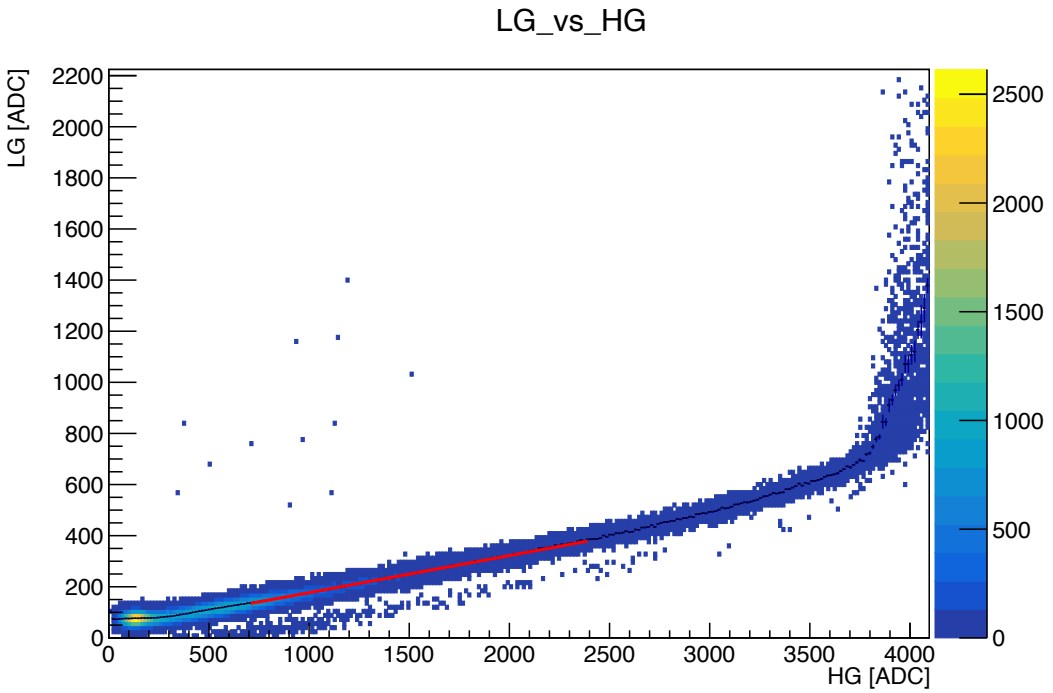


Figure 4.16: Example of low-gain ADC versus high-gain ADC for one MPPC channel [12].

4.4.2 Low-gain calibration

The HG readout provides good charge resolution for small hit charges. However, it has a limited dynamic range. Since the HG and LG amplitudes are digitized by 12-bit ADCs and the HG has larger amplification, the HG ADC value can become nonlinear or saturated for large hit signals, such as signals from Bragg peaks or vertex activities. The LG readout has a lower amplification and therefore a larger dynamic range.

LG calibration is performed using cosmic data. For each MPPC channel, hits with both valid HG and LG ADC are selected. Figure 4.16 shows the LG ADC versus the HG ADC for hits in one MPPC channel. It shows that when the HG ADC is between 500 and 2500, the LG ADC is linearly correlated with it. At higher HG ADC values, the HG response becomes nonlinear or saturated. In this region, LG ADC should be used to get the hit charge. A linear fit to the LG versus HG histogram over 500-2500 HG ADC is used to extract the LG calibration parameters. For hit charges above about 180 p.e.u, the LG ADC is used to estimate the hit charge.

4.4.3 Time over threshold (ToT) calibration

Since the HG and LG signals record only the maximum hit amplitude in a single event gate, they cannot measure the charge of consecutive hits in the same channel. This analog charge readout dead time affects the reconstruction of delayed tracks, such as Michel electrons produced about 2 μs after muons stop and decay in the SuperFGD. On the other hand, the timing readout is not affected by this analog charge readout limitation. The timing readout records the rising-edge and falling-edge timestamps of the hit as digitized timing counts, referred to as TDC counts. One TDC count corresponds to 1.25 ns. Time-over-Threshold (ToT) is defined as the time difference between the falling-edge and rising-edge TDC counts. Since ToT increases with hit amplitude, ToT is correlated with the hit charge. Therefore, the ToT calibration provides an alternative, although less precise, estimate of the hit charge when the HG or LG ADC measurement is unavailable. The charge estimated from this calibration is referred to as the ToT charge. The ToT calibration is performed by fitting

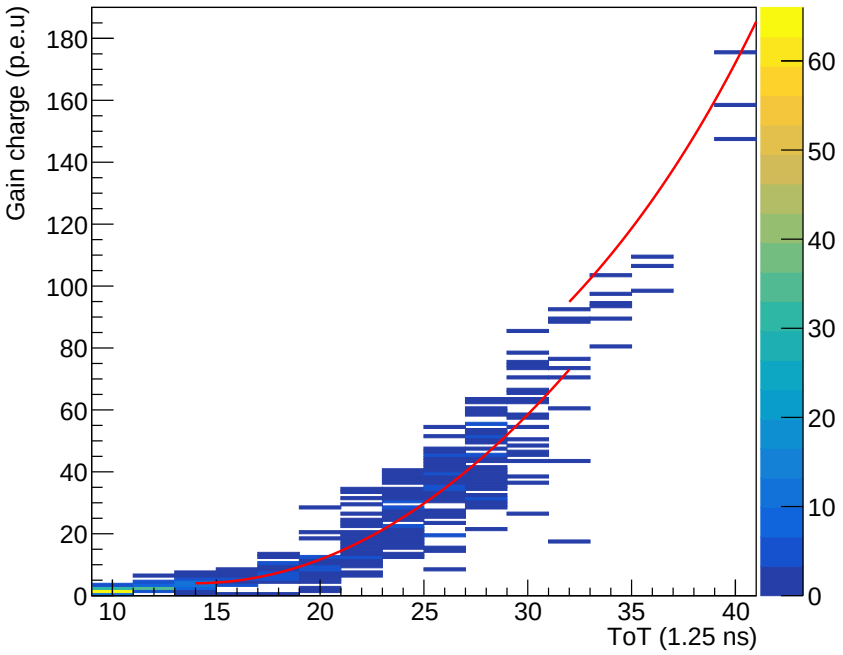


Figure 4.17: Gain calibrated hit charge versus hit ToT for one MPPC channel using June 2024 beam data. The ToT is in the unit of TDC count which is 1.25 ns per count. The red curve shows the fitted ToT calibration curve. The discontinuity in the calibration curve is due to the piecewise calibration function defined in Equation 4.3.

the histogram of hit charge obtained from the HG/LG calibration (gain charge) versus the hit ToT value with an empirical function. The input data for the calibration is neutrino

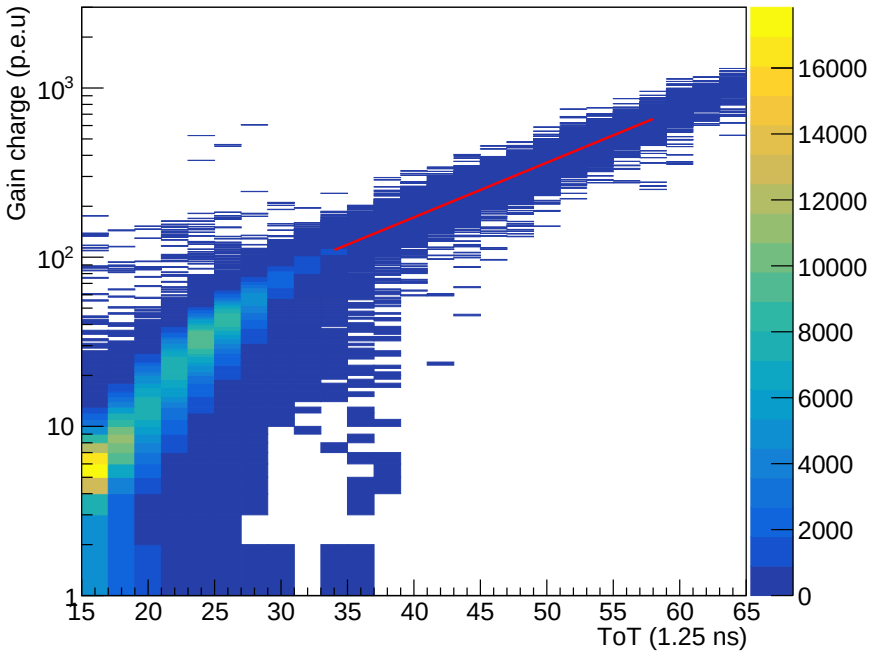


Figure 4.18: Gain calibrated hit charge versus hit ToT for all MPPC channels using June 2024 beam data. The red line shows the exponential fit $\exp\left[C \cdot (\mathrm{ToT} - 34) + D\right]$ in the range $34 \leq \mathrm{ToT} \leq 58$ TDC counts.

beam data and only hits with a valid gain calibrated charge and valid ToT are used. Figure 4.17 shows an example histogram of the gain calibrated hit charge versus the hit ToT for a single MPPC channel. Figure 4.18 shows the distribution for all MPPC channels.

For each channel, the range $14 \leq \mathrm{ToT} \leq 32$ TDC counts is calibrated using a quadratic function, $A(\mathrm{ToT}-14)^2+B$. The parameters A and B are obtained by fitting the distribution in the range $14 \leq \mathrm{ToT} \leq 28$ for each individual channel. The upper bound of 28 is chosen to avoid potential statistical fluctuations at larger ToT values. For $\mathrm{ToT} < 14$ TDC counts, the charge is estimated using a linear mapping, $\dfrac{B}{14}\,\mathrm{ToT}$, where B is the constant parameter obtained from the quadratic fit.

When $\mathrm{ToT} > 32$ TDC counts, the number of hit entries in individual channels becomes insufficient for a stable channel-by-channel calibration. Therefore, the ToT calibration in the range $\mathrm{ToT} > 32$ is performed using the all channel distribution shown in Figure 4.18. An exponential function, $\exp(C \times (ToT - 34) + D)$, is fitted to the all-channel distribution in the range $34 \leq ToT \leq 58$. The resulting exponential parameters are shared by all channels. To ensure the monotonicity of the calibration, for $\mathrm{ToT} > 32$, the ToT charge is taken as $N_{\mathrm{ToT}} = \max\left\{A(\mathrm{ToT} - 14)^2 + B,\ \exp\left(C \cdot (\mathrm{ToT} - 34) + D\right)\right\}$.

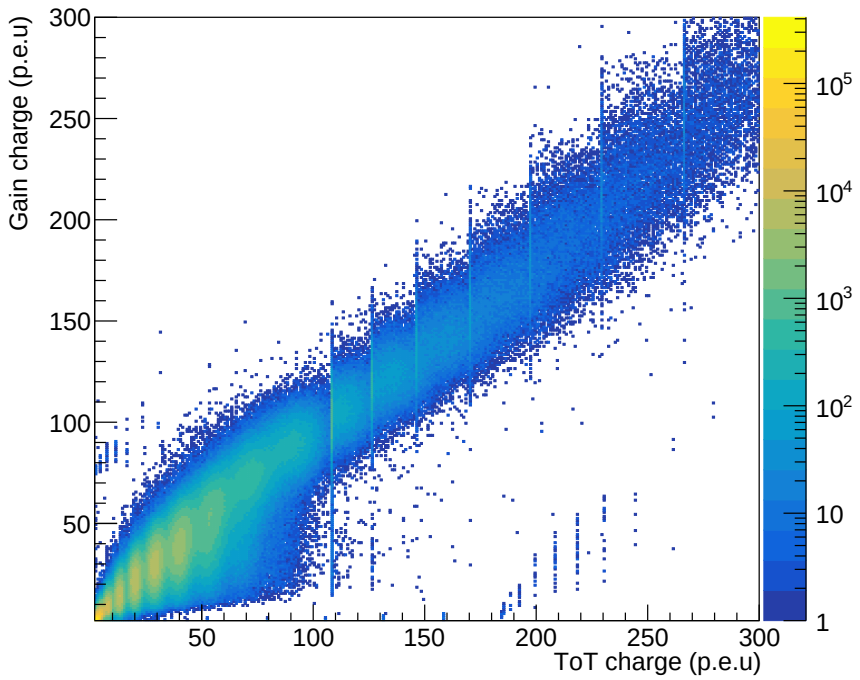


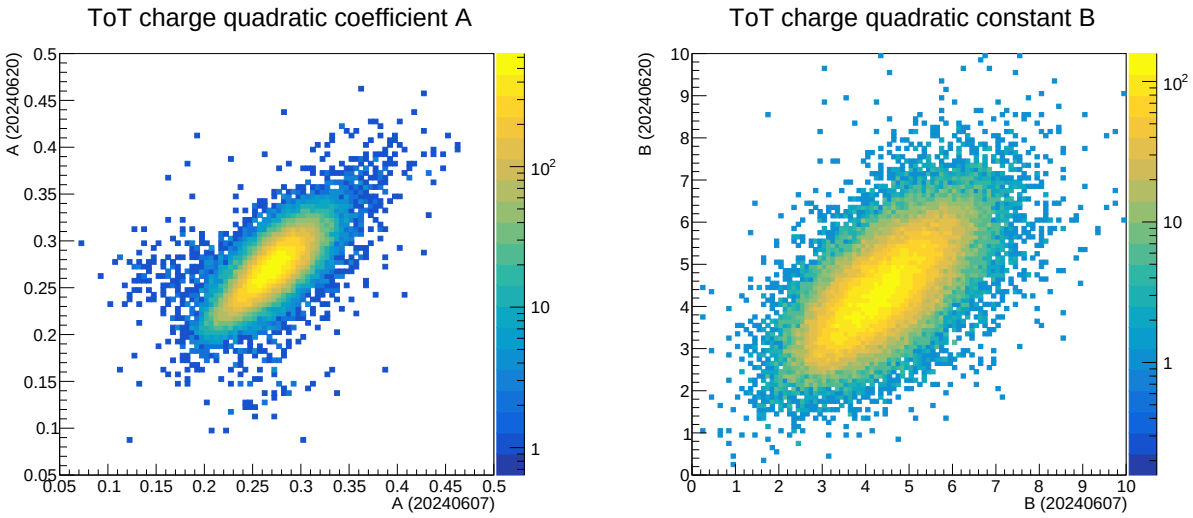
Figure 4.19: Comparison of the hit charges obtained from the gain calibration and from the ToT calibration.

In summary, the ToT calibration table contains four parameters: two quadratic parameters, A and B, and two exponential parameters C and D. The quadratic parameters are obtained by fitting the HG/LG calibrated hit charge versus hit ToT histogram in the range $14 \leq \text{ToT} \leq 28$ for each individual channel, while the exponential parameters are obtained by fitting the all-channel distribution in the range $34 \leq \text{ToT} \leq 58$, and are shared by all channels. The ToT charge is given by

$$N_{\text{ToT}} = \begin{cases} \dfrac{B}{14} \cdot \text{ToT}, & \text{if ToT} < 14, \\ A(\text{ToT} - 14)^2 + B, & \text{if } 14 \leq \text{ToT} \leq 32, \\ \max\left\{ \begin{array}{l} A(\text{ToT} - 14)^2 + B, \\ \exp\left[C \cdot (\text{ToT} - 34) + D\right] \end{array} \right\}, & \text{if ToT} > 32. \end{cases} \tag{4.3}$$

where N_{ToT} is the ToT charge in photoelectron units, and ToT is expressed in TDC counts, with one TDC count corresponding to 1.25 ns.

To evaluate the performance of the ToT charge calibration, two validation tests were carried out. The first checked the consistency between the hit charge from the HG/LG calibration and that from the ToT calibration. Hits with both a valid ADC and a valid



(a) Compare the quadratic coefficient A

(b) Compare the quadratic coefficient B

Figure 4.20: Compare quadratic calibration parameters A and B for two ToT tables. One table is extracted on June 7, 2024 and the other one is on June 20, 2024. There is a two-week gap between them.

ToT were selected. For each hit, the ADC-based charge was computed from the HG/LG calibration tables using Equation 4.2, and the ToT charge from the ToT calibration tables using Equation 4.3. Figure 4.19 compares the two estimates. They are strongly correlated, particularly in the high-charge region, showing that ToT can provide a usable alternative charge estimate.

The second test assessed the temporal stability of the ToT calibration. Several calibration tables were produced from beam data taken at different times, and their parameters were compared across the calibration periods. For each channel, the quadratic parameters A and B were extracted and compared table-to-table. Figure 4.20 shows an example for two tables taken two weeks apart (June 7 and June 20, 2024). The strong parameter correlation across time indicates that the ToT calibration is stable.

4.5 SuperFGD reconstruction

The calibrated MPPC hits are taken as input to the SuperFGD reconstruction, which reconstructs the three-dimensional pattern of energy deposits. The reconstruction builds tracks for charged particles' paths, clusters for localized hits that cannot be grouped into a track, and vertices of track endpoints [73]. Each reconstructed SuperFGD track forms a segment, which is then combined with the segments from the other sub-detectors by the global reconstruction. The main steps are summarized below.

- **2D MPPC hits → 3D cube hits.** 3D cube hits are reconstructed based on the timing and geometry of the 2D MPPC hits. A cube hit is built wherever three mutually orthogonal fibers, each carrying a hit, cross the same cube. The three fiber hits must be coincident within a 20 ns window. The measured fiber charge is then shared among the candidate cubes to estimate each cube's charge, with correction for fiber attenuation and total charge conservation. Among the reconstructed cube hits there are also ghost hits, which do not correspond to any real energy deposition. These ghost hits are rejected with a charge threshold and a neighboring-hit requirement [73].

- **3D hits → track segment.** A track is built from the reconstructed cube hits through a sequence of pattern-recognition steps [73]:

  – Hit clusters are formed from spatially connected, time-consistent hits using the DBSCAN algorithm.

  – Hits in a cluster are ordered into a sequence using a minimum spanning tree.

  – The ordered hit sequence is split into straight or smooth bending pieces at kinks.

  – Collinear pieces are merged into a single track segment.

  The track segment is represented as an ordered chain of nodes along its path, each node carrying a position, time and energy deposit. The track direction is reconstructed by fitting the node time against the distance along the track.

- **Momentum and particle identification.** The SuperFGD particle identification (PID) separates proton-like, pion-like, muon-like, and electron-like hypotheses through a Boosted Decision Tree Gradient (BDTG) [74]. Its input variables include the reconstructed track length, the total energy deposit, the node energies, the node energy fluctuations, the node-to-node distances, and the secondary tracks connected to the track. These variables encode the $\mathrm{d}E/\mathrm{d}x$ profile along the track and the Bragg peak at its end. The BDTG returns a weight for each of the four hypotheses, and the predicted particle type is the hypothesis with the highest weight. The track momentum is reconstructed with a separate BDTG regression, using the same track information together with the energy deposits of the connected secondary tracks [74]. Three regressors are trained, for the proton, pion, and muon hypotheses. Electrons are excluded because they produce electromagnetic showers in the SuperFGD, and their energy is measured elsewhere.

- **Global reconstruction.** Each SuperFGD segment is matched to the corresponding TPC, high-angle TPC and time-of-flight segments and combined into a single global track by the event reconstruction, providing the momentum, direction and particle identification.

Chapter 5

Michel Electron Tagging in the SuperFGD

A Michel electron is a delayed electron or positron produced by the decay of a stopped muon, $\mu^- \rightarrow e^- \bar{\nu}_e \nu_\mu$ or $\mu^+ \rightarrow e^+ \nu_e \bar{\nu}_\mu$. It provides a signature to identify muons in the SuperFGD. In the ν_μ CC inclusive analysis presented in Chapter 6, Michel electron tagging is used to identify muon candidates in the SuperFGD-contained sample. The muon is tagged through the spatial association between the stopping muon and the Michel electron in the SuperFGD, and through the delayed time between them.

In this chapter, Michel electron tagging is studied using ND280 reconstructed events. A control sample of stopping muons in the SuperFGD is developed, and the Michel electron produced from muon decay is tagged. The muon lifetime is extracted from the delayed-time distribution, providing a test of the SuperFGD detector response and reconstruction. The difference between the data and Monte Carlo (MC) Michel electron tagging efficiencies leads to a systematic uncertainty in the selection of the ν_μ CC inclusive SuperFGD-contained muon sample. It is treated as an efficiency-like systematic. The stopping-muon control sample selection is described first, followed by the Michel electron tagging of the selected muons.

5.1 Stopping muon control sample

The Michel electron is studied using a beam stopping-muon control sample, which selects events that have a muon crossing an HA-TPC and stopping in the SuperFGD fiducial volume (FV). The SuperFGD FV is the detector volume that excludes the two outermost cube layers. The HA-TPC provides the momentum, charge, and particle identification of the muon candidate. A schematic of a control-sample event is shown in Figure 5.1. The selection is performed in the `HighLAND2` framework. Its input is the Run 13c neutrino beam data, taken between June 6 and June 28, 2024, together with the corresponding beam and sand

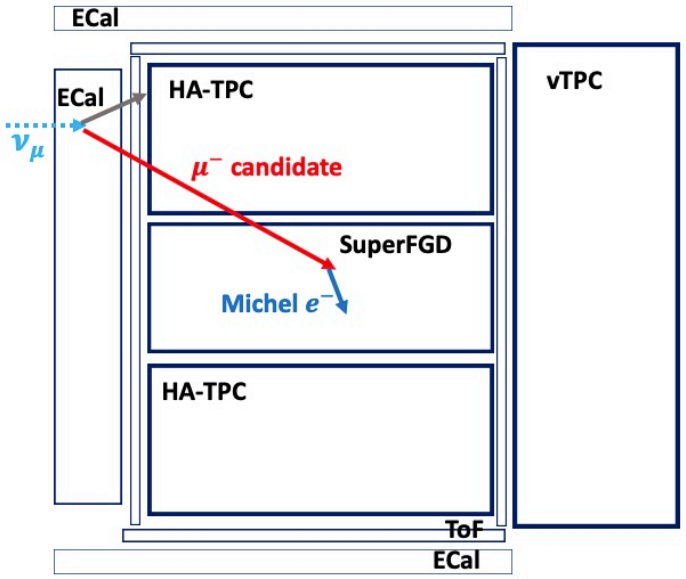


Figure 5.1: Schematic of an event in the stopping-muon control sample.

MC simulations, the same input used for the inclusive analysis (Section 6.1). The sand simulation simulates the neutrino interactions outside the ND280 in the surrounding sand.

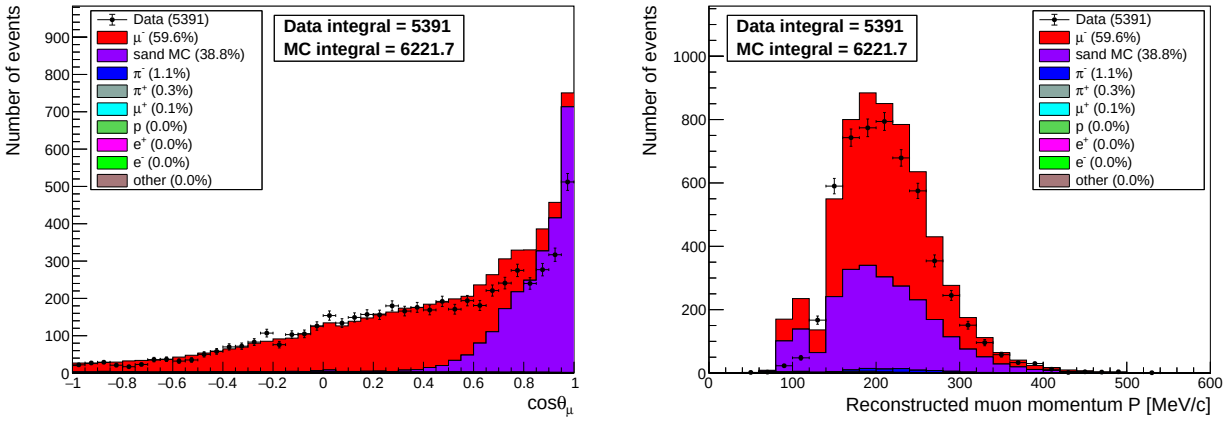
No flux weight or neutrino interaction model corrections are applied. The stopping-muon control sample is selected using the following steps, where an event is the collection of reconstructed objects in a single beam bunch:

- **Event quality:** The event is required to pass the standard data quality check. This requirement is applied to data events only.
- **Track direction convention:** For each track with both HA-TPC and SuperFGD segments, the reconstructed direction is forced to point from the HA-TPC toward the SuperFGD.
- **HA-TPC track selection:** All tracks with an HA-TPC segment are collected, and each is required to be of good quality, with more than 18 reconstructed HA-TPC clusters. The highest-momentum negatively charged HA-TPC track is selected as the candidate.
- **SuperFGD stopping requirement:** The candidate is required to have a reconstructed SuperFGD segment and to stop inside the SuperFGD fiducial volume.
- **HA-TPC muon PID:** The stopping muon candidate is required to pass the HA-TPC muon particle-identification cut. To obtain a high-purity muon sample, the control sample applies a tighter requirement than the inclusive analysis (Chapter 6): the track

is required to have a muon likelihood $L_\mu > 0.05$, which rejects protons. For tracks with HA-TPC momentum $p < 500$ MeV/c, an additional minimum-ionizing-particle (MIP) likelihood requirement $L_{\text{MIP}} > 0.8$ rejects electrons. Muons and pions at these momenta are minimum ionizing, so the MIP likelihood combines the two hypotheses, $L_{\text{MIP}} = (L_\mu + L_\pi)/(1 - L_p)$. The likelihood definitions for the muon, electron, pion, and proton hypotheses are given in Equation 6.2.

- **SuperFGD segment-length cut:** The reconstructed SuperFGD segment length of the candidate track is required to be long enough for a stopping muon of its HA-TPC entry momentum. This cut removes broken muon tracks. For example, a muon that actually exits the SuperFGD may be reconstructed into two broken tracks, and one reconstructed broken piece appears to be a stopping muon candidate.

- **Muon Bragg-peak cut:** The Bragg-peak cut complements the preceding SuperFGD segment-length cut in rejecting broken SuperFGD tracks. It requires the energy-deposit profile at the track end to exhibit the Bragg peak characteristic of a stopping muon, which a broken track does not show because it does not genuinely stop at the reconstructed endpoint.



(a) Reconstructed $\cos\theta_\mu$.

(b) Reconstructed momentum.

Figure 5.2: Reconstructed $\cos\theta_\mu$ and momentum of the muons selected in the stopping-muon control sample.

In the beam data sample, 5391 SuperFGD stopping-muon candidates are selected, compared with 6221.7 POT-weighted candidates in the MC sample. Figure 5.2 shows the reconstructed momentum and $\cos\theta_\mu$ of the selected SuperFGD stopping muon candidates, where θ_μ is the angle between the muon and the neutrino beam direction. In this figure, the sand MC is shown as a separate category in the stack, while the beam MC is broken down by

true particle type. The MC exceeds the data by 15.4% after POT normalization, which is expected because no flux weight or neutrino interaction model correction is applied to the beam or the sand MC. The excess is largest in the forward $\cos\theta_\mu$ region, where the sand component dominates. This does not bias the Michel electron tagging study, because the tagging efficiency is calculated per selected muon rather than from the event rate, and the selected sample is dominated by muons.

The MC distributions are broken down by the true particle type of the selected muon candidate, as summarized in Table 5.1. Of the selected candidates, 97.87% are true μ^-. The dominant contamination is π^-, which is expected because pions have a similar energy deposition $\mathrm{d}E/\mathrm{d}x$ to muons and are not distinguished by the HA-TPC PID. The remaining contamination from protons, electrons, and positrons is negligible. Requiring in addition that the true particle stops inside the SuperFGD fiducial volume gives a sample purity of 97.54%, so the control sample is a high-purity sample of SuperFGD stopping muons.

Table 5.1: True particle type of the selected stopping muon track in the beam and sand MC sample, with the MC POT normalized to the data POT.

Particle	MC events	Fraction [%]
μ^-	6089.3	97.87
π^-	80.5	1.29
μ^+	22.8	0.37
π^+	22.8	0.37
p	3.0	0.05
e^+	2.3	0.04
e^-	1.1	0.02
Total	6221.7	100

One limitation of this control sample is that the muon selection relies on the HA-TPC particle identification (PID), which carries an associated systematic uncertainty. A possible improvement is to use a cosmic-ray control sample. Cosmic-ray muons form a pure muon sample, so the HA-TPC PID is not needed and the associated systematic is avoided. Because the MC simulation of cosmic-ray events in the upgraded near detector is not yet available, this beam stopping-muon control sample is used for the Michel electron tagging systematic study.

5.2 Michel electron tagging

Michel electron tagging is applied to the selected stopping muon candidates based on the delayed time and spatial association:

- **Michel electron candidate:** The Michel electron candidates are tracks that have

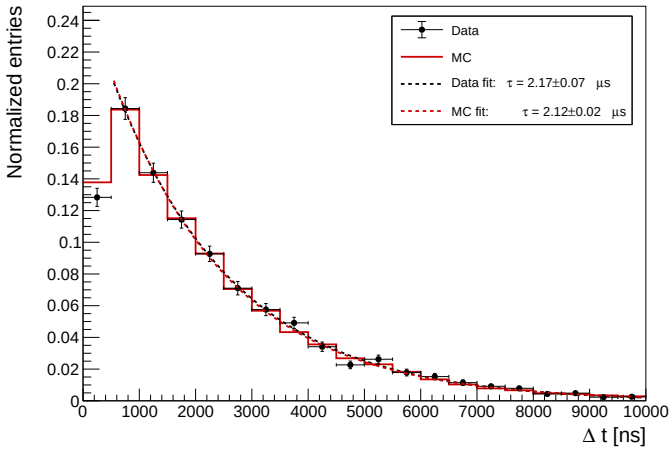


Figure 5.3: Delayed time distribution between the stopping muon candidate and the tagged Michel electron candidate. The distributions are normalized to unit area and fitted in the range 500 ns $< \Delta t <$ 10000 ns using equation 5.1.

at least two reconstructed SuperFGD nodes and are later than the stopping muon candidate track. They are reconstructed in the event bunch, in later bunches, and out of bunch.

- **Delayed time cut:** The delayed time between the stopping muon candidate and the Michel electron candidate must be greater than 200 ns. The Michel electron is produced at the muon stopping point, so many of its hits occur as consecutive hits in the same MPPC channels as the muon hits. Since the SuperFGD electronics has a dead time of about 200 ns for consecutive hits in the same channel, the delayed-time cut is set to 200 ns.

- **Distance cut:** The Michel electron candidate is required to start or end within 20 mm of the stopping muon candidate's endpoint.

Table 5.2: Summary of the Michel electron tagging efficiency for data and MC.

Sample	Selected muons	Michel-tagged	Tagging efficiency
Data	5391	3964	$(73.53 \pm 0.60)\%$
MC	6221.7	4804.6	$(77.22 \pm 0.19)\%$
Data/MC ratio $r_{\mathrm{CS}} = \varepsilon_{\mathrm{data}}/\varepsilon_{\mathrm{MC}}$			95.22%

For the MC sample, 4804.6 of the 6221.7 selected stopping-muon candidates have tagged Michel electrons, corresponding to a Michel electron tagging efficiency of $(77.22 \pm 0.19)\%$.

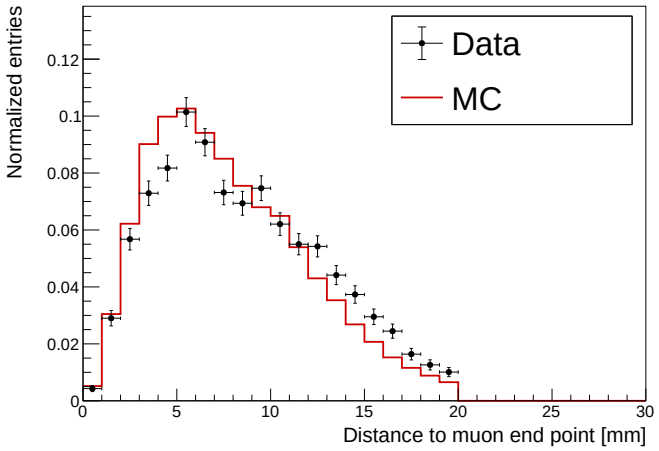


Figure 5.4: Distance distribution between the stopping muon candidate and the tagged Michel electron candidate.

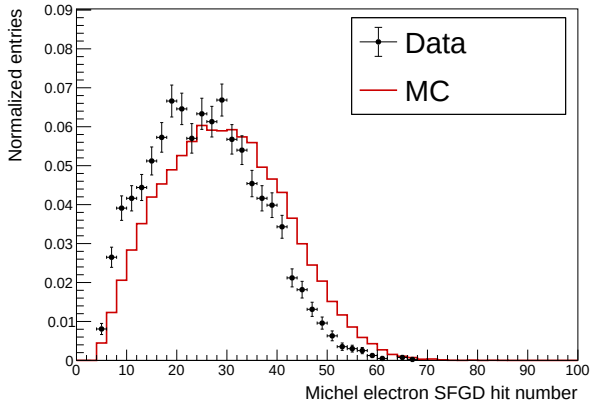
For the data sample, 3964 of the 5391 selected stopping-muon candidates have tagged Michel electrons, corresponding to a Michel electron tagging efficiency of (73.53±0.60)%. The Michel electron tagging efficiencies are summarized in Table 5.2, which are used to propagate the Michel electron tagging systematic in the inclusive ν_μ CC analysis in Chapter 6.

In the MC sample, 99.02% of the tagged Michel electron candidates are true electrons, indicating that the Michel electron false tagging rate is very low. Table 5.3 summarizes the true particle type of the tagged Michel electron candidate in the MC sample.

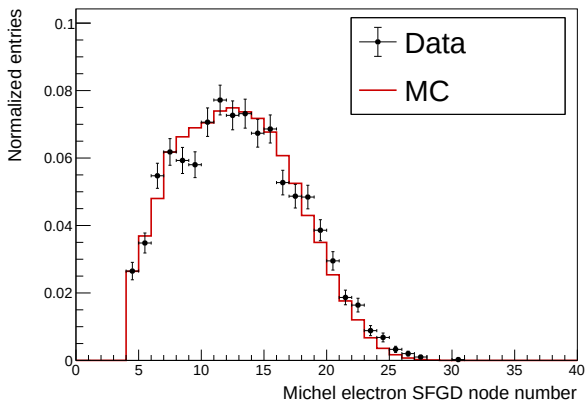
Table 5.3: True particle type of the tagged Michel-electron candidate with the MC POT normalized to the data POT.

Particle	MC events	Fraction [%]
e^-	4757.6	99.02
μ^-	31.9	0.66
e^+	12.4	0.26
n	2.3	0.05
p	0.4	0.01
Total	4804.6	100

The delayed time distribution between the stopping muon candidate and the tagged Michel electron candidate is shown in Figure 5.3. The distributions are normalized to unit area and fitted in the range 500 ns $< \Delta t <$ 10000 ns using an exponential function plus a constant term:



(a) SuperFGD hit number of tagged Michel electron candidates.



(b) SuperFGD node number of tagged Michel electron candidates.

Figure 5.5: Reconstructed SuperFGD hit and node number of the tagged Michel electron candidates.

$$f(\Delta t) = A \exp\left(-\frac{\Delta t}{\tau}\right) + C \tag{5.1}$$

For data, the fit gives $\tau = 2170.4 \pm 73.7$ ns, with $\chi^2/\text{ndf} = 13.43/16$. For MC, the fit gives $\tau = 2115.0 \pm 22.8$ ns, with $\chi^2/\text{ndf} = 18.54/16$. The number of degrees of freedom (ndf) is the number of bins minus the number of free parameters of the fit function. The fitted lifetimes are consistent with the muon lifetime within the fit uncertainties.

The distance distribution between the stopping muon candidate and the tagged Michel electron candidate is shown in Figure 5.4, and the SuperFGD hit and node numbers of the tagged Michel electron candidates are shown in Figure 5.5. The distance distribution in data is slightly shifted toward larger distances compared with MC, which is consistent with the lower Michel electron tagging efficiency in data, since larger distances move candidates toward the 20 mm cut boundary. The node number distributions agree between data and MC, whereas the hit number distribution shows a large difference. This difference indicates that the SuperFGD detector response is not exactly modeled in the simulation, which also gives rise to the data/MC difference in the tagging efficiency.

5.3 Summary

Michel electron tagging in the SuperFGD was studied at the reconstruction level using a beam stopping-muon control sample, in which the muon is identified by an HA-TPC track that crosses into the SuperFGD and stops inside its fiducial volume. The selection provides a

high-purity muon sample, 97.54% in MC. The muon lifetime extracted from the delayed-time distribution, 2170 ± 74 ns in data and 2115 ± 23 ns in MC, provides a test of the SuperFGD detector response and reconstruction.

The Michel electron tagging efficiency is $(73.53 \pm 0.60)\%$ in data and $(77.22 \pm 0.19)\%$ in MC. The data/MC difference in the tagging efficiency is propagated as an efficiency-like systematic to the SuperFGD-contained muon sample in the inclusive analysis.

A major limitation of this stopping muon control sample is that the selection relies on the HA-TPC particle identification, which carries an associated systematic uncertainty. A cosmic-ray sample can provide a pure sample of muons and would remove the HA-TPC PID systematic uncertainty, but the MC simulation of cosmic-ray events in the upgraded near detector is not yet available.

Chapter 6

ν_μ Charged-Current Inclusive Interactions with Upgraded ND280

The first physics analysis for the T2K upgraded near detector is the measurement of inclusive ν_μ charged-current (CC) interactions in the SuperFGD. In this analysis, the ν_μ CC interaction vertex is required to be inside the SuperFGD, and the produced muon can go to the HA-TPCs, the downstream vertical TPCs, or the SuperFGD. No requirements are placed on the hadronic final state. The measurement covers the full CC ν_μ interaction phase space and constrains the total CC ν_μ event rate. This chapter presents the selection of inclusive ν_μ CC interaction samples, including their efficiency and purity, as well as the propagation of the associated flux and detector systematic uncertainties. The chapter is based on T2K Tech Note 525 [13]. The analysis results demonstrate the performance of the upgraded ND280 detector and lay the foundation for future cross-section and oscillation analyses.

6.1 Inputs and corrections

Input samples

This analysis uses T2K neutrino-mode (FHC) data from Run 13c, taken between June 6 and June 28, 2024, together with the corresponding Monte Carlo (MC) simulation. Both the data and MC samples were processed in the `P8_v17` production using `ND280Software` version 14.39.

Neutrino interactions in the ND280 detector were simulated using the `NEUT` version 5.6.4 event generator [66]. Particle propagation through the detector was simulated using `Geant4` version 10.1.03.06 [67][75][76]. The simulation used the updated detector geometry introduced in the `P8_v17` production [13]. The analysis was performed using the `HighLAND2` framework, including the development of the signal sample selection, the development of control samples, and the evaluation and propagation of most of the systematic uncertainties.

Table 6.1 summarizes the protons on target (POT) for the data, NEUT beam MC, and sand MC samples.

T2K Run	Data POT	NEUT MC POT	Sand MC POT
Run 13c	1.57×10^{20}	28.34×10^{20}	6.90×10^{20}

Table 6.1: T2K Run 13c data sample and the corresponding POT used in this analysis for the data and MC samples.

Flux weights

The MC prediction has additional flux weights provided by the T2K beam group [77]. These weights account for the exact running conditions of the neutrino beamline and are applied to each MC event according to the true neutrino flavor, true neutrino energy, beam mode, and horn current. For the Run 13c neutrino mode sample, the relevant flux weights correspond to the 320 kA forward horn current and are taken from the `tuned23av1`.

NIWG weights

In addition to the nominal flux weights, the MC prediction is reweighted using the neutrino-interaction model weights provided by the T2K Neutrino Interaction Working Group (NIWG) [78]. These weights are applied event by event according to the interaction mode, neutrino flavor, target nucleus, and interaction kinematics.

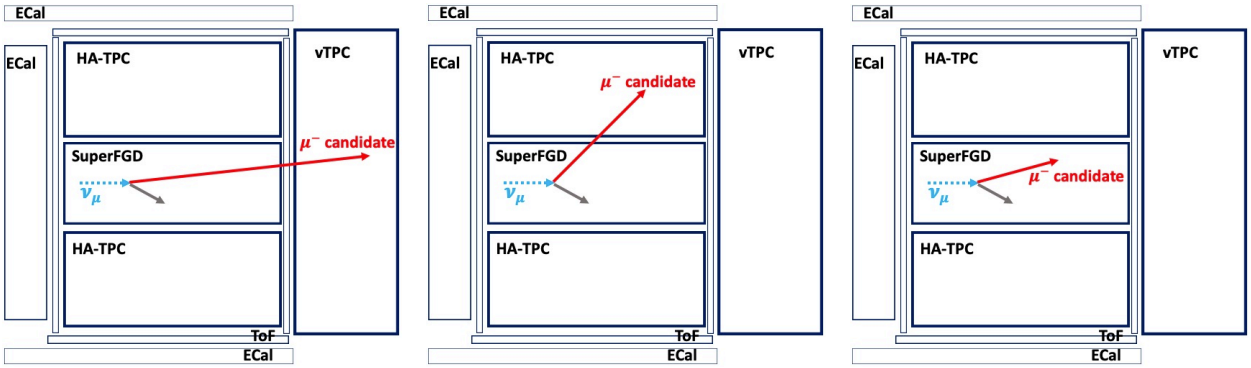
Event corrections

After the routine detector calibration, discrepancies can still exist between data and MC. These discrepancies are further reduced by a set of corrections applied before the event selection. These corrections include the vertical-TPC and HA-TPC dE/dx corrections, PID corrections, momentum resolution corrections, the flip kinematics correction used when reconstructed track directions are reversed, and the SFGD BDT/TMVA correction, which prepares variables used for SFGD-based PID and momentum estimation [13].

6.2 Event and signal topology definition

In Run 13c, a neutrino beam spill is about 5 μs and consists of eight bunches, whose centers are separated by approximately 580 ns, with a width of about 25 ns. `HighLAND2` distributes reconstructed objects in each spill in eight bunches according to their time. Each reconstructed object timestamp is checked within a $\pm 4 \times 35$ ns window around the corresponding bunch center. Objects outside the bunch windows are placed in an out-of-bunch container. In this analysis, an event is defined as a collection of reconstructed objects in one of the eight beam bunches.

The SuperFGD fiducial volume (FV) is defined as the detector volume that excludes the two outermost cube layers. The signal event is defined as an inclusive ν_μ charged-current



(a) Vertical TPC muon (b) HA-TPC muon (c) SuperFGD-contained muon

Figure 6.1: Schematic of the three subsamples used in the inclusive ν_μ charged-current analysis.

interaction with the true neutrino interaction vertex inside the SuperFGD FV that produces a μ^- particle. For the inclusive analysis, the signal has no requirements on the hadronic final state. The selected events are further divided into three mutually exclusive subsamples according to where the selected main muon candidate is reconstructed:

1. **TPC muon sample**: the selected muon candidate starts in the SuperFGD and goes to the downstream vertical TPC.

2. **HA-TPC muon sample**: the selected muon candidate starts in the SuperFGD and goes to a high-angle TPC.

3. **SuperFGD contained muon sample**: the selected muon candidate starts and stops inside the SuperFGD.

Figure 6.1 illustrates these three reconstructed topologies.

6.3 Event selection

Figure 6.2 shows the event selection flow. The common selection steps determine the track direction and categorize the track topology into the SuperFGD–TPC, SuperFGD–HA-TPC, and SuperFGD-contained track collections. After the common selection, a muon candidate is sought in each of these three collections. The event is then assigned to the TPC μ^-, HA-TPC μ^-, or SuperFGD-contained μ^- sample according to the detector in which the muon candidate is reconstructed. Background events are finally reduced by the veto cuts [13].

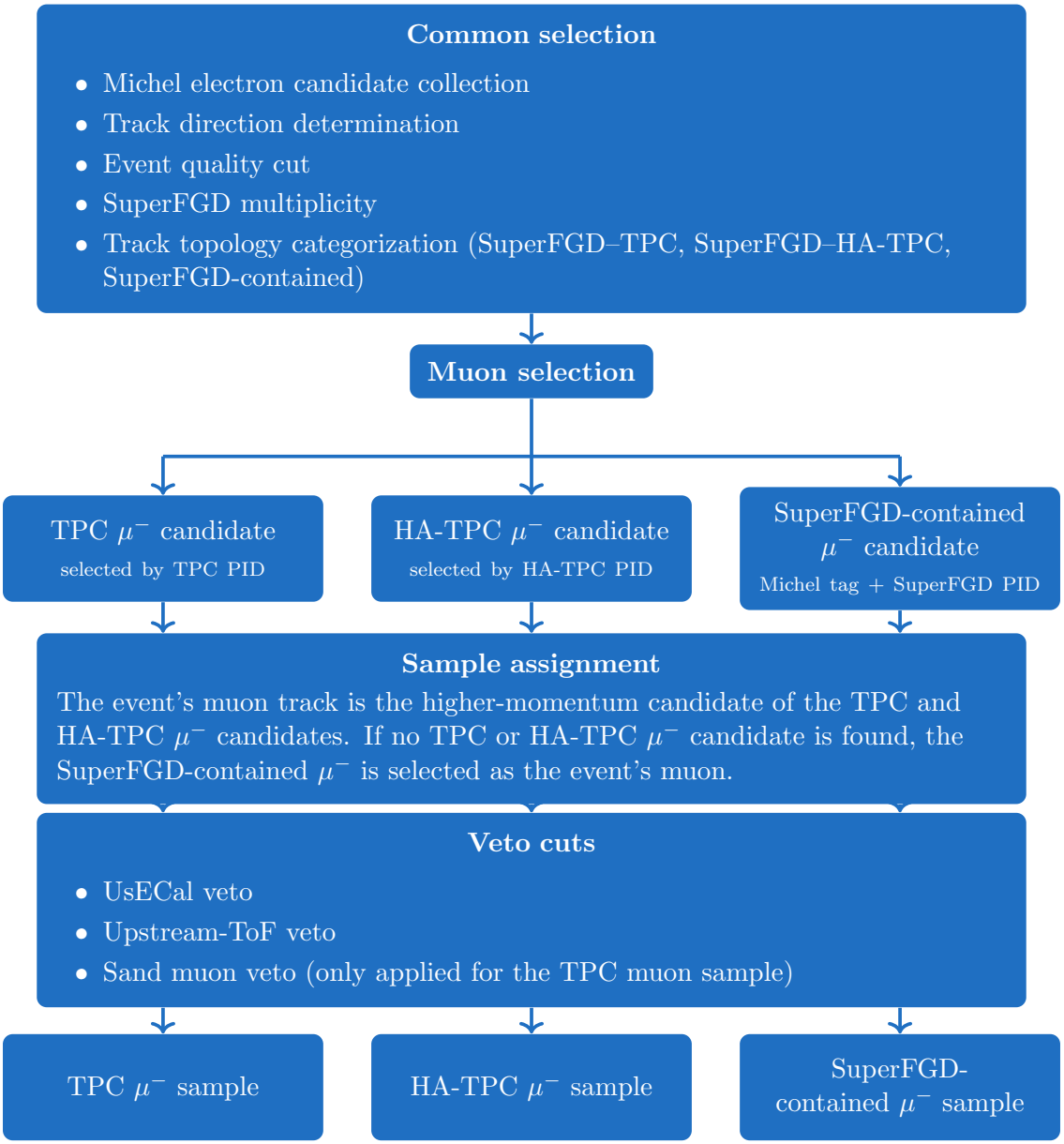


Figure 6.2: Selection flow for the ν_μ charged-current inclusive analysis with the upgraded ND280.

6.3.1 Common selection steps

1. **Michel electron candidate collection.** A Michel electron candidate is a track that is reconstructed later in time than the muon candidate. The candidates are required to have at least two reconstructed SuperFGD nodes and to be reconstructed in the event bunch, a later bunch, or the out-of-bunch window.

2. **Track direction determination.** The reconstructed track directions are determined using the reconstructed direction of SuperFGD segments and Michel electron candidates. In the current analysis, the SuperFGD–ToF timing is not used to determine the track direction.

   - **Forward-going convention for TPC and HA-TPC tracks:** Tracks with at least one TPC or HA-TPC segment are first forced to be forward-going in the z direction. This is the convention before applying any direction determination steps.
   - **Direction determination for outgoing HA-TPC tracks.** For tracks crossing an HA-TPC and containing a SuperFGD segment with more than 30 reconstructed nodes, the reconstructed direction of the SuperFGD segment is used to determine the track direction. The SuperFGD segment direction is reconstructed by fitting the node time against the node distance along the segment. The 30-node requirement ensures that the segment is long enough for the timing resolution to be sufficient, so that the time difference between the segment endpoints is significantly larger than the timing resolution [13].
   - **Direction determination for SuperFGD-contained tracks.** For SuperFGD-contained tracks with more than 40 reconstructed SuperFGD nodes, the direction is taken as the reconstructed direction of the SuperFGD track. The 40-node requirement is a conservative choice. A SuperFGD timing-resolution study indicates that the direction is well established for reconstructed tracks longer than about 30 cm [13].

     For shorter SuperFGD-contained tracks, the direction can be determined using Michel electron candidates. A Michel electron is expected near the endpoint of a stopped muon, or a stopped π^+ decaying as $\pi^+ \to \mu^+ \to e^+$. A Michel electron candidate is tagged as in Chapter 5, which requires the Michel electron candidate to be more than 200 ns later and within 20 mm of either track endpoint. The track direction is then set to point toward the end closer to the tagged Michel electron candidate.

3. **Event quality cut.** For data, the event is required to satisfy the standard good beam and ND280 data quality criteria based on the flags provided by the beam and ND280 DAQ groups [13]. MC events are not rejected by this cut.

4. **SuperFGD multiplicity cut.** The event is required to have at least one track with a SuperFGD segment.

5. **Track topology categorization.** Tracks with SuperFGD segments are further categorized into SuperFGD–TPC tracks, SuperFGD–HA-TPC tracks, and SuperFGD-contained tracks. These collections are used later for the muon candidate selection.

   - **SuperFGD–TPC tracks:** Tracks are required to start in the SuperFGD fiducial volume and have a vertical TPC segment. The vertical TPC segment is required to have at least 19 reconstructed TPC hit clusters. The tracks are separated according to their reconstructed charge into positive and negative collections, and each collection is sorted by decreasing reconstructed momentum.
   - **SuperFGD–HA-TPC tracks:** Tracks are required to start in the SuperFGD fiducial volume and have an HA-TPC segment with at least 19 reconstructed HA-TPC hit clusters. As for the SuperFGD–TPC tracks, the tracks are separated according to their reconstructed charge into positive and negative collections, and each collection sorted by decreasing reconstructed momentum.
   - **SuperFGD-contained tracks:** Tracks are required to start and stop in the SuperFGD fiducial volume and have at least two SuperFGD nodes. These candidates are sorted by decreasing number of reconstructed nodes.

6.3.2 Muon selection cuts

Muon candidates are selected separately from the SuperFGD–TPC, SuperFGD–HA-TPC, and SuperFGD-contained track collections. Only negatively charged TPC and HA-TPC tracks are considered.

1. **TPC and HA-TPC muon candidates.** The SuperFGD–TPC and SuperFGD–HA-TPC track collections are searched independently for muon candidates. For each collection, tracks are tested by (HA-)TPC particle identification (PID) in order of decreasing reconstructed momentum.

   The (HA-)TPC PID is based on the energy loss $\mathrm{d}E/\mathrm{d}x$ of the track in the (HA-)TPC. For each particle hypothesis i (muon, electron, pion, and proton), the reconstructed energy loss is compared with the expectation through a pull

   $$\delta_i = \frac{(\mathrm{d}E/\mathrm{d}x)_{\mathrm{recon}} - (\mathrm{d}E/\mathrm{d}x)_i^{\mathrm{exp}}}{\sigma_i^{\mathrm{exp}}}, \tag{6.1}$$

   where $(\mathrm{d}E/\mathrm{d}x)_i^{\mathrm{exp}}$ is the expected energy loss for hypothesis i and σ_i^{exp} is the resolu-

tion [79]. The likelihood for each hypothesis is defined as

$$L_i = P_i / \sum_i P_i \tag{6.2}$$

where the probability density functions are

$$P_i = \begin{cases} \prod_j \dfrac{1}{\sqrt{2\pi}\,\sigma_j(i)} \exp\left(-\dfrac{\delta_j^2(i)}{2}\right), & \text{vertical TPC,} \\ \dfrac{1}{\sqrt{2\pi}\,\sigma(i)} \exp\left(-\dfrac{\delta^2(i)}{2}\right), & \text{HA-TPC,} \end{cases} \qquad (i = \mu, e, \pi, p) \tag{6.3}$$

For tracks in the SuperFGD–TPC collection, the pull δ_i is computed for each TPC segment of the track, while for the HA-TPC collection, the pull δ_i is computed for only the HA-TPC segment, regardless of whether the track passes through TPCs subsequently. The muon likelihood L_μ and the MIP likelihood $L_{\text{MIP}} = (L_\mu + L_\pi)/(1 - L_p)$ are then used for the muon selection.

A negatively charged track is selected as the TPC (HA-TPC) muon candidate if it satisfies the muon-likelihood requirement $L_\mu > 0.05$, which rejects protons, and, in the low-momentum region where electron contamination is largest, the additional MIP-likelihood requirement $L_{\text{MIP}} > 0.5$ rejects electrons. The MIP-likelihood requirement is applied only to tracks with $p < 500$ MeV/c in the TPC and $p < 350$ MeV/c in the HA-TPC. The highest-momentum track passing these requirements in each collection is taken as the corresponding (HA-)TPC muon candidate.

2. **SuperFGD-contained muon candidates.** SuperFGD-contained muon candidates are selected among SuperFGD-contained tracks through Michel electron tagging and SuperFGD muon PID.

   - **Michel electron tagging.** A stopped SuperFGD-contained muon can decay and produce a Michel electron, so a SuperFGD-contained muon candidate is required to be associated with a Michel electron candidate near its reconstructed endpoint. The Michel electron candidate is tagged as in Chapter 5, which requires it to be more than 200 ns later than the track and to start or end within 20 mm of the track endpoint. Tracks with a tagged Michel electron candidate are selected as stopped-muon candidates and ordered by decreasing number of SuperFGD nodes.
   - **SuperFGD muon PID.** The stopped-muon candidates are required to be identified as muon-like by the SuperFGD PID described in Section 4.5. Since the candidate list is already ordered by decreasing number of reconstructed SuperFGD nodes, the first muon-like candidate in this list is selected.

3. **Selected muon candidate and sample assignment.** The final selected muon candidate of the event is chosen from the selected TPC, HA-TPC, and SuperFGD-contained muon candidates, and the branch of the sample (TPC μ^- sample, HA-TPC μ^- sample, and SuperFGD-contained μ^- sample) is assigned according to where this candidate is reconstructed. The TPC and HA-TPC muon candidates take precedence over the SuperFGD-contained candidate. If no TPC or HA-TPC muon candidate is found but a SuperFGD-contained muon candidate is found, the event is assigned to the SuperFGD-contained muon sample. If either a TPC or HA-TPC candidate is found, the SuperFGD-contained candidate is not used for the sample assignment.

   The SuperFGD-contained muon candidate is selected among SuperFGD tracks whose start and end points are both inside the SuperFGD fiducial volume. Such a track has no segment in any other sub-detector, so it can never coincide with a TPC or HA-TPC candidate. The same-track ambiguity arises only between the TPC and HA-TPC candidates. When both a TPC and an HA-TPC candidate are found and they are two different tracks, the candidate with the larger reconstructed momentum is taken as the event's muon track, and the event is assigned to the corresponding sample. If a single track is selected as both the TPC and the HA-TPC candidate, the event is assigned to the HA-TPC muon sample, since the HA-TPC is the first detector crossed after the track exits the SuperFGD. The start point of the selected muon candidate is taken as the reconstructed interaction vertex of the event.

6.3.3 Veto cuts

Due to reconstruction failures, neutrino interactions occurring outside the SuperFGD fiducial volume can be selected as signal events. For example, a track entering the SuperFGD may be incorrectly broken into two reconstructed tracks, with one track starting inside the SuperFGD and producing a falsely reconstructed vertex in the fiducial volume. Most of these backgrounds, including sand muons, originate upstream of the SuperFGD. The upstream detectors, including the UsECal and upstream ToF, are therefore used to veto such background events.

1. **UsECal veto cut.** Tracks with a segment in the upstream ECal are potential veto tracks. To exclude low-energy activity, only tracks whose upstream-ECal segment has a length of at least 40 mm are considered as veto track candidates. The distribution of the number of veto track candidates per event is shown in Figure 6.3.

   Figure 6.4 shows the distance between the veto track candidate and the muon candidate. For the HA-TPC muon sample, a veto track candidate close to the muon candidate typically indicates a background event, whereas a signal event's veto track candidate is typically farther from the muon candidate. Thus, a distance threshold of 400 mm is applied. Only veto candidates whose endpoint is within 400 mm of the

muon candidate's start point are treated as veto tracks. This distance requirement is not applied to the UsECal veto cut of the TPC or SuperFGD-contained muon samples. In all samples, any event containing one or more veto tracks is rejected.

2. **Upstream ToF veto cut.** Tracks starting outside the SuperFGD fiducial volume with a segment in the upstream ToF are also used as veto track candidates. Figure 6.5 shows the distribution of the number of veto track candidates per event. As for the upstream-ECal veto, for the HA-TPC muon sample, only tracks whose endpoint is within 400 mm of the muon candidate's start point are considered as veto track candidates. The TPC and SuperFGD-contained muon samples apply no such distance requirement. Any event with one or more veto track candidates is rejected. Figure 6.6 shows the distance between the veto track candidates and the muon candidate.

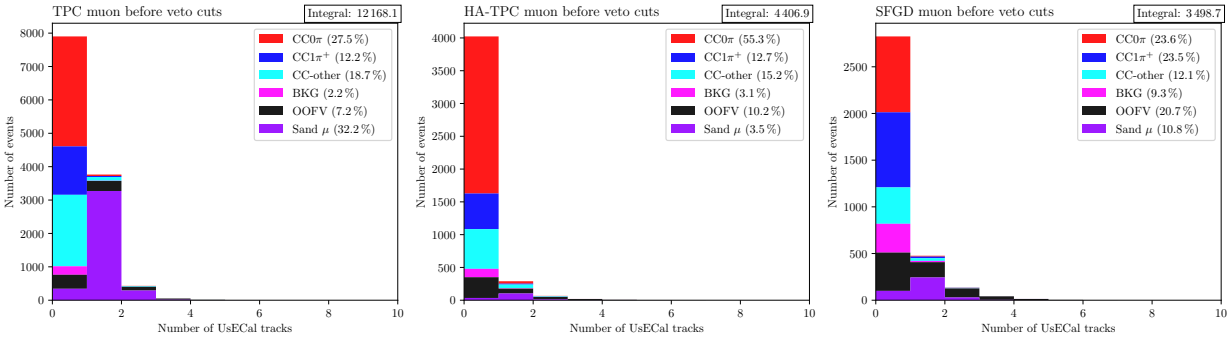


Figure 6.3: Number of selected UsECal veto track candidates before applying any veto cuts. The distributions are stacked by true topology [13].

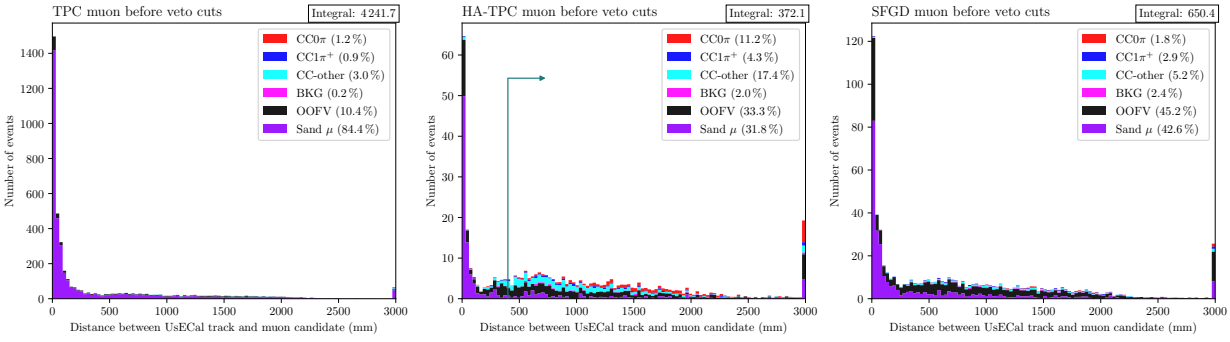


Figure 6.4: Distance between the selected UsECal veto-track and the muon track candidate before applying any veto cuts. The arrow indicates which events are kept in the cut for the HA-TPC muon sample, while for the TPC and SuperFGD-contained muon samples, all events in this histogram are rejected [13].

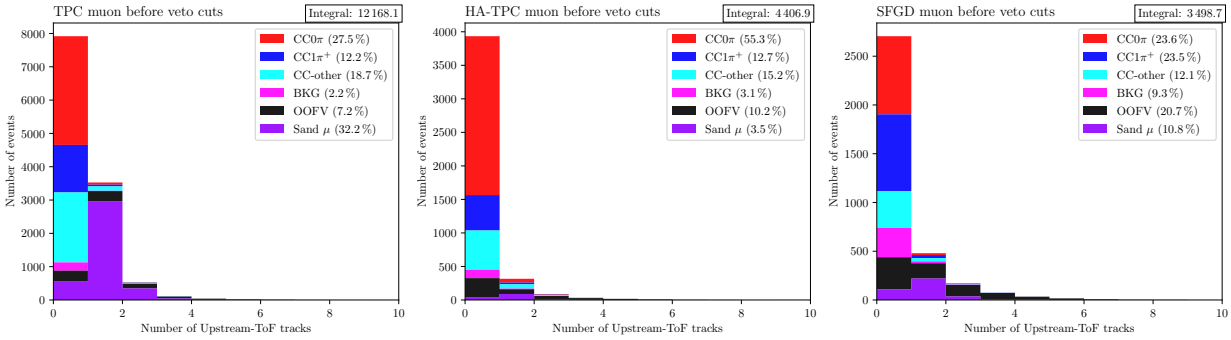


Figure 6.5: Number of selected upstream-ToF veto track candidates before applying any veto cuts. The distributions are stacked by true topology [13].

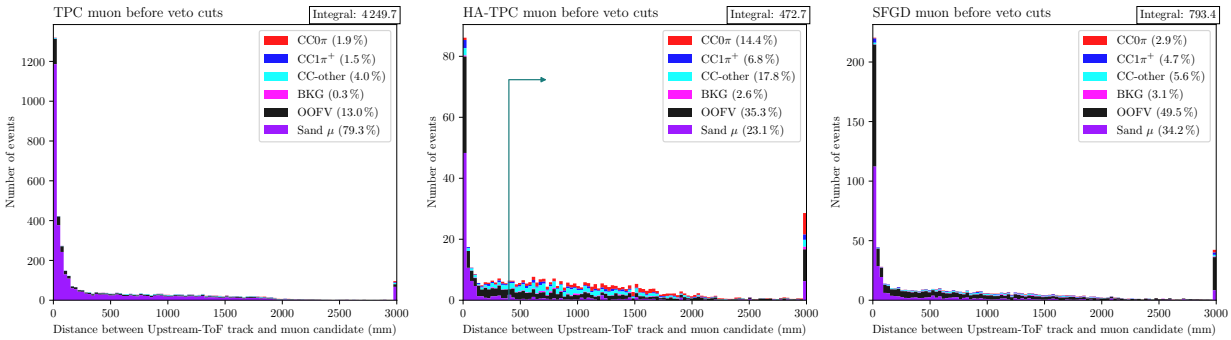


Figure 6.6: Distance between the selected upstream-ToF veto-track and the muon track candidate before applying any veto cuts. The arrow indicates which events are kept in the cut for the HA-TPC muon sample, while for the TPC and SuperFGD-contained muon samples, all events in this histogram are rejected [13].

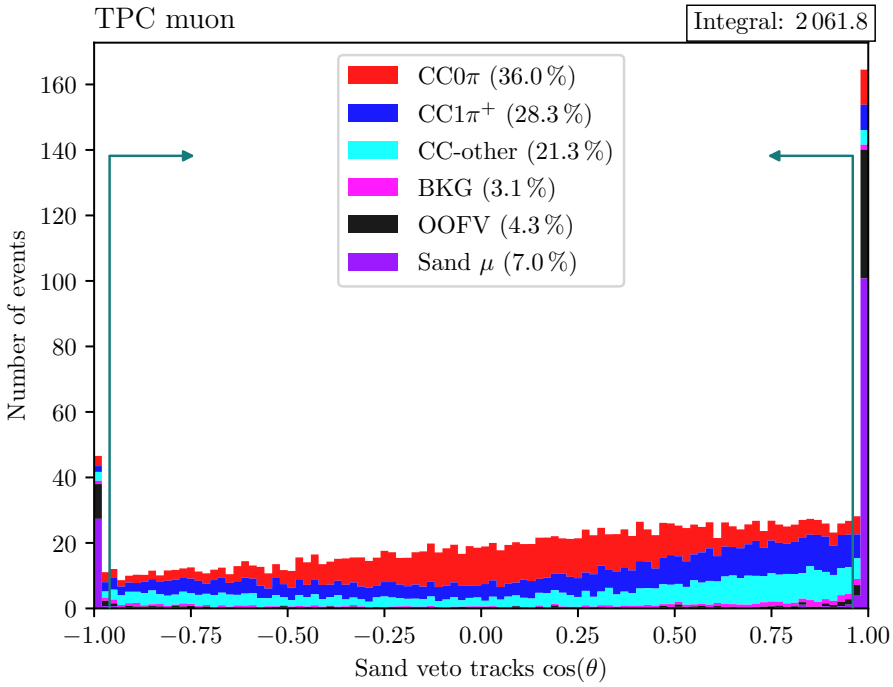


Figure 6.7: Scalar product of the directions of the two SuperFGD segments selected as candidates for the additional sand-muon veto, after the UsECal veto and Upstream-ToF veto cuts. The arrows indicate the events that are kept in this cut [13].

3. **Additional sand-muon veto.** An additional veto is applied only to the TPC muon sample. This cut targets through-going sand muon events that are broken by the reconstruction inside the SuperFGD and can therefore mimic an event vertex in the fiducial volume. The cut considers tracks with SuperFGD segments containing at least three nodes. If two SuperFGD segment endpoints are found outside the fiducial volume, the event is treated as a possible broken through-going track. The two segment directions are then compared, and the event is rejected when the absolute scalar product of the two directions $|\cos(\theta)| = |\boldsymbol{n}_1 \cdot \boldsymbol{n}_2|$ is at least 0.96. The distribution of the scalar product $\cos(\theta) = \boldsymbol{n}_1 \cdot \boldsymbol{n}_2$ is shown in Figure 6.7.

6.4 Selection results

6.4.1 Binning

The binning is chosen using MC samples and is in reconstructed momentum and in $\cos\theta_\mu$ of the selected muon candidate track. The θ_μ is the angle between the muon and the neutrino

direction. The neutrino direction is estimated as the direction from the averaged position of the neutrino parent decay points to the reconstructed interaction vertex. For each sample, 20 bins are used in each variable. The bin edges are determined from the MC samples such that each bin contains about the same number of events.

For the momentum binning, the range is restricted to 0–5 GeV/c for the TPC muon sample, 0–2 GeV/c for the HA-TPC muon sample, and 0–0.6 GeV/c for the SuperFGD-contained muon sample. Events with reconstructed muon momentum above these limits are placed in the last momentum bin. The resulting momentum and $\cos\theta_\mu$ bin edges are listed in Tables 6.2 and 6.3 [13].

This binning is used only to present the reconstructed muon kinematic distributions and to propagate the flux and detector systematic uncertainties to the binned reconstructed-level data/MC comparisons. It is not used for cross-section extraction or likelihood fitting.

Table 6.2: Reconstructed momentum bin edges (MeV/c) for the TPC muon, HA-TPC muon and SFGD-contained muon samples [13].

TPC muon
0–314
314–385
385–439
439–487
487–532
532–576
576–625
625–680
680–742
742–822
822–926
926–1074
1074–1277
1277–1536
1536–1841
1841–2220
2220–2673
2673–3202
3202–3899
3899–5000

HA-TPC muon
0–207
207–249
249–277
277–301
301–323
323–345
345–366
366–386
386–407
407–430
430–455
455–482
482–513
513–549
549–593
593–650
650–731
731–865
865–1139
1139–2000

SFGD muon
0–84
84–97
97–108
108–116
116–125
125–134
134–143
143–153
153–163
163–173
173–184
184–197
197–210
210–226
226–244
244–264
264–292
292–327
327–378
378–600

Table 6.3: Reconstructed $\cos\theta_\mu$ bin edges for the TPC muon, HA-TPC muon and SFGD-contained muon samples [13].

TPC muon
-1.0–0.586
0.586–0.695
0.695–0.758
0.758–0.803
0.803–0.837
0.837–0.864
0.864–0.885
0.885–0.904
0.904–0.920
0.920–0.934
0.934–0.946
0.946–0.956
0.956–0.965
0.965–0.972
0.972–0.979
0.979–0.984
0.984–0.989
0.989–0.993
0.993–0.997
0.997–1.0

HA-TPC muon
-1.0–(-0.144)
-0.144–0.024
0.024–0.144
0.144–0.227
0.227–0.295
0.295–0.355
0.355–0.414
0.414–0.467
0.467–0.516
0.516–0.564
0.564–0.607
0.607–0.651
0.651–0.694
0.694–0.733
0.733–0.771
0.771–0.809
0.809–0.846
0.846–0.883
0.883–0.926
0.926–1.0

SFGD muon
-1.0–(-0.904)
-0.904–(-0.771)
-0.771–(-0.636)
-0.636–(-0.504)
-0.504–(-0.386)
-0.386–(-0.273)
-0.273–(-0.171)
-0.171–(-0.074)
-0.074–0.022
0.022–0.122
0.122–0.216
0.216–0.309
0.309–0.408
0.408–0.505
0.505–0.597
0.597–0.685
0.685–0.770
0.770–0.850
0.850–0.929
0.929–1.0

6.4.2 Selected MC samples

The resulting MC samples of the inclusive ν_μCC selection, including the simulated beam and sand data, are discussed in this section. The distributions of the reconstructed kinematics of the event's selected muon candidate are presented in the following plots. The distributions are broken down by different truth categories: Figure 6.8 shows the breakdown by the true particle of the selected muon track, Figure 6.9 shows the breakdown by the true topology of the selected event, and Figure 6.10 shows the breakdown by the true reaction type.

For the momentum distributions, only the range used to define the binning is shown, up to 5, 2, and 0.6 GeV/c for the TPC, HA-TPC, and SuperFGD-contained muon samples. The $\cos\theta_\mu$ distribution of the TPC muon sample is shown from 0.5, where these candidates are almost entirely forward-going. Events outside the displayed range are collected in the nearest shown bin, the last bin in momentum and the first bin in $\cos\theta_\mu$, which produces the visible rise in the last momentum bin of the TPC muon sample.

The signal inclusive ν_μCC interactions are categorized by final-state topology into CC-0π (no mesons in the final state), CC-$1\pi^+$ (a single positive pion and no other mesons), and CC-other (all other ν_μCC final states). The background (BKG) category consists of NC, $\bar{\nu}_\mu$CC and ν_eCC interactions. The out-of-fiducial-volume (OOFV) category comprises events whose true neutrino vertex is outside the SuperFGD fiducial volume. The sand-muon (sand μ) category consists of neutrino interactions in the material outside the ND280 detector. No phase-space restriction is applied beyond the fiducial-volume requirement, so the signal spans the full outgoing-muon momentum and angle, including low-momentum, high-angle and backward-going muons. This is motivated by the design of the upgraded ND280 detector, where the high granularity of the SuperFGD is able to measure short charged tracks, and the HA-TPC and ToF systems provide nearly full angular coverage.

One of the dominant backgrounds of the signal sample comes from NC interactions in which the selected track is a negative pion, because a muon and a pion of the same charge produce similar energy deposits in the detectors and are difficult to separate. The OOFV contribution arises from broken tracks, where a through-going track is mistakenly reconstructed as starting inside the SuperFGD fiducial volume. An incorrectly determined track direction also contributes to the OOFV background, in which case a true positive pion can be selected as the muon candidate.

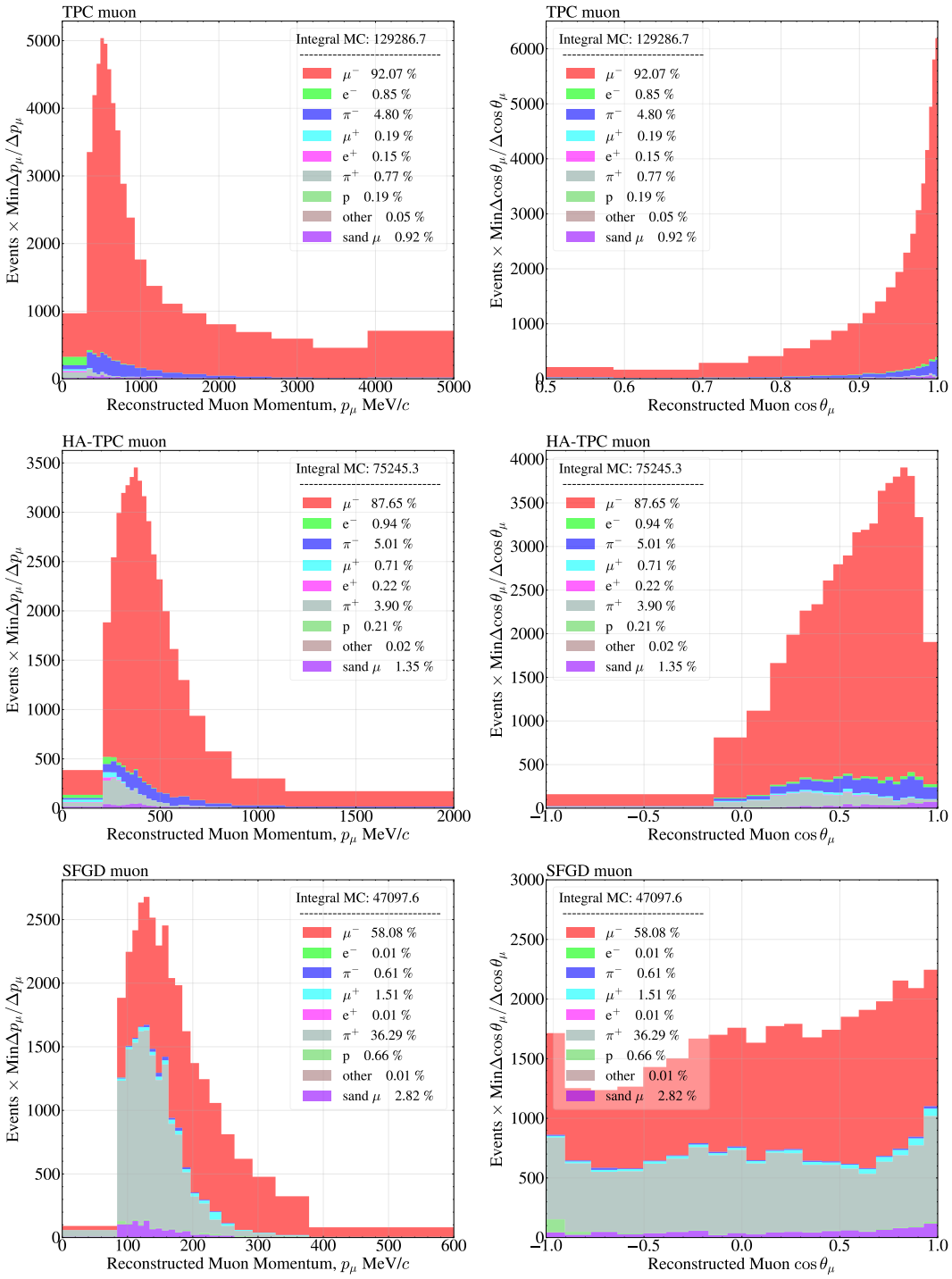


Figure 6.8: Reconstructed momentum and $\cos\theta_\mu$ of the muon candidate for the selected MC events in the three samples (TPC, HA-TPC and SuperFGD-contained muon) [13]. The stacking shows the true particle type of the muon candidate.

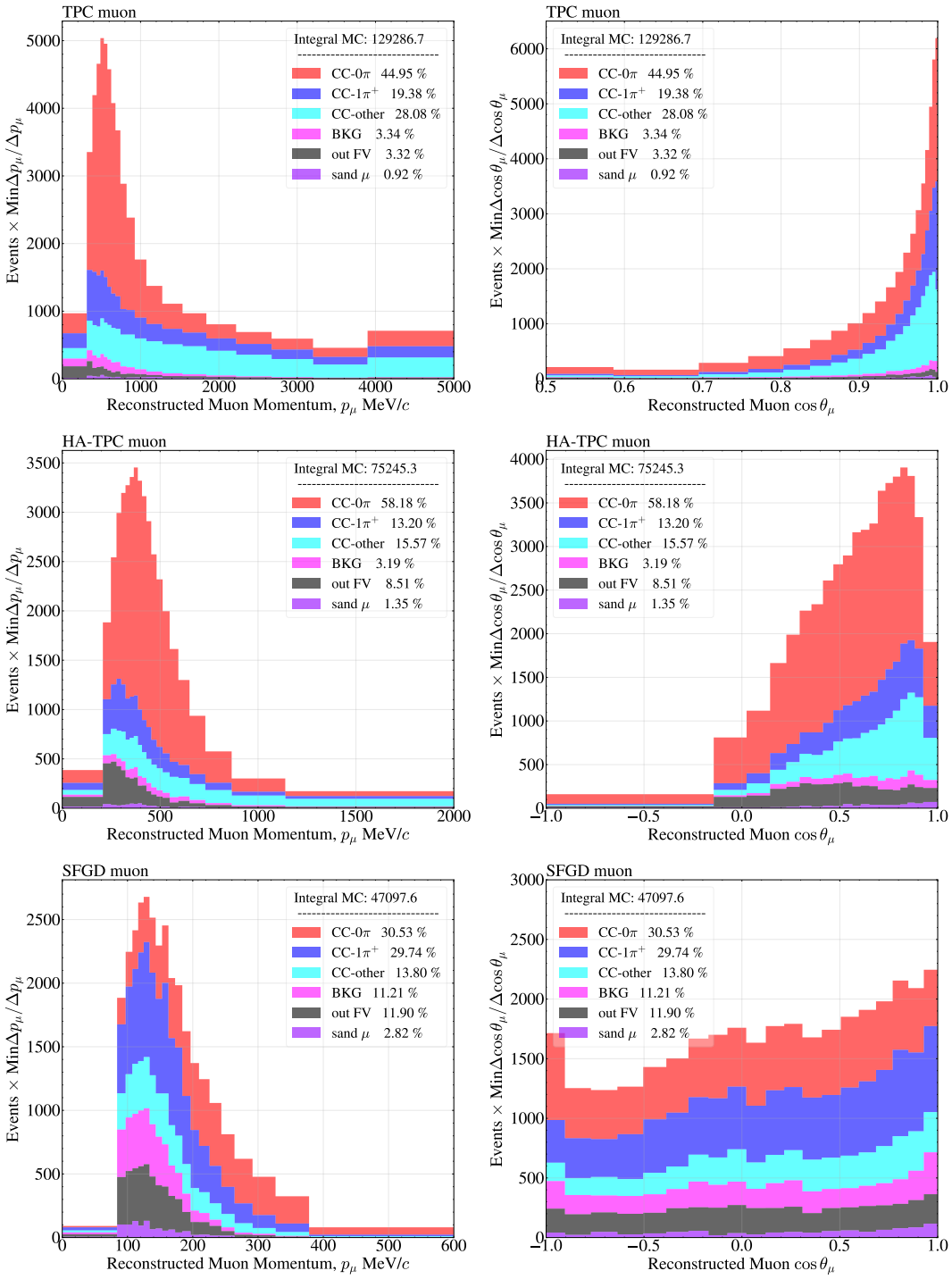


Figure 6.9: Reconstructed momentum and $\cos\theta_\mu$ of the muon candidate for the selected MC events in the three samples (TPC, HA-TPC and SuperFGD-contained muon) [13]. The stacking shows the true topology of the selected vertex.

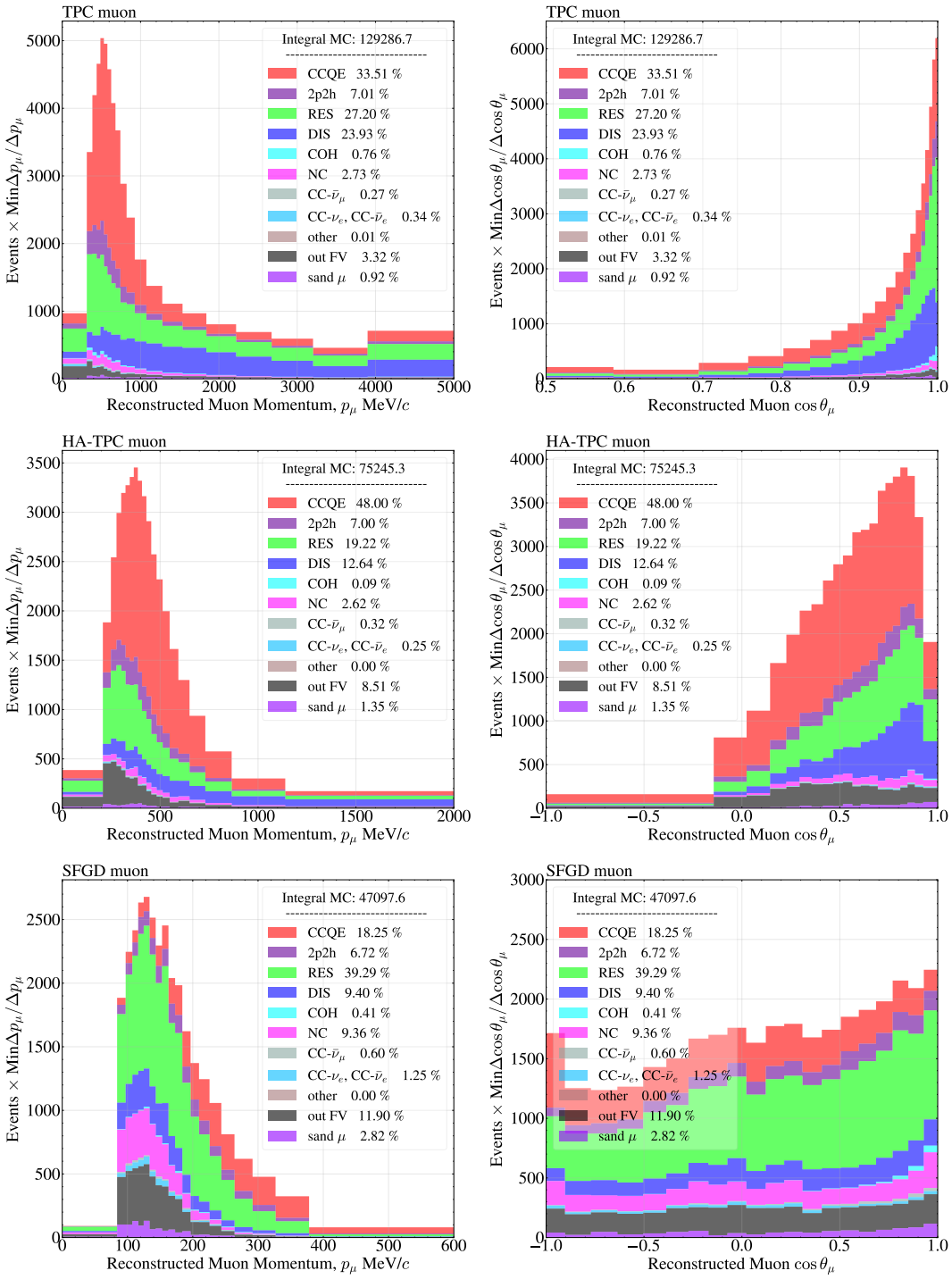


Figure 6.10: Reconstructed momentum and $\cos\theta_\mu$ of the muon candidate for the selected MC events in the three samples (TPC, HA-TPC and SuperFGD-contained muon) [13]. The stacking shows the true reaction type of the selected vertex.

6.4.3 Efficiency and purity

The purity of each sample is defined as [13]

$$\rho = \frac{\text{number of selected } \nu_\mu\text{CC events}}{\text{total number of selected events}}. \tag{6.4}$$

In this definition, the signal ν_μCC events are those with true topology CC-0π, CC-1π^+ or CC-other, regardless of whether the selected muon track is a true muon. Therefore, a selected ν_μCC event in which a non-muon track (for example, a pion) is incorrectly selected as the muon candidate is still considered a signal event and contributes to the numerator of Equation 6.4. This type of event counts as a ν_μCC topology in Figure 6.9 and a ν_μCC interaction in Figure 6.10, while appearing as a non-muon component in Figure 6.8. Such signal events with a muon candidate not correctly selected can populate an incorrect reconstructed-muon kinematic bin, and would be treated as background-like contributions in a future cross-section extraction. Figure 6.11 shows the purity as a function of the reconstructed momentum and $\cos\theta_\mu$ of the muon candidate for the three samples. In this figure, and in the efficiency figures that follow, the momentum axis covers a different range for each sample, reaching about 5000, 2000, and 600 MeV/c for the TPC, HA-TPC, and SuperFGD-contained samples, respectively.

The selection efficiency is quantified with two complementary definitions [13]. The topology-based efficiency ϵ_{det} is the efficiency to select a true ν_μCC interaction whose vertex is in the SuperFGD fiducial volume and whose true muon enters the TPC or HA-TPC, or is contained in the SuperFGD:

$$\epsilon_{\text{det}} = \frac{\substack{\text{selected events from true } \nu_\mu\text{CC in the SFGD FV} \\ \text{with the true muon entering the TPC or HA-TPC, or contained in the SFGD}}}{\substack{\text{true } \nu_\mu\text{CC interactions in the SFGD FV} \\ \text{with the true muon entering the TPC or HA-TPC, or contained in the SFGD}}}. \tag{6.5}$$

For the TPC and HA-TPC, events are included in Equation 6.5 if their true muon travels at least 20 cm through the detector's active volume, so that it is long enough to be reconstructed and associated with the sub-detector of interest. For the SuperFGD-contained sample the true muon is required to stop inside the SuperFGD. Figure 6.12 shows ϵ_{det} for each sample as a function of the true muon momentum and $\cos\theta_\mu$.

The overall efficiency ϵ refers to all true ν_μCC interactions in the fiducial volume, regardless of which detector the muon enters:

$$\epsilon = \frac{\text{selected events from true } \nu_\mu\text{CC interactions in the SFGD FV}}{\text{true } \nu_\mu\text{CC interactions in the SFGD FV}}. \tag{6.6}$$

Figure 6.13 shows the overall efficiency ϵ, split by the contributing samples, over the true muon momentum and $\cos\theta_\mu$. Figure 6.14 shows the 2D distribution of the overall efficiency ϵ in bins of the true muon momentum and $\cos\theta_\mu$.

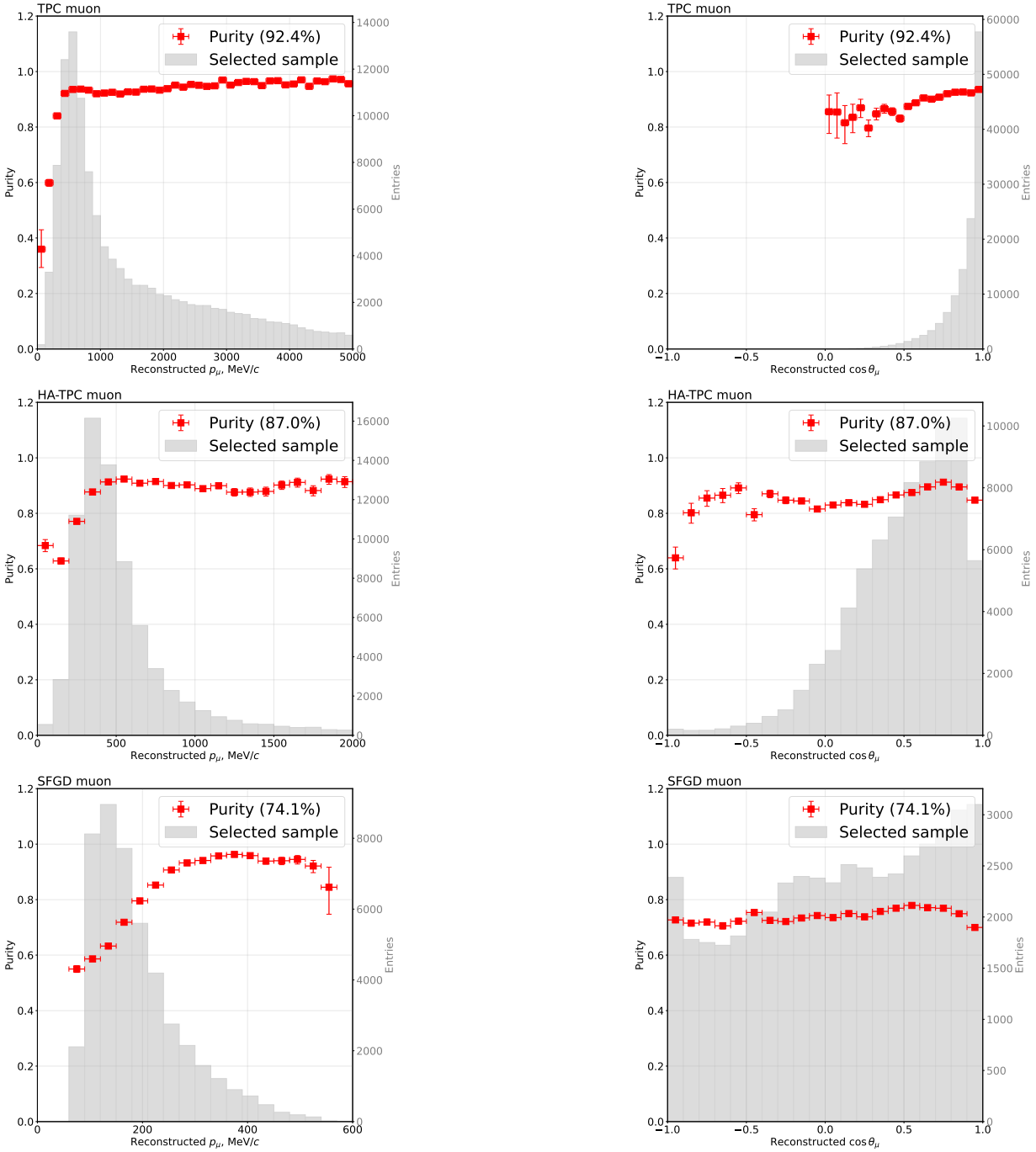


Figure 6.11: Selection purity as a function of reconstructed muon momentum (left) and $\cos\theta_\mu$ (right) for the TPC, HA-TPC and SuperFGD-contained muon samples [13]. Each sample is shown over its own momentum range, up to about 5000, 2000, and 600 MeV/c for the TPC, HA-TPC, and SuperFGD-contained samples, respectively.

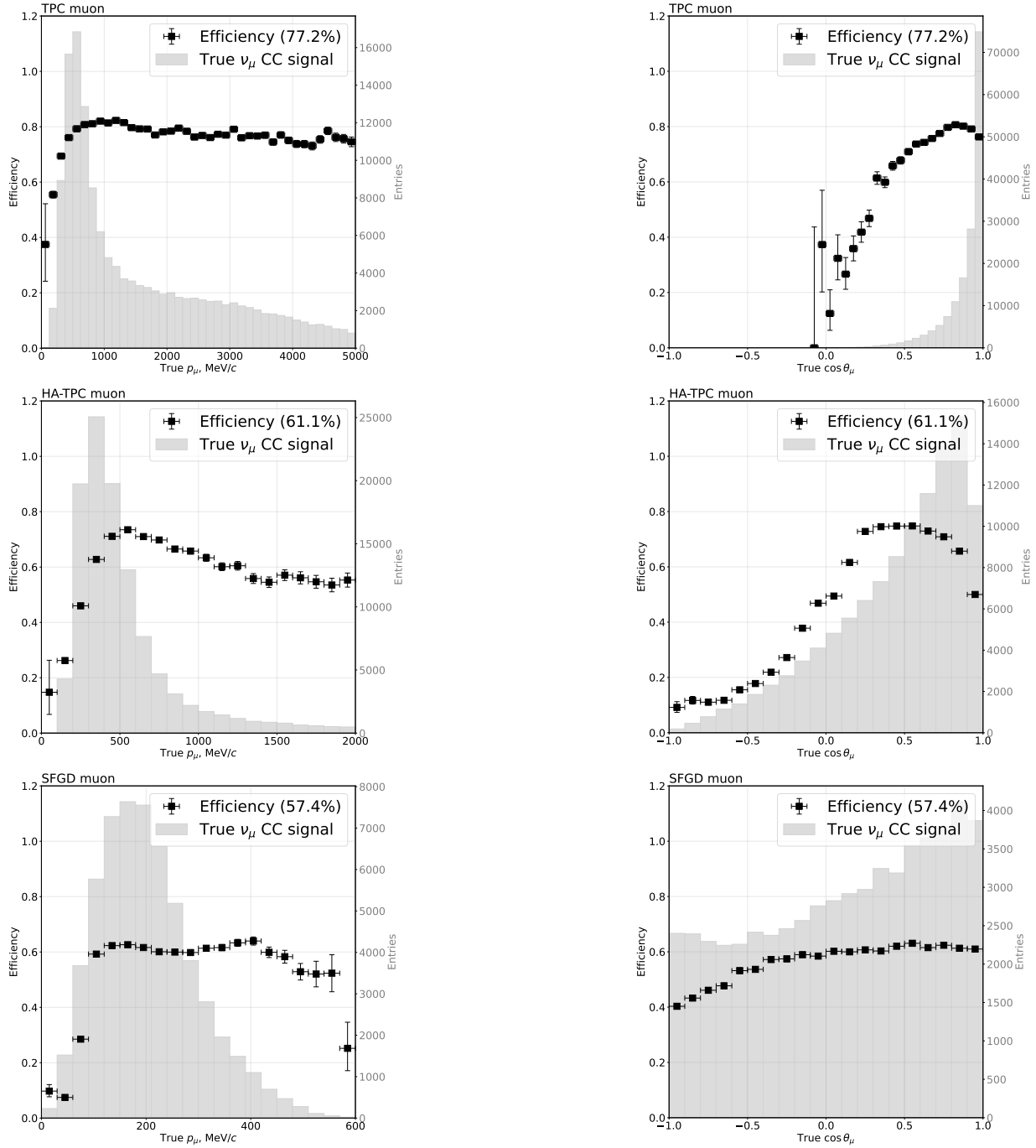


Figure 6.12: Selection efficiency ϵ_{det} as a function of true muon momentum (left) and $\cos\theta_\mu$ (right) for the TPC, HA-TPC and SuperFGD-contained muon samples [13]. Each sample is shown over its own momentum range, up to about 5000, 2000, and 600 MeV/c for the TPC, HA-TPC, and SuperFGD-contained samples, respectively.

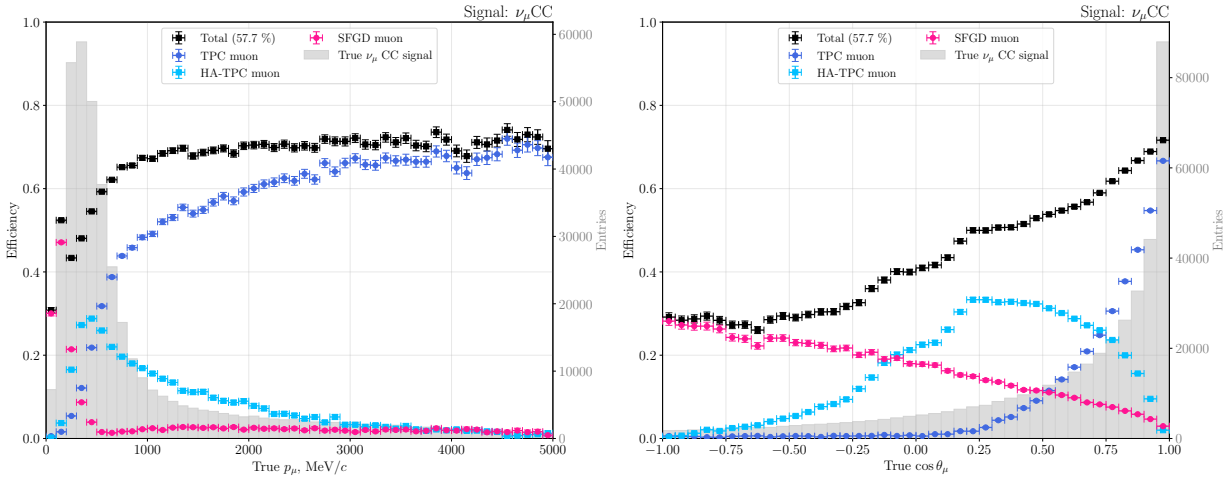


Figure 6.13: Overall ν_μCC selection efficiency ϵ as a function of the true muon momentum (left) and $\cos\theta_\mu$ (right), split into the TPC, HA-TPC and SuperFGD-contained muon samples. The total efficiency is given in the legend [13]. Each sample is shown over its own momentum range, up to about 5000, 2000, and 600 MeV/c for the TPC, HA-TPC, and SuperFGD-contained samples, respectively.

The two definitions provide complementary information. ϵ_{det} gives how well the analysis selects true ν_μCC events with a true muon reconstructed in different detectors, while ϵ gives how well the true ν_μCC events are selected overall, regardless of which detector the muon reaches. For $\cos\theta_\mu > 0$ the HA-TPC sample reaches an efficiency comparable to that of the TPC sample. For $\cos\theta_\mu < 0$ the HA-TPC efficiency drops, partly because the direction of the backward-going muon is not corrected properly. Since the track direction is forward-going by default and this analysis corrects the track direction using only the local SuperFGD timing rather than the SuperFGD–ToF time difference, only backward tracks with a SuperFGD segment of more than 30 nodes are correctly reversed and enter the selection, which lowers the efficiency in the backward region. This is expected to improve once the analysis includes the SuperFGD–ToF timing to determine the track direction. The overall efficiency ϵ is lower than ϵ_{det} because its denominator includes all true ν_μCC interactions regardless of which detector that the muon enters. This includes events in which the muon exits the SuperFGD sideways, which are not included in any analysis samples.

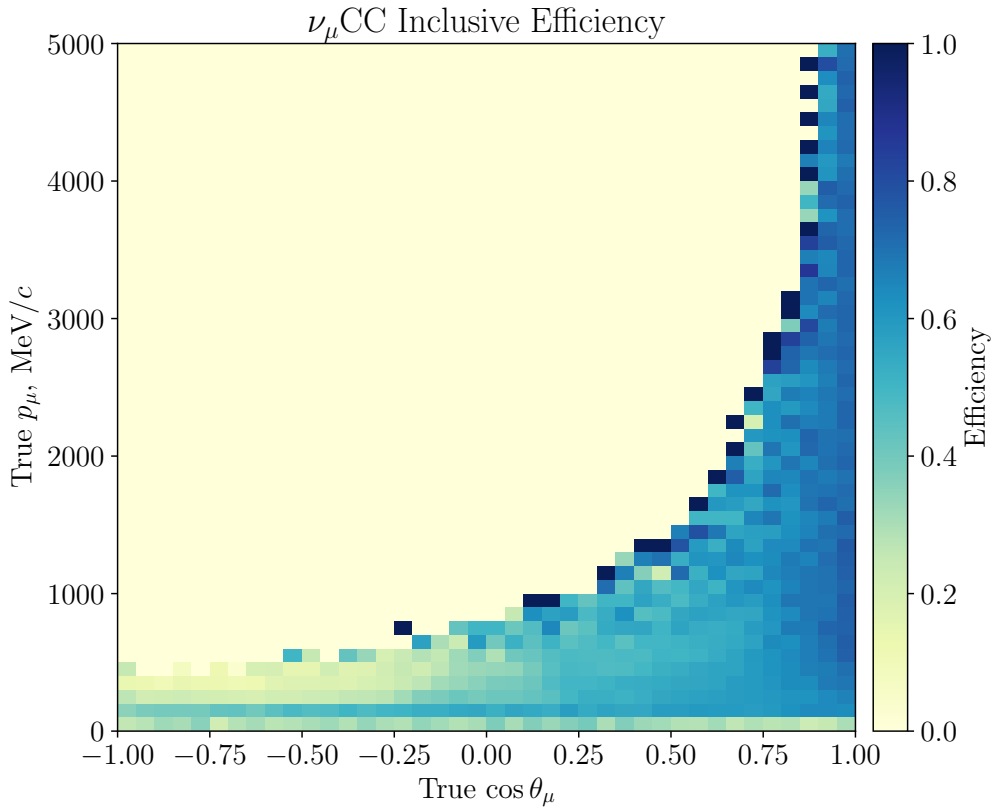


Figure 6.14: Two dimensional histogram of the overall ν_μCC-inclusive selection efficiency ϵ in bins of the true muon momentum p_μ and $\cos\theta_\mu$. The efficiency value is shown by the color scale [13].

6.4.4 Data and MC comparisons

This section presents the reconstructed-level comparison between data and the MC prediction for the three selected samples. The MC is normalized to the data POT. The uncertainty of the MC sample includes the statistical, detector systematic and flux systematic uncertainties. The neutrino cross-section model uncertainties are not included. The details of the systematic uncertainties are in Section 6.5.The comparison only characterizes the selected samples at the reconstruction level rather than providing a cross-section extraction or interaction-model tuning.

In addition to the nominal MC selection presented in the previous sections, the selection is repeated on the same MC inputs, reweighted using the best-fit flux and neutrino-interaction parameters of the 2024 pre-upgrade ND280 fit (ND OA2024) [80]. These best-fit values were obtained from a fit to the pre-upgrade FGD samples and are applied here only as an external reweighting. For the uncertainty of the post-fit reweighted MC selection, the relative systematic uncertainties of the nominal MC selection are reused rather than obtained by toy experiments with the ND OA2024 post-fit covariance matrix. The comparison of the reweighted MC with the data probes whether the pre-upgrade fit result also describes the extended phase space accessed by the upgraded detector, in particular the high-angle and backward-going tracks in the HA-TPC and SuperFGD-contained muon samples.

Total number of selected events

The numbers of selected events in data and in MC are summarized in Table 6.4, for both the nominal MC and the MC reweighted to the ND OA2024 best-fit parameters.

Table 6.4: Number of selected events in each sample for the data and for the MC prediction. The MC is normalized to the data exposure of 1.574×10^{20} POT.

		MC prediction	
Sample	Data	Nominal	ND OA2024 reweighted
TPC muon	7430	7181.0	8025.9
HA-TPC muon	4825	4179.3	5336.9
SFGD muon	2963	2615.9	2790.8

Comparison of the reconstructed distributions

The reconstructed muon-candidate momentum and $\cos\theta_\mu$ distributions in data and in the nominal MC are compared in Figure 6.15. The systematic uncertainties are propagated to the binned distributions with 500 toy experiments, in which the systematic parameters

are varied together and the uncertainty in a given bin is taken as the RMS of the spread in the number of selected events. The three error bands correspond to the MC statistical uncertainty, to the MC statistical and detector uncertainties, and to the MC statistical, detector and flux uncertainties.

The level of agreement between the data and the nominal MC selection is quantified with a χ^2 evaluated separately in bins of reconstructed momentum and $\cos\theta_\mu$, as listed in Table 6.5. The p-values are obtained from the χ^2 cumulative distribution for ndf = 20, equal to the number of bins in each sample. A χ^2 is calculated only for the nominal MC selection. The ND OA2024 post-fit flux covariance corresponds to the pre-upgrade flux, which differs from the 320 kA flux used in this analysis, and therefore cannot be applied to the χ^2 calculation for the post-fit reweighted MC.

Table 6.5: χ^2 and p-value of the nominal MC/data comparison for each sample, evaluated in bins of reconstructed muon momentum and $\cos\theta_\mu$.

	Muon momentum		Muon angle ($\cos\theta_\mu$)	
Sample	χ^2	p-value	χ^2	p-value
TPC muon	27.4	0.126	38.1	0.009
HA-TPC muon	29.8	0.074	51.8	1×10^{-4}
SFGD muon	15.7	0.735	70.9	$< 10^{-4}$

To show the effect of the pre-upgrade post-fit parameters on the data/MC comparison, Figure 6.16 shows the reconstructed muon momentum and $\cos\theta_\mu$ distributions for the nominal MC selection, the ND OA2024 post-fit reweighted MC, and the data. The reweighting is seen to move the prediction towards the data in all three samples. The closest agreement is found where the selected phase space coincides with that of the pre-upgrade FGD analysis. Beyond this overlap, the HA-TPC and SuperFGD-contained samples include the high-angle and backward-going tracks that were poorly covered before the upgrade, and the reweighting is found to improve the agreement in this region as well. Such behaviour suggests that a future fit that includes the upgrade samples would extend the reach into a part of the muon phase space beyond the pre-upgrade selection. Since the cross-section model uncertainties are not included in this analysis, whether the interaction-model parameters are flexible enough to describe the new phase-space regions while keeping the agreement in the pre-upgrade region is left for future analysis.

6.5 Systematic uncertainties

The predicted event rates are affected by uncertainties in the neutrino flux and in the detector response. Both flux and detector systematics are propagated to the binned reconstructed distributions with 500 toy experiments. In each toy experiment, the systematic

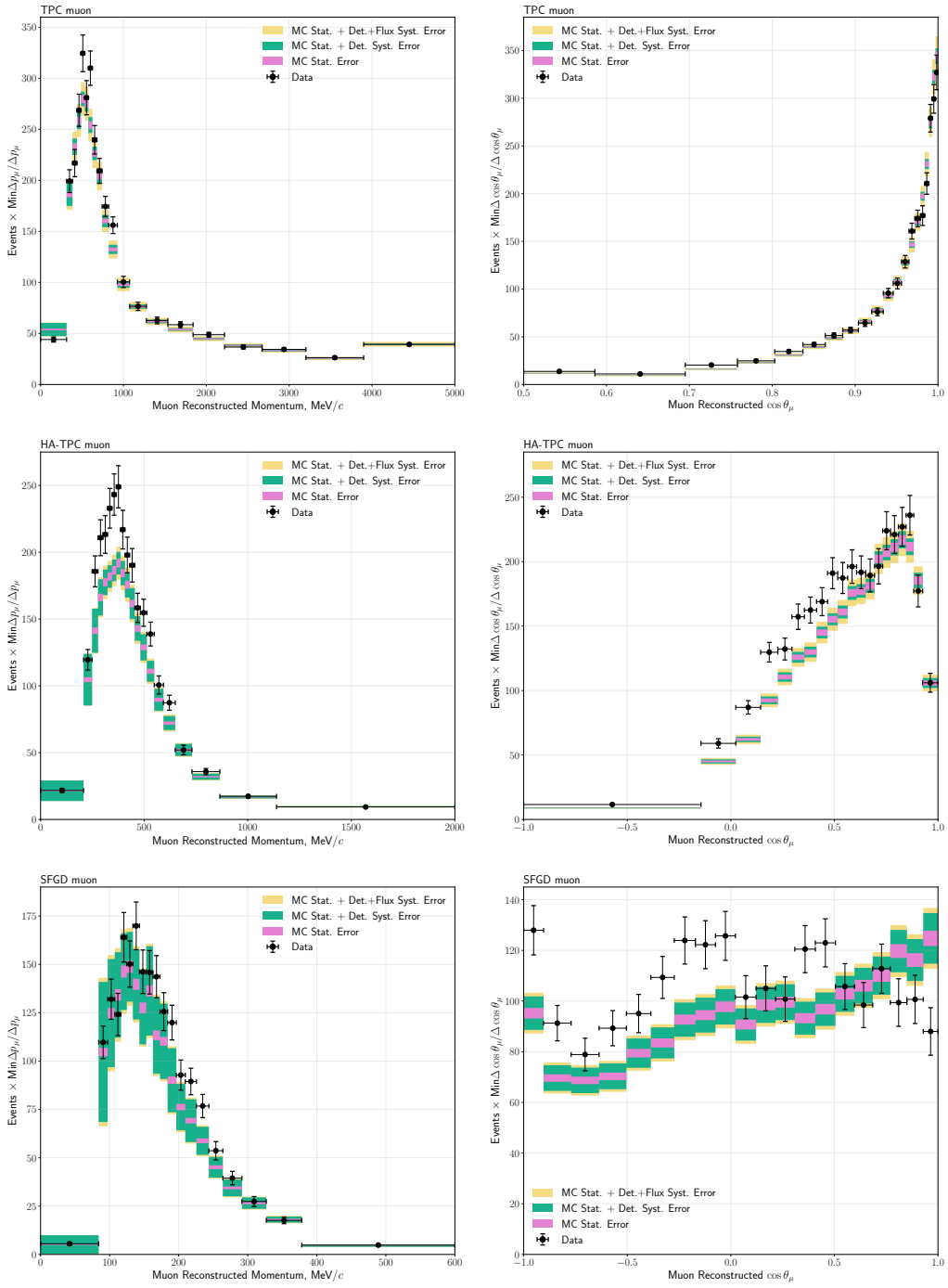


Figure 6.15: Reconstructed muon-candidate momentum (left column) and $\cos\theta_\mu$ (right column) for the ν_μCC inclusive TPC, HA-TPC and SuperFGD-contained muon samples (top to bottom). The error bands show the MC statistical uncertainty (pink), the MC statistical and detector systematic uncertainties (green), and the MC statistical, detector and flux systematic uncertainties (yellow) [13].

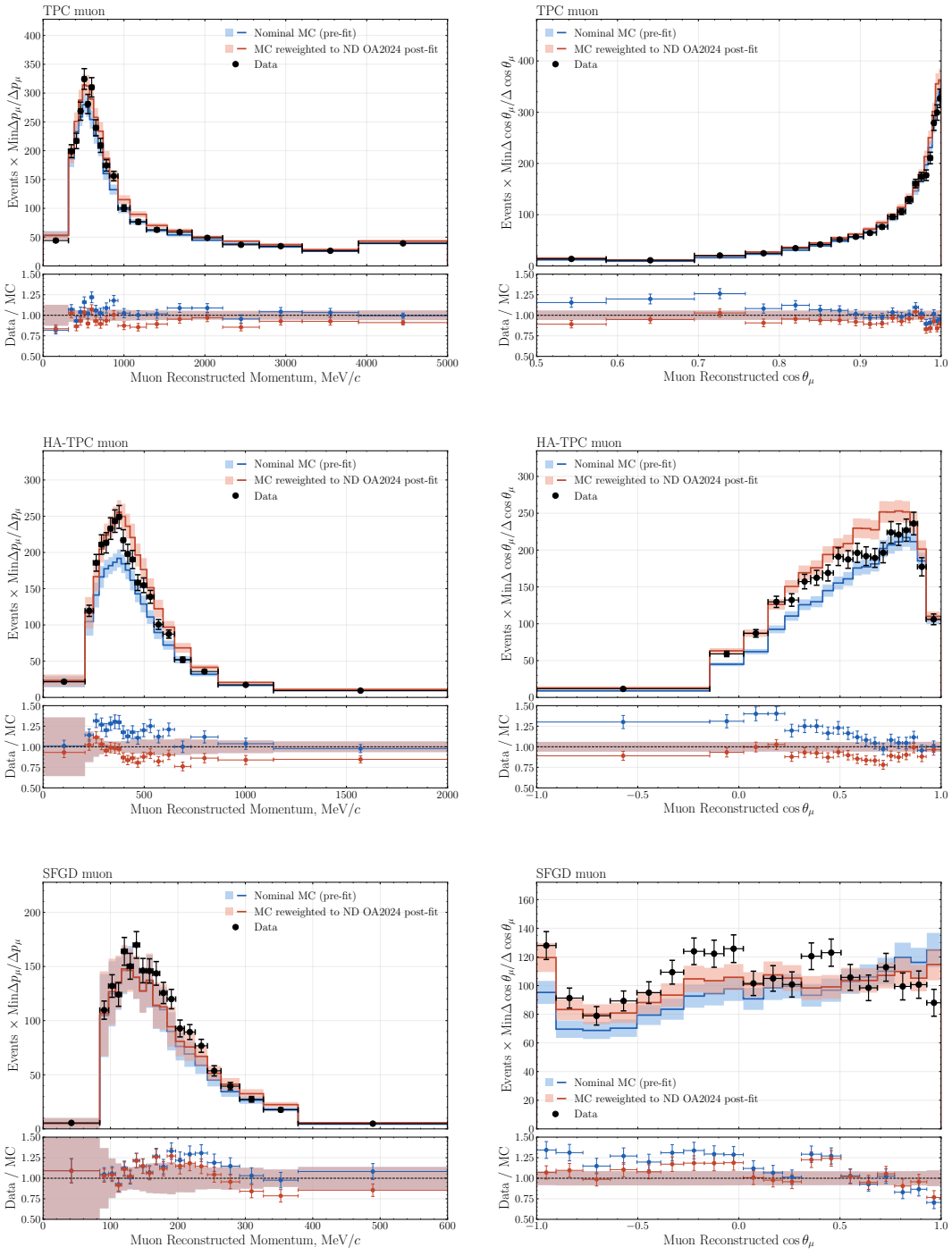


Figure 6.16: Reconstructed muon-candidate momentum (left) and $\cos\theta_\mu$ (right) for the ν_μCC inclusive TPC, HA-TPC and SuperFGD-contained muon samples (top to bottom), with the corresponding ratio shown beneath each panel. The data are compared with the nominal MC prediction and with the same model reweighted to the best-fit flux and neutrino-interaction parameters from the pre-upgrade FGD-based ν_μCC analysis (ND OA2024) [13].

parameters are varied within their uncertainties, and their effect on the selected sample is recomputed. The spread of the number of selected events over the toy experiments gives the uncertainty in each bin.

6.5.1 Flux systematic uncertainties

The MC prediction is corrected using the flux weights from the `tuned23av1`. The uncertainty on this flux prediction is implemented as an event-weight systematic using the corresponding `tuned23av1` flux covariance matrix. This analysis uses the Run 13c (FHC, 320 kA horn current) sample, so the relevant flux parameters are the 320 kA FHC bins of the `tuned23av1` covariance file. The flux uncertainty is parameterized in bins of true neutrino flavor and true neutrino energy, giving the 25 parameters listed in Table 6.6. The correlation matrix between these parameters is shown in Figure 6.17.

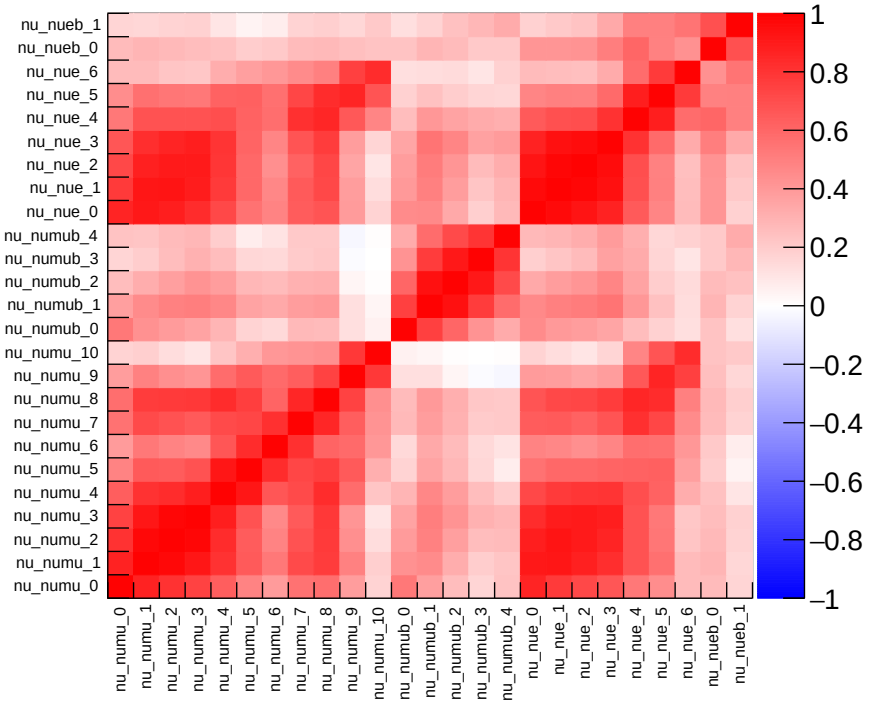


Figure 6.17: Correlation matrix for flux parameters.

Table 6.6: Flux systematic parameters used for the inclusive ν_μ CC analysis. The binning and relative uncertainties are taken from the flux covariance file `23av1_run1to13_banff.root` [13].

Parameter	Neutrino Energy (GeV)	Relative uncertainty
ν_μ Bin 0	$[0.0, 0.4)$	0.060
ν_μ Bin 1	$[0.4, 0.5)$	0.049
ν_μ Bin 2	$[0.5, 0.6)$	0.050
ν_μ Bin 3	$[0.6, 0.7)$	0.053
ν_μ Bin 4	$[0.7, 1.0)$	0.061
ν_μ Bin 5	$[1.0, 1.5)$	0.076
ν_μ Bin 6	$[1.5, 2.5)$	0.063
ν_μ Bin 7	$[2.5, 3.5)$	0.046
ν_μ Bin 8	$[3.5, 5.0)$	0.048
ν_μ Bin 9	$[5.0, 7.0)$	0.067
ν_μ Bin 10	$[7.0, 30.0)$	0.108
$\bar{\nu}_\mu$ Bin 0	$[0.0, 0.7)$	0.098
$\bar{\nu}_\mu$ Bin 1	$[0.7, 1.0)$	0.065
$\bar{\nu}_\mu$ Bin 2	$[1.0, 1.5)$	0.066
$\bar{\nu}_\mu$ Bin 3	$[1.5, 2.5)$	0.076
$\bar{\nu}_\mu$ Bin 4	$[2.5, 30.0)$	0.071
ν_e Bin 0	$[0.0, 0.5)$	0.054
ν_e Bin 1	$[0.5, 0.7)$	0.054
ν_e Bin 2	$[0.7, 0.8)$	0.056
ν_e Bin 3	$[0.8, 1.5)$	0.052
ν_e Bin 4	$[1.5, 2.5)$	0.047
ν_e Bin 5	$[2.5, 4.0)$	0.053
ν_e Bin 6	$[4.0, 30.0)$	0.078
$\bar{\nu}_e$ Bin 0	$[0.0, 2.5)$	0.096
$\bar{\nu}_e$ Bin 1	$[2.5, 30.0)$	0.112

6.5.2 Detector systematic uncertainties

The detector systematic uncertainties account for imperfect detector simulation, calibration and reconstruction. Most of them are evaluated using dedicated data and MC control samples. Each uncertainty is propagated in one of two ways, following the treatment established for the pre-upgrade ND280 analysis [79]. A *variation* systematic shifts a reconstructed quantity, such as a momentum or a particle-identification variable, before the selection is applied, so that it can change both which events are selected and the bin into which they fall. A *weight* systematic instead leaves the reconstruction unchanged and applies a weight to each selected event, used to scale an efficiency or a background normalisation. In both cases the uncertainty is propagated to the binned reconstructed distributions by generating toy variations of the corresponding parameters. The probability density function (PDF) of all systematics is assumed to be a Gaussian distribution, except the B-field distortion, which is assumed to be a uniform distribution. A brief introduction to each detector systematic is given below. The detailed evaluation of each is documented in the T2K Technical Note 525 [13]. The relative uncertainty from each individual detector systematic is shown in Appendix A.

Variation-like systematics

SFGD Momentum Bias. A bias in the reconstructed SFGD momentum due to dead material missing in the `P8_v17` simulation, revealed by a data/MC discrepancy between the HA-TPC and SFGD momentum.

(HA-)TPC Momentum Scale. Uncertainty in the absolute momentum scale of the vertical and high-angle TPCs, arising from the uncertainty on the magnetic field measurement.

(HA-)TPC Momentum Resolution. Data/MC differences in the TPC and HA-TPC momentum resolution. For the TPCs, the systematic is estimated from through-going tracks crossing neighbouring TPCs, comparing their independent momentum measurements. For the HA-TPCs, it is estimated from control samples of sand muons crossing a single HA-TPC and cosmic muons crossing two HA-TPCs.

TPC PID. Data/MC differences in the vertical-TPC particle identification based on the energy loss dE/dx. The PID pull is measured in muon, proton and electron control samples and compared between data and MC. The differences in the pull mean and width are propagated as a variation of the pulls.

HA-TPC PID. Similar to the TPC PID, evaluated using muon, proton and electron control samples.

B Field Distortion. The magnetic field is not perfectly uniform inside the detector. These distortions bias the reconstructed track momentum. The uncertainty in modelling the magnetic-field distortion is evaluated by varying the momentum uniformly between the fits obtained with and without the distortion correction. It is the only uncertainty treated as a flat rather than a Gaussian prior.

TOF Resolution. The SuperFGD segment timing is used for track-direction determination. The uncertainty on this timing resolution is evaluated by comparing the SuperFGD segment time resolution in data and MC.

SFGD Momentum Resolution. Data/MC difference in the SuperFGD BDT momentum resolution, evaluated with a HA-TPC-SFGD stopping control sample, and propagated as a momentum smearing.

Weight-like systematics

Pile Up. The selection vetoes external backgrounds using activity in the upstream ECal and ToF panel. In data, accidental activity from a background (e.g. a sand event) in the same bunch can veto a true signal event, decreasing the efficiency. Because the beam and sand MC are simulated separately, this pile-up effect is absent in the MC. A correction is applied to the MC to reproduce this efficiency drop, and the systematic is the data/MC difference in the UsECal activity rate per bunch, propagated as a weight.

Pion SI. Uncertainty in the modelling of pion secondary interactions in the detector material. The propagation follows pre-upgrade ND280 analyses, with a volume of interest added for the SuperFGD and surrounding material.

Proton SI. Uncertainty in the modelling of proton inelastic secondary interactions in the detector material, with a volume of interest added for the SuperFGD and surrounding material.

Charge ID. Uncertainty in correctly identifying a particle's charge sign from its curvature in the (HA-)TPCs. Evaluated from the data/MC difference in how often the local reconstructed charge sign matches the global reconstructed charge.

SFGD Mass. Uncertainty on the SuperFGD mass (fiducial volume, mechanical box, and electronics), arising from measurement uncertainties and simplifications in its simulation.

TPC Track Eff. Uncertainty in the efficiency of reconstructing a track in the vertical TPCs. Evaluated with a tag-and-probe method using a through-going muon control sample in which a muon is tagged by reference segments in the detectors upstream and downstream of the TPC, and the efficiency is how often a good track is then reconstructed in that TPC.

HA-TPC Track Eff. Uncertainty in the HA-TPC tracking efficiency, evaluated with a tag-and-probe method using cosmic muons. It is one of the leading uncertainties in the HA-TPC muon sample.

ToF Track Eff. Uncertainty in the efficiency of the ToF to reconstruct an object (cluster) where a track is expected. It is relevant because the ToF is used as an upstream veto. Evaluated using a control sample in which a HA-TPC track is extrapolated to a ToF plane where it is expected to cross, and the efficiency is how often a ToF cluster is actually reconstructed there, in data vs MC.

SFGD Track Eff. Uncertainty in the SuperFGD track-reconstruction efficiency, measured by a tag-and-probe method. The control sample consists of single HA-TPC tracks (momentum greater than 100 MeV/c) entering the SuperFGD from a HA-TPC, which tag where an SFGD object is expected. The efficiency is how often an SFGD object is then reconstructed there, compared between data and MC.

TPC Cluster Eff. Uncertainty in the efficiency of reconstructing charge clusters in the vertical TPCs, which affects the track-quality cut based on the number of nodes. Evaluated using high-momentum through-going muons crossing all three TPCs, where the expected number of clusters is known. The distribution of the number of clusters is compared between data and MC, and an additional inefficiency is applied to match the data.

HA-TPC Cluster Eff. Uncertainty in the efficiency of HA-TPC cluster reconstruction. Evaluated using high-momentum through-going muons parallel to the Z axis crossing a HA-TPC, where the expected number of clusters is known. An additional inefficiency is applied to match the data.

HA-TPC–TPC Matching Eff. Uncertainty in the efficiency that a HA-TPC segment and a vertical-TPC segment of the same track are matched into a single global track. It is evaluated using a control sample of high-quality TPC tracks propagated to the HA-TPC. Given a reconstructed HA-TPC segment, the efficiency is how often it is matched with the TPC segment into one global track.

TPC-SFGD Matching Eff. Uncertainty in the efficiency of matching a vertical TPC segment to a SuperFGD segment.

HA-TPC–SFGD Matching Eff. Uncertainty in the efficiency of matching a high-angle TPC segment to a SuperFGD segment. It is one of the leading sources of uncertainty for the HA-TPC muon sample.

SFGD–HA-TPC–ToF Matching Eff. Uncertainty in the efficiency of matching a SuperFGD–HA-TPC track to a ToF object.

OOFV. The out-of-fiducial-volume background is interactions reconstructed inside the SuperFGD fiducial volume but with a true vertex outside it. Two uncertainties are assigned: an event-rate uncertainty and a reconstruction uncertainty. The rate uncertainty evaluates the rate at which neutrino interactions occur in the surrounding detectors (PØD, ECals, SMRD) by comparing it between data and MC, while the rate in the magnet and electronics, which cannot be measured this way, is estimated from a NEUT/GENIE generator comparison. The reconstruction uncertainty covers the broken-track case: using a control sample of tracks that should be reconstructed as a single track crossing the SuperFGD, the SuperFGD breaking rate is compared between data and MC. A broken track originating outside the SuperFGD can leave a segment whose starting point falls inside the SuperFGD, faking an in-fiducial-volume vertex. The other failure modes carry no separate uncertainty:

wrong track direction is covered by the ToF timing systematic, and matching failure by the tracking and matching systematics.

Sand Muon. Uncertainty on the rate of sand muons. Muons from neutrino interactions in the material upstream of ND280 that enter the detector are a background. A normalization uncertainty is assigned, evaluated from the data/MC difference in the rate of sand tracks entering ND280, measured at the UsECal.

Michel Electron Tagging Eff. In the SuperFGD-contained sample the muon candidate is identified by tagging the Michel electron from muon decay, so a data/MC difference in the tagging efficiency directly affects the selection. The efficiency is measured in data and MC using a HA-TPC-SFGD stopping control sample. The Michel electron tagging efficiency is about 74% in data against 77% in MC, and it is one of the leading detector systematics for the SuperFGD-contained sample.

SFGD PID. Particle identification for SuperFGD-contained tracks uses a BDT, trained on particle-gun samples, that returns a response for the muon, pion, proton and electron hypotheses. In the SFGD-muon branch, the selected track is required to be muon-like. The data/MC difference in this identification is evaluated with HA-TPC–SFGD stopping control samples: a stopping-μ^- sample for the muon-PID efficiency and a stopping-π^+ sample for the pion-to-muon wrong-PID probability. The results are binned in the number of SuperFGD nodes and applied as an event weight. It is one of the leading uncertainties for the SuperFGD-contained sample.

6.5.3 Summary of the systematic uncertainties

Table 6.7 summarises the integrated relative systematic uncertainties for the three samples, where the integrated uncertainty is the uncertainty on the total number of selected events in a sample, summed over all reconstructed bins.

The flux uncertainty is about 5% and is similar for the three samples, while the total detector uncertainty depends strongly on the sample. It is 1.8% for the TPC, 2.5% for the HA-TPC, and 6.7% for the SuperFGD-contained sample. For the TPC and HA-TPC samples the flux therefore dominates the total uncertainty, whereas for the SuperFGD-contained sample the detector uncertainty dominates the total uncertainty. The leading detector uncertainties of the SuperFGD-contained sample include the Michel-electron tagging efficiency (5.1%), the SuperFGD tracking efficiency (3.2%) and the SuperFGD PID (2.4%). For the HA-TPC sample the leading detector sources are the HA-TPC tracking efficiency (2.0%) and the HA-TPC–SuperFGD matching efficiency (1.4%).

The relative systematic uncertainty as a function of the reconstructed muon momentum and $\cos\theta_\mu$ is shown in Figure 6.18, separately for the detector sources alone and for the detector and flux sources combined. The five largest contributors in each region are shown in Figure 6.19. The relative uncertainty is largest in the lowest momentum bins, reaching about 12% for the TPC sample, about 36% for the HA-TPC sample and approaching 100% in

the first bin of the SuperFGD-contained sample. This low-momentum systematic originates from the SuperFGD momentum bias for the TPC and HA-TPC samples, and from the SuperFGD momentum resolution for the SuperFGD-contained sample.

Systematic Error Source	TPC muon	HA-TPC muon	SuperFGD muon
SFGD Momentum Bias	0.02	0.08	< 0.01
(HA-)TPC Momentum Scale	< 0.01	< 0.01	< 0.01
(HA-)TPC Momentum Resolution	< 0.01	< 0.01	< 0.01
TPC PID	0.14	< 0.01	0.02
HA-TPC PID	0.02	0.34	0.03
B Field Distortion	< 0.01	< 0.01	0.00
ToF Resolution	< 0.01	0.31	0.01
SFGD Momentum Resolution	0.00	0.00	0.00
Pile Up	1.38	0.07	1.37
Pion SI	0.38	0.18	1.34
Proton SI	< 0.01	< 0.01	0.06
Charge ID	0.24	0.10	0.00
SFGD Mass	0.58	0.56	0.54
TPC Track Efficiency	0.33	0.27	0.26
HA-TPC Track Efficiency	0.41	1.97	0.17
ToF Track Efficiency	0.02	0.05	0.14
SFGD Track Efficiency	0.68	0.71	3.21
TPC Cluster Efficiency	< 0.01	< 0.01	0.00
HA-TPC Cluster Efficiency	< 0.01	0.11	0.00
HA-TPC–TPC Matching Efficiency	0.02	0.10	< 0.01
TPC–SFGD Matching Efficiency	0.29	0.00	< 0.01
HA-TPC–SFGD Matching Efficiency	0.78	1.44	0.14
SFGD–HA-TPC–ToF Matching Efficiency	0.00	< 0.01	0.00
OOFV	0.06	0.27	0.36
Sand Muon	0.02	0.03	0.06
Michel Electron Tagging Efficiency	0.00	0.00	5.10
SFGD PID	0.00	0.00	2.42
Total Detector	1.78	2.45	6.65
Flux	5.01	5.12	4.90

Table 6.7: Integrated relative systematic uncertainties (in %) from each detector and flux error source, evaluated for each ν_μCC sample [13].

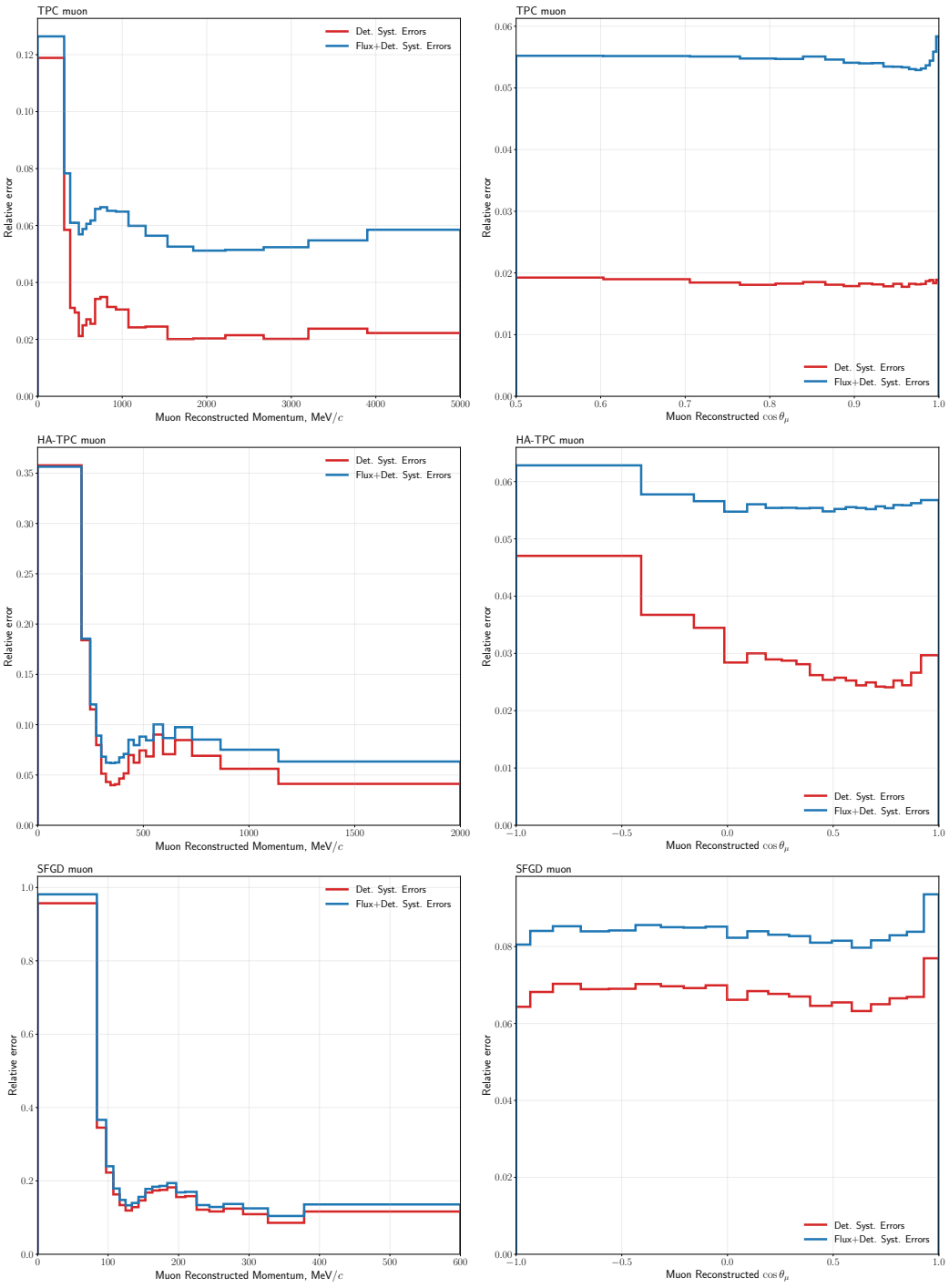


Figure 6.18: Relative systematic uncertainty on the reconstructed muon momentum (left) and $\cos\theta_\mu$ (right) for the TPC, HA-TPC and SuperFGD-contained samples. The red line is the detector-only systematics, and the blue line is the detector and flux systematics [13].

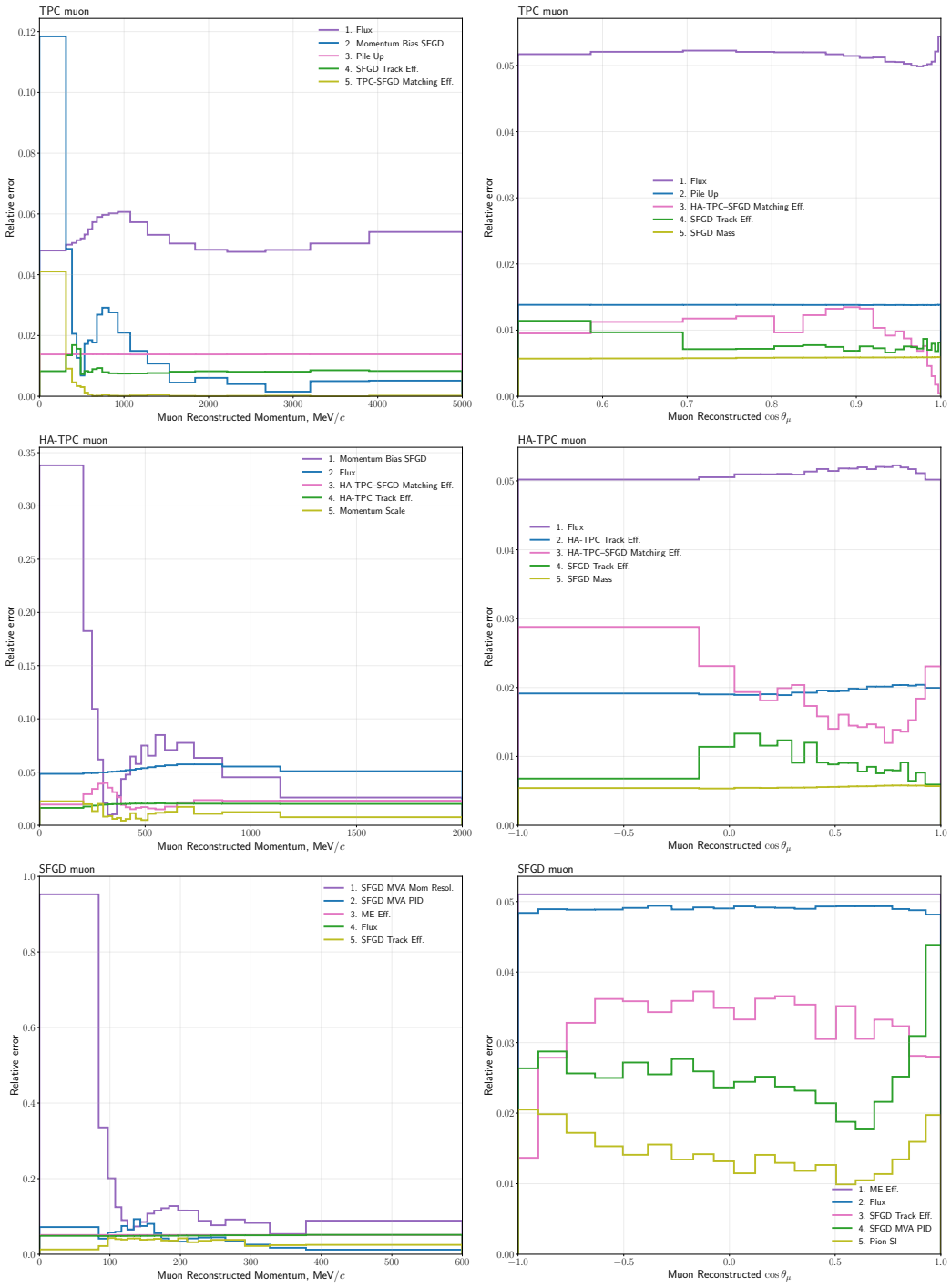


Figure 6.19: Five largest relative systematic uncertainties on the reconstructed muon momentum (left) and $\cos\theta_\mu$ (right) for the TPC, HA-TPC and SuperFGD-contained samples. The legend in each panel ranks the systematics [13].

6.6 Summary

This chapter has presented the first reconstructed-level selection of inclusive ν_μCC interactions with the upgraded ND280 detector. The inputs for this analysis are the neutrino-mode Run 13c data set of 1.574×10^{20} POT and the MC simulation provided by NEUT 5.6.4. The signal is defined as inclusive ν_μCC interactions in the SuperFGD fiducial volume. The selected muon candidates were divided into the TPC muon, HA-TPC muon, and SuperFGD-contained muon samples, according to where the candidate is reconstructed. The purity and efficiency of the selection were evaluated. Data-driven corrections were applied to the relevant detector responses, and the detector and flux systematic uncertainties were propagated to the reconstructed momentum and $\cos\theta_\mu$ distributions.

The three samples cover the outgoing-muon phase space from the forward, high-momentum region down to the low-momentum, backward-going region. The TPC muon sample selects the forward muons with good momentum reconstruction and is the purest of the three. The HA-TPC muon sample includes the high-angle tracks that motivated much of the upgrade. The SuperFGD-contained muon sample includes the low-momentum and backward-going muons that stop inside the SuperFGD. As the SuperFGD-contained muons have no TPC charge or momentum measurement, their selection relies strongly on the SuperFGD reconstruction, Michel-electron tagging, and a BDT-based particle identification, and the sample is less pure and has larger detector systematic uncertainties than the two TPC-based samples.

The data/MC agreement was further tested by performing the selection on the MC reweighted to the ND OA2024 best-fit parameters. This reweighting moves the MC closer to the data. These results are to be read as reconstructed-level checks of the selected samples. A future fit could test whether the phase-space region covered by the upgraded near-detector samples would further constrain the neutrino-interaction model.

The main limitation of the present selection is that the direction of the muon candidate is determined without the SuperFGD–ToF timing, which the `P8_v17` production does not yet provide. The track direction is instead taken to be forward-going by default from the reconstructed topology, and is corrected using the internal SuperFGD timing for sufficiently long SuperFGD segments and Michel-electron tagging for the short contained tracks. This weakens the identification of backward-going tracks and the rejection of out-of-fiducial-volume backgrounds.

Including the SuperFGD–ToF timing is the natural next step and is expected to improve the efficiency and purity in the backward-going regions. The selection and systematic uncertainty studies in this chapter also provide a starting point for exclusive cross-section measurements with the upgraded ND280 detector, and for including the upgraded near detector in T2K oscillation analyses.

Chapter 7

Conclusion

To further reduce the systematic uncertainties in the predicted neutrino event rate at Super-Kamiokande for the T2K neutrino oscillation measurement, ND280 was upgraded during the T2K–II phase, with the goal of reducing this uncertainty from 6% to about 4% [10]. The upgraded ND280 replaces the PØD detector and the central PØD-ECal module with a Super Fine-Grained Detector (SuperFGD), two High-Angle Time Projection Chambers (HA-TPCs), and six Time-of-Flight (ToF) planes. This dissertation focuses on the construction, commissioning, and calibration of the SuperFGD detector and its first physics analysis with the upgraded near detector, a selection of inclusive charged-current neutrino interactions.

The SuperFGD is the active neutrino-interaction target and three-dimensional charged-particle tracker of the upgraded ND280. After construction and commissioning, the upgraded ND280 began taking neutrino-beam data in June 2024.

Michel electron tagging in the SuperFGD was studied at the reconstruction level using a stopping-muon control sample. The muon lifetime extracted from the delayed time between the muon and the tagged Michel electron provides a test of the SuperFGD detector response and reconstruction. The tagging efficiency is $(73.53 \pm 0.60)\%$ in data and $(77.22 \pm 0.19)\%$ in MC. The data/MC difference in this efficiency is propagated as a systematic to the SuperFGD-contained muon sample in the inclusive analysis. One limitation of this study is that it uses neutrino-beam data and MC, in which the muon is identified using HA-TPC particle identification that carries an associated systematic uncertainty. A stopping-muon control sample based on cosmic-ray data would remove this uncertainty, and will be studied once the cosmic-ray Monte Carlo simulation of the upgraded near detector becomes available.

The first physics analysis with the upgraded ND280 is a reconstruction-level selection of inclusive ν_μ charged-current (CC) interactions in the SuperFGD fiducial volume. The results demonstrate the performance of the upgraded ND280 and provide a starting point for future neutrino cross-section and oscillation analyses. The analysis uses the neutrino-mode Run 13c data corresponding to 1.57×10^{20} protons on target and the MC simulation from NEUT 5.6.4. The selected sample is divided into the TPC muon, HA-TPC muon, and

SuperFGD-contained muon samples, according to where the muon produced from the neutrino interaction is reconstructed. The purity and efficiency of each sample were evaluated, and the detector and flux systematic uncertainties were propagated to the selected samples.

The flux uncertainty is about 5% for all three samples. The total detector uncertainty is 1.8% for the TPC sample, 2.5% for the HA-TPC sample, and 6.7% for the SuperFGD-contained sample. The data and MC comparison is shown in the reconstructed kinematic distributions of the selected muon candidate. We further compare data and MC by performing the selection on the MC samples with the flux and neutrino-interaction parameters reweighted to the ND OA2024 best-fit values. This reweighting moves the MC prediction closer to the data in all three samples.

The main limitation of the present selection is that the track direction is determined without the SuperFGD–ToF timing, because the `P8_v17` production does not yet provide it. The track direction is instead determined using the SuperFGD track-direction reconstruction and Michel-electron tagging. This limits the identification of backward-going tracks and the rejection of out-of-fiducial-volume backgrounds. The natural next step is to include the SuperFGD–ToF timing in the analysis, which should improve the efficiency and purity in the backward-going and low-momentum region.

In the future, the upgraded near-detector selection can be included in the T2K oscillation analysis. This will further constrain the flux and neutrino-interaction uncertainties, and improve the measurement of the neutrino oscillation parameters, in particular the CP-violating phase δ_{CP}, the mixing angles θ_{13} and θ_{23}, and the mass-squared difference Δm^2_{32}.

Bibliography

[1] T2K Collaboration. Beta decay spectrum for c-14. https://t2k-experiment.org/neutrinos/a-brief-history/betaspec/, 2021. Accessed: 2026-05-23.

[2] Cush. Standard model of elementary particles. Wikimedia Commons, 2019. URL https://commons.wikimedia.org/wiki/File:Standard_Model_of_Elementary_Particles.svg. Public domain. Accessed: 2026-05-23.

[3] J. A. Formaggio and G. P. Zeller. From eV to EeV: Neutrino Cross Sections Across Energy Scales. *Rev. Mod. Phys.*, 84:1307–1341, 2012. doi: 10.1103/RevModPhys.84.1307.

[4] L. Alvarez-Ruso et al. NuSTEC White Paper: Status and challenges of neutrino–nucleus scattering. *Prog. Part. Nucl. Phys.*, 100:1–68, 2018. doi: 10.1016/j.ppnp.2018.01.006.

[5] T2K Collaboration. Official plots and figures, 2026. Accessed 2026.

[6] J-PARC. Neutrino experimental facility. https://j-parc.jp/c/en/facilities/nuclear-and-particle-physics/neutrino.html, 2019. Accessed: 2026-07-15.

[7] K. Abe et al. Measurements of the T2K neutrino beam properties using the INGRID on-axis near detector. *Nucl. Instrum. Meth. A*, 694:211–223, 2012. doi: 10.1016/j.nima.2012.03.023.

[8] K. Abe et al. The T2K Experiment. *Nucl. Instrum. Meth. A*, 659:106–135, 2011. doi: 10.1016/j.nima.2011.06.067.

[9] Y. Fukuda et al. The Super-Kamiokande detector. *Nucl. Instrum. Meth. A*, 501:418–462, 2003. doi: 10.1016/S0168-9002(03)00425-X.

[10] K. Abe et al. T2K ND280 Upgrade - Technical Design Report. 1 2019.

[11] Dana Douqa. The SuperFGD for the T2K near detector upgrade. *J. Phys. Conf. Ser.*, 1690(1):012070, 2020. doi: 10.1088/1742-6596/1690/1/012070.

[12] S. Abe et al. The super fine-grained detector for the T2K neutrino oscillation experiment. *Nucl. Instrum. Meth. A*, 1092:171882, 2026. doi: 10.1016/j.nima.2026.171882.

[13] S. Arimoto, N. Baudis, M. P. Casado, A. Chalumeau, et al. Measurement of ν_μ Charged-Current Inclusive Interactions with Upgraded ND280. Technical Report T2K-TN-525, May 2026.

[14] Ivan Esteban, M. C. Gonzalez-Garcia, Michele Maltoni, Ivan Martinez-Soler, João Paulo Pinheiro, and Thomas Schwetz. NuFit-6.0: updated global analysis of three-flavor neutrino oscillations. *JHEP*, 12:216, 2024. doi: 10.1007/JHEP12(2024)216.

[15] J. Chadwick. The intensity distribution in the magnetic spectrum of β particles from radium (B + C). *Verh. Phys. Gesell.*, 16:383–391, 1914.

[16] Wolfgang Pauli. Pauli letter collection: letter to Lise Meitner. Typed copy, CERN Document Server, December 1930. URL `https://cds.cern.ch/record/83282`. Reference code: meitner_0393; accessed 2026-05-23.

[17] F. Reines and C. L. Cowan. Detection of the free neutrino. *Phys. Rev.*, 92:830–831, 1953. doi: 10.1103/PhysRev.92.830.

[18] C. L. Cowan, F. Reines, F. B. Harrison, H. W. Kruse, and A. D. McGuire. Detection of the free neutrino: A Confirmation. *Science*, 124:103–104, 1956. doi: 10.1126/science.124.3212.103.

[19] G. Danby, J. M. Gaillard, Konstantin A. Goulianos, L. M. Lederman, Nari B. Mistry, M. Schwartz, and J. Steinberger. Observation of High-Energy Neutrino Reactions and the Existence of Two Kinds of Neutrinos. *Phys. Rev. Lett.*, 9:36–44, 1962. doi: 10.1103/PhysRevLett.9.36.

[20] Martin L. Perl et al. Evidence for Anomalous Lepton Production in e+ - e- Annihilation. *Phys. Rev. Lett.*, 35:1489–1492, 1975. doi: 10.1103/PhysRevLett.35.1489.

[21] K. Kodama et al. Observation of tau neutrino interactions. *Phys. Lett. B*, 504:218–224, 2001. doi: 10.1016/S0370-2693(01)00307-0.

[22] S. Schael et al. Precision electroweak measurements on the Z resonance. *Phys. Rept.*, 427:257–454, 2006. doi: 10.1016/j.physrep.2005.12.006.

[23] Georges Aad et al. Observation of a new particle in the search for the Standard Model Higgs boson with the ATLAS detector at the LHC. *Phys. Lett. B*, 716:1–29, 2012. doi: 10.1016/j.physletb.2012.08.020.

[24] Serguei Chatrchyan et al. Observation of a New Boson at a Mass of 125 GeV with the CMS Experiment at the LHC. *Phys. Lett. B*, 716:30–61, 2012. doi: 10.1016/j.physletb.2012.08.021.

[25] Raymond Davis, Jr., Don S. Harmer, and Kenneth C. Hoffman. Search for neutrinos from the sun. *Phys. Rev. Lett.*, 20:1205–1209, 1968. doi: 10.1103/PhysRevLett.20.1205.

[26] John N. Bahcall, Neta A. Bahcall, and G. Shaviv. Present status of the theoretical predictions for the Cl-36 solar neutrino experiment. *Phys. Rev. Lett.*, 20:1209–1212, 1968. doi: 10.1103/PhysRevLett.20.1209.

[27] K. S. Hirata et al. Observation of B-8 Solar Neutrinos in the Kamiokande-II Detector. *Phys. Rev. Lett.*, 63:16, 1989. doi: 10.1103/PhysRevLett.63.16.

[28] P. Anselmann et al. Solar neutrinos observed by GALLEX at Gran Sasso. *Phys. Lett. B*, 285:376–389, 1992. doi: 10.1016/0370-2693(92)91521-A.

[29] J. N. Abdurashitov et al. Results from SAGE. *Phys. Lett. B*, 328:234–248, 1994. doi: 10.1016/0370-2693(94)90454-5.

[30] B. Pontecorvo. Mesonium and Antimesonium. *Sov. Phys. JETP*, 6:429–431, 1958.

[31] V. N. Gribov and B. Pontecorvo. Neutrino astronomy and lepton charge. *Phys. Lett. B*, 28:493, 1969. doi: 10.1016/0370-2693(69)90525-5.

[32] Y. Fukuda et al. Evidence for oscillation of atmospheric neutrinos. *Phys. Rev. Lett.*, 81:1562–1567, 1998. doi: 10.1103/PhysRevLett.81.1562.

[33] Y. Ashie et al. Evidence for an oscillatory signature in atmospheric neutrino oscillation. *Phys. Rev. Lett.*, 93:101801, 2004. doi: 10.1103/PhysRevLett.93.101801.

[34] Q. R. Ahmad et al. Measurement of the rate of $\nu_e + d \rightarrow p + p + e^-$ interactions produced by ^{8}B solar neutrinos at the Sudbury Neutrino Observatory. *Phys. Rev. Lett.*, 87:071301, 2001. doi: 10.1103/PhysRevLett.87.071301.

[35] A. B. McDonald et al. Direct evidence for neutrino flavor transformation from neutral-current interactions in SNO. *AIP Conf. Proc.*, 646(1):43–58, 2002. doi: 10.1063/1.1524553.

[36] K. Eguchi et al. First results from KamLAND: Evidence for reactor anti-neutrino disappearance. *Phys. Rev. Lett.*, 90:021802, 2003. doi: 10.1103/PhysRevLett.90.021802.

[37] Ziro Maki, Masami Nakagawa, and Shoichi Sakata. Remarks on the unified model of elementary particles. *Prog. Theor. Phys.*, 28:870–880, 1962. doi: 10.1143/PTP.28.870.

[38] Claudio Giganti, Stéphane Lavignac, and Marco Zito. Neutrino oscillations: The rise of the PMNS paradigm. *Prog. Part. Nucl. Phys.*, 98:1–54, 2018. doi: 10.1016/j.ppnp.2017.10.001.

[39] L. Wolfenstein. Neutrino Oscillations in Matter. *Phys. Rev. D*, 17:2369–2374, 1978. doi: 10.1103/PhysRevD.17.2369.

[40] S. P. Mikheev and A. Yu. Smirnov. Resonant amplification of neutrino oscillations in matter and solar neutrino spectroscopy. *Nuovo Cim. C*, 9:17–26, 1986. doi: 10.1007/BF02508049.

[41] K. Abe et al. Measurements of neutrino oscillation parameters from the T2K experiment using 3.6×10^{21} protons on target. *Eur. Phys. J. C*, 83(9):782, 2023. doi: 10.1140/epjc/s10052-023-11819-x.

[42] M. A. Acero et al. Improved measurement of neutrino oscillation parameters by the NOvA experiment. *Phys. Rev. D*, 106(3):032004, 2022. doi: 10.1103/PhysRevD.106.032004.

[43] B. Abi et al. Deep Underground Neutrino Experiment (DUNE), Far Detector Technical Design Report, Volume I: Introduction to DUNE. *JINST*, 15:T08008, 2020. doi: 10.1088/1748-0221/15/08/T08008.

[44] K. Abe et al. Hyper-Kamiokande Design Report. 5 2018.

[45] Zelimir Djurcic et al. JUNO Conceptual Design Report. 8 2015.

[46] R. A. Smith and E. J. Moniz. NEUTRINO REACTIONS ON NUCLEAR TARGETS. *Nucl. Phys. B*, 43:605, 1972. doi: 10.1016/0550-3213(75)90612-4. [Erratum: Nucl.Phys.B 101, 547 (1975)].

[47] M. Martini, M. Ericson, G. Chanfray, and J. Marteau. A unified approach for nucleon knock-out, coherent and incoherent pion production in neutrino interactions with nuclei. *Phys. Rev. C*, 80:065501, 2009. doi: 10.1103/PhysRevC.80.065501.

[48] J. Nieves, I. Ruiz Simo, and M. J. Vicente Vacas. Inclusive charged-current neutrino-nucleus reactions. *Phys. Rev. C*, 83:045501, 2011. doi: 10.1103/PhysRevC.83.045501.

[49] K. Abe et al. T2K neutrino flux prediction. *Phys. Rev. D*, 87(1):012001, 2013. doi: 10.1103/PhysRevD.87.012001. [Addendum: Phys.Rev.D 87, 019902 (2013)].

[50] Giuseppe Battistoni, S. Muraro, Paola R. Sala, Fabio Cerutti, A. Ferrari, Stefan Roesler, A. Fasso, and J. Ranft. The FLUKA code: Description and benchmarking. *AIP Conf. Proc.*, 896(1):31–49, 2007. doi: 10.1063/1.2720455.

[51] Alfredo Ferrari, Paola R. Sala, Alberto Fasso, and Johannes Ranft. FLUKA: A multi-particle transport code (Program version 2005). 10 2005. doi: 10.2172/877507.

[52] René Brun, F. Bruyant, Federico Carminati, Simone Giani, M. Maire, A. McPherson, G. Patrick, and L. Urban. GEANT Detector Description and Simulation Tool. 10 1994. doi: 10.17181/CERN.MUHF.DMJ1.

[53] N Abgrall et al. Measurements of Cross Sections and Charged Pion Spectra in Proton-Carbon Interactions at 31 GeV/c. *Phys. Rev. C*, 84:034604, 2011. doi: 10.1103/PhysRevC.84.034604.

[54] N. Abgrall et al. Pion emission from the T2K replica target: method, results and application. *Nucl. Instrum. Meth. A*, 701:99–114, 2013. doi: 10.1016/j.nima.2012.10.079.

[55] Lukas Berns. et al. Flux Prediction and Uncertainty with NA61/SHINE 2010 Replica Target Measurements (TN-401, v1.2). *T2K-TN-401*, page 120, 2022.

[56] S. Assylbekov et al. The T2K ND280 Off-Axis Pi-Zero Detector. *Nucl. Instrum. Meth. A*, 686:48–63, 2012. doi: 10.1016/j.nima.2012.05.028.

[57] P. A. Amaudruz et al. The T2K Fine-Grained Detectors. *Nucl. Instrum. Meth. A*, 696: 1–31, 2012. doi: 10.1016/j.nima.2012.08.020.

[58] N. Abgrall et al. Time Projection Chambers for the T2K Near Detectors. *Nucl. Instrum. Meth. A*, 637:25–46, 2011. doi: 10.1016/j.nima.2011.02.036.

[59] D. Allan et al. The Electromagnetic Calorimeter for the T2K Near Detector ND280. *JINST*, 8:P10019, 2013. doi: 10.1088/1748-0221/8/10/P10019.

[60] S. Aoki et al. The T2K Side Muon Range Detector (SMRD). *Nucl. Instrum. Meth. A*, 698:135–146, 2013. doi: 10.1016/j.nima.2012.10.001.

[61] K. Abe et al. First gadolinium loading to Super-Kamiokande. *Nucl. Instrum. Meth. A*, 1027:166248, 2022. doi: 10.1016/j.nima.2021.166248.

[62] K. Abe et al. Second gadolinium loading to Super-Kamiokande. *Nucl. Instrum. Meth. A*, 1065:169480, 2024. doi: 10.1016/j.nima.2024.169480.

[63] GUNDAM Organization. Gundam: A statistical fitting framework. `https://github.com/gundam-organization/gundam`. Accessed: 2026-04-07.

[64] Samira Hassani and Jean-Francois Laporte. Characterization of Charge Spreading and Gain of Encapsulated Resistive Micromegas Detectors for the Upgrade of the T2K Near Detector Time Projection Chambers. *PoS*, ICHEP2024:1063, 2025. doi: 10.22323/1.476.1063.

[65] Emanuele Villa. *Novel Technologies for Next-Generation Neutrino Experiments: Time-of-Flight Detector for T2K ND280, Beam Monitor for ProtoDUNE, and Online Supernova Pointing in DUNE*. Phd thesis, University of Geneva, 2025.

[66] Yoshinari Hayato and Luke Pickering. The NEUT neutrino interaction simulation program library. *Eur. Phys. J. ST*, 230(24):4469–4481, 2021. doi: 10.1140/epjs/s11734-021-00287-7.

[67] S. Agostinelli et al. GEANT4 - A Simulation Toolkit. *Nucl. Instrum. Meth. A*, 506: 250–303, 2003. doi: 10.1016/S0168-9002(03)01368-8.

[68] P. Billoir, C. Giganti, M. Guigue, et al. HA-TPC Simulation and Reconstruction. Technical Report T2K-TN-466, 2023.

[69] A. Blondel et al. A fully active fine grained detector with three readout views. *JINST*, 13(02):P02006, 2018. doi: 10.1088/1748-0221/13/02/P02006.

[70] Hamamatsu Photonics K.K. *Datasheet for S13360 Series MPPCs*. Hamamatsu Photonics K.K. URL `https://www.hamamatsu.com/content/dam/hamamatsu-photonics/sites/documents/99_SALES_LIBRARY/ssd/s13360_series_kapd1052e.pdf`. Accessed: 2026-05-07.

[71] M. Antonova et al. Baby MIND: A Magnetized Segmented Neutrino Detector for the WAGASCI Experiment. *JINST*, 12(07):C07028, 2017. doi: 10.1088/1748-0221/12/07/C07028.

[72] WEEROC. *CITIROC1A Datasheet*. WEEROC, 2019. URL `https://www.weeroc.com/read_out_chips/citiroc-1a/`. Accessed: 2026-05-09.

[73] C McGrew. Pattern Recognition for the SuperFGD. Technical Report T2K-TN-431, 2022.

[74] X Zhao. SFGD Track PID and Momentum Reconstruction. Technical Report T2K-TN-491, 2025.

[75] J. Allison et al. Recent developments in Geant4. *Nucl. Instrum. Meth. A*, 835:186–225, 2016. doi: 10.1016/j.nima.2016.06.125.

[76] John Allison et al. Geant4 developments and applications. *IEEE Trans. Nucl. Sci.*, 53: 270, 2006. doi: 10.1109/TNS.2006.869826.

[77] J.-B. Plançon, M. Buizza Avanzini, et al. Validation of the 320 kA flux with the NuMu MultiPi selection using run13c and run8air data. Technical Report T2K-TN-524, 2026.

[78] C. Bronner, S. Dolan, T. Holvey, et al. NIWG Model and Uncertainty Recommendation for the 2024 Oscillation Analysis. Technical Report T2K-TN-493, May 2024.

[79] P. Bartet, S. Bordoni, R. Castillo, G. Catanesi, et al. ν_μ CC event selections in the ND280 tracker using Run 2+3+4 data. Technical Report T2K-TN-212, 2015.

[80] E. Atkin et al. OAR11B Physics Analysis Summary for the Near Detector. Technical Report T2K-TN-498, 2024-2026.

[81] A. Blanchet et al. GUNDAM: Generalized and Unified Neutrino Data Analysis Methods. Technical Report T2K-TN-458.

[82] J. Ji et al. The Markov Chain Monte Carlo Algorithm in GUNDAM. Technical Report T2K-TN-476.

[83] T. Doyle et al. Constraining the flux and cross-section models for the 2021 oscillation analysis using ND280 data. Technical Report T2K-TN-423.

[84] Nicholas Metropolis, Arianna W. Rosenbluth, Marshall N. Rosenbluth, Augusta H. Teller, and Edward Teller. Equation of State Calculations by Fast Computing Machines. *The Journal of Chemical Physics*, 21(6):1087–1092, 1953. doi: 10.1063/1.1699114.

[85] Christophe Andrieu and Johannes Thoms. A tutorial on adaptive MCMC. *Statistics and Computing*, 18(4):343–373, 2008. doi: 10.1007/s11222-008-9110-y.

[86] Gareth O. Roberts, Andrew Gelman, and Walter R. Gilks. Weak convergence and optimal scaling of random walk Metropolis algorithms. *Annals of Applied Probability*, 7(1):110–120, 1997. doi: 10.1214/aoap/1034625254.

[87] Clark McGrew. TSimpleMCMC: A simple MCMC template for use with ROOT. `https://github.com/ClarkMcGrew/root-simple-mcmc`. Accessed: 2026-06-20.

[88] Andrew Gelman, John B. Carlin, Hal S. Stern, David B. Dunson, Aki Vehtari, and Donald B. Rubin. *Bayesian Data Analysis*. Chapman and Hall/CRC, Boca Raton, FL, third edition, 2014.

Appendix A

Impact of Individual Systematic Uncertainties

This appendix collects the impact of each individual systematic uncertainty on the selected samples. In every figure the relative systematic uncertainty is shown as a function of the reconstructed muon momentum (left) and $\cos\theta_\mu$ (right) for the TPC, HA-TPC and SuperFGD-contained muon samples (top to bottom). The variation-type systematics are shown first, followed by the weight-like detector and flux systematics.

A.1 Variation-type systematics

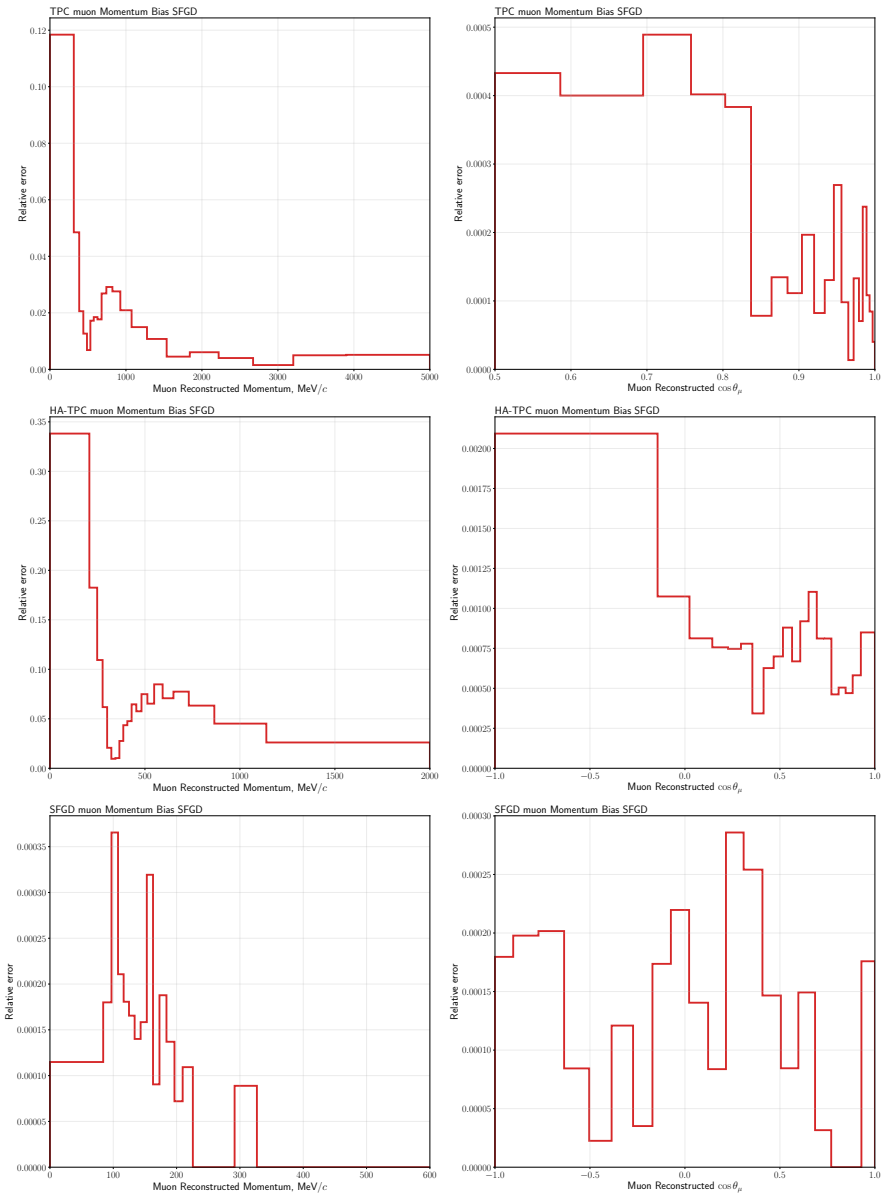


Figure A.1: Relative systematic uncertainty from the SuperFGD momentum bias [13].

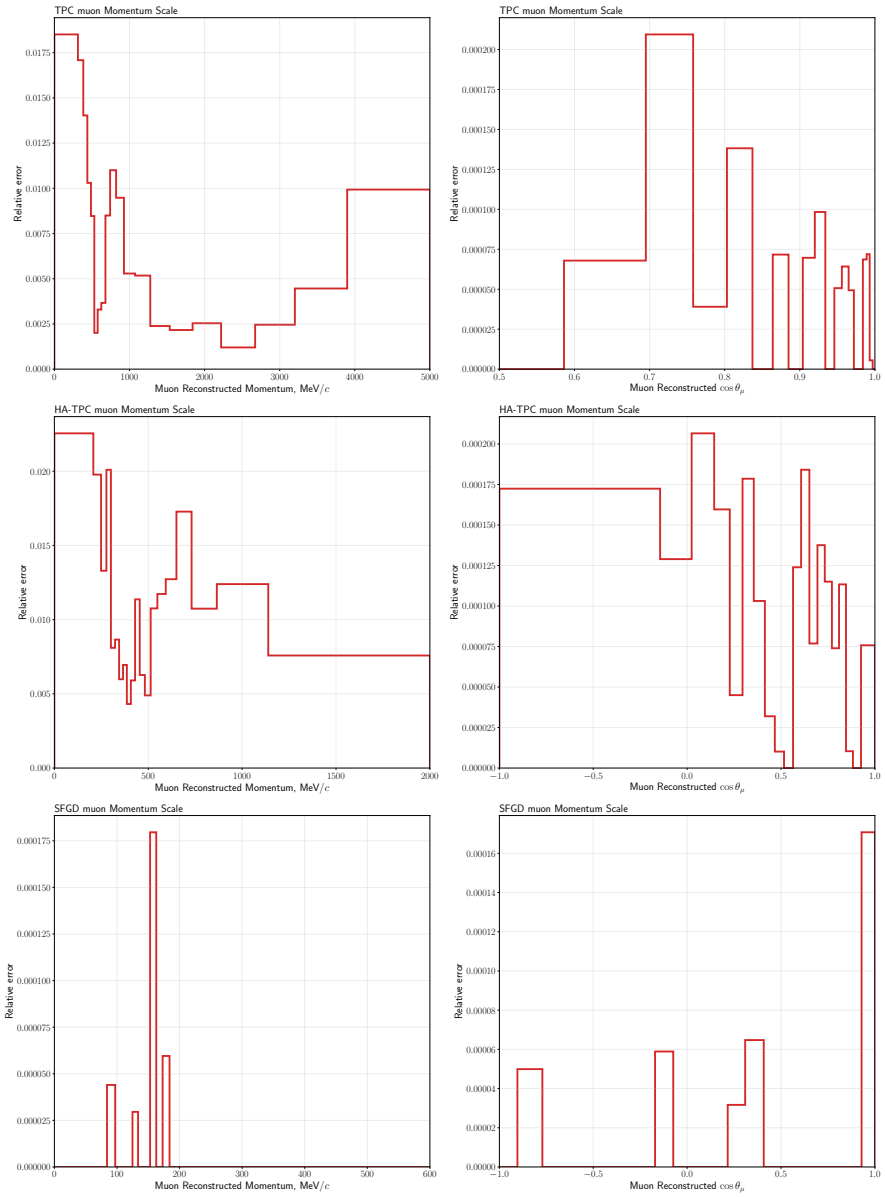


Figure A.2: Relative systematic uncertainty from the momentum scale [13].

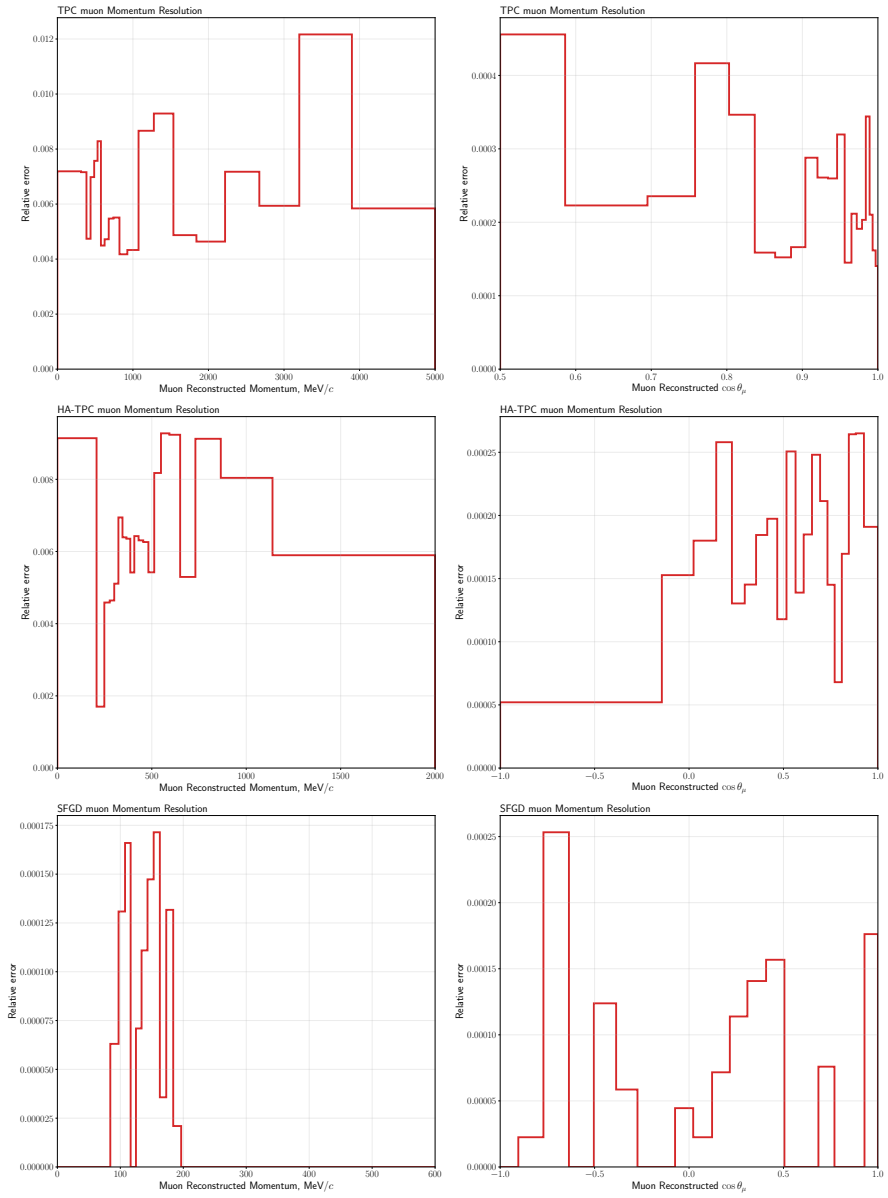


Figure A.3: Relative systematic uncertainty from the momentum resolution [13].

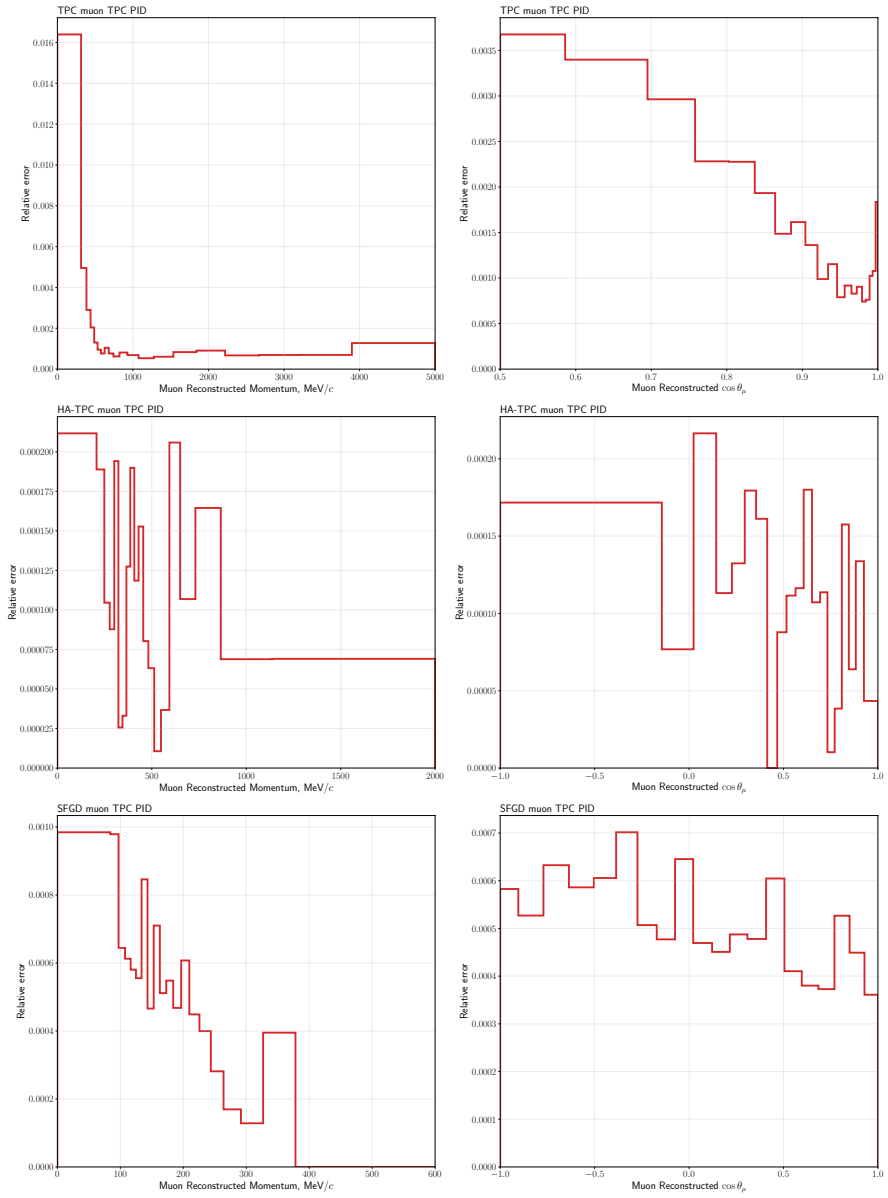


Figure A.4: Relative systematic uncertainty from the TPC PID [13].

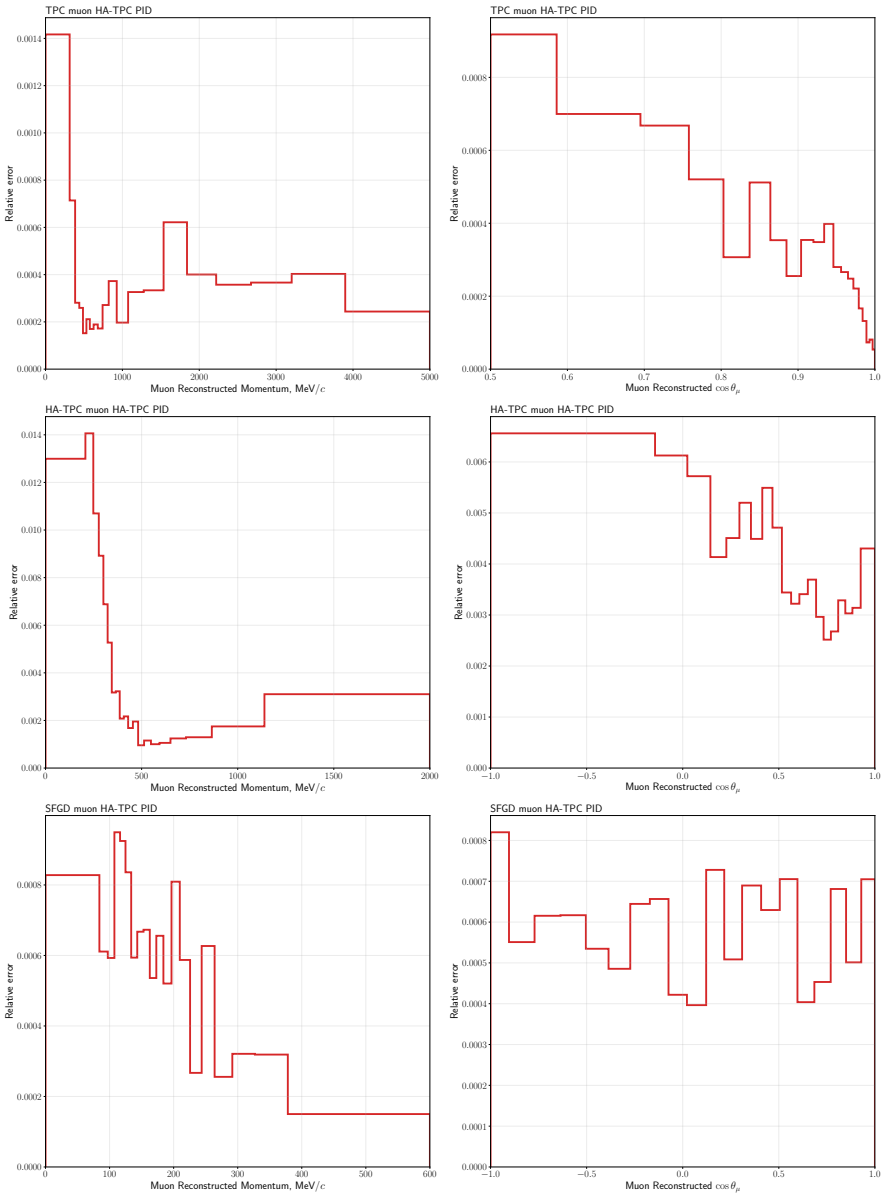


Figure A.5: Relative systematic uncertainty from the HA-TPC PID [13].

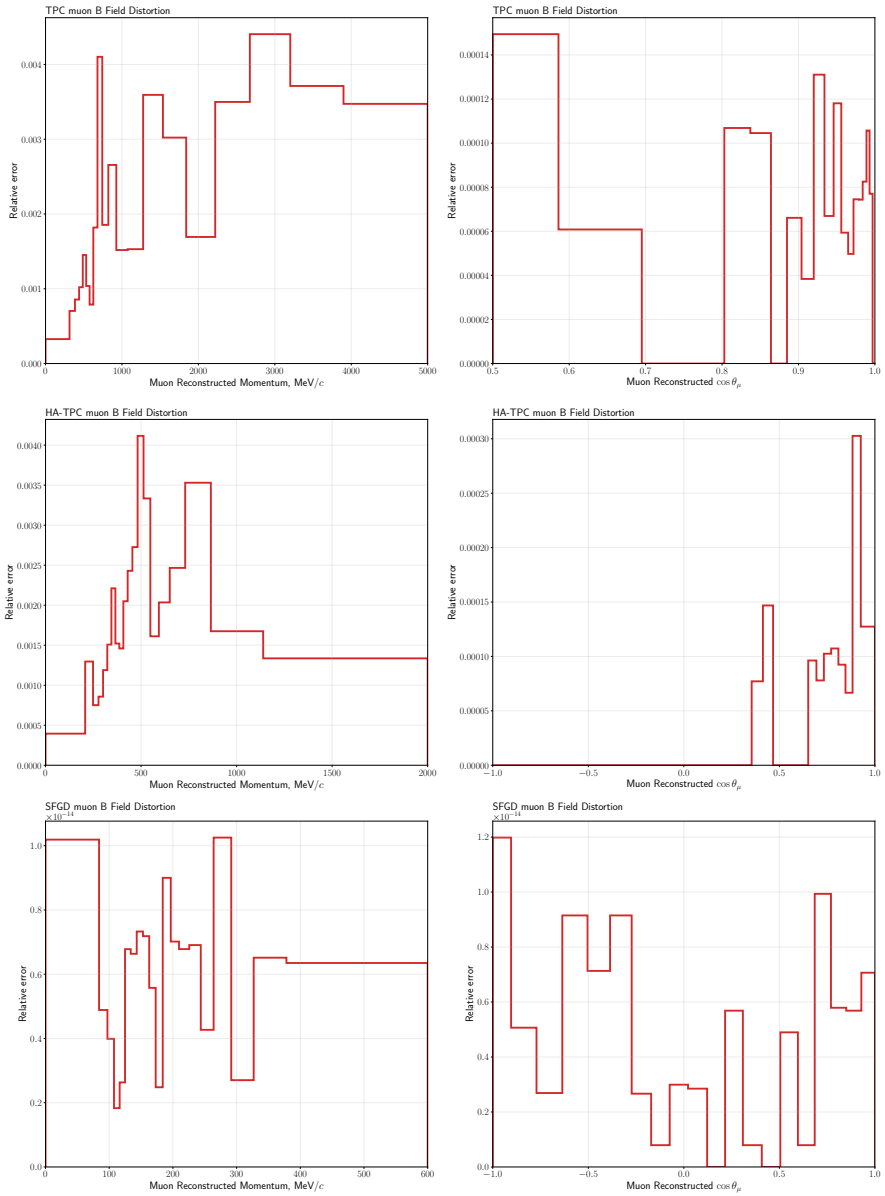


Figure A.6: Relative systematic uncertainty from the magnetic-field distortion [13].

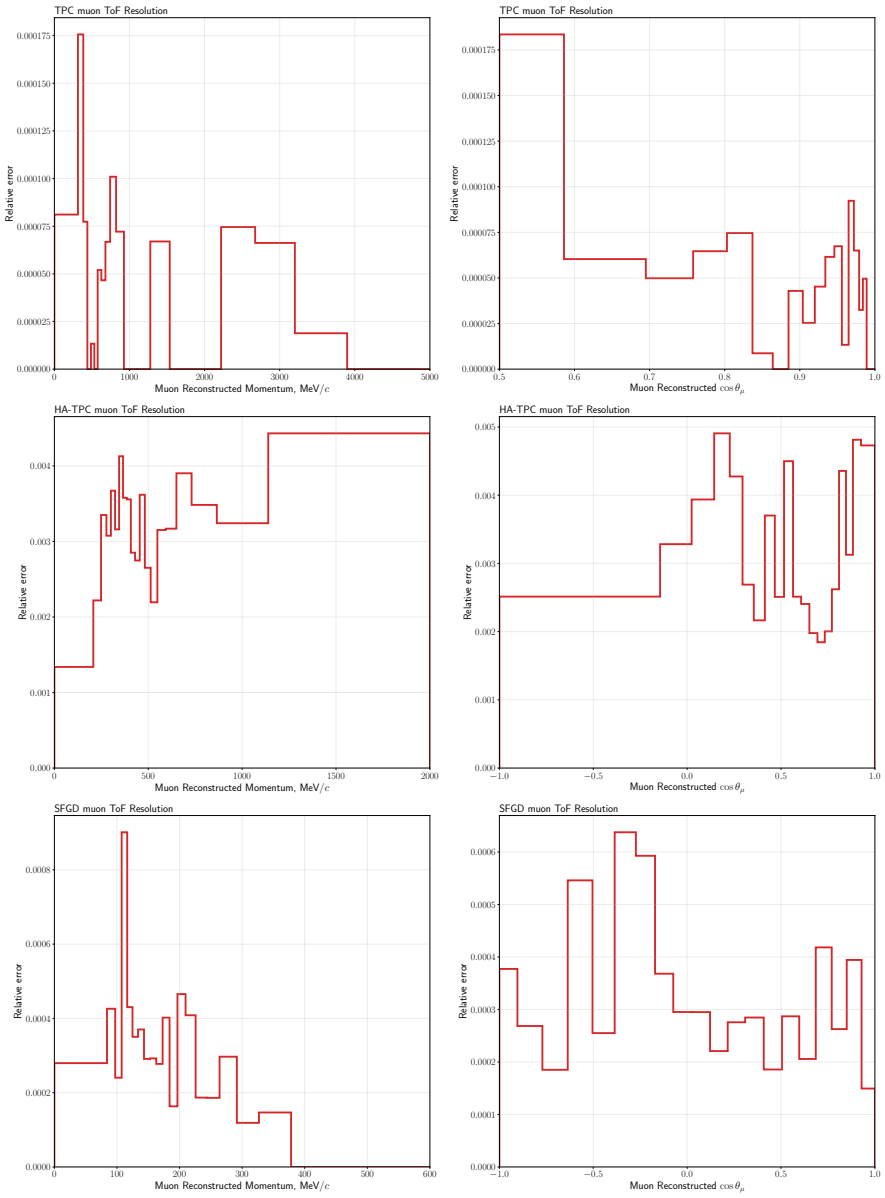


Figure A.7: Relative systematic uncertainty from the ToF resolution [13].

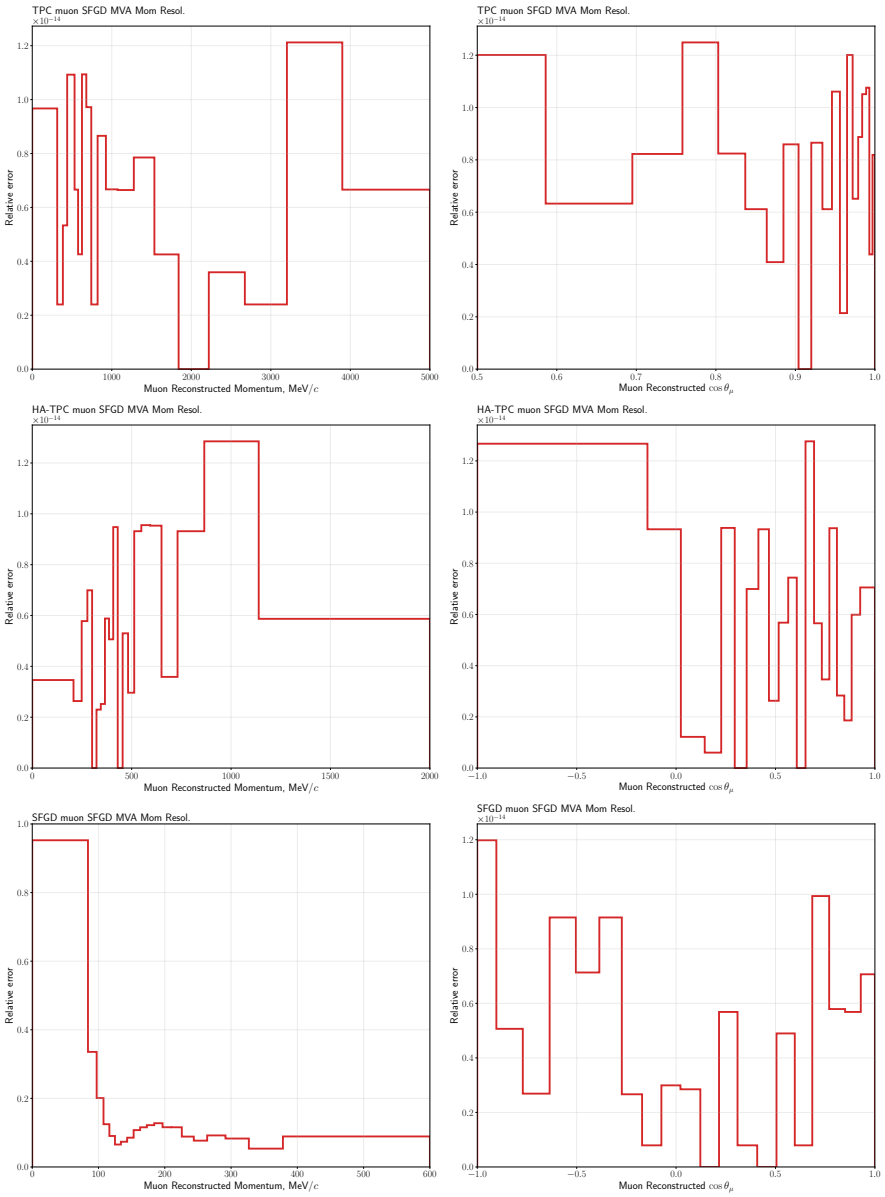


Figure A.8: Relative systematic uncertainty from the SuperFGD momentum resolution [13].

A.2 Weight-like systematics

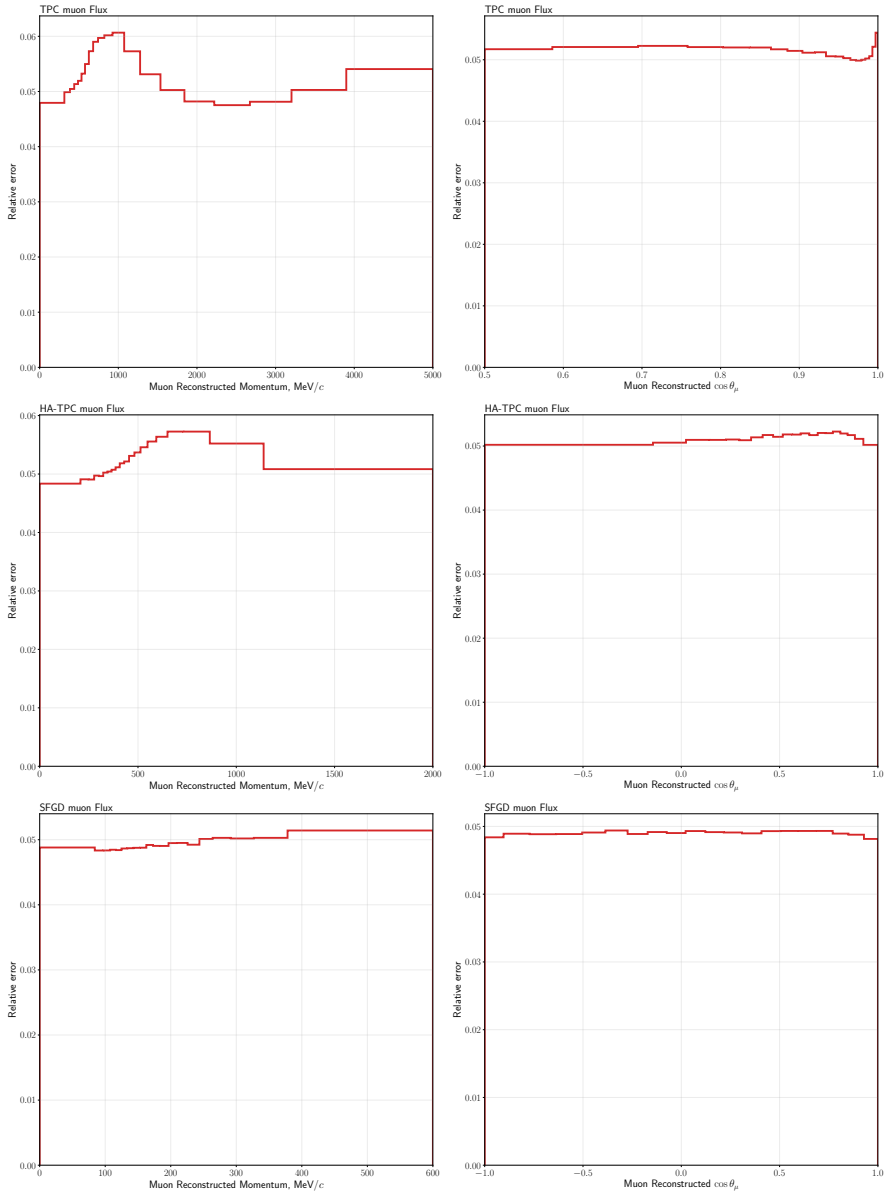


Figure A.9: Relative systematic uncertainty from the flux [13].

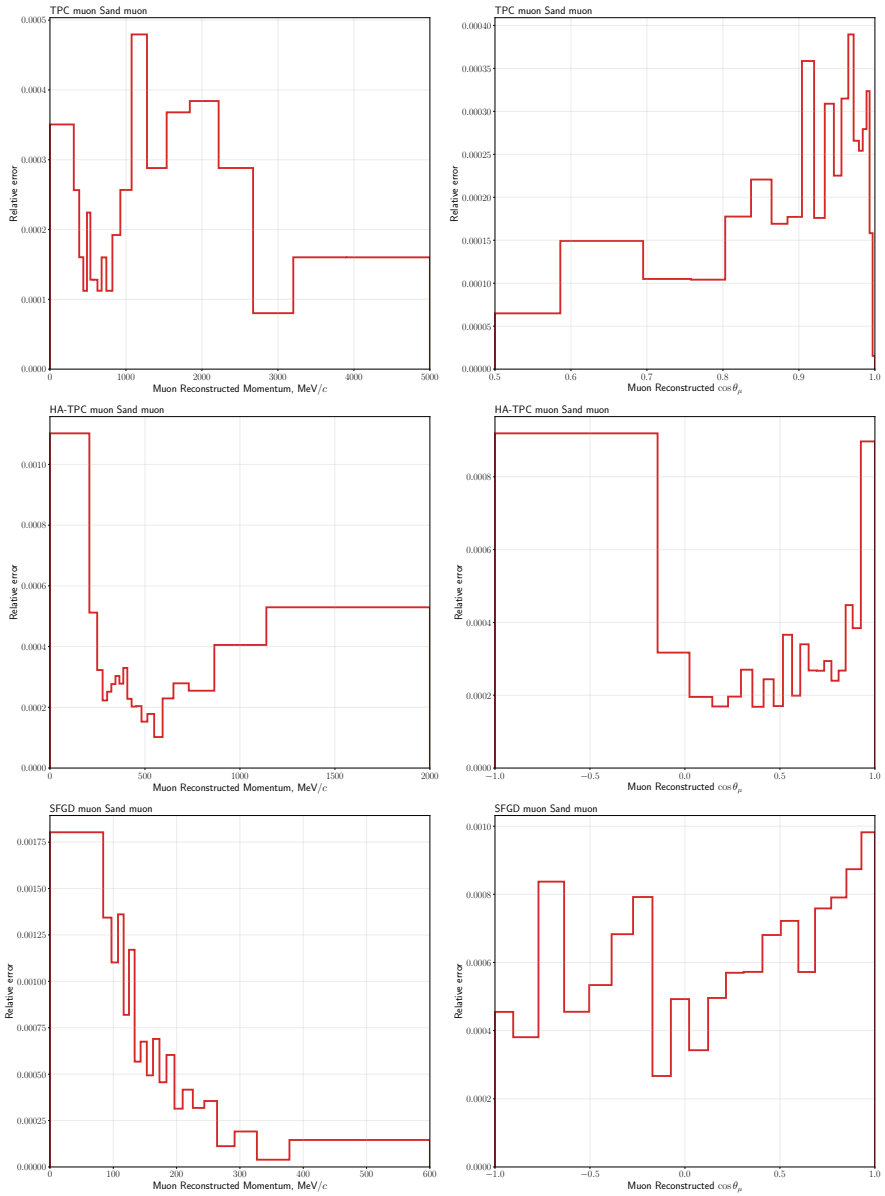


Figure A.10: Relative systematic uncertainty from the sand-muon background [13].

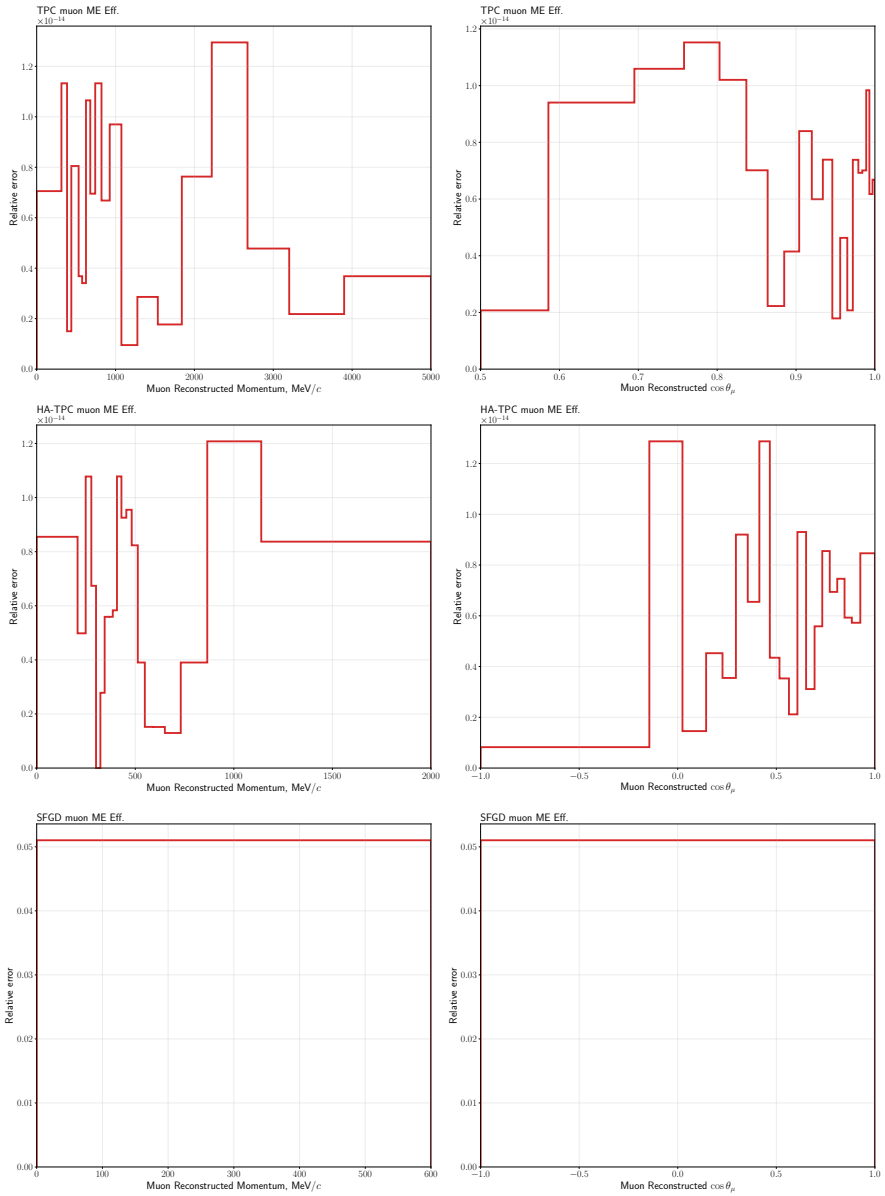


Figure A.11: Relative systematic uncertainty from the Michel-electron tagging efficiency [13].

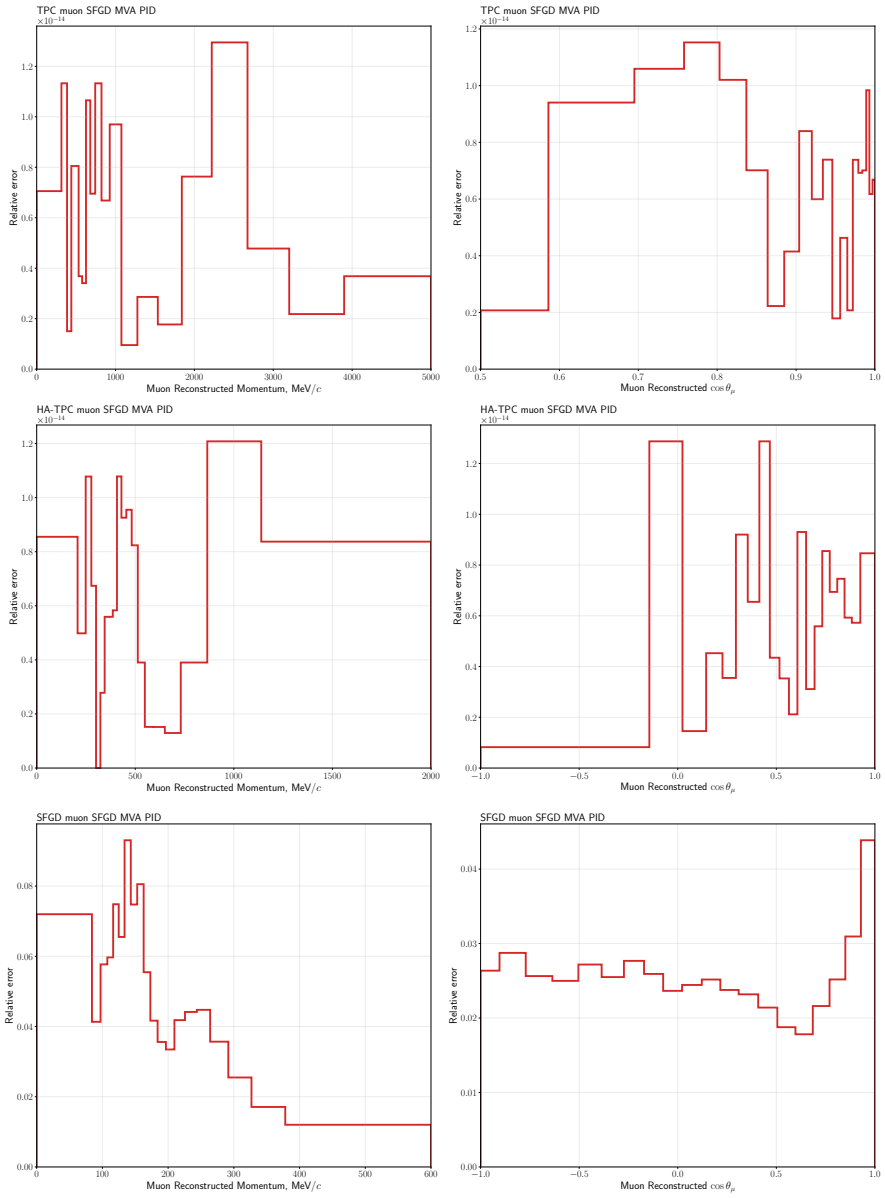


Figure A.12: Relative systematic uncertainty from the SuperFGD PID [13].

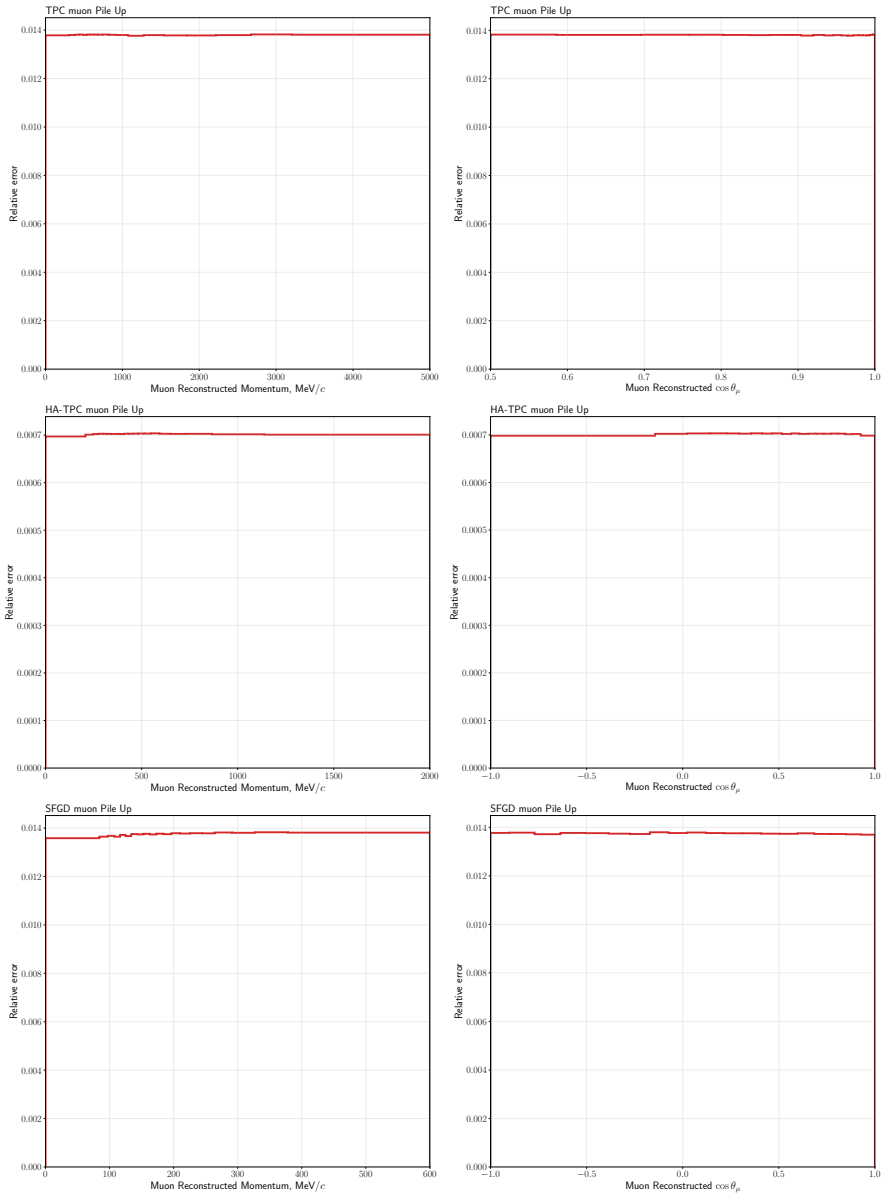


Figure A.13: Relative systematic uncertainty from the pile-up [13].

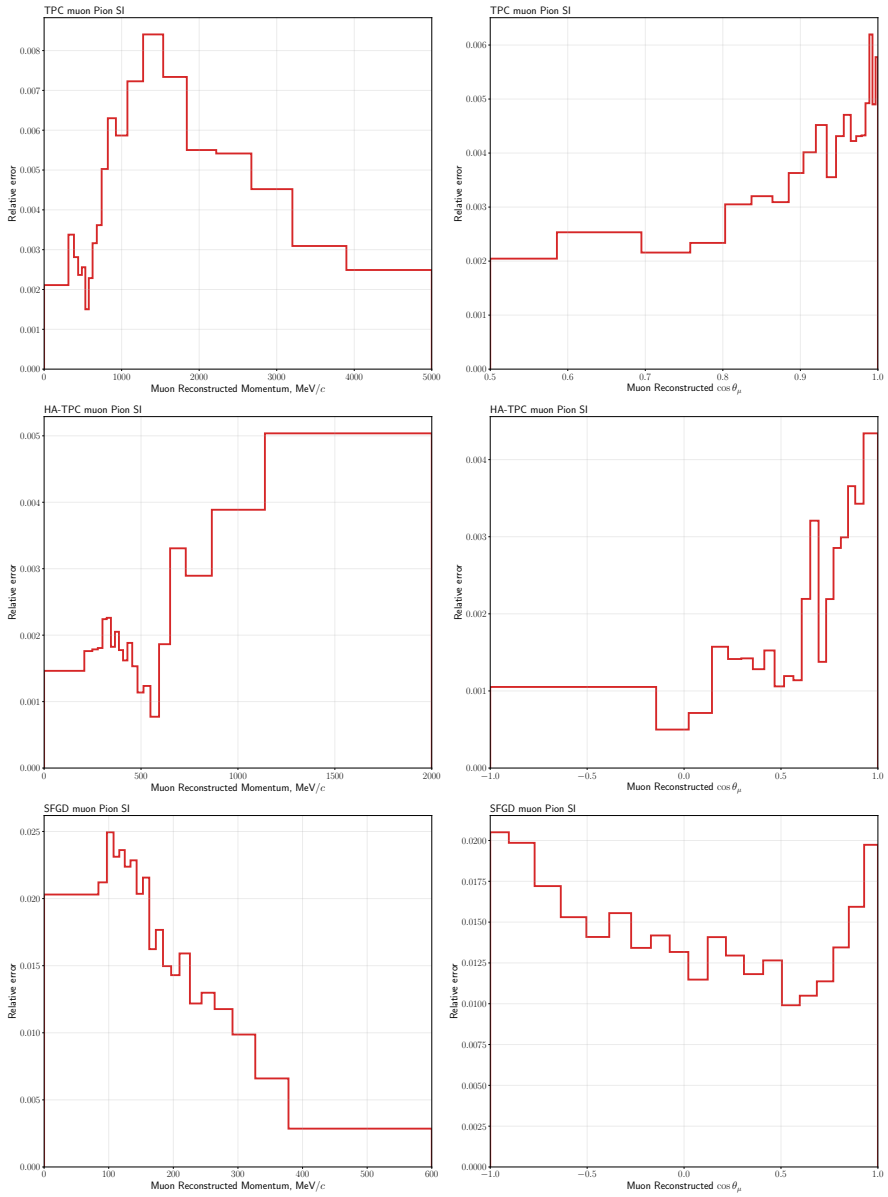


Figure A.14: Relative systematic uncertainty from the pion secondary interactions [13].

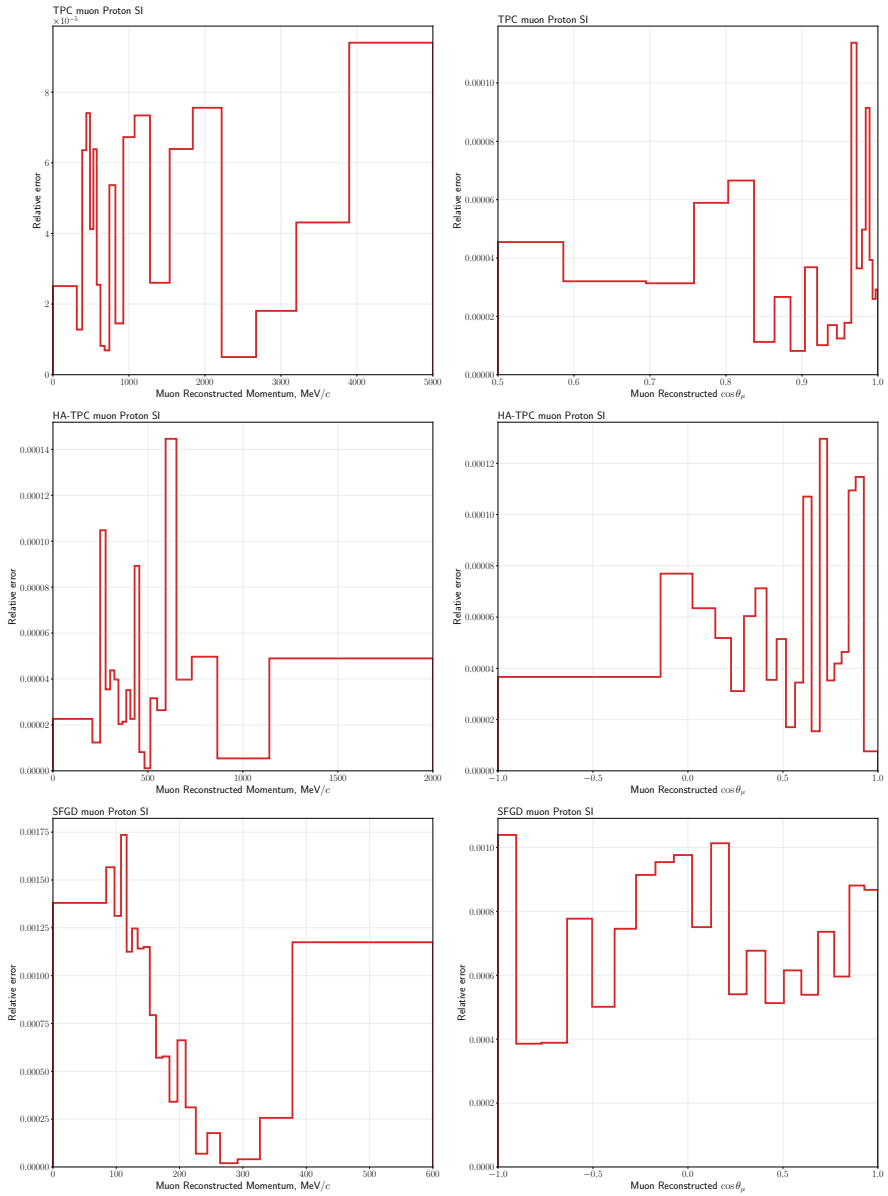


Figure A.15: Relative systematic uncertainty from the proton secondary interactions [13].

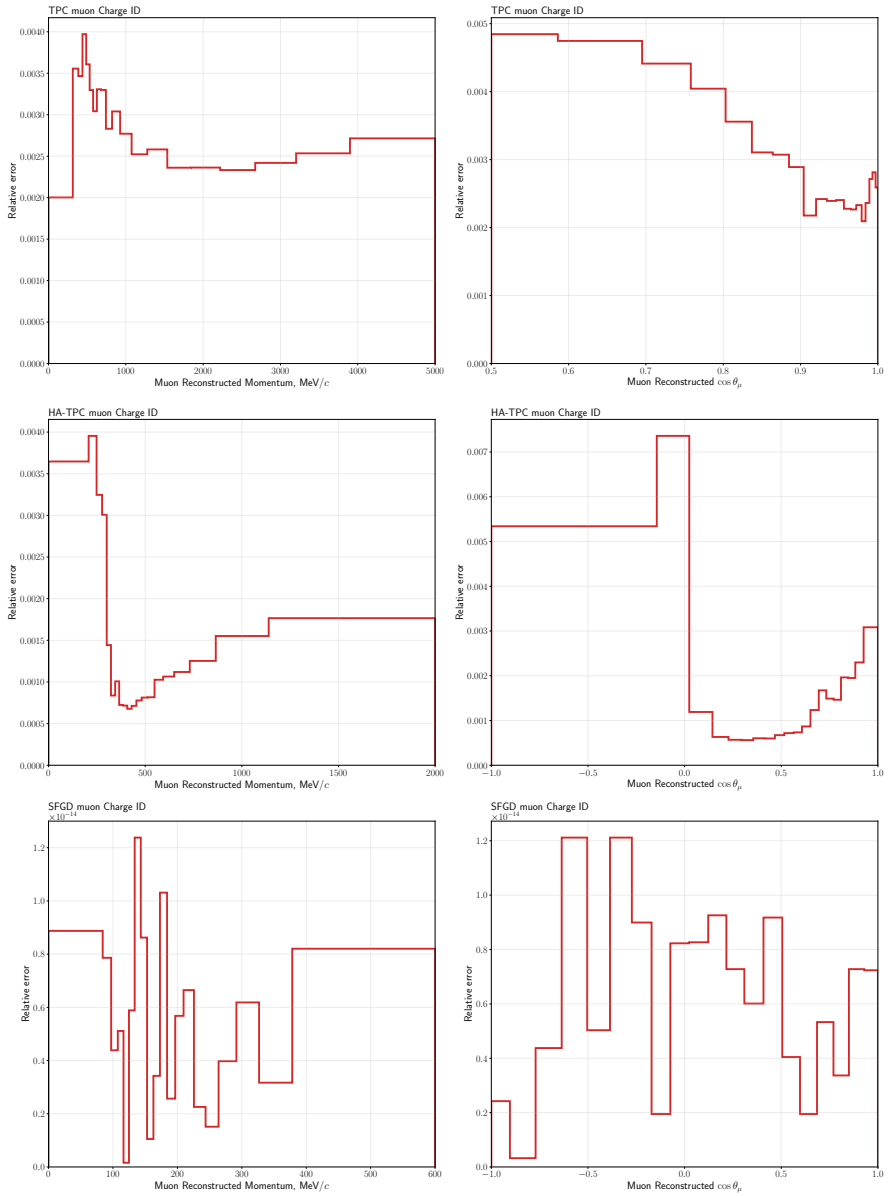


Figure A.16: Relative systematic uncertainty from the charge identification [13].

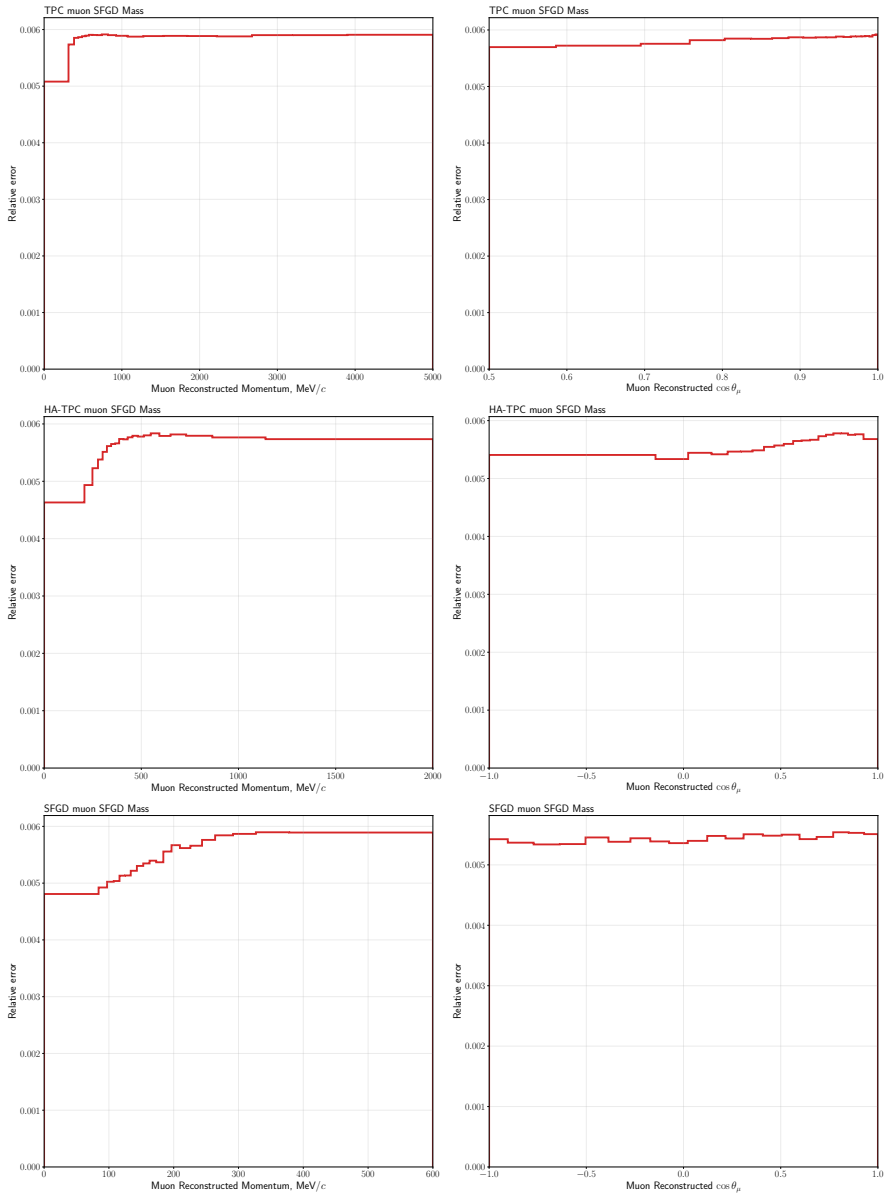


Figure A.17: Relative systematic uncertainty from the SuperFGD mass [13].

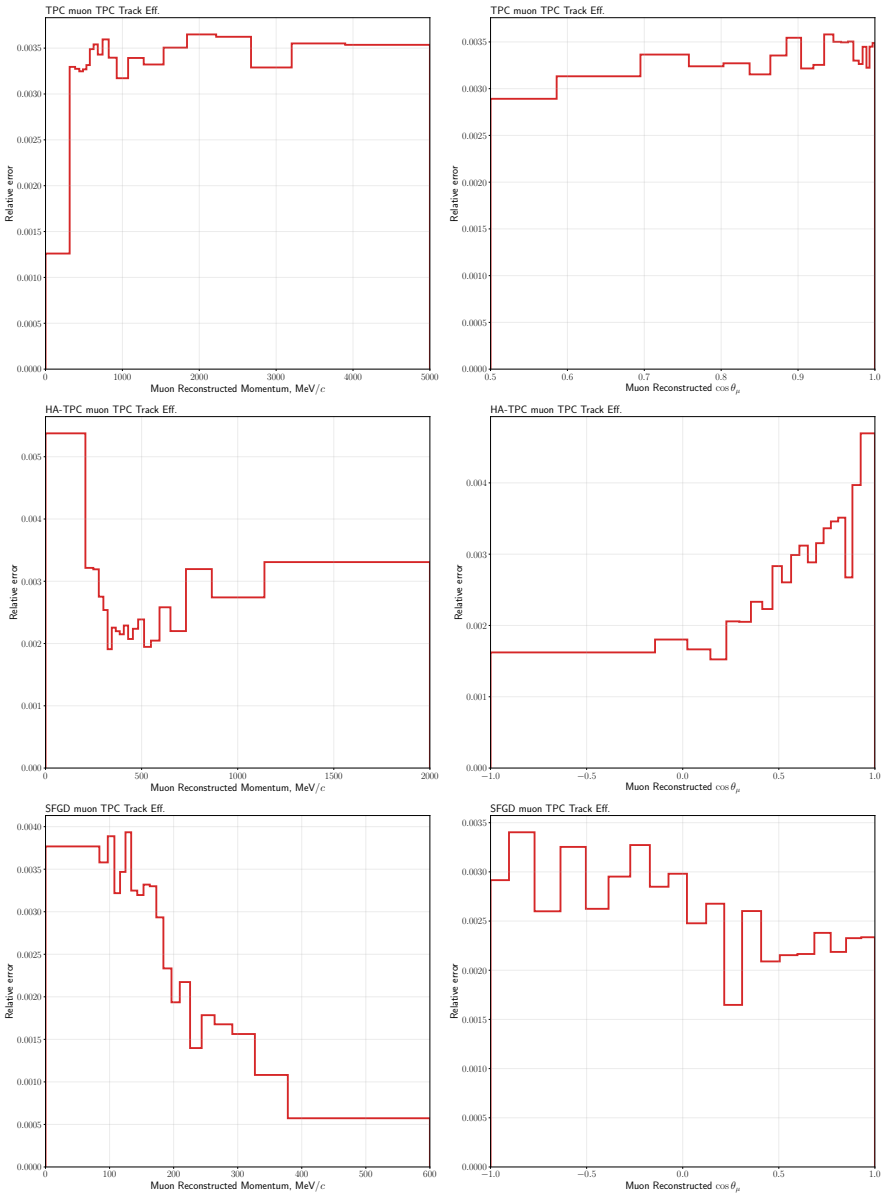


Figure A.18: Relative systematic uncertainty from the TPC tracking efficiency [13].

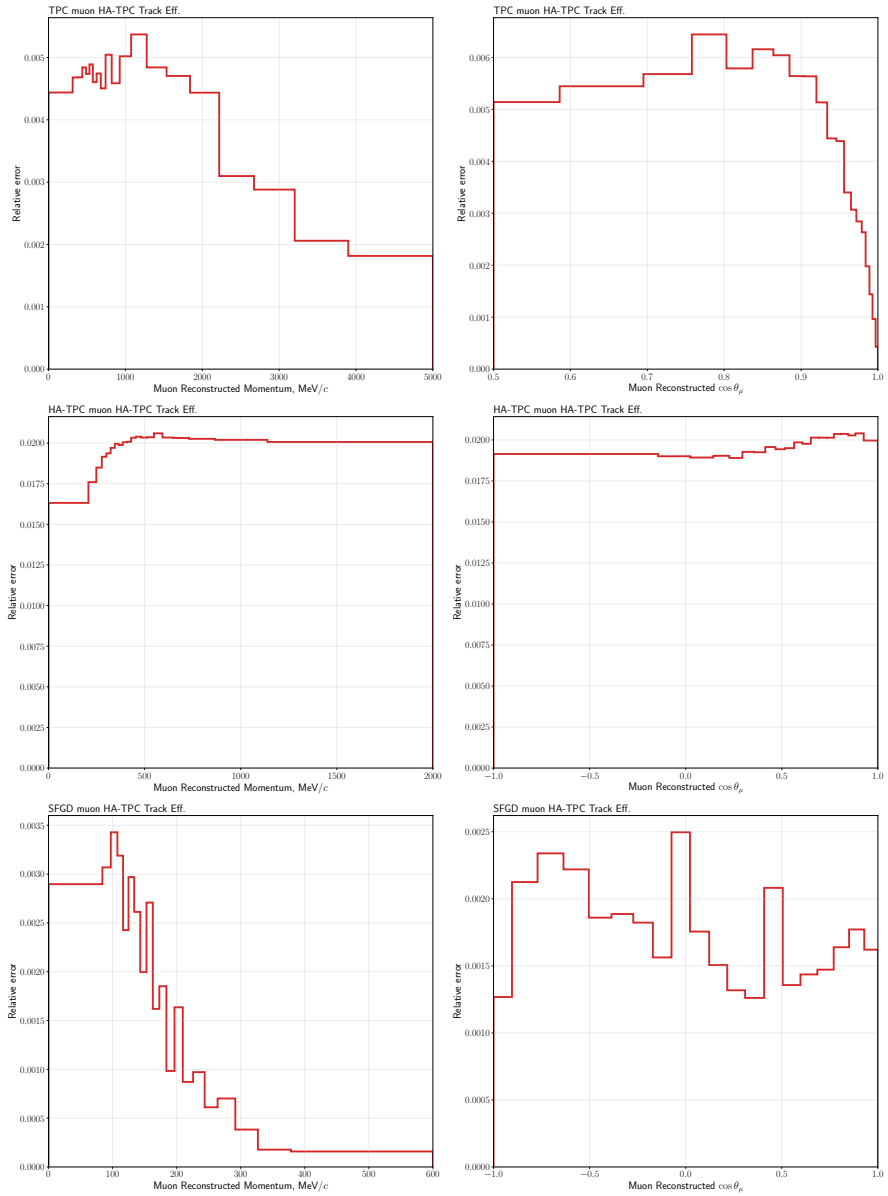


Figure A.19: Relative systematic uncertainty from the HA-TPC tracking efficiency [13].

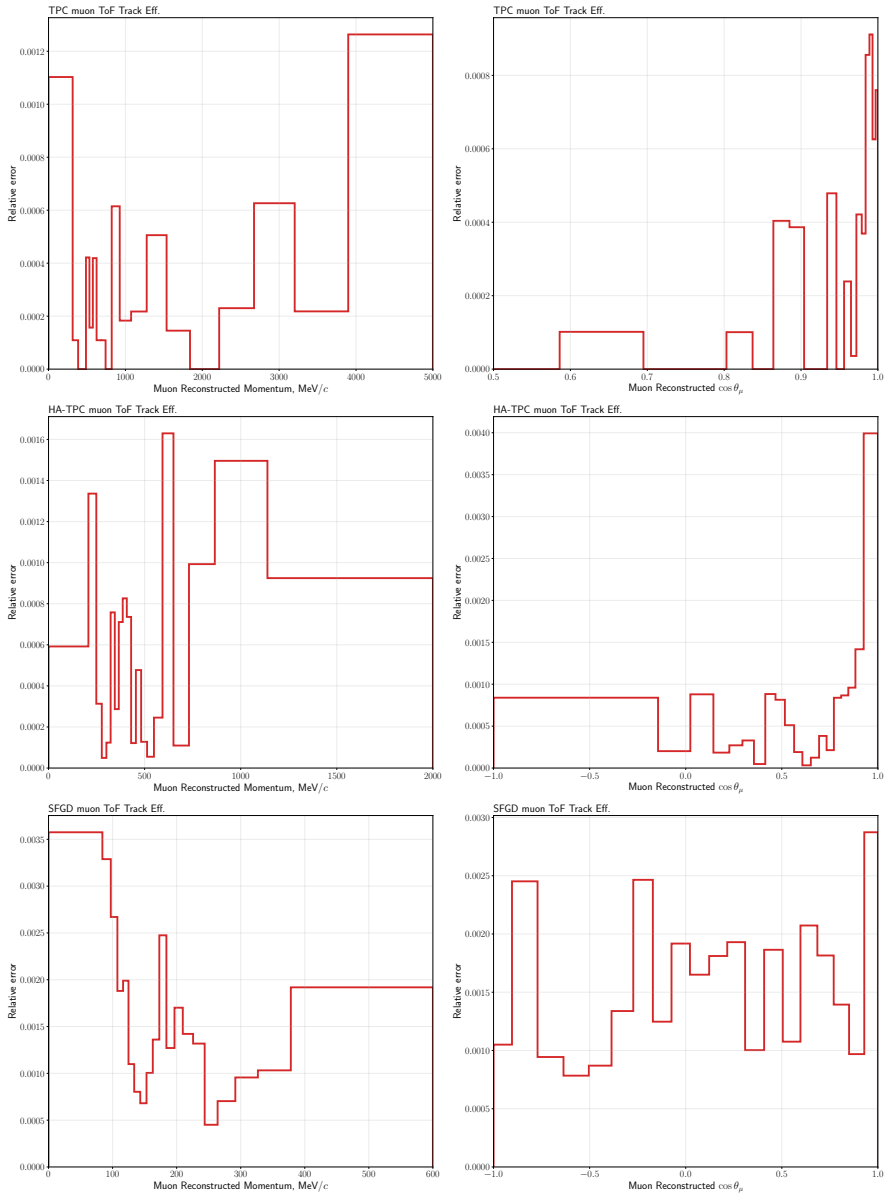


Figure A.20: Relative systematic uncertainty from the ToF tracking efficiency [13].

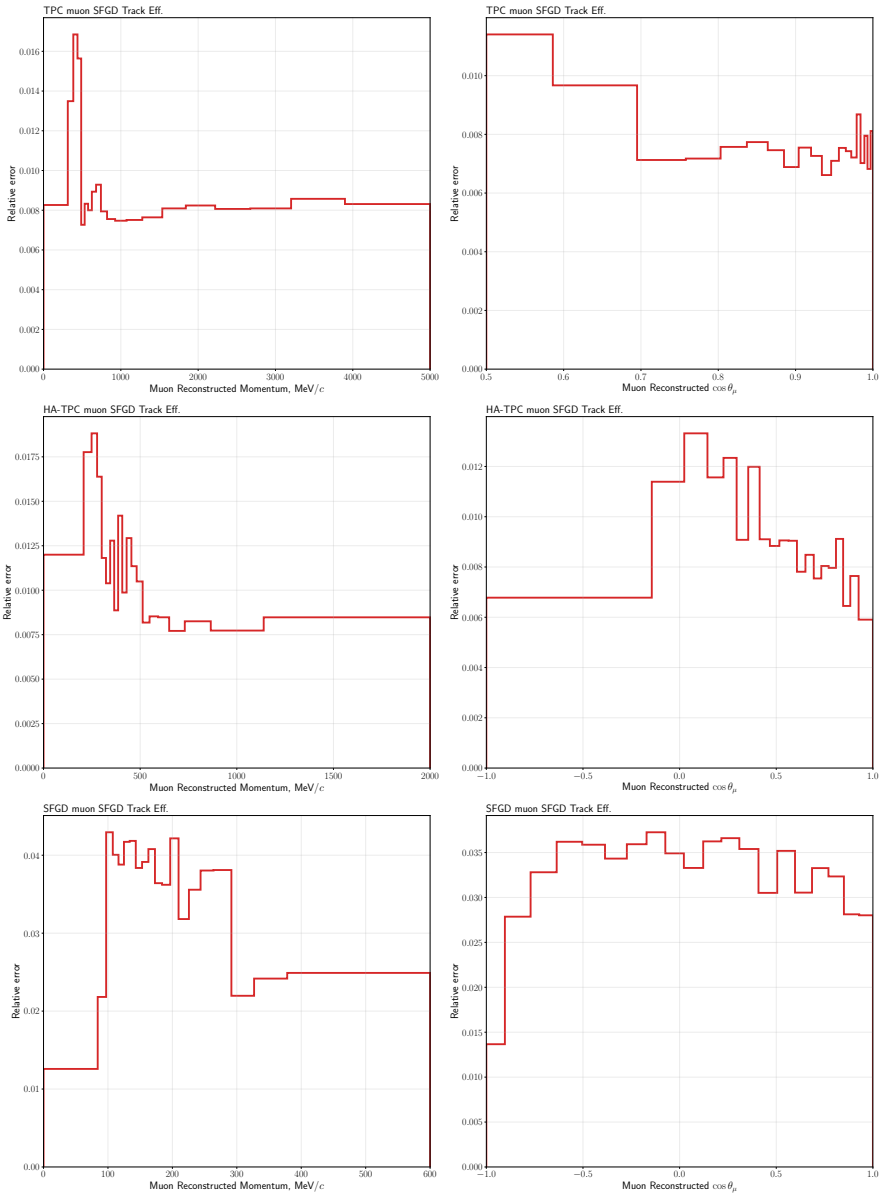


Figure A.21: Relative systematic uncertainty from the SuperFGD tracking efficiency [13].

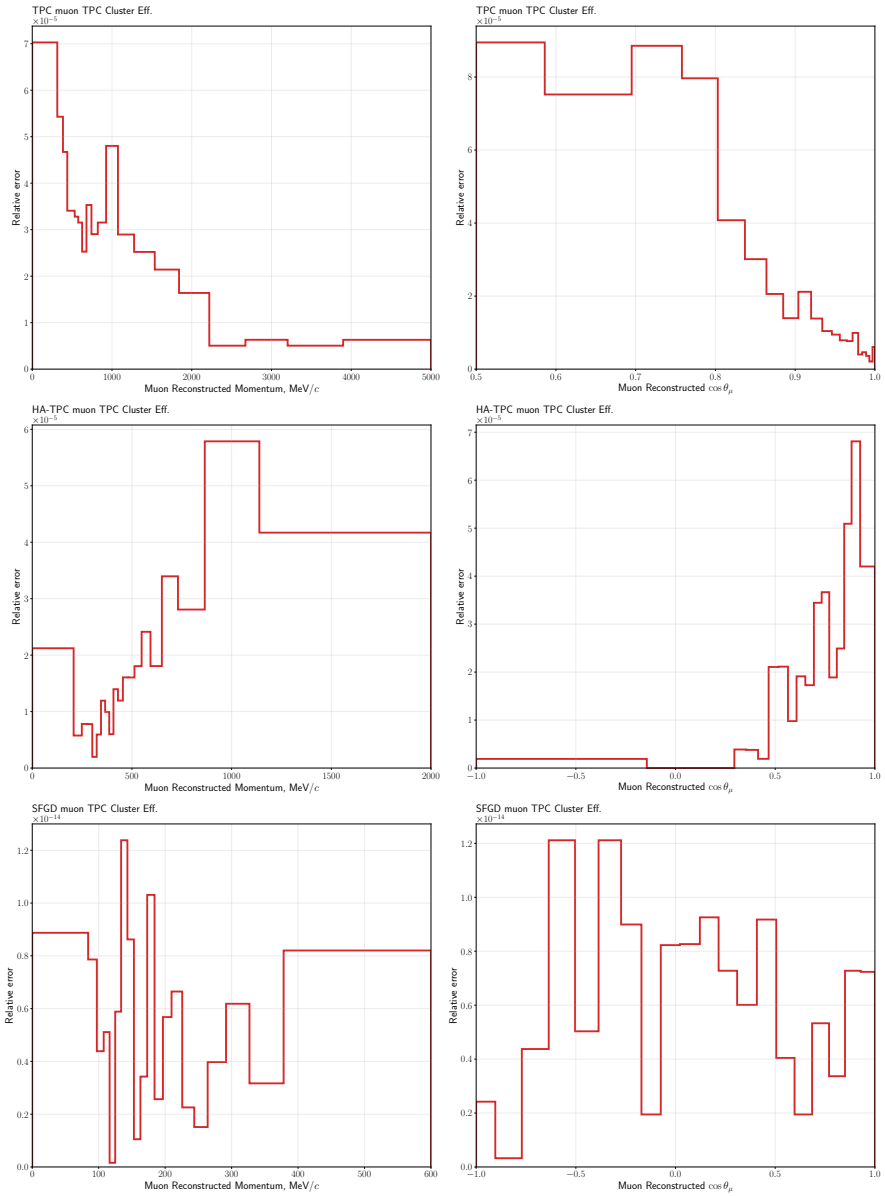


Figure A.22: Relative systematic uncertainty from the TPC cluster efficiency [13].

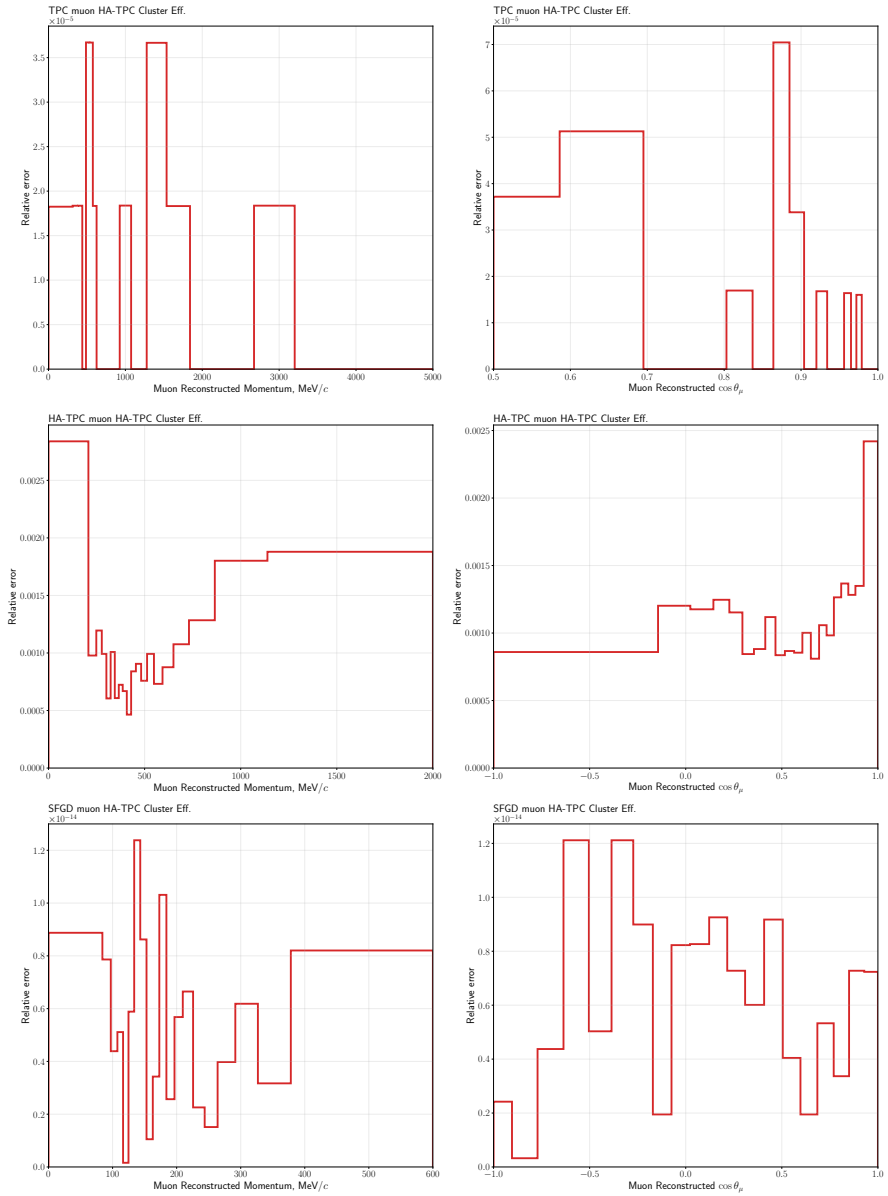


Figure A.23: Relative systematic uncertainty from the HA-TPC cluster efficiency [13].

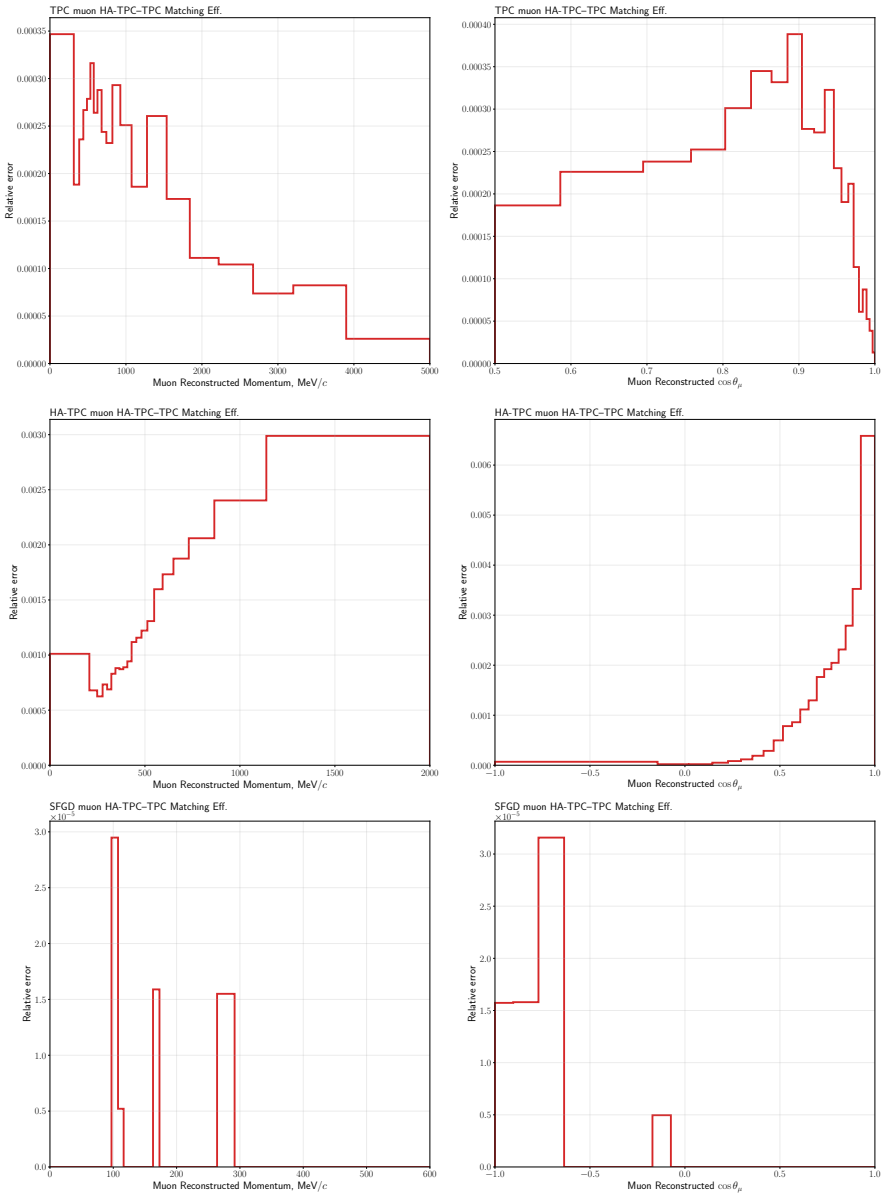


Figure A.24: Relative systematic uncertainty from the HA-TPC–TPC matching efficiency [13].

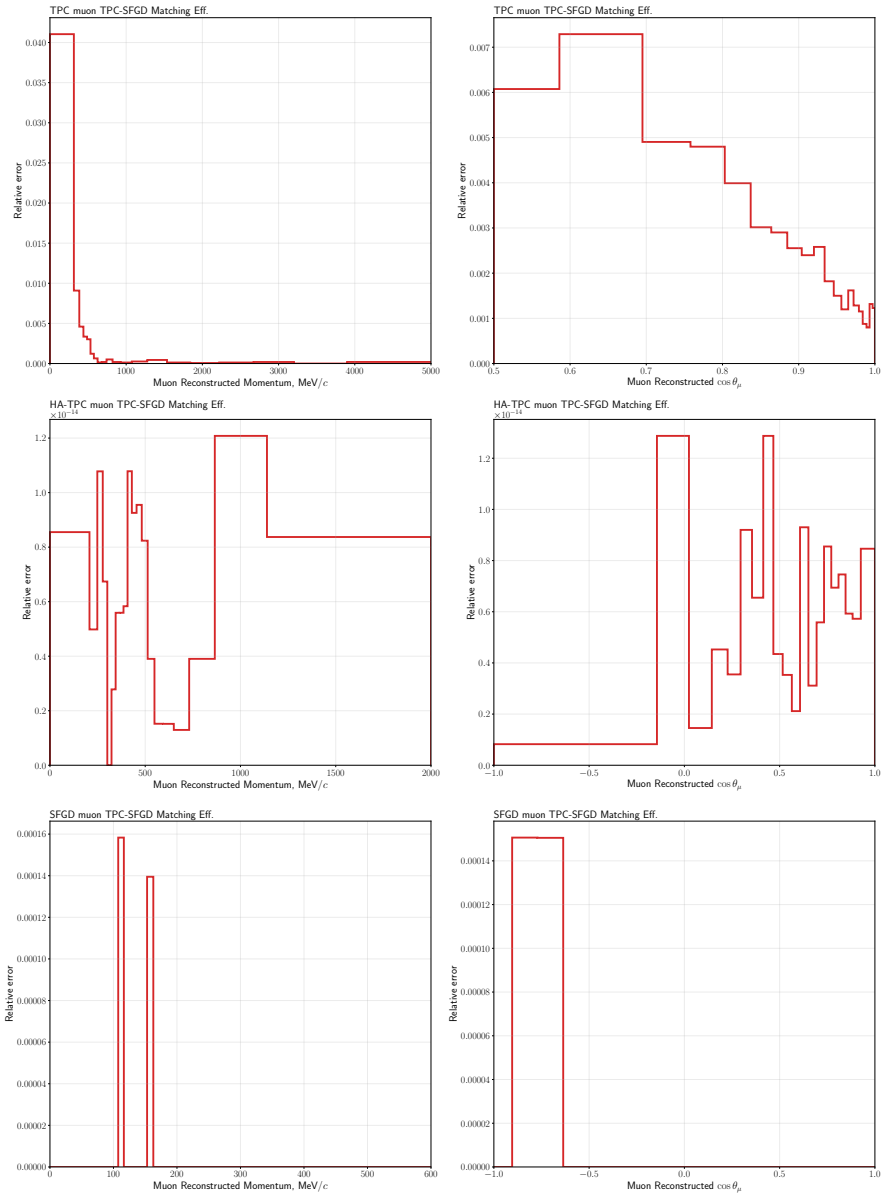


Figure A.25: Relative systematic uncertainty from the TPC–SuperFGD matching efficiency [13].

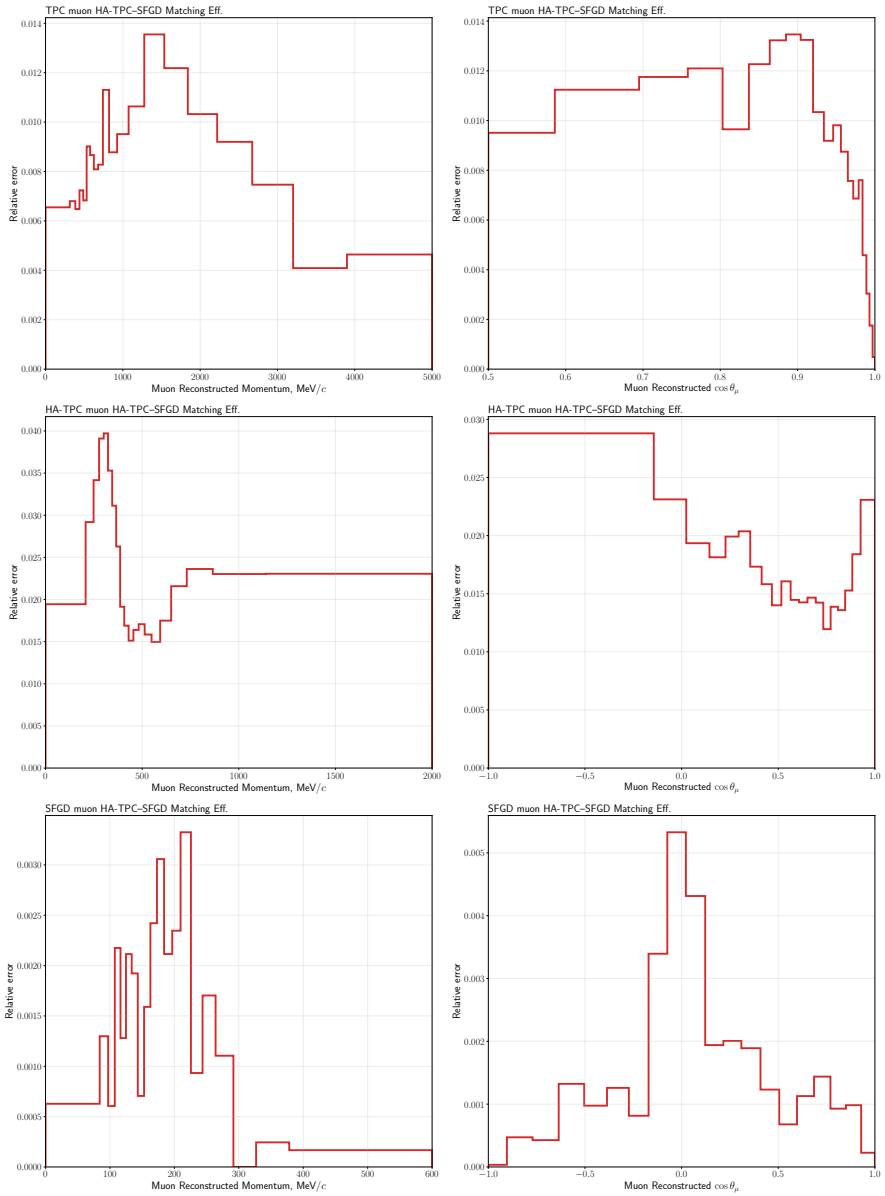


Figure A.26: Relative systematic uncertainty from the HA-TPC–SuperFGD matching efficiency [13].

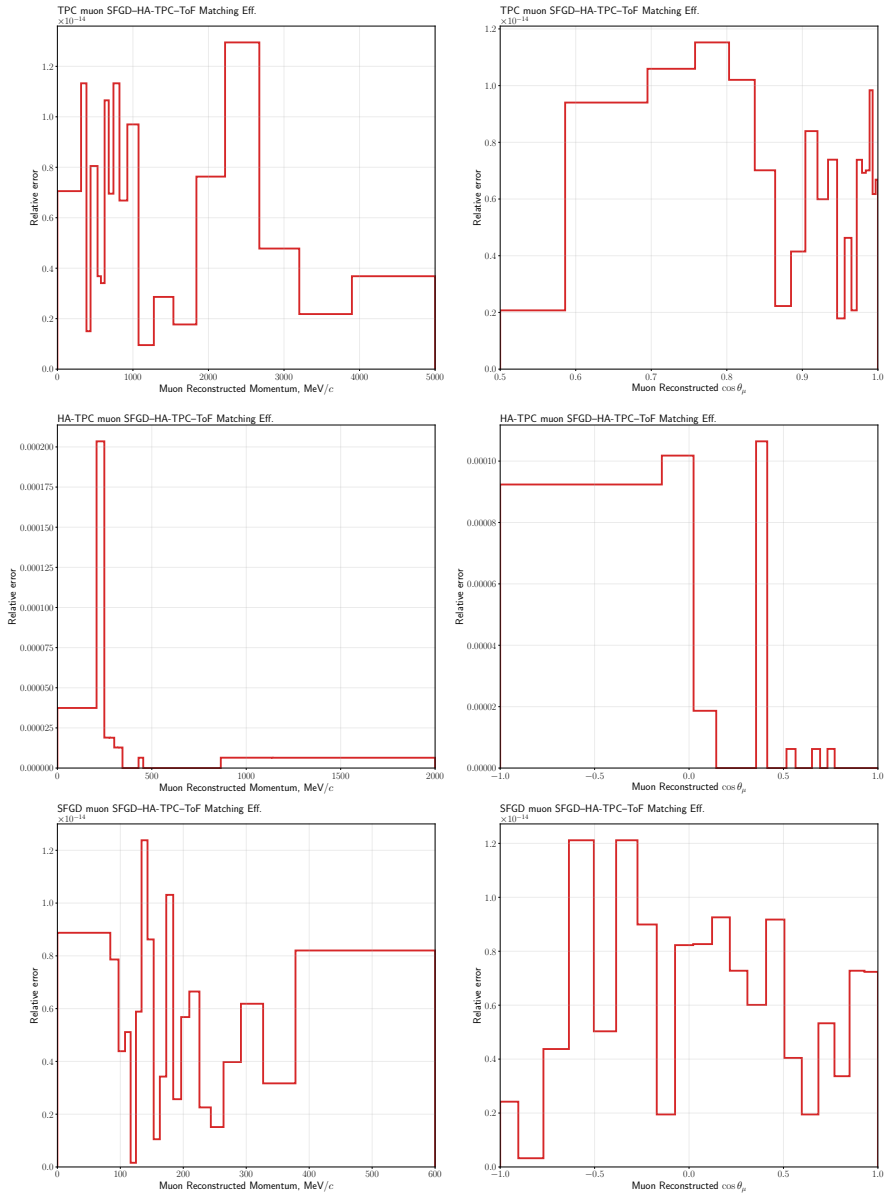


Figure A.27: Relative systematic uncertainty from the SuperFGD–HA-TPC–ToF matching efficiency [13].

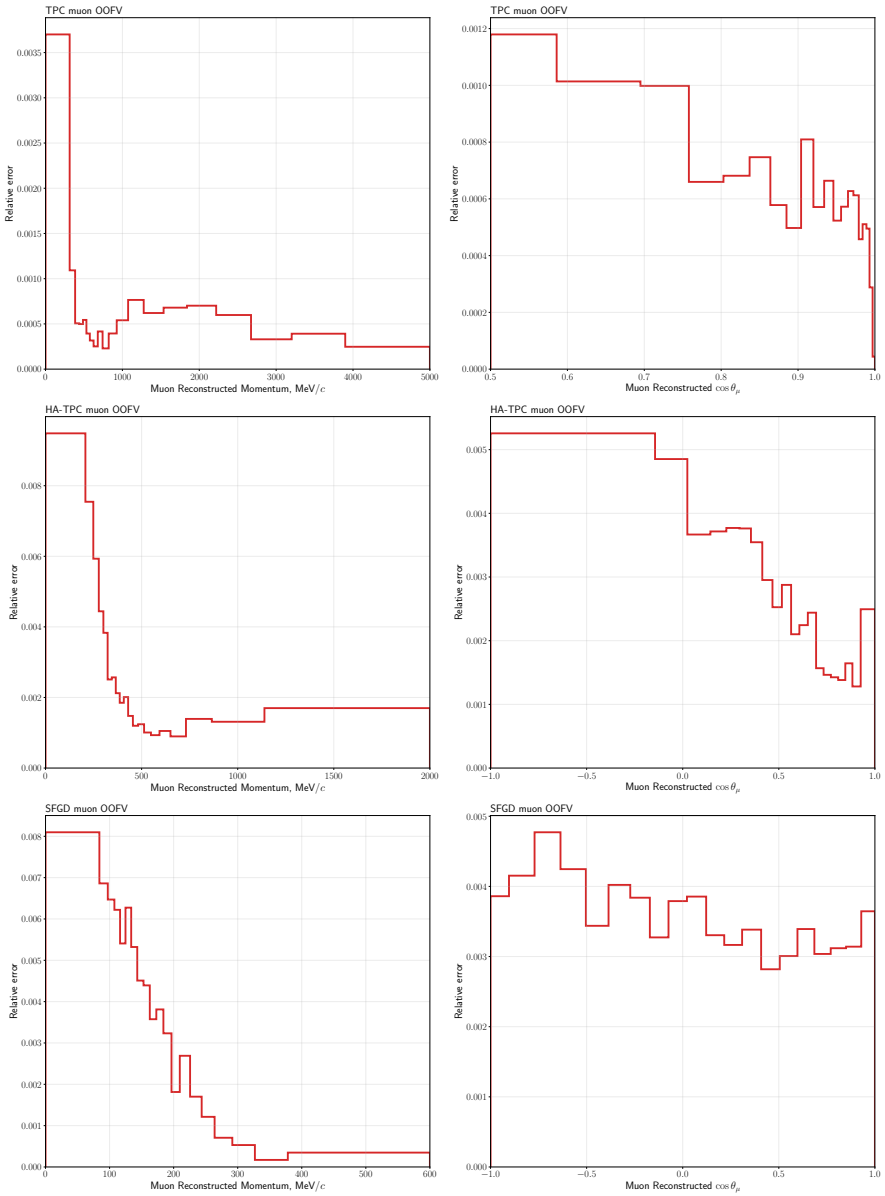


Figure A.28: Relative systematic uncertainty from the out-of-fiducial-volume background [13].

Appendix B

Markov Chain Monte Carlo in GUNDAM

Future neutrino experiment data analysis involves a large number of samples and a highly correlated parameter space. To overcome these challenges, a new fitting framework, GUNDAM (Generalized and Unified Neutrino Data Analysis Methods), was designed [63]. The development of GUNDAM is in the context of physics sensitivity studies for the ND280 Upgrade, and is based on two earlier T2K fitters: BANFF (near detector) and Super-xsllhFitter (cross section) [81]. GUNDAM can perform both frequentist analysis and Bayesian analysis. For the frequentist analysis, GUNDAM utilizes the `Minuit2` package to determine the best-fit parameter values that maximize the likelihood, together with their covariance matrix [81]. For Bayesian analysis, GUNDAM applies a Markov Chain Monte Carlo (MCMC) algorithm to sample the parameters' posterior distributions [82]. The GUNDAM frequentist fit has been validated against BANFF using the 2022 Oscillation Analysis (OA2022) near detector fit [81]. This chapter validates the GUNDAM MCMC algorithm using the same OA2022 near detector inputs, whose likelihood is defined in T2K Technical Note 423 [83] and is not introduced here. Since the validation involves Bayesian inference, this chapter first introduces Bayesian inference as background.

B.1 Bayesian inference and MCMC

In the Bayesian framework, the knowledge of the parameters after observing the data is accessed through the posterior probability distribution, given by Bayes' theorem,

$$P(\boldsymbol{\theta} \mid D) = \frac{\mathcal{L}(D \mid \boldsymbol{\theta})\,\pi(\boldsymbol{\theta})}{P(D)} \;\propto\; \mathcal{L}(D \mid \boldsymbol{\theta})\,\pi(\boldsymbol{\theta}), \tag{B.1}$$

where $\mathcal{L}(D \mid \boldsymbol{\theta})$ is the likelihood, $\pi(\boldsymbol{\theta})$ is the prior, and $P(D)$ is a normalization constant given by

$$P(D) = \int \mathcal{L}(D \mid \boldsymbol{\theta})\, \pi(\boldsymbol{\theta})\, d\boldsymbol{\theta}. \tag{B.2}$$

Usually, the posterior distribution cannot be evaluated analytically, since the integral in Equation B.2 is over a high-dimensional parameter space, on the order of 700 parameters for the OA2022 near detector inputs. Instead, the posterior can be explored with Markov Chain Monte Carlo (MCMC), which generates Markov chains whose samples are distributed according to the posterior distribution $P(\boldsymbol{\theta} \mid D)$. In a Markov chain, each step depends only on the previous one. The chain is started from an initial parameter set and when the chain is long enough its distribution approaches the posterior. The commonly used MCMC algorithm is the Metropolis algorithm [84], which is also implemented in GUNDAM. At each step, a candidate step $\boldsymbol{\theta}'$ is proposed from a symmetric distribution centered on the current step $\boldsymbol{\theta}_n$, taken here as a Gaussian $\mathcal{N}(\boldsymbol{\theta}_n, \Sigma)$ with proposal covariance Σ. The candidate is accepted with probability

$$\alpha = \min\left(1,\ \frac{P(\boldsymbol{\theta}' \mid D)}{P(\boldsymbol{\theta}_n \mid D)}\right). \tag{B.3}$$

This ratio can be expressed as

$$\frac{P(\boldsymbol{\theta}' \mid D)}{P(\boldsymbol{\theta}_n \mid D)} = \frac{\mathcal{L}(D \mid \boldsymbol{\theta}')\, \pi(\boldsymbol{\theta}')}{\mathcal{L}(D \mid \boldsymbol{\theta}_n)\, \pi(\boldsymbol{\theta}_n)}, \tag{B.4}$$

where the normalization constant $P(D)$ cancels and does not need to be evaluated. A candidate with a higher posterior probability than the current step is always accepted, and a candidate with a lower posterior probability is accepted with a probability equal to the posterior ratio. The procedure for generating the chain is summarized in Algorithm 1. The efficiency of the sampling depends strongly on the proposal covariance matrix Σ. If the proposed steps are too small, the acceptance rate is too high, the chain explores the parameter space slowly, and successive steps are strongly correlated. If the proposed steps are too large, most candidates are rejected. The sampling is most efficient when the proposal covariance is proportional to the posterior covariance [85], and when the step size is tuned so that the fraction of accepted candidates is close to an optimal acceptance rate [86].

B.2 The MCMC algorithm in GUNDAM

GUNDAM applies `TSimpleMCMC` which is a publicly available MCMC software package to generate Markov chains [87]. The package is integrated into GUNDAM by `AdaptiveMcmc`. Its main features are:

- Shares most of the code with the MINUIT fitter, including the input preparation and the likelihood calculation.

Algorithm 1 Metropolis algorithm

- Initialise a random starting point $\boldsymbol{\theta}_0$.
- At step n, generate the next step $\boldsymbol{\theta}_{n+1}$ by:
  1. Propose a candidate $\boldsymbol{\theta}'$ from a symmetric distribution $\boldsymbol{\theta}' \sim \mathcal{N}(\boldsymbol{\theta}_n, \Sigma)$.
  2. Compute the acceptance ratio $\alpha = \min(1,\ P(\boldsymbol{\theta}' \mid D)/P(\boldsymbol{\theta}_n \mid D))$.
  3. Draw a random number $r \sim \mathcal{U}(0,1)$:
     if $r < \alpha$: accept, $\boldsymbol{\theta}_{n+1} = \boldsymbol{\theta}'$.
     else: reject, $\boldsymbol{\theta}_{n+1} = \boldsymbol{\theta}_n$.
- Repeat until enough steps are sampled.

- Is configured by YAML/JSON files, like the MINUIT fitter.
- Can generate a new MCMC chain or continue an existing one.
- Can start the chain from the parameters' prior values or from a random point.
- Can take a user-defined matrix as the initial proposal covariance.
- Applies the Metropolis algorithm. During the run, the proposal covariance matrix is periodically updated from the accumulated chain history, and the step size is tuned toward a target acceptance rate (Adaptive MCMC).
- Supports a configurable burn-in stage, during which the proposal covariance and the scale factor are tuned so that the chain can sample the posterior distribution with high efficiency.

Before GUNDAM generates an MCMC chain, it first reads the configuration files to define its requirements for a statistical analysis. A long MCMC chain consists of a sequence of short chains, where each short chain continues from the last step of the previous one. The length and the number of the short chains are user-defined.

In GUNDAM MCMC, the next step $\boldsymbol{\theta}_{n+1}$ is drawn from a Gaussian proposal $\sim \mathcal{N}(\boldsymbol{\theta}_n, \Sigma)$, where $\boldsymbol{\theta}_n$ is the current step and Σ is the proposal covariance matrix. Σ can be written in terms of a scale factor s and a matrix C as $\Sigma = s^2 C$. Both s and C can be updated from the past steps to optimize the sampling efficiency. An acceptance rate of 23.4% has been recommended as optimal [86]. GUNDAM monitors the acceptance rate while generating new steps: when it is too high (low) over some number of recent steps, the scale parameter s is adjusted to a higher (lower) value. The optimal matrix C, on the other hand, is the covariance matrix of the posterior distribution [85]. To approach this, C is estimated from the accumulated steps: $C_{ij}^{\text{new}} = (1-w)C_{ij}^{\text{old}} + w(\theta_i^{\text{new}} - \bar{\theta}_i)(\theta_j^{\text{new}} - \bar{\theta}_j)$, where w is a weight

and $\bar{\theta}_i$ is the running average of the previous steps in the ith dimension. Unlike the scale factor s, which is adjusted frequently, the matrix C is refreshed only between short chains and held fixed within each.

The choice of the initial s and C is important for making the MCMC chain converge quickly and sample the posterior distribution with high efficiency. The algorithm sets the initial scale parameter to $s = \sqrt{1/d}$, where d is the dimension of the parameter space. The initial matrix C can be user-defined. In practice, we use the post-fit covariance matrix from the MINUIT fit with the same inputs, as it is a good approximation of the posterior covariance matrix. After this tuning phase, the proposal covariance matrix Σ should be fixed while sampling the posterior distribution to avoid any bias.

B.3 Validate the MCMC algorithm using the OA2022 near detector inputs

In this section, we validate the MCMC algorithm using the OA2022 near detector inputs. We demonstrate that, with a proper choice of the initial proposal covariance, GUNDAM can generate MCMC chains that converge quickly and sample the posterior distributions efficiently.

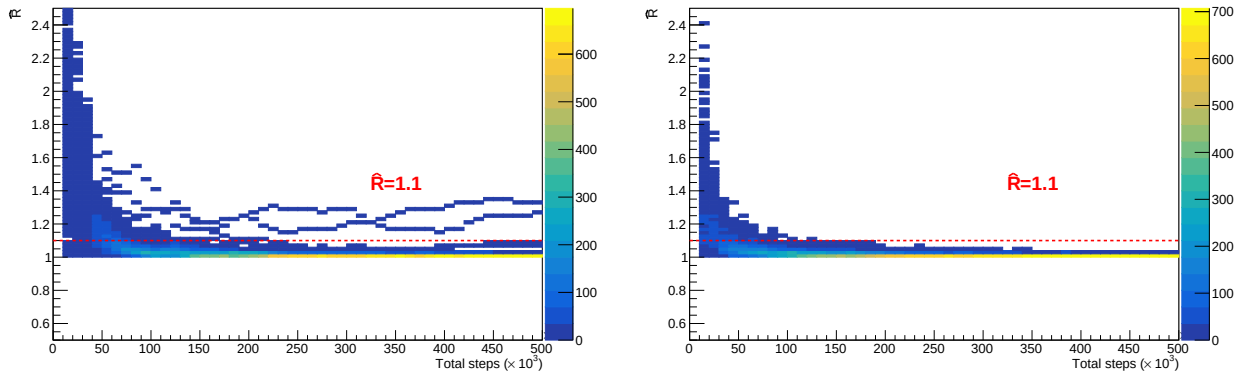
As introduced in the previous section, we take the MINUIT post-fit covariance matrix as the initial proposal matrix C, since it approximates the posterior covariance well. We therefore first perform a MINUIT fit and use its post-fit covariance as the starting C.

We run three independent MCMC chains from random starting points. In the first phase, the chains go through burn-in, during which they reach the high-probability region of the posterior and optimize their proposal covariances. Once the chains have converged, each is continued as multiple long chains, using the optimized proposal covariance, to sample the posterior distribution. In the following sections, we first show the convergence of the chains and the optimization of the proposal covariance, then study the posterior distribution they sample.

B.3.1 Burn-in steps

The burn-in steps aim at making the MCMC chains converge to the posterior distribution and at optimizing the proposal covariance matrix. As in Section B.2, the starting s is $\sqrt{1/d}$ and the starting C is the post-fit covariance matrix from the MINUIT fit. During the burn-in steps, s is continuously updated to maintain an acceptance rate of approximately 23.4%. The matrix C, however, is held fixed during the initial warm-up steps, while the chains move into the high-probability region. Afterwards, C is optimized from the accumulated steps until it becomes stable.

We consider the MCMC chains to have converged to the posterior distribution when all parameters of the three chains are well mixed and stable. We monitor the mixing and sta-



(a) Warm-up phase (first 0.5 million steps).

(b) After covariance optimization (5.0–5.5 million steps).

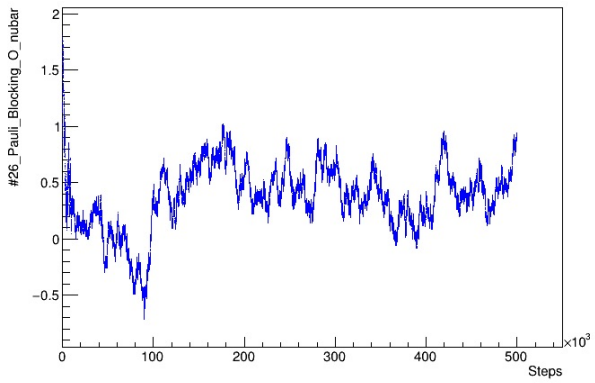
Figure B.1: $\hat{R}$ of the three MCMC chains as a function of chain length. Each plot is the distribution of $\hat{R}$ over all MCMC parameters, evaluated from the first n steps of the window ($n = 10\,000,\ 20\,000,\ \ldots,\ 0.5$ million). In (a), evaluated over the first 0.5 million steps, two parameters remain above 1.1. In (b), evaluated over the 5.0–5.5 million step window, all parameters are below 1.1.

tionarity of the parameters by the potential scale reduction $\hat{R}$. For each MCMC parameter, we calculate the $\hat{R}$ of the first n steps of the three chains. $\hat{R}$ is given by

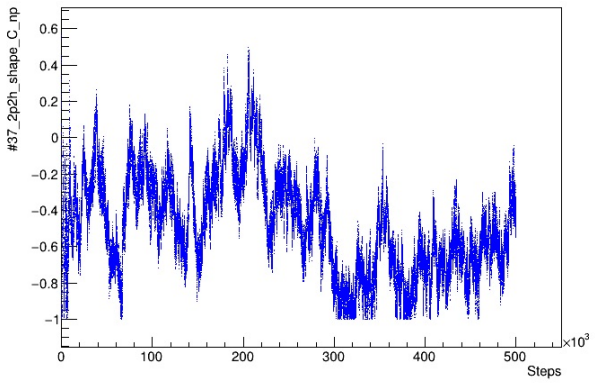
$$\hat{R} = \sqrt{\frac{[(n-1)/n]W + (1/n)B}{W}} \tag{B.5}$$

where W is the within-chain variance and B is the between-chain variance. The numerator $\hat{V} = [(n-1)/n]W + (1/n)B$ is a weighted variance which overestimates the posterior variance assuming overdispersed starting points but is an unbiased estimator after convergence. The denominator W, however, is expected to be less than $\hat{V}$ but will approach the posterior variance when the MCMC chains are long enough. From this point of view, $\hat{R}$ is greater than 1.0 and will approach 1.0 when we have more MCMC steps. We set $\hat{R} < 1.1$ as the criterion that the chains are long enough that all parameters are stable and well mixed, i.e. that the chains have converged. When calculating $\hat{R}$, each chain is split into two halves that are treated as separate sequences, which avoids the scenario in which chains are well mixed but not yet stable [88]. The full procedure is given in Appendix C.

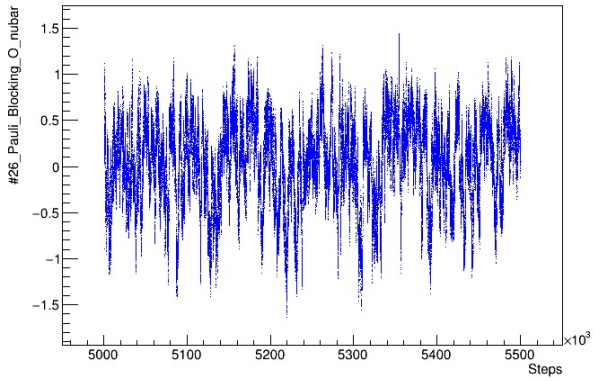
We ran 0.5 million steps for each of the three chains to reach the high-probability region. Figure B.1a shows the $\hat{R}$ within the first 0.5 million steps. After 0.5 million steps, some parameters' $\hat{R}$ are still not well below 1.1. `Pauli Blocking O nubar` and `2p2h shape C np` have the largest $\hat{R}$. Figure B.2a and Figure B.2b show the traces of these two parameters in one of the three chains, which indicates that they have not converged to their posterior



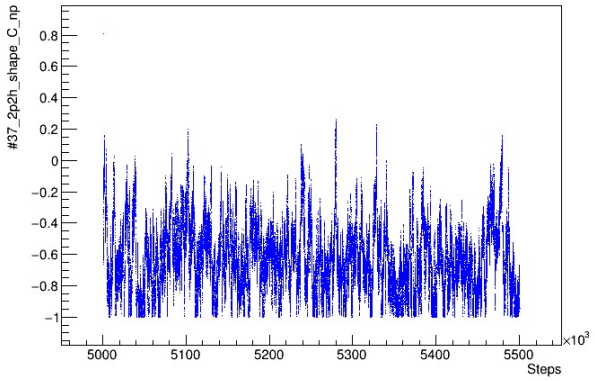
(a) `Pauli Blocking O nubar`, steps 0–0.5 million.



(b) `2p2h shape C np`, steps 0–0.5 million.

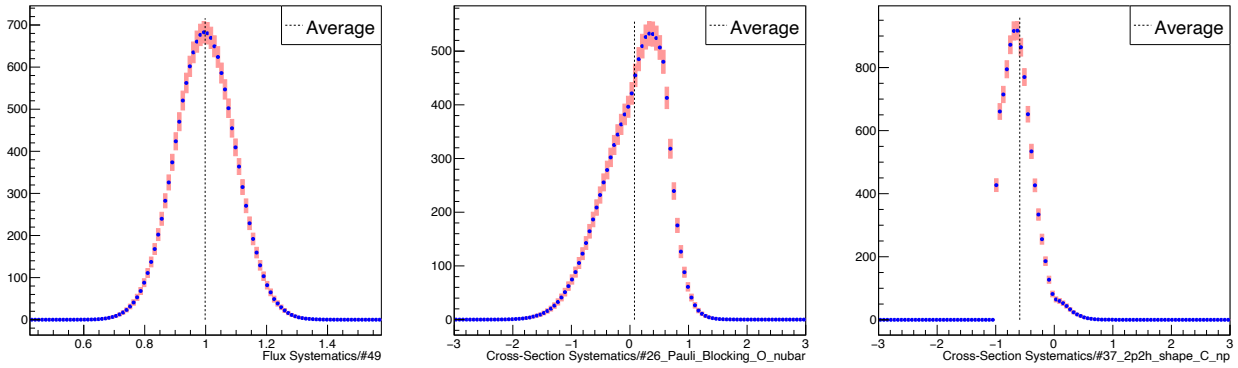


(c) `Pauli Blocking O nubar`, steps 5.0–5.5 million.



(d) `2p2h shape C np`, steps 5.0–5.5 million.

Figure B.2: Traces of the two slowest-converging parameters, `Pauli Blocking O nubar` (left) and `2p2h shape C np` (right), in one of the three chains. Top row: the first 0.5 million (warm-up) steps, before covariance optimization, where neither parameter has converged. Bottom row: the 5.0–5.5 million step window, after optimization, where both traces are stationary and weakly autocorrelated.



(a) `NDANuModeNueb6`. (b) `Pauli Blocking O nubar`. (c) `2p2h shape C np`.

Figure B.3: Examples of posterior distributions. The histograms are scaled to the parameters' effective sample size, and the error bars account for a finite effective sample size.

distributions. The choice of the initial matrix C did not make these two parameters converge quickly. The MINUIT post-fit covariance is a poor approximation of the posterior covariance for parameters whose response is non-smooth or whose best-fit value lies near a physical boundary, so it provides a poor starting proposal and makes them converge slowly. Since only a few parameters have not converged, we assume that the distribution of the accumulated steps is close enough to the posterior distribution and can be used to optimize the matrix C.

We ran another five million steps to optimize the matrix C. The matrix C is fixed within a short chain and updated between two consecutive short chains. The improving matrix C can accelerate the parameters' convergence. All parameters have converged after another five million steps, which is shown by the $\hat{R}$ of the last 0.5 million steps. Discarding the first five million steps of all three chains, Figure B.1b shows the $\hat{R}$ of the first n steps of all parameters, which are below 1.1 once n exceeds about 0.2 million steps. Figure B.2c and Figure B.2d are the traces of the last 0.5 million steps of `Pauli Blocking O nubar` and `2p2h shape C np` in a chain. The stable traces and the small correlation between the steps indicate that these two parameters have converged.

After the 5.5 million burn-in steps, all three starting chains have converged to the posterior distribution and their proposal covariance matrices have been optimized.

B.3.2 MCMC posterior samples

The three converged chains are continued with multiple independent long chains, using the optimized proposal covariance matrices, to sample the posterior distribution.

Specifically, each converged chain is continued as six independent chains of six million steps. These six chains start from the last step of the converged chain and use its optimized

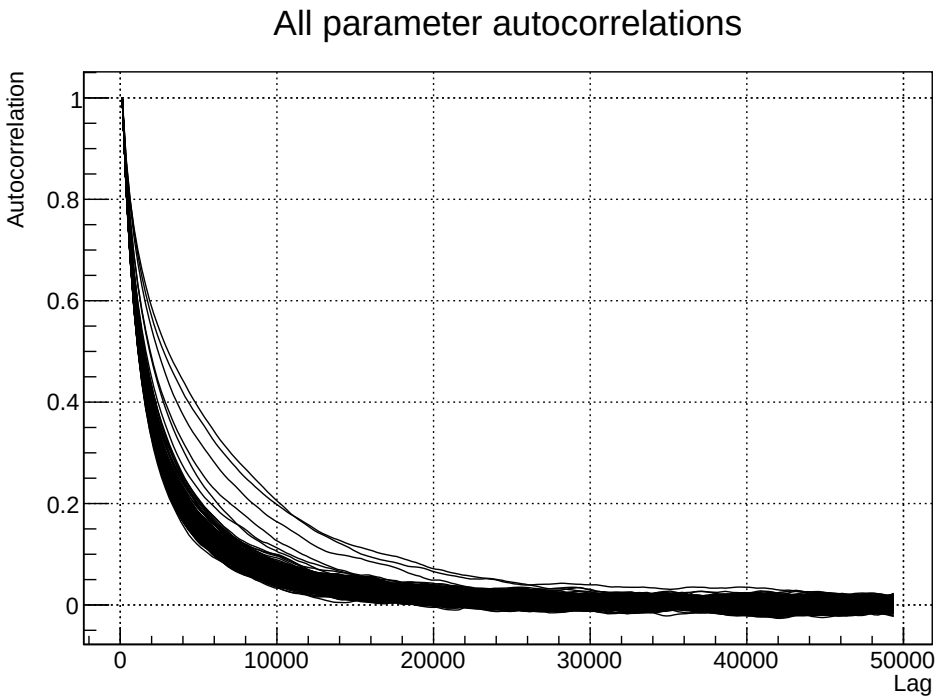


Figure B.4: Auto-correlation as a function of lag for all parameters.

proposal covariance matrix. The proposal covariance matrix is held fixed throughout the sampling to avoid any bias. Because the six chains share the same starting step, they are correlated at the beginning. The first one million steps of each are therefore discarded so that the chains become independent. Applying this procedure to all three converged chains yields 18 independent chains with a total of 90 million steps.

Figure B.3 shows examples of the marginalized posterior distributions sampled by the chains, for a flux parameter `NDANuModeNueb6` and for the two slowest-converging cross-section parameters, `Pauli Blocking O nubar` and `2p2h shape C np`.

Figure B.4 shows the auto-correlations of all parameters as a function of the lag. They decrease below 0.1 for lags larger than $20,000$. The effective sample size N_{eff} of a parameter is calculated using Equation B.6, where $\rho(k)$ is the auto-correlation at lag k, and the sum $1 + 2\sum_{k=1}^{\infty} \rho(k)$ is truncated at a lag of $50,000$.

$$N_{eff} = \frac{N}{\sum_{k=-\infty}^{\infty} \rho(k)} = \frac{N}{1 + 2\sum_{k=1}^{\infty} \rho(k)} \tag{B.6}$$

With 90 million total steps, the effective sample size of a parameter is about 15,000. From the central limit theorem, the statistical uncertainty of the sample mean of a parameter can be estimated as $\hat{\sigma}/\sqrt{N_{eff}}$, where $\hat{\sigma}$ is the standard deviation of the parameter's posterior

distribution. Relative to $\hat{\sigma}$, this is $1/\sqrt{N_{eff}} \approx 0.8\%$, which is negligible, so the effective sample size obtained from 90 million steps is large enough for this study.

B.3.3 Comparisons of MINUIT and MCMC data fit results

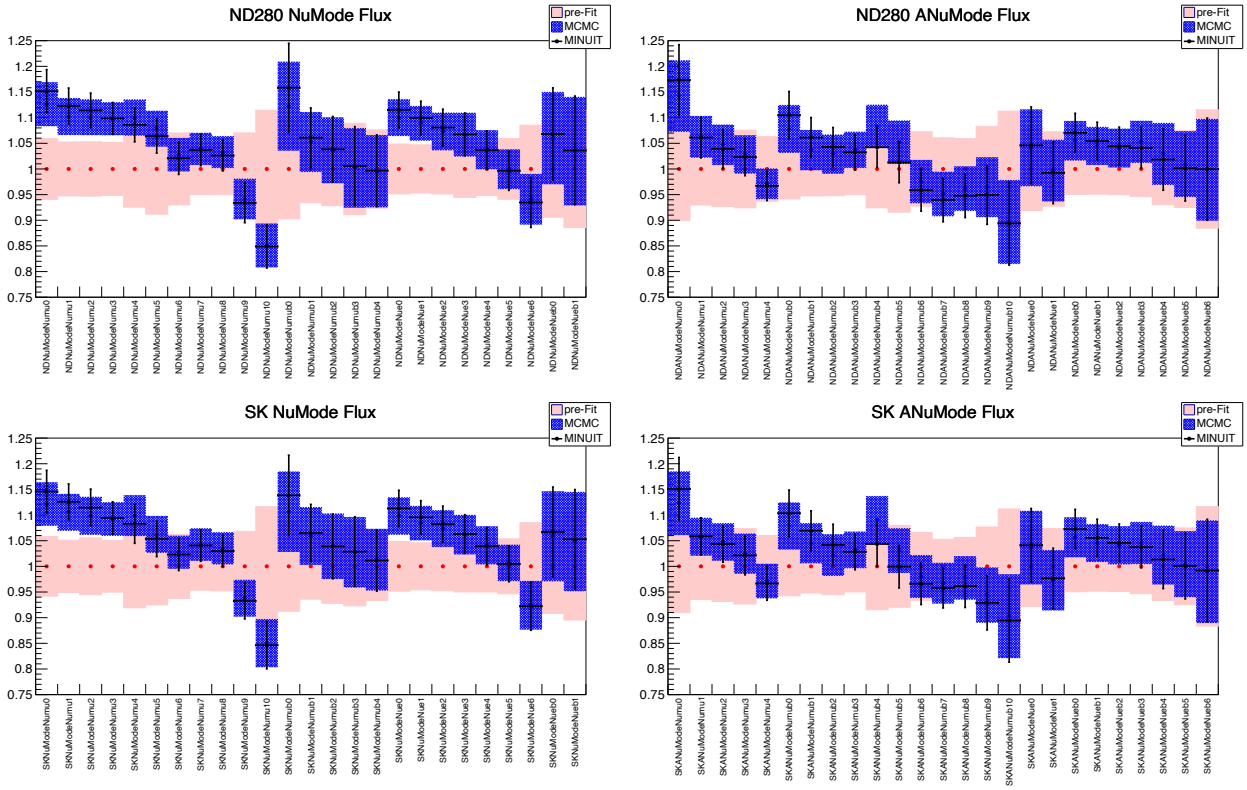


Figure B.5: Comparison between GUNDAM MINUIT and GUNDAM MCMC in terms of the flux parameters obtained from the data fit. The red points and pink error bands represent pre-fit central values and pre-fit errors. The black points and error bars indicate the post-fit values and errors of MINUIT. The blue points and error bands correspond to the posterior central values and errors of MCMC.

The parameter posterior central value is estimated as the average of the posterior sample, and the posterior uncertainty is estimated as the standard deviation of the sample. The results of the MINUIT and MCMC data fits are shown in Figure B.5 (flux), Figure B.6 (detector), and Figures B.7 and B.8 (cross-section). Overall the results show good agreement, except for a few parameters, which can be attributed to the marginalization effect, non-Gaussian posterior distributions, or differences in the implementation of these parameters in MINUIT and MCMC. For example, `2p2h shape C np` shows different post-fit central

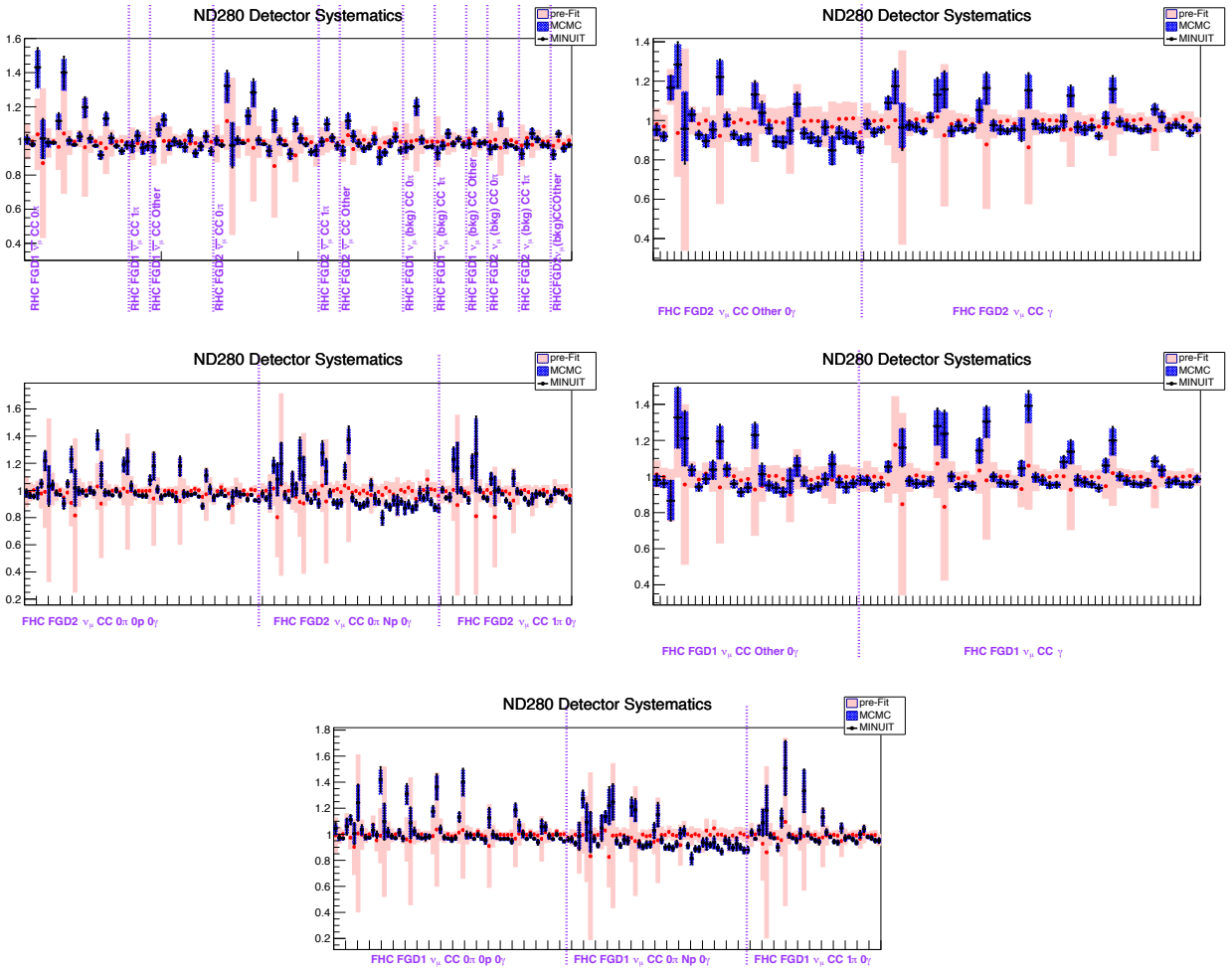


Figure B.6: Comparison between GUNDAM MINUIT and GUNDAM MCMC in terms of the detector parameters obtained from the data fit. The red points and pink error bands represent pre-fit central values and pre-fit errors. The black points and error bars indicate the post-fit values and errors of MINUIT. The blue points and error bands correspond to the posterior central values and errors of MCMC.

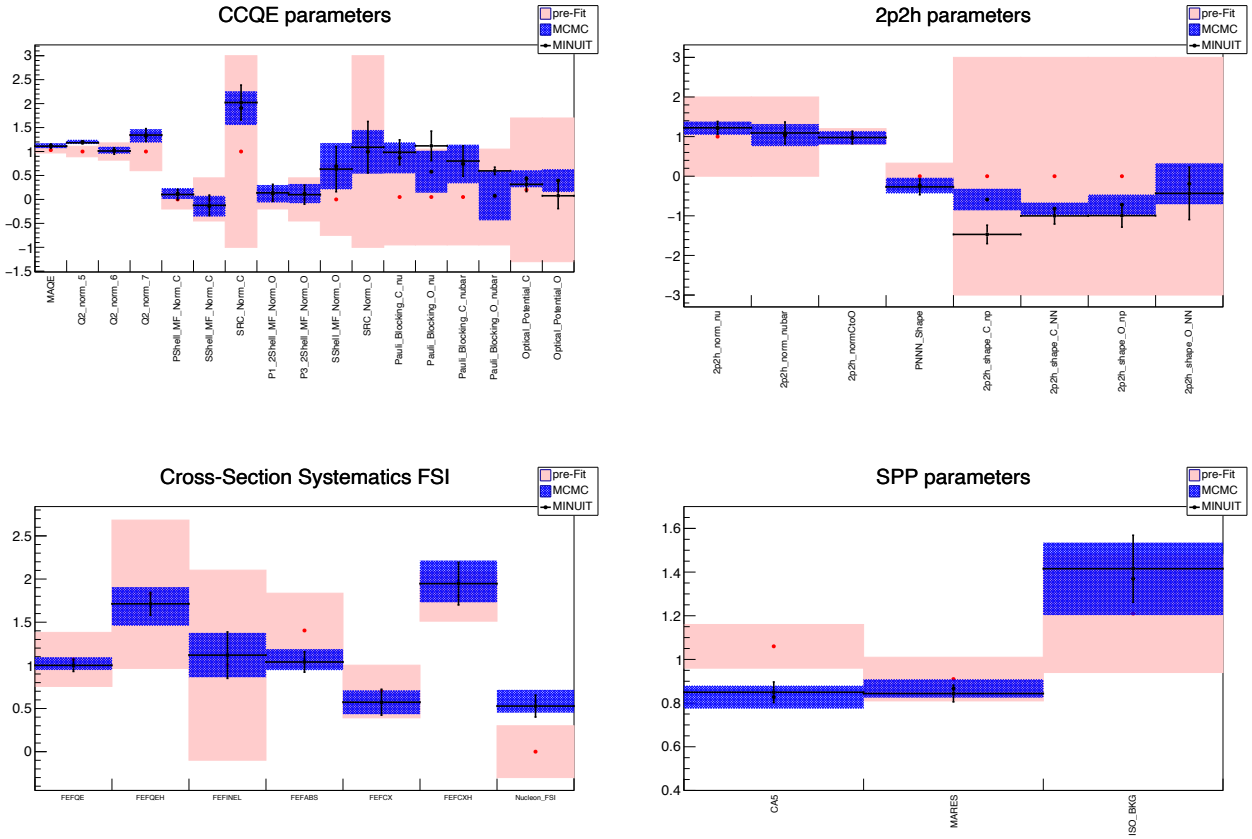


Figure B.7: Comparison between GUNDAM MINUIT and GUNDAM MCMC in terms of the cross-section parameters obtained from the data fit (part 1 of 2). The red points and pink error bands represent pre-fit central values and pre-fit errors. The black points and error bars indicate the post-fit values and errors of MINUIT. The blue points and error bands correspond to the posterior central values and errors of MCMC.

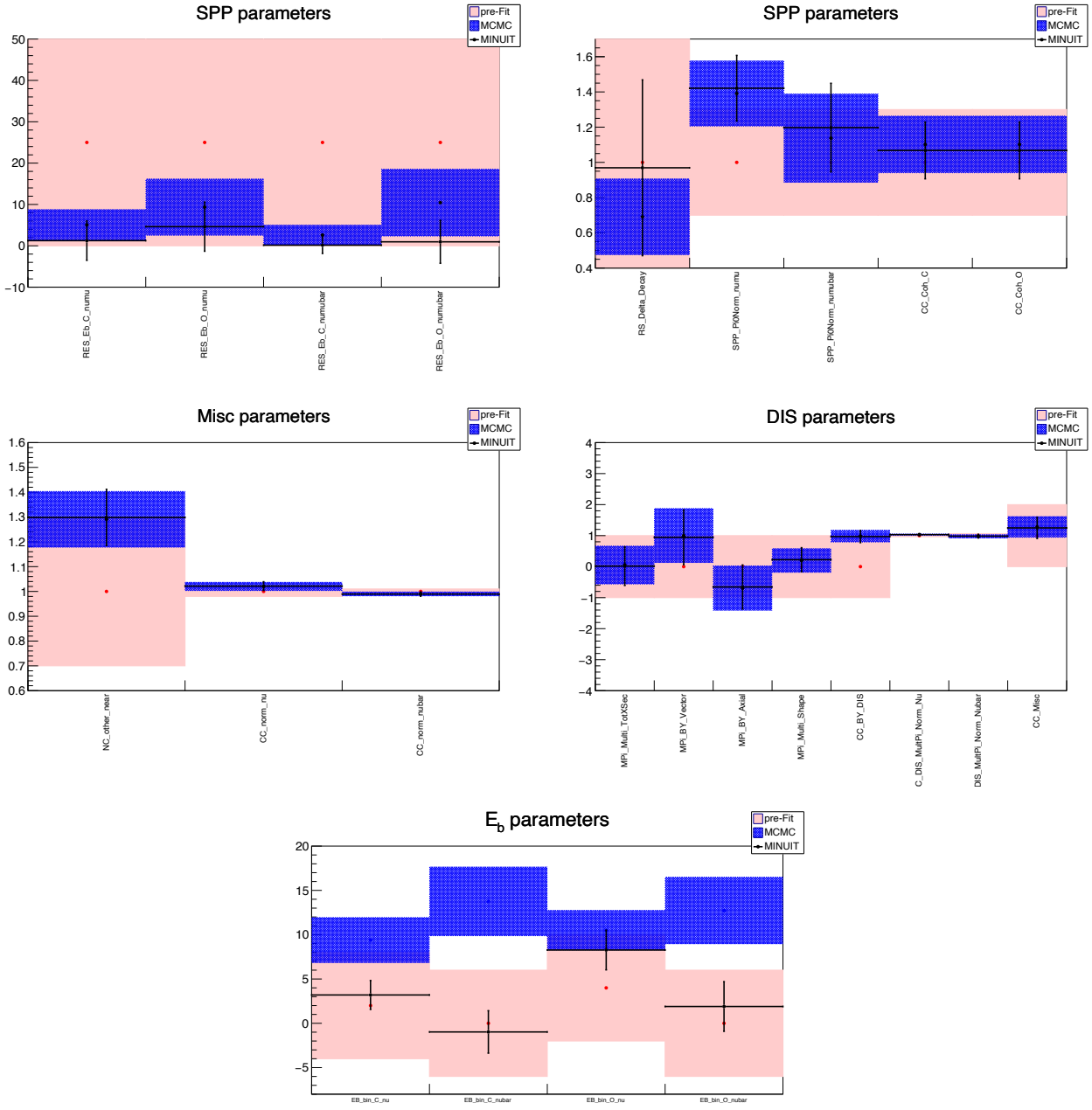


Figure B.8: Comparison between GUNDAM MINUIT and GUNDAM MCMC in terms of the cross-section parameters obtained from the data fit (part 2 of 2). The red points and pink error bands represent pre-fit central values and pre-fit errors. The black points and error bars indicate the post-fit values and errors of MINUIT. The blue points and error bands correspond to the posterior central values and errors of MCMC.

values in MINUIT and MCMC because MINUIT mirrors this parameter's spline at the boundary -1. Once the mirrored MINUIT value is folded back into the physical space, the two agree [83].

B.4 Summary

This chapter introduces the MCMC algorithm in the GUNDAM fitting framework. GUNDAM applies an adaptive MCMC algorithm to sample the posterior distributions of the parameters. To make the chain converge to the posterior quickly, a good initial proposal covariance matrix is essential, which can be the MINUIT post-fit covariance matrix. To sample the posterior with high efficiency, GUNDAM optimizes the proposal covariance and the proposal step size based on the past steps.

GUNDAM MCMC is validated using the OA2022 near detector inputs. The consistency between the GUNDAM MINUIT and MCMC results shows the reliability of GUNDAM MCMC. The procedures of choosing the initial proposal covariance matrix, studying the convergence of the MCMC chains, and sampling the posterior distribution can serve as a reference for future Bayesian analyses with GUNDAM MCMC, including upcoming T2K analyses and future experiments such as DUNE.

Appendix C

Potential Scale Reduction

The procedure to calculate the potential scale reduction of a random variable follows the reference [88]. Assuming that we have m MCMC chains and each chain has n total steps, the random variable that we are interested in (e.g. likelihood values, or a parameter value in a given dimension) is denoted as θ_{ij} (the ith of the n steps in chain j). Letting $\bar{\theta}_{\cdot j} = \frac{1}{n}\sum_{i=1}^{n}\theta_{ij}$ and $\bar{\theta}_{\cdot\cdot} = \frac{1}{m}\sum_{j=1}^{m}\bar{\theta}_{\cdot j}$, we compute the between-sequence variance B and the within-sequence variance W:

$$B = \frac{n}{m-1}\sum_{j=1}^{m}(\bar{\theta}_{\cdot j} - \bar{\theta}_{\cdot\cdot})^2 \tag{C.1}$$

$$W = \frac{1}{m(n-1)}\sum_{j=1}^{m}\sum_{i=1}^{n}(\theta_{ij} - \bar{\theta}_{\cdot j})^2 \tag{C.2}$$

Finally, we define the potential scale reduction of the random variable θ:

$$\hat{R} = \sqrt{\frac{[(n-1)/n]W + (1/n)B}{W}} \tag{C.3}$$

With dispersed starting points, the numerator $[(n-1)/n]W + (1/n)B$ overestimates the marginal posterior variance of θ at the early stage of the MCMC chains. Meanwhile, W underestimates the variance, since the MCMC chains have not explored all parts of the posterior distribution. In this case, $\hat{R}$ is larger than 1.0. When the number of steps is large enough, both W and the numerator $[(n-1)/n]W + (1/n)B$ approach the posterior variance, and $\hat{R}$ converges to 1.0.

When calculating $\hat{R}$ we split each chain into the first half and the second half. For example, if we have three chains and want to calculate $\hat{R}$ of the first $2n$ steps, we split each chain into the first n steps and the second n steps. We then apply Equations C.1–C.3 to calculate $\hat{R}$ with chain length n and chain number $m = 6$. This avoids the condition that the MCMC chains are well mixed but not stable [88]. We monitor the parameter's mixing and

stationarity by $\hat{R}$ and set $\hat{R} < 1.1$ as the criterion that the MCMC chains are long enough for convergence.